Synthesis, Characterization and Catalytic Performance of Dedicated Ceria-Zirconia Catalysts for HCl Oxidation Reaction

Cumulative dissertation

Presented by

Yu Sun

Submitted to the

Faculty of Biology and Chemistry

For the degree of

Doktor der Naturwissenschaften

(*Dr. rer. nat.*)

Justus Liebig University Giessen, Germany

Giessen, September 2024

This thesis is accepted as a doctoral dissertation in fulfillment of the requirements for the degree of *Doctor Rerum Naturalium* by the Faculty of Biology and Chemistry, Justus Liebig University Giessen, Germany.

1st. Reviewer Prof. Dr. Herbert Over

Institute of Physical Chemistry, Justus Liebig University Giessen

2nd. Reviewer Prof. Dr. Yanglong Guo

Research Institute of Industrial Catalysis, East China University of Science & Technology

“I declare that I have completed this dissertation single-handedly without the unauthorized help of a second party and only with the assistance acknowledged therein. I have appropriately acknowledged and cited all text passages that are derived verbatim from or are based on the content of published work of others, and all information relating to verbal communications. I consent to the use of an anti-plagiarism software to check my thesis. I have abided by the principles of good scientific conduct laid down in the charter of the Justus Liebig University Giessen „Satzung der Justus-Liebig-Universität Gießen zur Sicherung guter wissenschaftlicher Praxis“ in carrying out the investigations described in the dissertation.”

Location, date	Signature

Acknowledgements

Most likely, Giessen is the place I've been dreaming about most often over the past few years, because the scenes that come up so often in dreams are places where people have fond memories of but can't go back to. The completion of a doctoral thesis is always very challenging and I am very grateful to all my collaborators for their help and support along the way.

I would like to show my deepest appreciation to Prof. Dr. Herbert Over. I am truly grateful to have had the opportunity to benefit from his thoughtful approach to academic matters, his extensive theoretical knowledge, and his dedication to research work. I am truly thankful for his guidance which has helped me to gain a more systematic and profound understanding of the Deacon reaction and of cerium oxide. Additionally, I appreciate his genuine care for me, which helped me to adapt more easily to life in Germany. I would like to express my gratitude once again for these experiences in Germany: Dankeschön!

I would also like to express my gratitude to Prof. Dr. Yanglong Guo for his invaluable guidance, he opened the door to the fascinating field of catalysis. From the initial selection of topics to the subsequent guidance of experiments, his support was instrumental in my doctoral journey. I would also like to express my gratitude for the support provided during my application for the CSC for overseas study, which presented me with the valuable opportunity to expand my horizons.

I want to extend my gratitude to Prof. Dr. Bernd M. Smarsly, who co-supervised my research at Justus Liebig University Giessen. I am immensely grateful for his generous support in providing equipment for the preparation and characterization of catalysts. Additionally, he offered innovative suggestions greatly benefited my research.

I would like to express my gratitude to Prof. Dr. Franziska Hess of Technische Universität Berlin for her invaluable assistance with the JMAK model. She has developed an excellent model and contributed significantly to the manuscript. I would like to extend my gratitude to Prof. Dr. Igor Djerdj of the J. J. Strossmayer University of Osijek for his invaluable assistance in the Rietveld refinement of the XRD data.

I would like to extend my gratitude to all the other professors from the Research Institute of Industrial Catalysis (RIIC) in Shanghai, including Prof. Dr. Yun Guo, Prof. Dr. Wangcheng Zhan, Prof. Dr. Li Wang and Prof. Dr. Aiyong Wang.

I would like to express my gratitude to all those at AG Over, AG Smarsly and RIIC, who have assisted me and provided invaluable support.

I would like to extend my gratitude to Gabi Scheller and Antonella D'Ambrosio for their invaluable assistance with the organizational issues.

I thank Dr. Chenwei Li, Dr. Zheng Wang, Dr. Wei Wang and Dr. Yu Wang for continuous support in Germany.

I thank Dr. Pascal Cop for the support in the OSC/OSCc apparatus.

I thank Dr. Omeir Khalid for the CO oxidation reaction apparatus and SEM analysis.

I thank Dr. Joachim Sann and Dr. Tim Weber for the help with XPS measurement and analysis.

I thank Dr. Xiaohan Guo for the TEM and ICP measurements.

I would like to express my gratitude to Dr. Sebastian Werner and Dr. Kevin Turke for their assistance with the N_2-sorption experiments. There are, in fact, a considerable number of samples.

I thank Dr. Christian Sack, Dr. Marcel J. S. Abb, Dr. Phillip Timmer, Dr. Volkmar Koller, Dr. Dongsheng Qiao, Dr. Wenbo Zhang, Dr. Xiang Zheng, Dr. Chuanhui Zhang, Dr. Chengcheng Tian, Dr. Chao Wang, Dr. Qing Zhang, Dr. Chenhao Du, Dr. Wenchao Hua, Dr. Xinwei Yang, Dr. Yijie Lao, Dr. Bo Lin, Dr. Yuanqing Ding, Dr. Guangtao Chai, Dr. Mingqi Li, Hao Lu, Min Ding, Hongyou Wang, Zhanhui Wen, Mengpan Wang, Dongdong Song and Xing Chen for their happy and fruitful discussion.

I gratefully acknowledge the China Scholarship Council (CSC) for the financial support for the two years' research at Physical-Chemistry institute in Justus Liebig University Giessen.

Finally, I would like to thank my family for their unconditional support. They give me the strength to keep going.

Zusammenfassung

Die heterogen katalysierte Oxidation von HCl zu Cl_2 (Deacon-Prozess) stellt einen nachhaltigen Weg zur Rückgewinnung von Chlor aus HCl-haltigen Gasströmen in der chemischen Industrie dar. Es konnte nachgewiesen werden, dass CeO_2-basierte Materialien das Potenzial besitzen, als effektive Katalysatoren für die HCl-Oxidationsreaktion zu fungieren und eine wirtschaftlich sinnvolle Alternative zu kommerziellen RuO_2-basierten Materialien darzustellen. Die Forschungsarbeiten fokussieren sich darüber hinaus auf $Ce_xZr_{1-x}O_2$-Mischoxide sowie CeO_2 auf ZrO_2-Trägern (CeO_2@ZrO_2), mit dem Ziel, die Beziehungen zwischen Struktur, Sauerstoffspeicherkapazität und katalytischer HCl-Oxidationsaktivität und -lebensdauer aufzuklären. Des Weiteren werden zeitaufgelöste und empfindliche *In-situ*-Deaktivierungs- und Reaktivierungsexperimente durchgeführt, um detaillierte Einblicke in den Chlorierungs-Dechlorierungs-Prozess zu gewinnen.

Obwohl die erhöhte Deacon-Aktivität durch die Kombination von CeO_2 mit ZrO_2 in fester Lösung erreicht werden kann, wie in zahlreichen Studien berichtet wurde, kann die eindeutige Beziehung zwischen OSC und Aktivität durch die Tatsache verfälscht werden, dass sich $Ce_xZr_{1-x}O_2$ in mehreren Schlüsselparametern, wie beispielsweise der spezifischen Oberfläche, unterscheiden. Dementsprechend wurden im Rahmen dieser Arbeit zunächst $Ce_xZr_{1-x}O_2$-Mischkristalle in Abhängigkeit von der Zusammensetzung x durch die Co-Präzipitationsmethode entwickelt, wobei eine konstante spezifische Oberfläche von 46 ± 2 m^2/g beibehalten wurde. Folglich lässt sich festhalten, dass der OSCc-Wert ein geeignetes Kriterium zur Beschreibung der katalytischen HCl- und CO-Oxidationsreaktion darstellt. Aus der linearen Beziehung zwischen der HCl-Oxidationsaktivität und dem OSCc-Wert, der wiederum linear mit der CO-Oxidationsaktivität zusammenhängt, lässt sich ableiten, dass die HCl-Oxidationsreaktion an den $Ce_xZr_{1-x}O_2$-Katalysatoren über den Mars-van Krevelen-Mechanismus abläuft.

Des Weiteren wurden die Auswirkungen des Kalzinierungsprozesses auf die strukturellen Eigenschaften sowie die katalytische Aktivität von CeO_2@ZrO_2-Katalysatoren in einer systematischen Untersuchung analysiert. Die Oberfläche der ZrO_2-Teilchen wurde mit CeO_2 in unterschiedlichen Konzentrationen nach der Methode der beginnenden Nassimprägnierung beladen und bei verschiedenen Temperaturen kalziniert. Der Katalysator, der fünf Stunden lang bei 600 °C kalziniert wurde, führte zur Bildung einer hochdispersen CeO_2-Schicht, die eine Anreicherung von Ce^{3+}-Spezies aufwies. Die Beobachtung einer 1-2 nm dicken CeO_2-Benetzungsschicht führt zu der Schlussfolgerung, dass diese für die hohe spezifische Aktivität bei der katalytischen Oxidation von HCl verantwortlich ist. Somit lässt sich ableiten, dass die verbesserte Stabilität der bei 600 °C kalzinierten CeO_2-Schicht auf die Bildung einer scharfen Grenzfläche zum ZrO_2-Träger zurückzuführen ist.

Schließlich wurden zwei "Deaktivierungs-Reaktivierungs"-Zyklen bei 430 °C über frischem CeO_2 bzw. 20CeO_2@ZrO_2-Katalysator durchgeführt, wobei das Reaktionsgasgemisch gewechselt wurde. Es konnte festgestellt werden, dass die Aktivität des 20CeO_2@ZrO_2-Katalysators nach dem zweiten Deaktivierungs-/Reaktivierungszyklus durch Sauerstoffeinwirkung bei 430 °C vollständig wiederhergestellt werden kann. Demgegenüber nimmt die Aktivität des reinen CeO_2-Katalysators nach jedem Zyklus allmählich ab. Dies lässt den Schluss zu, dass die 20CeO_2@ZrO_2-Katalysatoren eine bessere Regenerationsleistung aufweisen als der CeO_2-Katalysator. Des Weiteren wird ein einfaches Modell auf Basis des Johnson-Mehl-Avrami-Kolmogorov-Ansatzes entwickelt, um den Reoxidationsprozess des Katalysators zu erklären. Diese Beobachtung lässt sich durch eine schnellere Keimbildungsrate in den geträgerten 20CeO_2@ZrO_2-Katalysatoren im Vergleich zum reinen CeO_2-Katalysator modellieren. Diese Beobachtung lässt sich durch die zahlreichen Keimbildungsstellen erklären, die durch die große Oberfläche von ZrO_2 bereitgestellt werden.

Abstract

The heterogeneously catalyzed oxidation of HCl to Cl_2 (Deacon process) represents a sustainable route to the recovery of chlorine from HCl-containing streams in the chemical chemistry. It has been demonstrated that CeO_2-based materials have the potential to act as effective catalysts for the HCl oxidation reaction, offering an economically viable alternative to those based on RuO_2 commercial materials. The thesis continues to focus on $Ce_xZr_{1-x}O_2$ mixed oxides and supported CeO_2 on ZrO_2 (CeO_2@ZrO_2) catalysts, with the aim of elucidating the relationship between structure, oxygen storage capacity and catalytic HCl oxidation activity and durability. Moreover, rapid and sensitive *in situ* deactivation and reactivation experiments are devised to gain insight into the "chlorination-dechlorination" process.

Although the enhanced Deacon activity can be achieved by combining CeO_2 with ZrO_2 in solid solution reported by numerous studies, a clear-cut relationship between OSC and the activity may be obscured due to the fact that previous studies have suffered from the limitation that $Ce_xZr_{1-x}O_2$ differ in several key parameters, such as specific surface area. Accordingly, in this thesis, we initially developed $Ce_xZr_{1-x}O_2$ solid solutions as a function of the composition *x* through the co-precipitation method, maintaining a constant specific surface area at 46 ± 2 m^2/g. It can therefore be stated that the OSCc value is an appropriate descriptor of the catalytic HCl and CO oxidation reaction. From the linear relationship between the oxidation activity of HCl and OSCc, which in turn is linearly related to the activity of CO oxidation, it can be concluded that the HCl oxidation reaction over the $Ce_xZr_{1-x}O_2$ catalysts proceeds *via* the Mars-van Krevelen mechanism.

Furthermore, the effect of calcination process on the structural properties and catalytic performance of CeO_2@ZrO_2 catalysts was systematically investigated. CeO_2 with varying concentrations were loaded onto the surface of ZrO_2 particles using the incipient wetness impregnation method and calcined at different temperatures. The catalyst, which was calcined at 600 °C for a period of 5 h, resulted in the formation of a highly dispersed CeO_2 layer, which exhibited an enrichment of Ce^{3+} species. The observed 1-2 nm thick CeO_2 wetting layer is responsible for the high specific activity observed in the catalytic oxidation of HCl. Moreover, enhanced stability of the CeO_2 layer calcined at 600 °C can be attributed to the formation of a sharp interface with the ZrO_2 support.

Lastly, we applied two "deactivation-reactivation" cycles at 430 °C over fresh CeO_2 and $20CeO_2$@ZrO_2 catalyst respectively by switching the reaction gas mixture. It was unexpected that the activity of the $20CeO_2$@ZrO_2 catalyst can be fully restored by oxygen exposure at 430 °C after the second deactivation/reactivation cycle, whereas the activity of the pure CeO_2 catalyst decreases gradually after each cycle. Apparently, $20CeO_2$@ZrO_2 catalyst exhibits superior regeneration performance to that of the CeO_2 catalyst. Furthermore, a straightforward model is devised based on the Johnson-Mehl-Avrami-Kolmogorov approach to elucidate the reoxidation process of the catalyst. This observation is modelled by a faster nucleation rate in the supported $20CeO_2$@ZrO_2 catalysts compared to the pure CeO_2 catalyst. This can be explained by the abundant nucleation sites provided by the high surface area of ZrO_2.

List of Abbreviations

MDA	Methylene diphenyl diamine
MDI	Methylene diphenyl diisocyanate
TDA	Toluene diphenyl diamine
TDI	Toluene diphenyl diisocyanate
OSC	Oxygen storage capacity
OSCc	Complete oxygen storage capacity
SSA	Specific surface area
BET	Brunauer-Emmett-Teller
ICP-AES	Inductively coupled plasma atomic emission spectroscopy
XRD	X-ray diffraction
XPS	X-ray photoelectron spectroscopy
TEM	Transmission electron microscopy
STEM	Scanning transmission electron microscopy
HR-TEM	High-resolution transmission electron microscopy
HAADF-STEM	High-angle annular dark field scanning transmission electron microscopy
AC-HRTEM	Aberration-Corrected high resolution transmission electron microscopy
XEDS	X-ray energy-dispersive spectroscopy
SEM	Scanning electron microscopy
H_2-TPR	Hydrogen temperature programmed reduction
TAP	Temporal analysis of products
PGAA	Prompt gamma activation analysis
FTIR	Fourier-transform infrared spectroscopy
STY	Space time yield
GHSV	Gas hourly space velocity
WHSV	Weight hourly space velocity
DFT	Density functional theory
JMAK	Johnson-Mehl-Avrami-Kolmogorov
MvK	Mars-van Krevelen
L-H	Langmuir-Hinshelwood

Table of Contents

1. Introduction

1.1 Motivation and Outline

Chlorine chemistry plays an indispensable role in the manufacture of a range of essential chemicals, polymers and pharmaceuticals.[1,2] Currently, approximately 100 million tons of Cl_2 are utilized annually, participating in over 50% of all commercial processes including the chlor-alkali industry, the polyurethanes industry, and pharmaceutical chemicals.[2-4] However, the production of chlorine-free materials such as polyurethanes inevitably results in the formation of a significant amount of by-product HCl (cf. **Figure 1)**. In the synthesis of diisocyanates, the reaction of $COCl_2$ with MDA or TDA results in the production of chlorine-free MDI or TDI, accompanied by the formation of HCl as a by-product.[5] For every mole of MDI or TDI produced, 4 moles of HCl by-product are formed. It is evident that the rapid demand for MDI and TDI, coupled with the increasing demand for Cl_2 and the surplus of by-product HCl, necessitates the development of an efficient recycling method for Cl_2 from HCl.

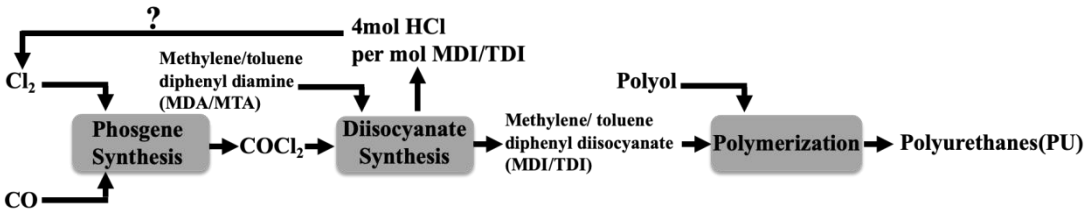

Figure 1. Simplified flowsheet of polyurethanes (PU) production. Adapted from ref. **1, 5**.

The catalytic oxidation of HCl to Cl_2 (Deacon reaction), originally devised by Henry Deacon in 1868, provides a sustainable route for the recovery of chlorine from HCl-containing streams.[6-10] The process offers a number of advantages, including a reduction in energy consumption, greater flexibility in the handling of raw gas HCl, and a reduction in environmental impact.

$$4HCl+O_2 \leftrightharpoons 2Cl_2+2H_2O \quad \Delta H= -113.6 \text{ KJ/mol} \qquad \textit{Eq. 1}$$

Nevertheless, a significant challenge associated with the HCl oxidation reaction is the stability of the catalyst, which is readily lost by bulk chlorination.[11,12] As the original catalyst, copper is susceptible to bulk chlorination, resulting in the formation of $CuCl_2$. The catalyst is gradually lost during operation since $CuCl_2$ is volatile at a reaction temperature above 400 °C, the industrialization of this process has yet to be realized.[6-9,13-15] Since 1999, Sumitomo Chemicals has commercialized an active and stable RuO_2/SiO_2/rutile-TiO_2 catalyst.[5,16] Even for industrial Ru-based catalysts, they remain scarce, with a high and dramatically fluctuating market price, and face an additional challenge in the form of the potential formation of volatile RuO_4. A concise review of Deacon catalysts is presented in **Chapter 1.2** accordingly.

CeO_2 turns out to be a promising alternative for RuO_2 due to its superior catalytic performance at an elevated temperature and lower price.[17] The observed CeO_2 activity is related to the presence of oxygen vacancies in CeO_2 during the Deacon reaction. It has been demonstrated that calcination of CeO_2 at 1173 K optimises the oxygen storage capacity (OSC) and exhibits the highest activity when compared with CeO_2 calcined at other temperatures. The observed stability

arises from the remarkable resistance of CeO_2 against chlorination. What is more, the $CeCl_3$ phase can be fully oxidized to CeO_2 by increasing the oxygen content or reaction temperature.

Subsequently, CeO_2-ZrO_2, as the most well-known and established component in numerous catalytic applications, particularly for oxidation reactions, has been widely developed (cf. **Chapter 1.3**).[18-21] In the Deacon process, the incorporation of ZrO_2 into CeO_2 to form $Ce_xZr_{1-x}O_2$ mixed oxides or supported CeO_2 on ZrO_2 powder has been demonstrated to enhance the catalytic activity, as well as lead to an improvement in stability through the prevention of CeO_2 chlorination.[22-26,28]

It is commonly acknowledged that the activity of $Ce_xZr_{1-x}O_2$ solid solutions in an oxidation reaction is correlated to the OSC.[21,27] $Ce_xZr_{1-x}O_2$ mixed oxides with a variety of morphologies and structures, including irregular morphology, nanofibers, nanorods and even kappa-phase with a notable increase in OSC, has been extensively examined in the Deacon reaction.[23, 24, 28-30] It is worth noting that such studies are subject to certain limitations. Firstly, the reducing agent employed in the OSC process differs from that used for the HCl oxidation. Furthermore, as-prepared $Ce_xZr_{1-x}O_2$ exhibit notable differences in several crucial parameters simultaneously. Sample exhibiting different Zr contents also possess different BET surface areas, while samples with comparable BET surface areas undergo phase separation between CeO_2 and ZrO_2 in inhomogeneous $Ce_xZr_{1-x}O_2$ mixed oxides. Therefore, a clear-cut correlation between OSC and performance in the Deacon reaction, as observed in the aforementioned $Ce_xZr_{1-x}O_2$, has yet to be established. In doing so, in the present thesis we firstly devised $Ce_xZr_{1-x}O_2$ solid solutions by the co-precipitation method as a function of the composition *x* with a constant specific surface area (SSA) in order to explore the relationship between OSC and activity of CO and HCl oxidation reactions as well as the OSC and compositions (cf. **Chapter 2.1**).

Moreover, superior Deacon performance was achieved with CeO_2 supported on performed ZrO_2 particles.[26] The optimal catalyst composition was identified as 9 wt.% CeO_2 supported on ZrO_2 (CeO_2/ZrO_2), and the catalysts were calcined at 900 °C for 5h. The remarkable activity of CeO_2/ZrO_2 can be attributed to the co-existence of nanostructured CeO_2 and Ce-Zr mixed oxides. However, the calcination temperature of 900 °C was not optimized, but rather adopted from the optimum performance of bulk-CeO_2 in HCl oxidation. As of yet, the following questions regarding the Deacon process over CeO_2@ZrO_2 remain unresolved: how does the heat treatment affect the performance and what is the chemical nature of the active phase? It remains unclear whether there are synergistic effects operative between CeO_2 and ZrO_2 when calcining at low temperatures? With these questions in mind, we proceeded to design CeO_2@ZrO_2 catalysts with varying concentrations of CeO_2 load on the surface of ZrO_2 particles and calcined at different temperatures. These samples were then evaluated under different reaction conditions (cf. **Chapter 2.2**).

As previously stated, one of the most significant challenges associated with the Deacon reaction is the stability of the catalyst which is susceptible to loss through bulk chlorination.[11,17,31-33] The deactivation of ceria-based catalysts in the HCl oxidation reaction is achieved *via* selective bulk chlorination of the active ceria component, which results in the formation of $CeCl_3 \times nH_2O$. It has been demonstrated that the $CeCl_3$ phase can be fully oxidised to CeO_2 through an increase in the oxygen content. It is therefore meaningful to devise a rapid and straightforward method for detecting the deactivation-reactivation of the Deacon process, with a view to gaining a deeper understanding of the kinetics of chlorination/dechlorination of different CeO_2-based catalysts.

Lastly, this thesis presents a study of the deactivation-reactivation process conducted using *in-situ* UV-Vis analytics in a flow reactor. The two types of CeO_2-based Deacon catalysts were utilized: namely, pure CeO_2 (cf. **Chapter 2.1**) and $20CeO_2@ZrO_2$ (cf. **Chapter 2.2**). Furthermore, to provide a rationale for the observed kinetics, we developed a simple model based on the Johnson-Mehl-Avrami-Kolmogorov (JMAK) approach for the reactivation of the catalyst starting from the chlorinated phase (cf. **Chapter 2.3**).

State-of-the-art analysis (X-ray diffraction (XRD), quantitative XRD: Rietveld-refinement, Raman spectroscopy, N_2 physisorption experiments, Inductively coupled plasma atomic emission spectroscopy (ICP-AES), Transmission and scanning transmission electron microscopy (TEM/STEM), X-ray photoelectron spectroscopy (XPS)) are applied to provide an accurate structural and compositional characterization of the fresh and used materials. The HCl and CO catalytic oxidation measurements are conducted in a home-made fixed-bed flow reactor (cf **Chapter 1.4**). The experiments of oxygen storage capacity (OSC) are carried out by using a stainless-steel tube (**Chapter 1.4**).

1.2 Review on Deacon Catalysts

In general, according to different active sites, catalysts can be mainly classified into three types: (i) copper-based catalyst, (ii) ruthenium-based catalyst and (iii) cerium-based catalyst.

1.2.1 Cu-based catalyst

$CuCl_2$/pumice catalyst was first discovered by Deacon in 1868, while the rapid deactivation of this catalyst restricted its application due to the easy volatilization of copper chloride above 400 °C.[6-9] Subsequently, researchers have been dedicated to the optimization of Cu-based catalysts in global.

In the 1960s, Shell company employed Cu-Dy-K/SiO_2 catalyst in the air oxidation fluidized-bed process named Shell-Chlor process.[13-15] This catalyst reveals high HCl conversion, reaching a value that approach the equilibrium conversion of 77% at 365 °C. Moreover, the activity can be maintained after about 2000 h on stream at temperature up to 400 °C. The industrial Shell-Chlor process was successfully established with a capacity of 30 kilo tons Cl_2 per annum. However, the Shell-Chlor process was eventually abandoned owing to the volatilization of cupric chloride and the corrosion issues caused by unreacted HCl in the presence of H_2O.

The rare-earth elements, including Ce, La and Sm, are employed extensively as dopants to modify the traditional copper-based catalysts.[34-39] The $Cu_{2.4}CeV_{0.5}O_x$ catalyst, alongside newly identified $CeVO_4$ phase was prepared using the sol-gel method by Wang *et al*., achieving STY of 2.26 g-Cl_2/(g-cat·h) with stable catalytic conversion at approximately 83%, which was maintained over 600 h.[39] Advanced techniques including *in-situ* DRFITS, ToF-SIMS combined with ab-initio calculations elucidate that the strong O_2 adsorption ability from Ce and V oxides promotes the O_v replenishment cycle, thus reducing the accumulation of Cu-Cl and inhibiting the deactivation of CuO. Fei *et al*. prepared CuO-CeO_2 composite oxides supported on Y-type zeolite catalysts and subsequently evaluated their performance on catalytic HCl oxidation in a fixed-bed reactor.[36] CuO(12)-CeO_2(13)/Y containing 12 wt.% CuO and 13 wt.% CeO_2 exhibits the highest STY value of 1.37 g-Cl_2/(g-cat·h) under the reaction condition of O_2/HCl =1, T=382 °C. In-depth characteristic studies demonstrate that the superior activity can be mostly attributed to the existence of well-dispersed CuO.

Cu-K-La/γ-Al_2O_3 catalyst with the weight ratio of $CuCl_2$: KCl: $LaCl_3$ = 3: 1: 2, developed by Guo *et al.*,[34,35] exhibits a superior catalytic activity with STY of 0.98 g-Cl_2/(g-cat·h) and displays extraordinary stability over 9600 h on stream under the reaction condition of O_2/HCl = 1/2, T = 340 °C. Cu-K-Sm/γ-Al_2O_3 catalyst was subsequently investigated by same research group, which reveals enhanced performance compared to Cu-K-La/γ-Al_2O_3 catalyst.[36] The characterization results evidence that absorption of oxygen and the transformation of $Cu^{2+} \leftrightharpoons Cu^{+}$ can be enhanced by introduction of samarium, which in turn can lead to an improvement in the catalytic performance. The reaction kinetics studies were conducted over supported Cu-based catalyst, assuming that O_2 adsorption is the rate-controlling step where can typically describe the reaction behavior of HCl catalytic oxidation over supported Cu-based catalysts.[40,41]

It has recently been demonstrated that transition metals, in particular manganese (Mn) and cobalt (Co), can be incorporated into supported Cu-based catalysts as promoters.[42,43] The CuO(12)-MnO_x(13)/γ-Al_2O_3 and CuO(12)-CoO_x(13)/γ-Al_2O_3 catalysts demonstrate unparalleled stability for at least 1000 h with HCl conversion of about 80% at a reaction temperature of 390 °C.

Interestingly, no obvious phase transition is observed in XRD pattern for the used either MnO_x or CoO_x modified catalyst even at lower O_2/HCl = 0.5. This observation indicates that either MnO_x or CoO_x may serve to impede the chlorination (Cl poisoning) of active copper species.

Furthermore, research is being conducted into the potential modification of novel structures to Cu-based catalyst.[44,45] A robust copper-based catalyst based on a delafossite structure ($CuAlO_2$, cf. **Figure 2**), devised by Pérez-Ramírez *et al*., displays an outstanding lifetime with more than 1000 h on stream under the condition of O_2/HCl = 4, T =380 °C. However, the catalyst suffers from a bulk morphological change and a considerable copper loss of 40% after the stability test. In order to enhance the activity of $CuCrO_2$, they prepared a $CuCrO_2$-CeO_2 composite via mechanochemical activation of 30 wt.% $CuCrO_2$ and 70 wt.% CeO_2 powders. The STY of 30$CuCrO_2$-70CeO_2 catalyst can reach to 0.7 g-Cl_2/(g-cat · h) under the reaction condition of O_2/HCl = 2, T = 380 °C. In addition, the 30$CuCrO_2$-70CeO_2 catalyst present a remarkably stable chlorine production efficiency under 200 h on stream, accompanied by negligible loss of active species. XRD results demonstrate that the well-designed delafossite structure can stabilize the copper and chromium species, and activity experiments conducted with varying HCl/O_2 ratios indicate that the presence of ceria facilitates the re-oxidation step, thus boosting the catalytic activity on HCl oxidation.

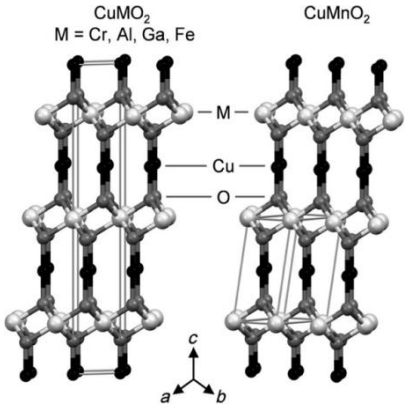

Figure 2: Rhombohedral structure of delafossite common to $CuCrO_2$, $CuAlO_2$, $CuGaO_2$, and $CuFeO_2$ (left) and the distorted $CuMnO_2$ with a monoclinic structure (right). Adapted from ref. **44**.

Perez-Ramírez and co-workers also investigated reaction mechanism of CuO catalyst in the HCl oxidation reaction through the temporal analysis of products (TAP) method.[46] XRD results of fresh and used catalysts reveal that primary active species is copper(hydr)oxychloride. The catalyst follows a combination of Mars-van Krevelen (MvK) and Langmuir-Hinshelwood (L-H) mechanism during the HCl oxidation process. In particular, the mechanistic study suggests that an active and stable copper-based catalyst can be acquired by controlling the degree of surface chlorination.

In all, although several of modification strategies have been employed to optimize the copper-based catalyst, including the addition of dopants and structural adjustment. At present, there is no commercially viable copper-based Deacon catalyst in the fix-bed reactor. The ability to regulate the degree of surface chlorination may prove instrumental in addressing the bottleneck stability issue. It is also important to note that maintaining the reaction temperature below 400 °C is not sufficient, the elevated temperature encountered at hot spot also necessitates serious consideration.

1.2.2 Ru-based catalyst

The RuO_2-based catalyst has been the subject of considerable interest since 1999, particularly as a commercial component in the Deacon reaction.[5,16] Researchers prepared a variety of either powder catalysts (e.g. supported ruthenium catalyst, ruthenium-based mixed fibers/oxides) or ultra-thin single-crystalline films to deepen understanding on the structural variations and clarify the extreme stability of ruthenium species on HCl oxidation.

A significant advancement in the recycling of Cl_2 from HCl oxidation was made upon successful synthesis of the RuO_2/rutile-TiO_2 catalyst by Sumitomo Chemicals in 1999.[5,16] The RuO_2/rutile-TiO_2 catalyst exhibits remarkable activity at lower reaction temperature in contrast to conventional copper-based catalysts. Moreover, HCl conversion of RuO_2/rutile-TiO_2 catalyst can be kept above 85% at least for two years. Subsequent *ex situ* X-ray absorption fine structure (EXAFS) and field emission scanning transmission electron microscopy (FE-STEM) experiments on the fresh catalyst suggest that an ultra-thin RuO_2 layer formed on the surface of rutile-TiO_2 due to the structural matching between RuO_2 and TiO_2. This kind of structure dramatically improves the catalytic performance. To better understand the size effect of RuO_2 on the final morphology of Ru species upon oxidative thermal treatment, Xiang *et al*. synthesized RuO_2/P25-TiO_2 catalysts with various RuO_2 sizes, inspired by the specific morphology of RuO_2/rutile-TiO_2 catalysts.[47] TEM images of RuO_2/P25-TiO_2 suggest that the shape of RuO_2 species changes from sub-2 nm particles to epitaxial layers either under the condition of the Deacon reaction or by direct heat treatment without HCl, and this typical transformation process promotes its performance on HCl oxidation. A further thermodynamic model demonstrates that this redistribution process is co-driven by thermal instability and interfacial lattice matching between RuO_2 and TiO_2. In order to prevent the sintering of active ruthenium species and enhance the thermal stability of RuO_2/TiO_2 catalyst further, RuO_2/SiO_2/rutile-TiO_2 catalyst was developed, comprising nano-size RuO_2 and SiO_2 as a promoter on a rutile-TiO_2.[16] The growth of crystalline RuO_2 can be efficiently suppressed through the introduction of SiO_2. A comparative study was also conducted on RuO_2/TiO_2 and RuO_2/TiO_2-SiO_2 with varying amounts of SiO_2 applied in the Deacon process by Zhu *et al*.[48] The addition of an appropriate amount of SiO_2 (1wt.%) to RuO_2/TiO_2 can result in notable improvements in sintering-resistant properties, due to the geometric effects of SiO_2 facilitating the dispersion of RuO_2 on the surface of TiO_2. An industrial plant employing a RuO_2/SiO_2/rutile-TiO_2 catalyst with a Cl_2 production capacity of 100 kilo tons per annum was successfully operated by Sumitomo Chemicals in 2003.

Besides, the optimization of rutile-TiO_2 carrier *via* doping of metal oxides including CeO_2 and SnO_2, have also been reported.[49,50] Either Ce- or Sn-doped rutile-TiO_2 materials were synthesized and employed as supports for the active RuO_2. The insertion of either Ce or Sn into the TiO_2 lattice expand the lattice parameter, which enhance the dispersion of Ru species. Consequently, a low RuO_2 loading of 0.5-1 wt.% can also allow for a high catalytic performance.

Moreover, the investigation of RuO_2-TiO_2 nanofibers were conducted by Over's group, they prepared electrospun RuO_2 and RuO_2-TiO_2 nanofibers with well-defined morphology for the evaluation of morphological stability on HCl oxidation.[51] SEM images reveal that the incorporation of TiO_2 can enhance the morphological stability of RuO_2-TiO_2 nanofibers during the HCl oxidation process (cf. **Figure 3**). Recently, Over *et al*. synthesized $Ru_{0.3}Ti_{0.7}O_2$ *via* the conventional sol-gel method, evaluated the Deacon reaction activity of fresh $Ru_{0.3}Ti_{0.7}O_2$ catalyst and performed H insertion *in-situ* in the reactor at 250 °C.[52] The H-treated catalyst displays

markedly enhanced performance compared to the fresh catalyst, and the H-treated catalyst runs stably after 3h on stream. The catalytic activities of catalyst can be well recovered after several of cycling between activation by hydrogen and deactivation by oxygen. The hydrogen-induced lattice strain in $Ru_{0.3}Ti_{0.7}O_2$ accompanied by altered electronic properties is likely to be the underlying cause of the observed enhancement in catalytic activity.

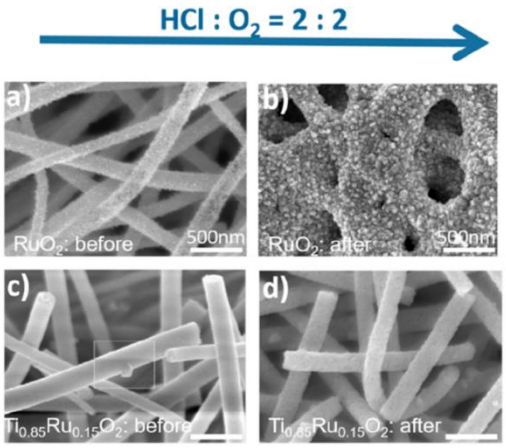

Figure 3: High resolution SEM images of RuO_2 **a, b**) and $Ti_{0.85}Ru_{0.15}O_2$ **c, d**) mixed nanofibers before **a, c**) and after **b, d**) HCl oxidation reaction in a flow reactor under oxidizing feed gas composition (p(HCl) = p(O_2) = 200 mbar; buffer gas p(Ar) = 600 mbar: Ar/HCl/O_2 = 6/2/2; total flow rate 50 mL min^{-1} (sccm)) at 380 °C for 2 h. Adapted from ref. **62**.

In 2007, another ruthenium-based catalyst, namely RuO_2/SnO_2-Al_2O_3 catalyst,was reported by BMS.[53,54] The RuO_2/SnO_2-Al_2O_3 catalyst exhibits high activity, with a STY of 2.7 g-Cl_2/(g-cat·h) and remarkable longevity with a duration of 7000 h, under the reaction condition of O_2/HCl = 1/2, T= 280-380 °C. Similarly, the lattice matching between the active ruthenium phase and the SnO_2 support facilitate the epitaxial growth of film-like RuO_2 on SnO_2, resulting in the formation of highly active and durable catalyst. The presence of Al_2O_3 hinders the interaction of the formed Ru-OH species in the reaction and suppresses the sintering of active phase, thereby enhancing the stability of the catalyst. Pérez-Ramírez *et al*. have reported that the HCl oxidation process over RuO_2/SnO_2-Al_2O_3 catalyst is ready for large-scale application. Teschner *et al*. proposed details regarding the surface state of RuO_2/SnO_2-Al_2O_3 catalyst and its mechanistic insights over HCl oxidation through an integration of theoretical and experimental investigations.[55,56] HR-TEM images of RuO_2/SnO_2 catalyst reveal the presence of ruthenium species comprising 1-3 monolayer (ML)-thick RuO_2 film and larger RuO_2 particles with size of 2-4nm. Subsequent density functional theory (DFT) calculations indicate that HCl oxidation reaction is structure sensitive, with RuO_2 (110) facet identified as the most active, followed by (100) facet and (101) facet. Moreover, bilayer RuO_2(110)/SnO_2(110) was far more active than 1 ML RuO_2(110)/SnO_2(110). Experiments in TAP and prompt gamma activation analysis (PGAA) explicate that catalytic HCl oxidation on RuO_2/SnO_2 catalyst follows L-H mechanism and verify that catalytic reactivity is directly proportional to the concentration of specific oxygen species.

It has recently been reported that some other carriers may also show potential for a Ru-based supported catalyst, as some include Al-MgF_2[57,58] and ZrO_2-Al_2O_3[59]. Zhu *et al*. have reported that the incorporation of Al into MgF_2 enhances the activity of RuO_2/Al-MgF_2 catalyst when calcining at an optimal temperature of 400 °C. It has been demonstrated that the incorporation of Al into rutile MgF_2 framework can modify the cell parameters of MgF_2 to a degree close to that observed in RuO_2 thereby modulating the chemical environment surrounding RuO_2; this results

in an improvement in catalytic performance. Notably, RuO_2/Al-MgF_2 can even show better stability in comparison to benchmarking $RuO_2/SiO_2/TiO_2$ and RuO_2/SnO_2-Al_2O_3 catalysts under the catalytic oxidation of HCl with an upper-bound HF concentration of 400ppm. Zhou *et al*. prepared RuO_2/ZrO_2-Al_2O_3 catalyst.[59] The performance evaluation shows that after high temperature holding in nitrogen at 673 K for 72 h, the activity of RuO_2/ZrO_2-Al_2O_3 catalyst increased by a factor of 1.59 in comparison to that of RuO_2/Al_2O_3 catalyst. It has been demonstrated that the dispersity of Ru is obviously improved, RuO_2(110) crystal plane is fully exposed, and Zr atoms enter RuO_2 lattice to form $Ru_xZr_yO_z$ species which have altered the lattice parameters of RuO_2, finally leading to the obviously improved activity and stability in the HCl catalytic oxidation reaction.

In addition to powder catalysts, model catalysts have been further employed for getting a clear-cut understanding of the structure and mechanism of a given process. Over *et al*. devised single-crystalline RuO_2(110) model to clarify the extreme stability of ruthenium species on HCl oxidation at the atomic-scale.[60-62] The comprehensive results of high-resolution core level shift spectra (HRCLS), thermal desorption spectra (TDS), low-energy electron diffraction (LEED) techniques together with CO redox reaction experiments, demonstrate that the RuO_2(110) surface can be chlorinated to $RuO_{2-x}Cl_x$(110) under the HCl oxidation condition through the partial replacement of bridging surface oxygen species (Obr) by bridging chlorine species (Clbr) (cf. **Figure 4**). It is unexpected that the chlorination process ceased when Clbr atoms replaced the majority of Obr atoms. This suggests that the chlorination process of RuO_2(110) is self-limiting. The $RuO_{2-x}Cl_x$(110) surface (**cf. Figure 4**), formed by such an ingenious chlorination process, is conducive to the extraordinary activity and stability of ruthenium-based catalysts in the HCl oxidation reaction.

Subsequently Over and co-workers shed light on the mechanistic aspects on HCl oxidation over RuO_2(110) and RuO_2(110)/TiO_2(110) with combination of HRCLS spectra and DFT experiments.[62,63] It has been found that the HCl oxidation reaction proceed, over both RuO_2(110) and RuO_2(110)/TiO_2(110) surfaces, *via* L-H scheme along the rows of Ru_{cus} atoms (coordinatively unsaturated ruthenium, cf. **Figure 4**). The most energy-demanding step is the recombination of surface chlorine atoms to form Cl_2 molecules. In addition, Pérez-Ramírez *et al*. discussed the mechanism of HCl oxidation on RuO_2/TiO_2 powder catalyst by performing TAP experiments. TAP experiments verify that the HCl oxidation process on the RuO_2(110)/TiO_2(110) powder catalyst predominantly follows a L-H mechanism with a minor MvK mechanism.[64,65]

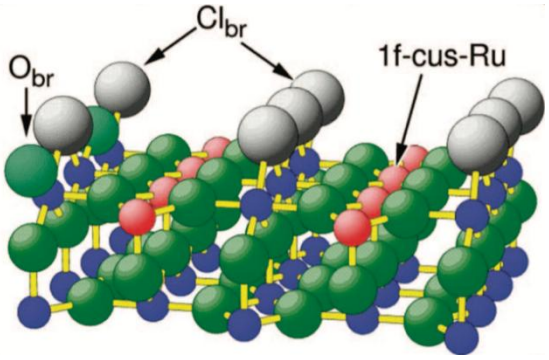

Figure 4: Schematic representation of $RuO_{2-x}Cl_x$ (110) surface. Adapted from ref. **62**.

Overall, ruthenium-based catalysts display an exceptional catalytic activity and longevity on the HCl oxidation reaction. The underlying mechanisms of industrial $RuO_2/SiO_2/TiO_2$ and RuO_2/SnO_2-Al_2O_3 catalysts have been extensively clarified. However, the ruthenium-based systems still present several intricate challenges. The initial issue is that the cost of the catalysts is significantly influenced by the fluctuating market price of Ru. Consequently, a potential increase in the price of Ru may diminish the advantages of the catalysts. Secondly, potential formation of volatile RuO_4 species at hot-spot during the reaction remains a significant factor limiting the operational lifespan of the catalyst. It would be beneficial to investigate the potential of an alternative catalyst based on a cost-effective and highly active metal for the oxidation of HCl.

1.2.3 Ce-based catalyst

CeO_2 has attracted the attention of researchers because of its widespread use in redox processes in many areas of research, particularly oxidation reactions.[18-21] In 2012, Pérez-Ramírez and colleagues proposed a systematic study of pure CeO_2 catalyst on HCI oxidation as an alternative to RuO_2-based catalysts for chlorine recycling.[17] Since then, a variety of CeO_2-based materials including CeO_2, CeO_2-ZrO_2 mixed oxides, CeO_2@ZrO_2 supported catalyst and others, have been prepared by many research groups, with either undefined mixed oxides or well-defined starting morphologies to study relationship between the structure and Deacon activity/stability. Furthermore, the reaction mechanism was also proposed by means of a dedicated experimental design in conjunction with DFT modelling.

Systematic study of pure CeO_2 catalyst on HCl oxidation was initially proposed by Pérez-Ramírez, it can be observed that the activity is related to the presence of oxygen vacancies in CeO_2 during the Deacon reaction.[17] CeO_2 calcined at 1173 K maximized the OSC and thus exhibited the highest activity compared with CeO_2 calcined at other temperatures (cf. **Figure 5**). DFT investigations put forward the mechanism of HCl oxidation on pure CeO_2 system. The Deacon reaction starts by the adsorption of HCl on the CeO_2 surface resulting in the formation of $O_{lat}H$ group and a Cl atom at the surface vacancy (Cl_{vac}). *(i)* A HCl molecule can then adsorb, forming a water molecule and leaving a Cl atom on top of a Ce atom on the surface, designated as Cl_{top}. *(ii)* The external Cl_{top} atom can displace the already formed water molecule H_2O_{lat} from the lattice, thereby creating a vacancy that is subsequently filled by the Cl_{top} atom, resulting in the formation of second Cl_{vac}. *(iii)* One of the oxygen atoms from the subsurface layer can diffuse towards the surface, pushing a Cl_{vac} atom toward the outer surface, i.e., converting Cl_{vac} in Cl_{top}, resulting in the formation of an oxygen vacancy at a subsurface position. The energy required for this elementary step is 2.15 eV. *(iv)* The activation of Cl_{vac} results in the formation of an oxygen vacancy, which is subsequently filled by the dissociative adsorption of one-half of a molecule of oxygen from the gas phase. *(v)* Finally, HCl is capable of adsorbing on this surface to form an $O_{lat}H$ and a Cl_{top}. The subsequent evolution of Cl_2 occurs in the gas phase. Inspired by the above study, Over *et al*. conducted further investigation into the most critical step $Cl_{vac} \rightarrow Cl_{top}$ employed synchrotron-based methods (HRCLS, XANES) together with first-principles DFT. The peroxo species are demonstrated to be a crucial component in the reoxidation of Cl_{vac}-CeO_{2-x}(111), inducing the displacement of $Cl_{vac} \rightarrow Cl_{top}$ reaction.[91]

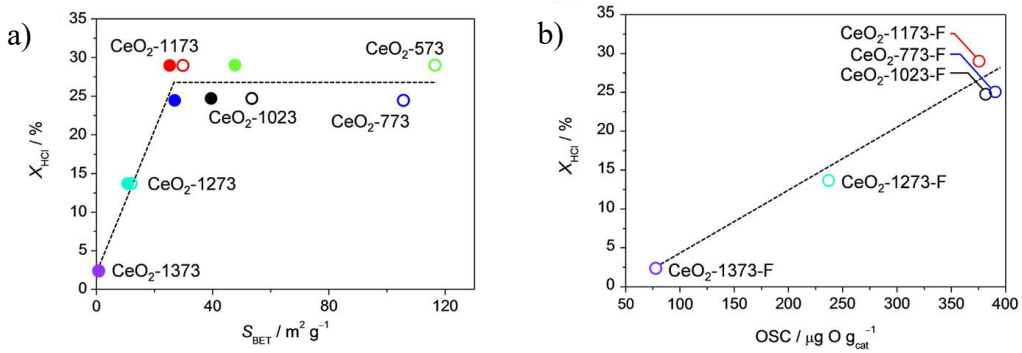

Figure 5: HCl conversion *versus* **a)** surface area of fresh (open symbols) and used (solid symbols) CeO_2 samples and **b)** OSC, measured at 573 K, of fresh CeO_2 samples. Conditions: inlet mixture of 10 vol.% HCl and 20 vol.% O_2 balanced in N_2, T_{bed} = 703 K, W/F0 (HCl) = 11.2 g h mol^{-1}, P = 1 bar, and time-on-stream = 3 h. Adapted from ref. **17**.

The catalytic activity of CeO_2 calcined at 1173 K under reaction conditions of different HCl/O_2 feed mixtures was also investigated by Pérez-Ramírez *et al*.[17] The results from kinetic analysis indicate that the catalytic activity can be enhanced by an increase in the oxygen content. XRD results of spent CeO_2 catalysts demonstrate that CeO_2 can be preserved in O_2-rich feeds (O_2/HCl $\geqslant$ 0.75), whereas $CeCl_3$ can be detected in O_2-lean feeds (O_2/HCI $\leqslant$ 0.25). In contrast to the behavior observed for copper-based catalysts, the formation of the $CeCl_3$ phase during the reaction is relatively stable at temperatures of 430 °C. Furthermore, the $CeCl_3$ phase can be fully oxidized to CeO_2 by increasing the oxygen content. Besides, *in situ* infrared spectroscopy and PGAA study demonstrate that elevated temperatures and oxygen concentrations can facilitate the desorption of Cl and the absorption of OH, thereby suppressing the chlorination of CeO_2 and enhancing the catalytic performance.[31] Although PGAA is a highly sensitive characterization technique, it still requires the use of a neutron source, which excludes this method from standard analysis. Furthermore, the data acquisition process is time-consuming, which precludes the possibility of conducting a kinetic analysis of the rapid reactivation process. It is therefore still of interest to develop a rapid and straightforward method for detecting "deactivation-reactivation" of the Deacon process.

Pure CeO_2 powder catalyst tends to suffer from bulk chlorination under HCl-rich feeds accompanied by structural and morphological variations. However, it is challenging to discern these changes in powder samples under typical reaction conditions. It is therefore meaningful to develop materials with well-defined morphologies to visualize alterations in morphology during the Deacon process.

The ceria electro-spun nanofibers and shaped-controlled CeO_2 particles, discovered by Over *et al.*,were subjected to test in the HCl oxidation reaction.[51] Pure CeO_2 nanofibers (NFs) were evaluated under more oxidizing (mild) reaction condition of HCl: O_2: Ar=1: 2: 7 and HCl-richer (harsh) reaction condition of HCl: O_2: Ar = 2: 2: 6. It can be clearly observed that the morphology of CeO_2 NFs can be preserved under mild condition after 60h. In contrast, the morphology of CeO_2 NFs was severely destroyed under harsh condition, accompanied by the occurrence of $CeCl_3$.

CeO_2 nanorods, cubes and octahedrons with different preferential exposed facets of (110), (100) and (111) were prepared, respectively (cf. **Figure 6a-c**).[66] In terms of activity, CeO_2 nanorods exhibit the highest activity followed by cubes and octahedrons under mild condition. This very same trend has also been observed for the complete oxygen storage capacity (OSCc), indicating

a correlation between the observed activity STY and the OSCc. In terms of stability, both nanorods and nanocubes can remain stable, whereas octahedrons display a clearly continuous deactivation after 1h on stream under harsh condition. TEM images of used shape-controlled CeO_2 subjected to harsh condition reveal that CeO_2 nanaocubes and octahedrons have undergone significant deterioration, whereas no discernible change can be observed in CeO_2 nanorods. TEM results also evidence that oxygen concentration in the reaction feed plays a key role in the missing stability due to bulk chlorination of the CeO_2.

Subsequently, CeO_2 nanocubes were subjected to mild reaction condition for 24 hours at varying temperatures.[67] Interestingly, CeO_2 nanocubes suffer from rapid deactivation at a reaction temperature below 380 °C and the deactivation process can be suddenly suppresses when reaction temperature increase to 390 °C. Rietveld analysis of XRD scans and TEM images (cf. **Figure 6g**) reveal that the deactivation process is paralleled by bulk chlorination of the nanocubes, higher temperature is favorable to a lower chlorination degree thereby enhancing the catalytic stability.

In addition, to verify the influence of water in the feed mixtures on the catalytic stability of CeO_2 nanocubes, experiments were carried out under dry and wet mild conditions at 380 °C. The activity of the nanocubes declines markedly during the initial 8 hours of operation and remains stable for the rest of the 16-hour period under dry condition. XRD and TEM images of used nanocubes reveal the presence of $CeCl_3$ and a partial loss of the regular cube shape (cf. **Figure 6h**). In contrast, CeO_2 nanocubes exhibit minimal deactivation and remain stable for 24 hours under humid condition, well preserved CeO_2 nanocubes can be clearly observed from TEM images of used catalyst (cf. **Figure 6i**). It can be inferred that the addition of a small amount of water (1%) effectively inhibits chlorination and preserves the catalyst morphology, thereby enhancing its durability.

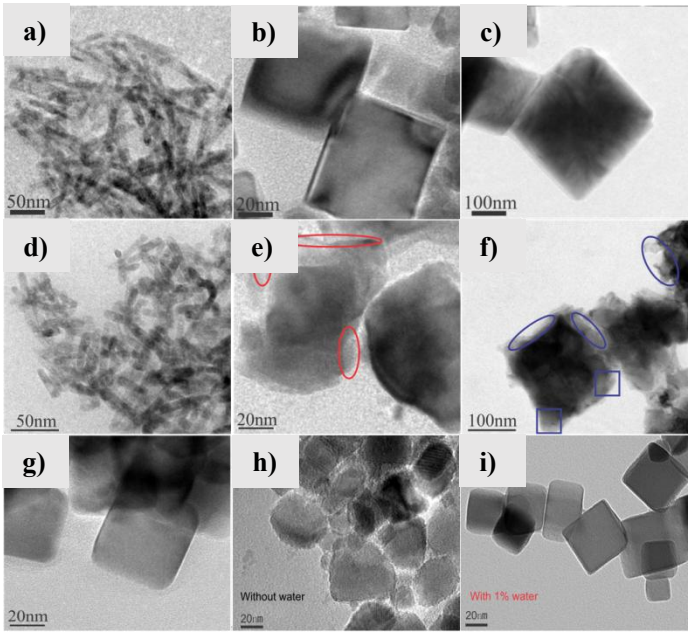

Figure 6: TEM images of as-prepared shape controlled CeO_2 particles: **a)** nanorods, **b)** cubes, **c)** octahedrons. Used CeO_2 particles after harsh reaction conditions at 430 °C for 24h for 60 h: **d)** rods, **e)** cubes, **f)** octahedrons. Used CeO_2 cubes after dry, mild conditions at **g)** 430 °C and **h)** 380 °C for 24 h. **i)** used CeO_2 cubes after humid, mild condition at 380 °C for 24 h. Adapted from ref. **66, 67**.

In order to enhance the activity and stability of ceria, a number of dopants were employed to modify pure CeO_2 catalysts. A systematic investigation of doped ceria catalysts was initiated through the doping of trivalent elements (La, Sm, Gd, Y) and tetravalent elements (Hf, Zr, Ti) into pure ceria. The introduction of Zr and Hf into CeO_2 results in an enhancement of catalytic activity relative to undoped ceria.[32] In contrast, the incorporation of trivalent dopants leads to a reduction in catalytic efficiency. The impact of aliovalent (Gd), isovalent (Zr), and aliovalent/isovalent (Pr and Tb) doped mesoporous $Ce_{0.9}M_{0.1}O_2$ on the OSC as well as on the catalytic stability were also investigated by Smarsly *et al*.[68] Pure mesoporous CeO_2 is quite stable under harsh condition at 430 °C, whereas the activity of $Ce_{0.9}Pr_{0.1}O_2$ with much higher OSCc value drops to almost zero within a few hours on stream. It can be indicated that high concentration of oxygen vacancies may even allow Cl to diffuse at least into subsurface parts perhaps even into the bulk material, leading to the formation of $CeCl_3$ and thereby deactivating the catalyst. Finally, they found that ZrO_2 can be taken as a suitable dopant to stabilize the CeO_2 catalyst, thus enhancing the reducibility of ceria without introducing charge-compensating and oxygen vacancies in the system.

Based on the enhanced performance of Zr-doped ceria, plenty of research were employed to enhance the comprehension of CeO_2-ZrO_2 catalysts during the Deacon reaction, including shape-controlled, nanofibers, mixed-oxide and supported catalysts.

The stability experiments of $Ce_xZr_{1-x}O_2$ nanorods were conducted under harsh condition (Ar: HCl: O_2=6.5: 2.5: 1) at 430 °C for 24h.[25] The STY of CeO_2 nanorods exhibits a continuous decline during the initial 8h, after which it remains constant. XRD evidence that CeO_2 nanorods suffer from bulk chlorination after reaction, meanwhile a complete destruction and transformation of CeO_2 nanorods into a cuboid structure can be detected from TEM. In contrast, the catalyst can keep stable when alloying 5% Zr into CeO_2, and the morphology of $Ce_{0.05}Zr_{0.95}O_2$ nanorods exhibit slight widening under harsh condition after 24h test. A further increase in zirconia content to 20% ($Ce_{0.8}Zr_{0.2}O_2$ nanorods) allows for extreme stability under the same harsh condition. Furthermore, there is no evidence of bulk chlorination or morphological changes in the used $Ce_{0.8}Zr_{0.2}O_2$ nanorods.

The evaluation of $Ce_xZr_{1-x}O_2$ NFs under mild condition was also conducted which allowed for a straightforward assessment of the stability test.[23,24,69] The as-prepared $Ce_xZr_{1-x}O_2$ NFs exhibit a single cubic/tetragonal solid solution structure, with no evidence of phase separation. STY of $Ce_xZr_{1-x}O_2$ NFs increase gradually with increasing Ce loading up to 30%. However, further increases in Ce concentration cannot lead to an enhanced activity. Furthermore, the morphological stability of $Ce_xZr_{1-x}O_2$ NFs is evaluated under harsh condition. The doping of ceria with 33% zirconia ($Ce_{0.67}Zr_{0.33}O_2$) has been observed to inhibit the bulk chlorination, thereby maintaining $Ce_xZr_{1-x}O_2$ NFs morphology under harsh condition.

Fei *et al*. devised $Ce_xZr_{1-x}O_2$ mixed oxides with a constant surface area, by a soft reactive grinding method.[28] The remarkable activity and the highest OSC can be achieved as for $Ce_{0.5}Zr_{0.5}O_2$ catalyst with a phase split of CeO_2 and ZrO_2. In addition, kappa phase κ-$Ce_2Zr_2O_8$ was prepared by Over *et al*, the ordering of the solid solution $Ce_{0.5}Zr_{0.5}O_2$ into the so-called κ-$Ce_2Zr_2O_8$ phase leads to a profound increase of the OSC.[29,30] However, it is found that the oxidation of HCl is not affected by the high OSCc value. Currently, as for $Ce_xZr_{1-x}O_2$ mixed oxides, previous studies suffer from the fact that $Ce_xZr_{1-x}O_2$ differ in several important parameters at the same time: samples exhibiting different Zr contents also possess different BET

surfaces areas; samples with constant surface area while exhibit phase split of CeO_2 and ZrO_2. These shortcomings impede a clear-cut correlation between activity and the OSC as well as between the composition and activity (cf. **Figure 7**).

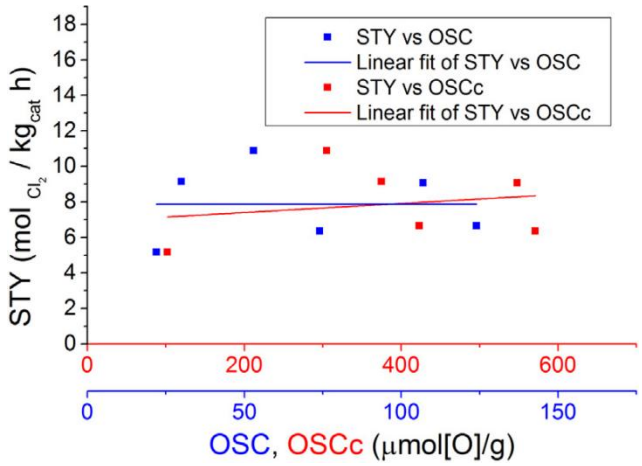

Figure 7: HCl oxidation activity of the electrospun $Ce_xZr_{1-x}O_2$ nanofiber samples *versus* their respective plain and complete oxygen storage capacity (OSC and OSCc, respectively). The activity data at the end of 60 h Deacon reaction experiments at 703K with "mild" feed composition are used here. Adapted from ref. **69**.

As noted above, the formation of $Ce_xZr_{1-x}O_2$ through the substitution of a portion of CeO_2 with ZrO_2 has the potential to enhance both the catalytic activity and stability. In 2013, a feasible approach to commercialize cerium-based catalyst was developed by Pérez-Ramírez *et al*. Initially, they selected various carriers (ZrO_2, Al_2O_3, TiO_2) to support CeO_2 and calcined these catalysts at 900 °C for 5h.[26] CeO_2/ZrO_2 displays a superior activity compared with CeO_2/Al_2O_3 and CeO_2/TiO_2. A sharp increase in STY can be observed when increasing ceria concentration to 11 wt.%, and then the activity keeps roughly constant with an increase of ceria over 11 wt.%. The excellent activity of CeO_2/ZrO_2 can be traced to the co-existence of nanostructured CeO_2 and Ce-Zr mixed oxide (cf. **Figure 8**). *In situ* PGAA evidences that higher Cl coverage is unfavorable to the catalytic activity. Finally, CeO_2/ZrO_2 pellets (diameter=3mm, length=4mm) are prepared and tested in a pilot plant, and it shows a long-term stability of 700h on stream.

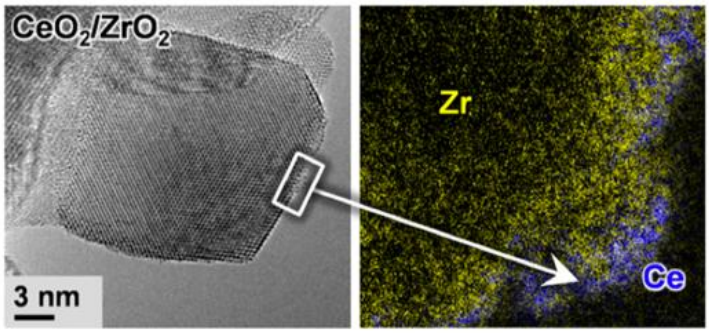

Figure 8: HRTEM and EELS images of fresh CeO_2/ZrO_2-1. Adapted from ref. **26**.

Thus, cerium-based catalysts, as a promising alternative to RuO_2, exhibit an outstanding activity and stability at an elevated temperature. Nevertheless, several scientific questions on cerium-based catalysts, particularly the ceria-zirconia system, have not been settled so far. The further development of dedicated ceria-zirconia materials for the Deacon process is extremely appealing.

1.3 Introduction on Typical Ceria and Ceria-Zirconia Materials

As mentioned in **Chapter 1.2**, cerium-based catalyst systems are highly desirable for HCl oxidation. In this chapter, the structural properties of ceria and ceria-zirconia materials are briefly introduced.

1.3.1 Structural properties of CeO_2 materials

Ceria, as the oxide form of the most abundant rare earth element cerium, are widely employed in environmental catalysis, energy field and halogen chemistry over the past decades.[18-21,70] CeO_2 crystallizes in the fluorite structure with typical face-centered cubic (f.c.c.) unit cell, in which each Ce atom at the corner of the cube is coordinated with eight adjacent oxygen atoms, and each oxygen atom is coordinated with four adjacent Ce atom (cf. **Figure 9**). Generally, Ce^{4+} can be reduced to Ce^{3+} by releasing oxygen following Kröger-Vink notation (cf. **Eq. 2**), which is accompanied by the formation of oxygen vacancies. In particular, the fluorite structure of $CeO_{2-\delta}$ can still be retained even after the loss of considerable amounts of oxygen from its lattice. The oxidation from Ce^{3+} to Ce^{4+} can also take place when oxygen fill up vacancies. Therefore, both Ce^{3+} and Ce^{4+} oxidation states can appear at non-stoichiometric $CeO_{2-\delta}$. It has been established that the unit-cell parameter of $CeO_{2-\delta}$ increases in line with an increase in defect concentration δ due to the larger ionic radius of Ce^{3+} (0.143nm) in comparison with Ce^{4+} (0.097nm).[21,71,72]

As for CeO_2 materials, the quantification of absorb/release lattice oxygen under oxidizing/reducing conditions is called oxygen storage/release capacity (OSC). The OSC can either be treated under dynamic conditions (fast or dynamic or plain: OSC) or under steady state conditions (total or complete OSC: OSCc).[18,27,73] In the OSC experiments the oxide is reduced mostly by molecular hydrogen or CO, while the reduced oxide is re-oxidized with molecular O_2 gas; the required amount of O_2 for the re-oxidation step defines the value of the OSC.

Altogether, the unique properties of ceria materials including low redox potential of Ce^{4+}/Ce^{3+} oxidation states and outstanding OSC are key factors in their catalytic applications.

$$2\,Ce_{Ce} + O_O \rightarrow 2\,Ce'_{Ce} + V_O^{\bullet\bullet} + \frac{1}{2}O_2 \quad \textit{Eq. 2}$$

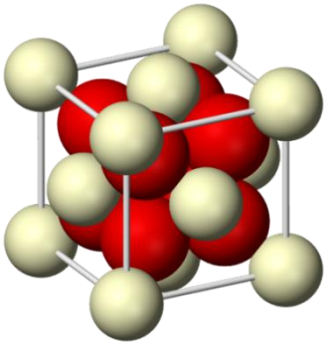

Figure 9: Crystal structure of CeO_2. Ce atom is in yellow, O atom is in red.

1.3.2 Structural properties of $Ce_xZr_{1-x}O_2$ materials

The fluorite-structured CeO_2 can be capable of forming solid solution with varieties of metal oxides. $Ce_xZr_{1-x}O_2$ material is the most well-known and well-established component in numerous of catalytic applications. Ceria-zirconia solid solutions, $Ce_xZr_{1-x}O_2$, adopt three possible structures: monoclinic (*m*), tetragonal (*t*, *t*′, *t*″), and cubic phase (*c*). However, the identification of crystal structure of homogeneous $Ce_xZr_{1-x}O_2$ is challenging since the tetragonal phase comprises one stable (*t*) and two metastable (*t'*, *t''*) phases with same $P4_2/nmc$ space group. Herein, the c/a_F (a_F is the unit-cell parameter *a* of the pseudo-cubic fluorite cell) ratio of both *t* and *t'* phase is higher than 1 while the c/a_F ratio of *t''* phase is equal to 1. Yashima *et al.* conducted an in-depth discussion on different phases of $Ce_xZr_{1-x}O_2$ through the combination of XRD, Raman, differential scanning calorimetry (DSC), neutron diffraction and HR-TEM.[74-77] The identification of most relevant phases of $Ce_xZr_{1-x}O_2$ are summarized in **Table 1**. After annealing at moderate temperatures (below 1055 °C), a monoclinic ($P2_1/c$) structure can be identified when the ceria concentration $x < 0.12$, and $Ce_xZr_{1-x}O_2$ with $x \geq 0.9$ possesses a cubic ($Fm3m$) structure. The *t* phase appears when the ceria concentration $x > 0.12$, and the transition from *t* to *t'* starts at $x \geq 0.20$. *t''* phase, as the intermediate between *t'* and cubic phase, presents at $x \geq 0.65$. It should be noted that the phase boundary is closely related to process of nucleation and growth. Therefore, the phase boundaries of various of $Ce_xZr_{1-x}O_2$ materials require more specialized studies through incorporation between its characterization results and corresponding references of **Table 1**.

The extensive utilization of $Ce_xZr_{1-x}O_2$ in catalytic reactions can be primarily attributed to its exceptional oxygen storage capacity, For a coordination number of 8, the ionic radius of Zr^{4+} is 0.084nm, while that of Ce^{4+} is 0.097nm.[78] In the case of pure CeO_2, the unit cell volume increases when Ce^{4+} is reduced to Ce^{3+}. However, the stress energy caused by this increase in unit cell volume restricts further reduction from Ce^{4+} to Ce^{3+}. The introduction of smaller Zr^{4+} ions into the CeO_2 framework can offset the increase of volume that arises from the reduction of Ce^{4+} ions, thereby lowering the formation energy of oxygen vacancies and generating a greater number of oxygen vacancies. The structural distortion resulting from the substitution of Ce^{4+} by Zr^{4+} also favors enhanced oxygen mobility.[79] Consequently, both features contribute to an increased oxygen storage capacity in the $Ce_xZr_{1-x}O_2$ material.

Table 1. Identification of most relevant phases of $Ce_xZr_{1-x}O_2$ materials below 1055 °C

Composition / x	Crystal structure	Space group	Unit-cell parameters
$0 \leq x < 0.12$	Monoclinic (m)	$P2_1/c$	$a_m \neq b_m \neq c_m$
$0.12 \leq x < 0.20$	Tetragonal (t)	$P4_2/nmc$	$c/a_F > 1$
$0.20 \leq x < 0.65$	Tetragonal (t')	$P4_2/nmc$	$c/a_F > 1$
$0.65 \leq x < 0.90$	Tetragonal (t'')	$P4_2/nmc$	$c/a_F = 1$
$0.90 \leq x \leq 1$	Cubic (c)	$Fm3m$	$c/a_F = 1$

1.3.3 Structural properties of supported CeO_2/ZrO_2 materials

In addition, a different ceria-zirconia catalyst system, CeO_2 supported on preformed ZrO_2 (CeO_2/ZrO_2), has been studied in the literature. Calvino *et al*. prepared CeO_2/ZrO_2 and CeO_2/YSZ by dry impregnation method and subjected them to a high-temperature reduction/oxidation atmosphere.[80,81] **Figure 10a** illustrates the epitaxial growth of the oxidized kappa phase on top of the zirconia surfaces after CeO_2/ZrO_2 catalyst is subjected to severe reduction followed by mild oxidation treatment (SRMO). With STEM-XEDS images (cf. **Figure 10b**) the authors identify the layer morphology of a $Ce_2Zr_2O_8$ kappa phase supported on YSZ after submitted CeO_2/YSZ catalyst to additional SRMO-SRSO (severe reduction followed by severe oxidation treatment)-SRMO treatment. The treatment results in the reconstruction of the CeO_2/ZrO_2 catalyst structure, leading to superior oxygen storage properties particularly in terms of low-temperature capacity and thermal stability. Furthermore, Chueh and coworkers reported the successful growth of single crystalline coherently strained CeO_2 (100) layer on a single crystalline yttrium-stabilized ZrO_2 substrate (YSZ (100)) with a thickness of up to 2.7 nm, employing the pulsed laser deposition method.[82] Smarsly *et al* prepared a well-defined CeO_2 thin layer at mesporous ZrO_2 thin films using ALD, thereby elucidating the influence of the CeO_2 layer thickness on the physicochemical properties.[83] XP spectra exhibit that Ce^{3+} concentration correlates with the ceria layer thickness, in which the Ce^{3+} dominates at lower number of ALD cycles and decrease gradually with increasing number of ALD cycles (thicker CeO_2 layer). In further studies, the influence of the as-prepared CeO_2 thin layer on its catalytic properties including the OSCc/OSC and the catalytic performance especially in oxidation reactions should be addressed.

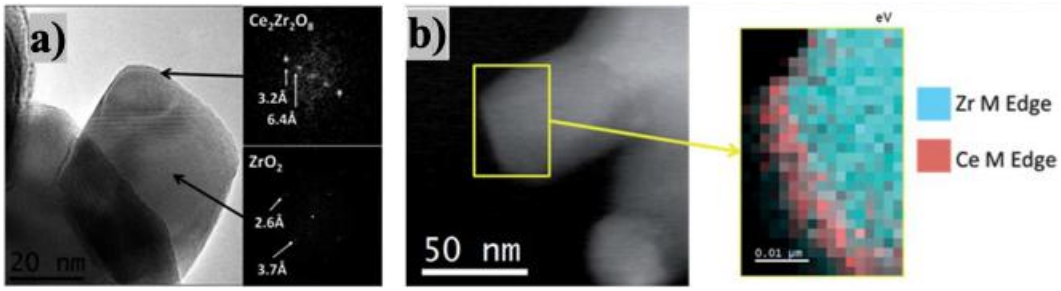

Figure 10: a) HR-TEM image on the 2.2% CeO_2/ZrO_2 after the SRMO treatment. **b)** STEM-XEDS images on the 1.9% CeO_2/YSZ after the SRMO-SRSO-SRMO treatment, spectrum image showing the distribution of Ce (red) and Zr (blue). Adapted from ref. **81**.

1.4 Experimental Approach

1.4.1 Preparation and determination of $Ce_xZr_{1-x}O_2$ solid solutions with a constant SSA

Ceria-zirconia solid solutions with different ratios of Ce/Zr were synthesized by the co-precipitation method. The hydrogen peroxide was first dropped into the $Ce(NO_3)_3 \cdot 6H_2O$ solution to obtain a molar ratio of H_2O_2/Ce of 1.5. The corresponding amount of $ZrO(NO_3)_2 \cdot nH_2O$ solution was then mixed with the solution to attain a molar ratio of Ce/Zr=(1-x)/x. The precipitation of ceria-zirconia precursor was achieved by dropping an ammonia solution into the solution keeping the pH at around 9.5. The precipitate was stirred for 18h and then washed with deionized water several times until pH value of around 7 was reached. The precipitate was then dried overnight at 120 °C and calcined at various temperatures (between 700 °C and 800 °C) for 5h in order to ensure a constant SSA among the various $Ce_{1-x}Zr_xO_2$, x=0,…1 samples. The samples are referred to as CZXXX with XXX being the atomic percentage (% unit) of cerium.

Prior to conducting N_2 physisorption experiments with Autosorb 6 of Quantachrome at 77 K, the samples were degassed in vacuum for 12 h at 393 K. The SSA was determined using the BET (Brunauer-Emmett-Teller) method.

The SSA of all samples remains invariant at 46 ± 2 m^2/g by by selecting an appropriate calcination temperature. The SSA of each sample was measured twice to estimate the scattering among the BET surface data (cf. **Chapter 2.1**).

1.4.2 Preparation and structure identification of supported CeO_2@ZrO_2 catalysts

The supported x mol.% CeO_2 on ZrO_2 catalysts with varying ceria concentrations (x=2.5, 5, 8, 11, 15, 20) were prepared by the incipient wetness impregnation method. For example, for the synthesis of the 5 mol.% CeO_2@ZrO_2 sample, the 0.27g $Ce(NO_3)_3 \cdot 6H_2O$ precursor was firstly mixed with 1.5ml H_2O. ZrO_2 support (1.46 g) was subsequently mixed with the above $Ce(NO_3)_3 \cdot 6H_2O$ solution, followed by stirring for 18 h at room temperature. The mixture was then dried in air at 80 °C for 12h and calcined in air at various temperatures (between 500 and 900 °C) for 1h, 5h or 10h. The monoclinic ZrO_2 sample was purchased from Saint-Gobain NorPro in pelletized form (diameter = 3 mm, length = 4 mm). The ZrO_2 particles were crushed and dried in air at 160 °C for 2h prior to impregnation. Nomenclature of the CeO_2@ZrO_2 samples: xCeO_2@ZrO_2-y, with *x* corresponds to the molar percentage of CeO_2, *y* refers to the calcination temperature in °C for 5h. For comparison reasons pure ZrO_2 was calcined at 600 °C and 900 °C for 5h in each case and employed in catalytic tests.

The CeO_2@ZrO_2 structure was identified through systematic application of state-of-the-art analytical techniques, including XRD, Raman, Rietveld refinement, XPS, HRTEM with XEDS map, AC-HRTEM and others.

1.4.3 HCl Catalytic oxidation measurement

The Deacon reaction was conducted in a custom fixed-bed flow reactor (cf. **Figure 11**). The reactor comprises the gas supply, the quartz tube reactor, heated by a computer-controlled furnace, and UV/vis analytics (Ocean Optics USB4000 with a DH-2000-BAL light source) for chlorine quantification. The following gases were used in the reaction measurements: HCl 4.5, O_2 5.0 and Ar 5.0 from AirLiquide, and the flow rate of gases was controlled by digital mass flow controllers (MKS Instruments 1179B). Prior to feeding the gas mixture into the reactor, Ar was dried using a water absorption cartridge (ALPHAGAZTM purifier H2O-free, AirLiquide). The absorbance at a wavelength of λmax = 329 nm (absorption maximum of chlorine) is proportional to the chlorine space time yield (STY) that is defined as the molar amount of product per time and mass catalyst.

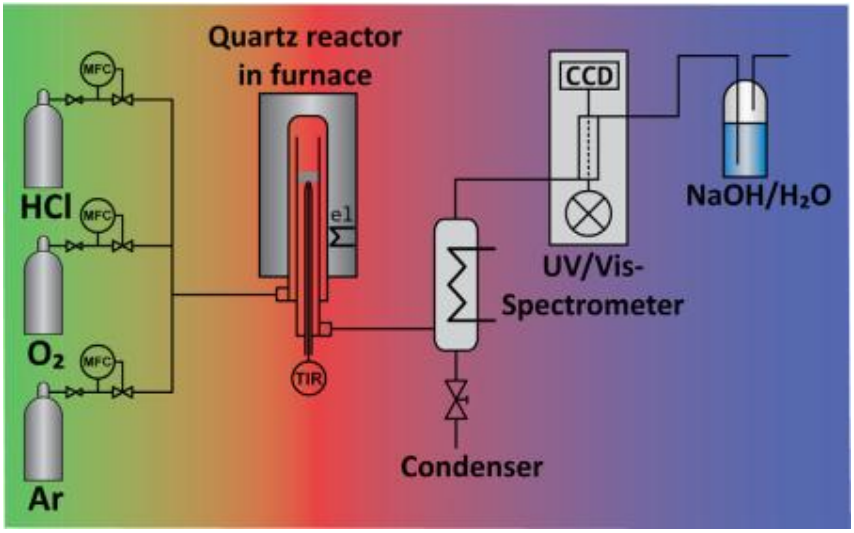

Figure 11: Schematic diagram of the flow reactor, consisting of the gas supply (green), the electrically heated reactor (red) and the chlorine quantification by UV-vis (blue). Adapted from ref. **69**.

(i) Correlation between UV-Vis signal and STY

The Beer-Lambert law was employed to determine the Cl_2 concentration. Typically we can get the A/Extinction value during the course of test, thus enabling the concentration of Cl_2 to be calculated in accordance with the parameters set out in ***Eq. 3***.

$$\text{The Absorbance or Extinction; A/Extinction} = -\log_e \frac{It}{I0} = \varepsilon * l * c \quad \textit{Eq. 3}$$

ε = absorptivity of Cl_2 (constant value and taken from NIST data bank and counterchecked by iodometry by integrating the absorbance over the time period t_1 to t_2)
l= the thickness of the Cl_2 in the cell (fixed value)
c= concentration of Cl_2

Prior to undertaking the UV-Vis run, it is essential to establish a correlation between the UV-Vis signal and STY. In accordance with the ***Eq. 4***, the critical value that must be obtained is the fixed value of **ε*l**.

$$\int_{t1}^{t2} (Extinction) * dt = \varepsilon * l * \int_{t1}^{t2} c * dt \quad \textit{Eq. 4}$$

Hereinto, $\int_{t1}^{t2} (Extinction) * dt$ can be calculated from the UV-Vis spectra (cf. **Figure 12**).

$$(\int_{t1}^{t2} c * dt) = \int_{t1}^{t2} \frac{Cl2\ outcome}{gas\ flow} dt = \frac{1}{gas\ flow} \int_{t1}^{t2} Cl_2\ outcome * dt \quad \textbf{Eq. 5}$$

The amount of Cl_2 produced between t_1 and t_2 can be derived from iodometry method.

Consequently, the value of the constant **ε*l** can be obtained.

STY is derived from the molar concentration *c* of Cl_2, the volumetric flow rate *v*, and the mass of the catalyst m_{cat} according to STY=c*v*/m_{cat}.

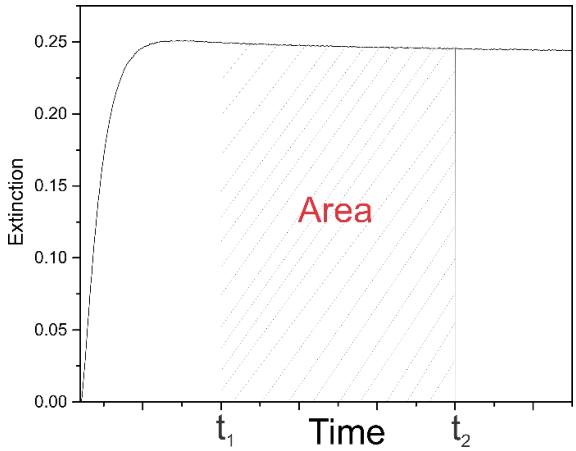

Figure 12: The extinction value as a function of time on stream.

(ii) Calibration of the extinction in the UV-Vis signal to absolute Cl_2 concentrations

To obtain a reliable STY value from the UV-Vis signal, two different reaction conditions at 430 °C included Ar: HCl: O_2 = 10.5: 1.5: 3 and Ar: HCl: O_2 = 11: 3: 1 were employed in the calibration experiments, with the 20 mol.% CeO_2@ZrO_2 model catalyst. The extinction value of obtained from UV-Vis analysis under both conditions are 0.21 and 0.13 (cf. **Figure 13**), respectively. It can be observed that a stable extinction value can be achieved over a 20 minutes on stream. Concurrently, the product Cl_2 is absorbed by the KI solution over the same 20 minutes on stream. The amount of Cl_2 can be quantified by iodometry using the reaction ***Eq. 6*** and ***Eq. 7*** and quantifying the amount of consumed $Na_2S_2O_3$ (cf. ***Eq. 8***). The consumption of $Na_2S_2O_3$ can be observed to be 3.8 mL and 2.4 mL for **Figure 13a** and **Figure 13b**, respectively.

$$I^- + 2KI + Cl_2 = 2KCl + I_3^- \quad \textbf{Eq. 6}$$

$$I_3^- + 2Na_2S_2O_3 = 2NaI + Na_2S_4O_6 + I^- \quad \textbf{Eq. 7}$$

$$n(Na_2S_2O_3) = ½ * n(Cl_2) \quad \textbf{Eq. 8}$$

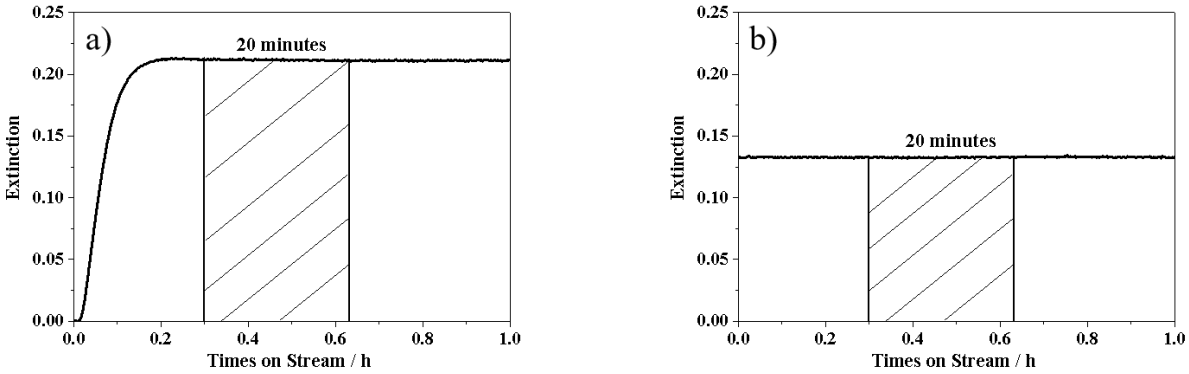

Figure 13: The extinction value as a function of time on stream at 430 °C under different reaction conditions: **a)** Ar: HCl: O_2 = 10.5: 1.5: 3, **b)** Ar: HCl: O_2 = 11: 3: 1.

Based on above results, Cl_2 concentration can be calculated by the consumption of $Na_2S_2O_3$. In summary, the calibrated STY formula is presented below and employed in the "reactivation-deactivation" experiments.

$$STY(mol\text{-}Cl_2/(kg\text{-}cat*h)) = 2.7273*Extinction\ value*0.001/Mass\ of\ catalyst\ (kg)$$

(iii) In situ Deacon reaction activity test

Besides catalytic activity tests, the flow reactor with the UV-Vis analytics can be employed to quantify the degree of chlorination of the catalyst after the Deacon reaction (cf. **Figure 14**). In doing so we reoxidized the chlorinated catalysts by oxygen exposure and the replaced chlorine from the catalyst is quantified by UV-Vis spectroscopy. Since the sensitivity of the UV-Vis spectroscopy is high and the data acquisition is quite fast enough, this dechlorination process of the once (partly) chlorinated catalyst can be followed in-situ as a function of time. Before above experiments, iodometry is employed to calibrate the extinction in the UV-Vis signal to absolute Cl_2 concentrations.

The proposed method for quantifying the degree of catalyst chlorination is in-situ, but not operando, since we have to switch the reaction mixture and then determine the degree of chlorination in the same apparatus. In particular, we developed a reliable measurement protocol shown in **Figure 14** with the total flow is set to 15 $cm^3STPmin^{-1}$ (sccm) and the catalyst is kept at 430 °C. Each reaction step is followed by a purging step with pure Ar to remove the weakly held species from the reactor walls until the baseline of the chlorine UV-Vis signal is stable. The Deacon reaction experiments is first carried out under so-called “mild” condition with the feeds ratio of Ar: HCl: O_2 = 10.5: 1.5: 3. After the catalytic activity has reached steady state, the activity in terms of space time yield (STY) can be determined. Subsequently pure Ar is purged and the deactivation experiment is performed under so-called “harsh” condition with a feed ratio of Ar: HCl: O_2 = 9: 4.5: 1.5. When the catalyst has fully deactivated due to in-depth chlorination, pure Ar is purged. To quantify the degree of chlorination of the deactivated CeO_2-based catalyst, it is exposed to 50 vol. % O_2 (balanced by argon) for 5h at the reaction temperature until the deactivated catalyst is fully reoxidized. During reactivation, oxygen replaces chlorine in the catalyst that can be quantified by UV-Vis spectroscopy. After completion of the reactivation step, the reactor is purged with Ar. This terminates the first deactivation/reactivation cycle. The deactivation/reactivation cycle is repeated twice in order to quantify the activity loss due to restoration.

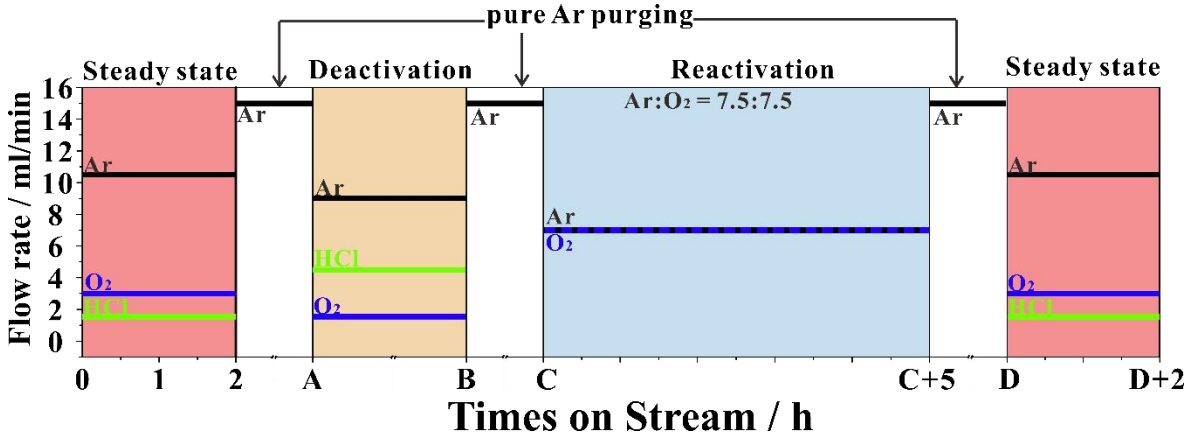

Figure 14: The measurement protocol (reaction feed composition) for determining the degree of chlorination of a CeO_2-based catalyst after full deactivation. The total flow rate is always 15 sccm and the catalyst is kept at 430°C. Steady state activity experiments are performed before and after restoration (reactivation).

1.4.4 CO catalytic oxidation measurement

The oxidation experiments of CO were carried out in another home-built fixed-bed flow reactor. The design comprises the gas supply, the quartz tube reactor, heated by a furnace, and analytics for the CO_2 quantification. The flow rates of gases (CO Praxair, quality 4.7, O_2 Praxair, quality 5.0 and N_2, Linde) were controlled by digital mass flow controllers (SevenStar D07-19B). The nitrogen-balanced reaction feeds contain 1 vol. % CO, 10 vol. % O_2 and 89 vol. % N_2 that passed the reactor tube with flow rate of 90 $cm^3STPmin^{-1}$ (sccm). For the catalytic tests, 10 mg of catalyst was supported between two quartz wool wads. The furnace was firstly heated to 150 °C with a rate of 20 $K \cdot min^{-1}$, held for 10 min, and then heated to of 250 °C with a rate of 20 $K \cdot min^{-1}$, held for 10 minutes, and to 350 °C with a rate of 20 $K \cdot min^{-1}$, held for 10 minutes, and finally to 430 °C (reaction temperature) with a rate of 20 $K \cdot min^{-1}$, held for 30 minutes. The gas composition was monitored online using the X-Stream-CO_2 analyzer (Rosement). The STY of CO_2 was calculated on the basis of the CO_2 concentration in the outlet gas stream.

1.4.5 OSC/OSCc measurement

The experiments of oxygen storage capacity (OSC) were carried out by using a stainless-steel tube (i.d. 4 mm, length 60mm) connected to the gas inlet system by stainless steel leads (i.d. 1.6 mm) *via* Swagelok tube fittings. The catalyst (30 mg) was dried at 120 °C for 5h and loaded into the reactor, supported between two quartz wool wads. The OSC reactor containing the sample was heated to 430 °C with a rate of 10 $K \cdot min^{-1}$ using the same furnace and temperature control as for the HCl oxidation experiments. Carbon monoxide (Praxair, quality 4.7) was employed as the reducing agent while oxygen (Praxair, quality 5.0) serves as the oxidizing agent. The stream selector (VICI multi-position valve with an outlet for unused streams) allows to switch software-controlled at specified time intervals between three gases (CO, O_2 and Ar: with a flow rate of 2 sccm each) and mix them with the Ar carrier stream (18 sccm). After leaving the OSC reactor, the gases pass through a Swagelok sintered stainless steel filter (pore size 2 µm) and reach the microvolume thermal conductivity detector (VICI TCD2) operated with pure argon as the base line (detector temperature 373 K, filament temperature 423 K).

To determine the plain or dynamic oxygen storage capacity (OSC), the stream selector was switched to CO for 2s and to O_2 for 2s alternatively with a 80s Ar purge step in between. Using additional O_2 pulse as a reference, the amount of adsorbed oxygen was calculated that corresponds to the (dynamic) OSC. The complete oxygen storage capacity (OSCc) was determined by reducing the catalyst with a sufficiently long sequence of CO pulses each 10s long accompanied by 80s Ar pulse pauses. Subsequently, the selector was switched to O_2 for ten pulses of 2s duration separated by 80s pure Ar pulses were applied. The total amount of consumed oxygen is taken to be the OSCc.

2. Results and Discussions

2.1 Oxygen Storage Capacity versus Catalytic Activity of $Ce_xZr_{1-x}O_2$ solid solutions

We firstly prepared $Ce_xZr_{1-x}O_2$ solid solutions as a function of the composition *x* with a constant SSA by the co-precipitation method. In order to obtain $Ce_xZr_{1-x}O_2$ solid solutions with a constant SSA, the samples were calcined at various temperatures (between 700 and 800°C) for 5h. The SSA of all samples remain constant at 46 $\pm$ 2 m^2/g by selecting an appropriate calcination temperature. The SSA of each sample was measured twice to allow for the estimation of potential scattering amongst the BET surface data. In comparison to pure ZrO_2 and CeO_2, the ceria-zirconia solid solutions require slightly higher calcination temperatures between 700 °C and 800 °C to maintain the BET surface area (cf. **Table 2**). As the concentration of Ce is increased from 0% to 16%, the calcination temperature reaches a maximum value (790 °C).

Table 2. SSA and corresponding calcination temperature of $Ce_xZr_{1-x}O_2$, (CZxxx: xxx percentage of Ce)

Samples	BET surface area (m^2/g)		Calcination Temperature (°C)
	1st time	2nd time	
CZ000	45.9	44.9	615
CZ002	47.7	48.4	650
CZ005	44.5	45.8	700
CZ007	45.2	47.5	700
CZ010	46.1	45.9	730
CZ013	46.6	45.6	730
CZ016	47.6	44.6	790
CZ020	46.9	45.5	780
CZ030	47.4	44.4	750
CZ040	48.1	48.1	760
CZ050	45.7	45.0	730
CZ060	46.4	46.2	740
CZ070	46.2	47.5	750
CZ080	47.4	44.9	720
CZ090	48.4	47.5	710
CZ100	46.3	47.4	540

Subsequently, a systematic characterisation was developed to ensure reconciliation with the nominal bulk stoichiometry, as defined by the concentration of Ce and Zr precursors. As illustrated in **Figure 15**, the cell dimension, calculated by Rietveld refinement based on a distorted cubic structure reveals a linear dependence on *x*, the nominal concentration of ceria as defined by the preparation. A similar expansion of the cell parameter has been reported summarized for $Ce_{1-x}Zr_xO_2$ powder samples and is summarized in the Vegard plot.[84, 85] Moreover, XPS experiments were conducted on the freshly prepared ceria-zirconia solid solutions with the objective of quantifying the concentration of Ce in the near-surface region.

The concentration of Ce in the surface region, derived from the Zr 3d and Ce 4d spectra, exhibits a roughly linear dependence on *x*, thus being reconciled with the nominal bulk stoichiometry as given by the concentration of Ce and Zr precursors.

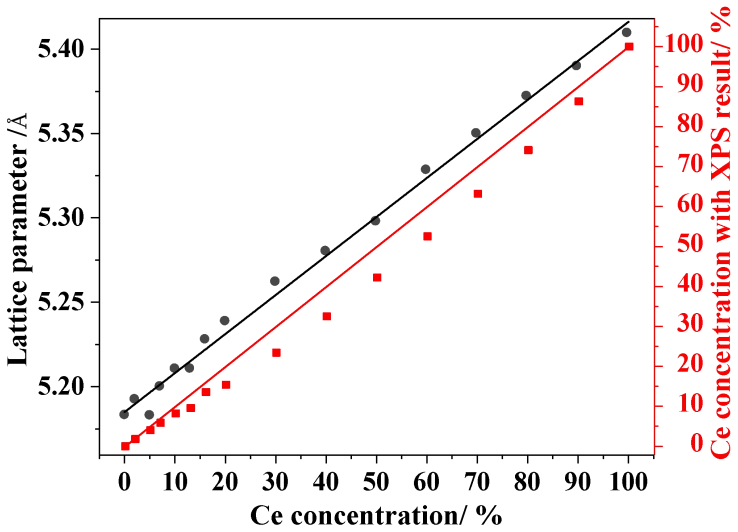

Figure 15: The cell parameter calculated by Rietveld refinement in comparison with the Ce concentration calculated by XPS.

The OSC experiments and the catalytic tests were conducted at a constant reaction temperature of 430 °C. As shown in **Figure 16b**, the correlation between OSCc and the activity in the CO oxidation reaction is indeed close, since the OSC experiments and the catalytic tests are conducted at the same reaction temperature of 430 °C and with the same reductant, namely CO. The data set for activity as a function of Ce concentration (*x*) exhibits three distinct linear regions, which are reflected in the OSCc data. The identical trends observed in the OSCc and the activity of the CO oxidation reaction over $Ce_xZr_{1-x}O_2$ catalysts, suggest that the OSCc determined in this study is at least proportional to the true OSCc. Furthermore, we can conclude that the CO oxidation proceeds *via* a MvK mechanism, where the reduction of the oxide by CO is the rate-limiting step.

With regard to the HCl oxidation reaction, the reducing agent is HCl, which differs from CO (used in OSC experiments). Additionally, the products are not identical (Cl_2 and H_2O *versus* CO_2). As the activity of the HCl oxidation reaction also follows the aforementioned trend in the OSCc, the trends in activity of CO and HCl oxidation are found to be strikingly similar. From these findings, we can infer that the HCl oxidation reaction also proceeds *via* a MvK mechanism, with the reduction of the oxide by HCl exposure being rate-limiting.

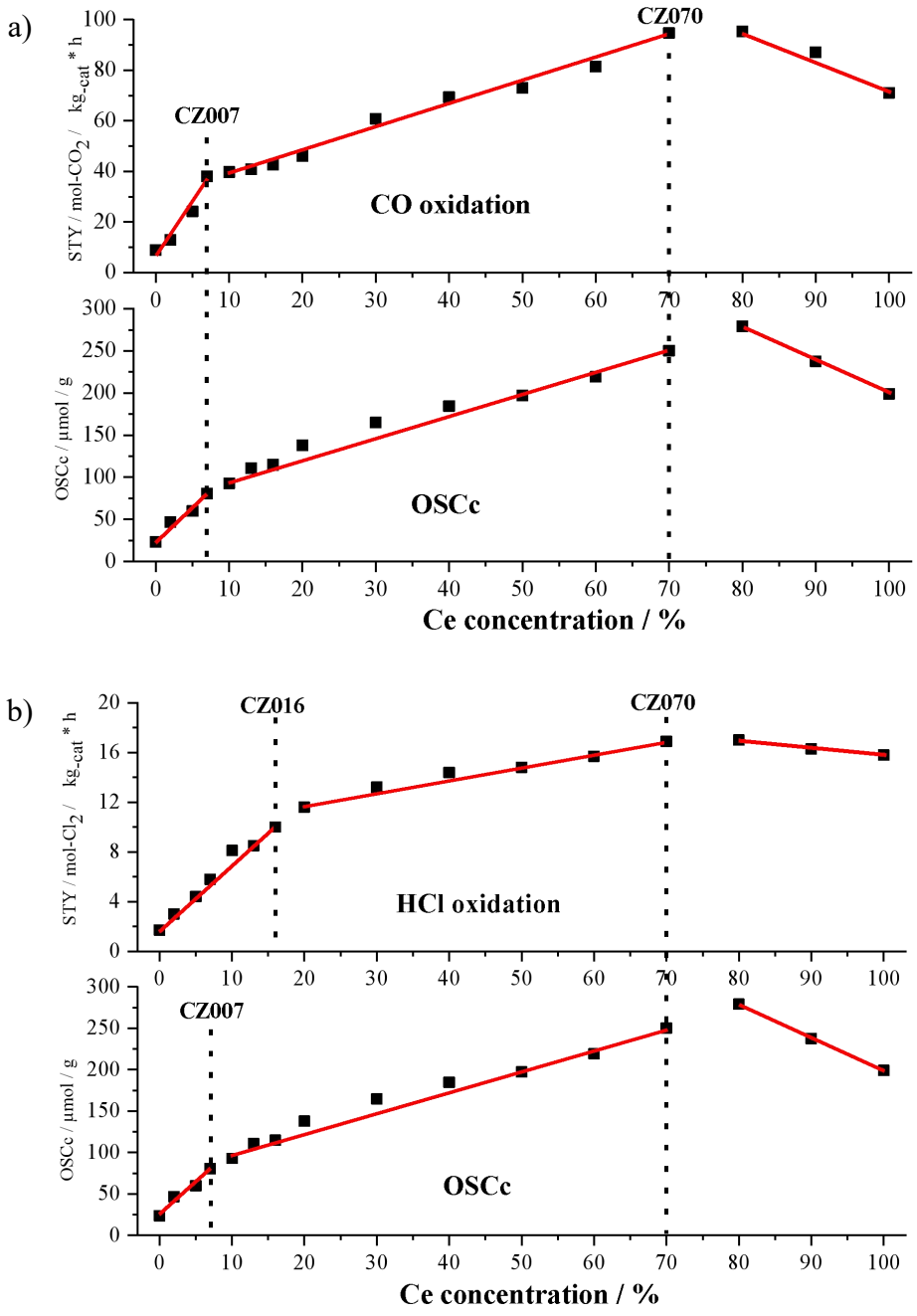

Figure 16: Direct comparison of the Space-time yield (STY) per kilogram of catalyst in the **a)** CO and **b)** HCl oxidation reaction for as-prepared CZxxx samples (xxx = 0-100) with the complete OSC (OSCc). The reaction temperature during the reaction was 430 °C. CO oxidation reaction conditions can be referred to **Chapter 1.4**. HCl oxidation reaction: A total flow rate of 15 sccm was applied and the reaction condition: N_2: HCl: O_2 = 7: 1: 2.

2.2 Determination of Highly Active and Stable Layer Morphology of CeO_2@ZrO_2

A systematic investigation was conducted on the CeO_2-supported on ZrO_2 catalyst (CeO_2@ZrO_2) with varying concentrations of ceria load on the surface of ZrO_2 particles and calcined at different temperatures. These samples were then evaluated under a range of reaction conditions. Calcination of CeO_2@ZrO_2 at 600 °C for 5 hours (cf. **Figure 17a**) demonstrates a pronounced increase in the Deacon activity with increasing CeO_2 concentration up to 5 mol.% CeO_2; this is followed by a gradual rise up to 20 mol.% CeO_2. A calcination temperature of 900 °C is deemed sufficient to induce Ce-Zr intermixing,[26] yet the resulting activity is markedly inferior to that observed for a calcination at 600 °C (cf. **Figure 17b**).

Apparently, two questions emerge in mind: firstly, how to explain the steep rise in activity with increasing concentration of Ce to 5wt.%, and secondly, why the activity of the catalyst calcined at 900°C is inferior to that observed for a calcination at 600°C? With these questions in mind we undertook a systematic characterization to gain insight.

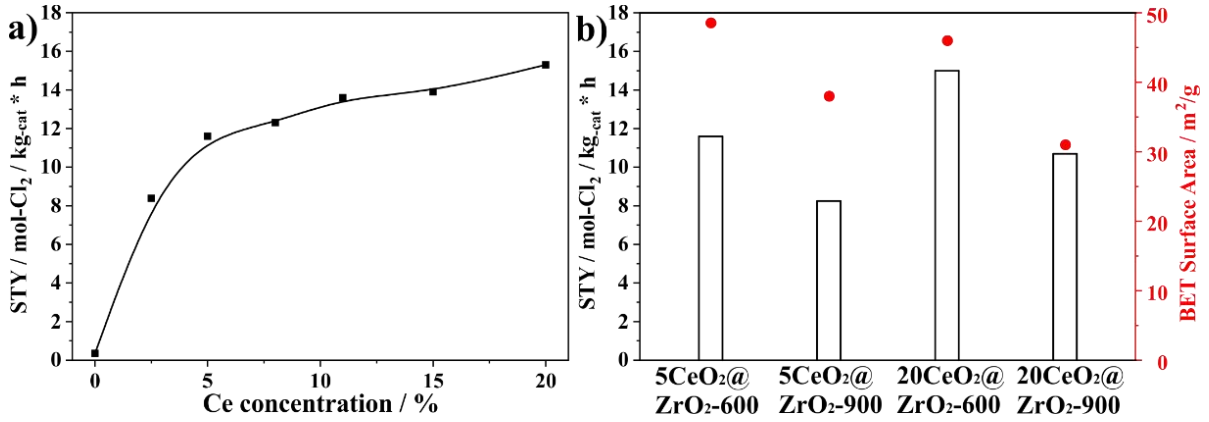

Figure 17: a) Activity data of the HCl oxidation reaction for xCeO_2@ZrO_2-600 with different molar ceria concentrations. **b)** Activity data of the HCl oxidation reaction and BET surface area for 5CeO_2@ZrO_2 and 20CeO_2@ZrO_2 which was calcined to 600 ºC and 900 ºC for 5h. The activity data are given as STY (black, right scale) for a reaction mixture Ar: HCl: O_2 = 10.5: 1.5: 3 and a flow rate of 15 sccm, 30 mg of catalyst and a reaction temperature of 430 °C. The BET surface areas of the pristine materials (i.e. prior to the HCl oxidation reaction) are given in red (right scale).

TEM was initially employed for the direct distinction of catalyst morphologies. It is evident that CeO_2 forms a layer with a thickness of approximately 1-2 nm on the supporting ZrO_2 particle in 5CeO_2@ZrO_2-600 (cf. **Figure 18b**). Furthermore, there is no discernible attachment of CeO_2 particles to ZrO_2 observed. In contrast, the 20CeO_2@ZrO_2-600 sample reveals, as observed under TEM (cf. **Figure 18c**), a thin CeO_2 layer on which small CeO_2 particles (approximately 6 nm) adhere. For purposes of comparison, similar TEM experiments are presented for the 20CeO_2@ZrO_2-900 sample (cf. **Figure 18d**). At higher calcination temperatures (900 °C), the CeO_2-related particles are no longer observed. Instead, a crystalline CeO_2 thin layer is present, forming an interface with a mixed $Ce_xZr_{1-x}O_2$ underlayer. It should be noted that TEM is a local method, and the results may not be representative of the entire sample. To strengthen our conclusion, some sensitive characterizations, such as Raman spectroscopy and XPS, were employed.

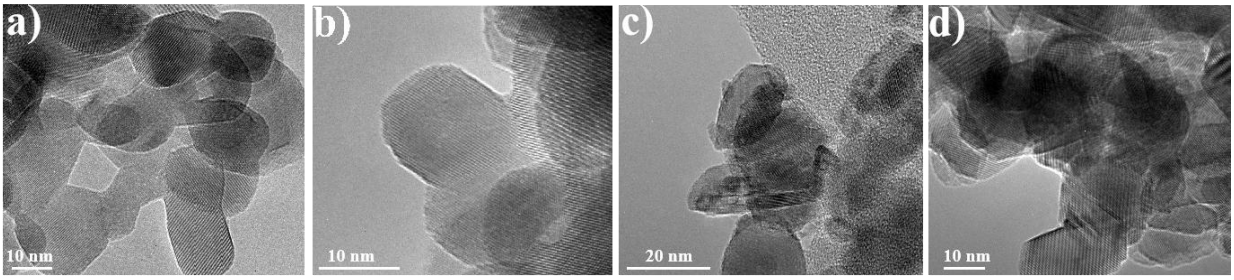

Figure 18: High-Resolution TEM images of **a)** ZrO_2 calcined at 600°C for 5 h, **b)** $5CeO_2@ZrO_2$-600, **c)** $20CeO_2@ZrO_2$-600, **d)** $20CeO_2@ZrO_2$-900.

In general, Raman spectroscopy is more sensitive than XRD to the presence of a $Ce_xZr_{1-x}O_2$ solid solution. From visual inspection of the Raman spectra in question, it is evident that the predominant phonon mode at approximately 470 cm^{-1} exhibits a notable dependence on the calcination temperature and CeO_2 content.[92]

In the case of the $5CeO_2@ZrO_2$ sample, the band observed at 460-480 cm^{-1} consists of a superposition of pure CeO_2 and pure ZrO_2 Raman spectra for calcination temperatures of 300 °C and 600 °C. This finding is compatible with the coexistence of pure CeO_2 and ZrO_2. Upon increasing the calcination temperature to 900 C ($5CeO_2@ZrO_2$-900), the CeO_2-related peak is no longer discernible (**red circle 1** in **Figure 19**), with only the ZrO_2-related band at 476 cm^{-1} remaining. While the ZrO_2-related peak at 476 cm^{-1} slightly shifts to lower wavenumber which can be attributed to the presence of Ce-Zr mixed oxides.[26, 86, 87] Given that the two Raman spectra ($5CeO_2@ZrO_2$-300 and $5CeO_2@ZrO_2$-600) are practically identical, it can be concluded that Ce-Zr intermixing in $5CeO_2@ZrO_2$-600 can be safely ruled out for a calcination temperature of 600 °C. The band observed at 460-480 cm^{-1} in the $20CeO_2@ZrO_2$-600 sample can be also attributed to a superposition of pure CeO_2 and pure ZrO_2 Raman spectra and therefore pointing toward a coexistence of CeO_2 and ZrO_2. For the $20CeO_2@ZrO_2$-900 sample (**red circle 2** in **Figure 19**), the CeO_2-related feature changes drastically with calcination temperature. It would appear that a greater proportion of CeO_2 is combined with ZrO_2 to form the $Ce_xZr_{1-x}O_2$ solid solution in the $20CeO_2@ZrO_2$-900 sample.

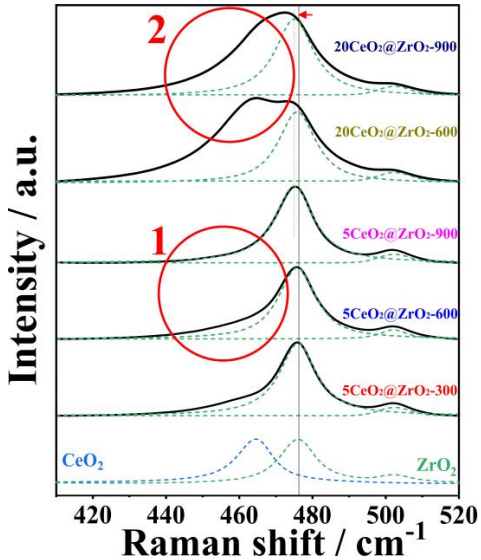

Figure 19: High resolution Raman spectra of $5CeO_2@ZrO_2$ and $20CeO_2@ZrO_2$ that were calcined to 300 ºC, 600 ºC and 900 ºC for 5h.

Furthermore, given the morphology of the CeO_2 layer covering partly the ZrO_2 particle, it can be posited that the apparent Ce-related XP spectra signal will be enhanced and that of the Zr-related signal will be dampened. Altogether such structure will lead to an apparent increase in the Ce concentration. It can be deduced from the Ce 4d and Zr 3d XPS signals that the Ce concentration are 14% and 53% for $5CeO_2@ZrO_2$-600 and $20CeO_2@ZrO_2$-600, respectively. This is 2-3 times higher than the nominal concentration of 5 mol.% and 20 mol.%, respectively. Meanwhile, the OSCc value of $5CeO_2@ZrO_2$-600 is 23 µmol (O)/g, which is practically identical to the OSC value of $5CeO_2@ZrO_2$-600 (25 µmol (O)/g (cf. **Figure 20b**). Quite in contrast, the data for $20CeO_2@ZrO_2$-600 are markedly disparate. It is well established that OSC represents the capacity of oxygen in the near-surface region of CeO_2, whereas OSCc is the capacity of surface and bulk CeO_2 oxygen storage.[18,70] These findings are in accordance with the morphology that a CeO_2 thin layer covers a significant portion of the ZrO_2 particle surface.

In order to determine the concentration of Ce^{3+} in the surface selvedge region, the photoelectron emission spectroscopy of the Ce 3d was analyzed.[88-90] The Ce 3d-spectra (cf. **Figure 20a**) demonstrate that the Ce^{3+} concentration of $5CeO_2@ZrO_2$-600 in comparison to that of Ce is significantly increased in contrast to pure CeO_2 and $20CeO_2@ZrO_2$-600 (cf. **Figure 20a**). The $Ce^{3+}/(Ce^{3+}+Ce^{4+})$ ratio doubles from 24% for CeO_2 and $20CeO_2@ZrO_2$-600 and to 48% in $5CeO_2@ZrO_2$-600. This may be correlated with the observed improvement in performance by the ultrathin CeO_2 layer in the Deacon process.

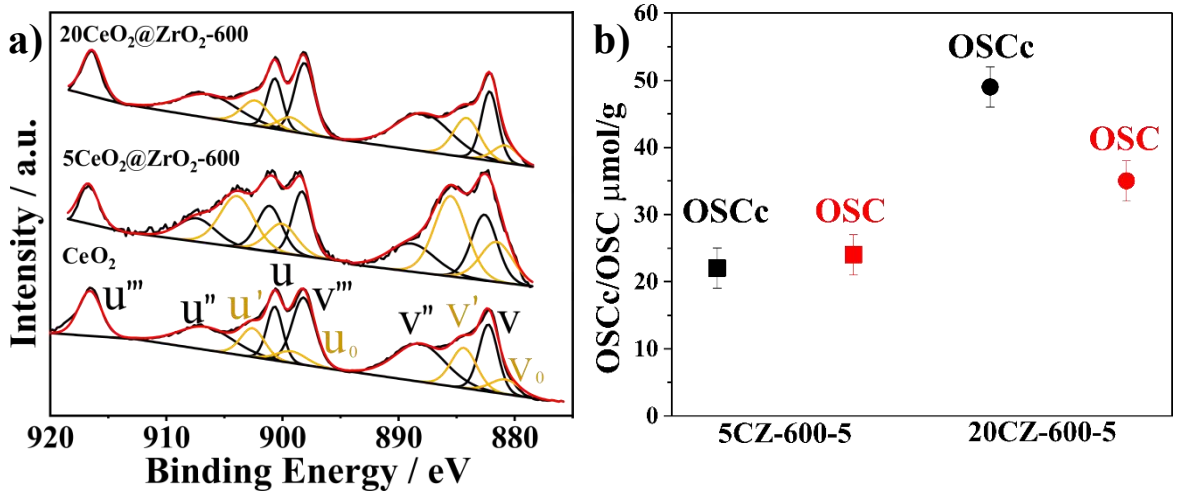

Figure 20: a) The Ce 3d XP spectra of fresh CeO_2, $5CeO_2@ZrO_2$-600 and $20CeO_2@ZrO_2$-600 samples including a deconvolution into Ce^{4+} and Ce^{3+}. The Ce^{4+} peaks are labelled by v, v'', v''', u, u'', u''' in black, while the Ce^{3+} peaks are labelled by v', v_0, u', u_0 in yellow. **b)** Plain oxygen-storage capacity, complete oxygen-storage capacity (OSC and OSCc, respectively) of $CeO_2@ZrO_2$-600. $5CeO_2@ZrO_2$-600: square, $20CeO_2@ZrO_2$-600: disk

In all, it can thus be seen that the catalytically active phase is reconciled with the CeO_2 thin layer on ZrO_2 particle, and that this dispersion process of CeO_2 saturates already with 5 mol.% of CeO_2. The surplus CeO_2 at higher mol.% (i.e. above 5%) results in the growth of CeO_2 particles attached to the $CeO_2@ZrO_2$ particles, thereby minimally altering the active CeO_2 surface area concomitant with a slight increase in activity.

The stability experiments of different Ce-based catalysts under the harshest condition (cf. **Figure 21**) were employed to identify superior stability of CeO_2 thin layer.

The fastest deactivation occurs for a pure CeO_2 powder sample (average particle size of 10 nm) with a similar BET surface area to that of $5CeO_2@ZrO_2$-600. It is noteworthy that the catalyst $5CeO_2@ZrO_2$-900 exhibits complete deactivation after 16 hours of operation, which is a notable decline in stability compared to the $5CeO_2@ZrO_2$-600. Additionally, the $20CeO_2@ZrO_2$-900 exhibits a pronounced decline in stability during the initial 5 hours of operation, a rate of deactivation that is considerably faster than that observed for $20CeO_2@ZrO_2$-600. From this observation, in combination with characterizations (XRD, Raman, XPS, TEM, cf. **Chapter 4.2**) of deactivated samples, we can infer that a 1-2 nm thick wetting layer of CeO_2 attached to ZrO_2 is chemically more stable against chlorination than a mixed $Ce_xZr_{1-x}O_2$ layer ($5CeO_2@ZrO_2$-900) or a CeO_2 layer attached to a $Ce_xZr_{1-x}O_2$ interface ($20CeO_2@ZrO_2$-900).

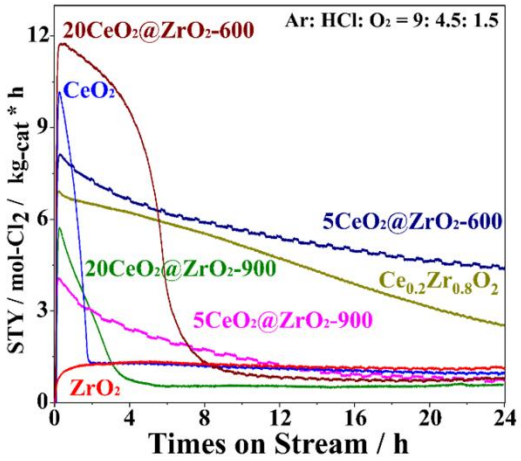

Figure 21: Deacon activity experiments of CeO_2, ZrO_2, $Ce_{0.2}Zr_{0.8}O_2$, $5CeO_2@ZrO_2$-600, $5CeO_2@ZrO_2$-900, $20CeO_2@ZrO_2$-600 and $20CeO_2@ZrO_2$-900 at T = 430 °C (flow rate 15 sccm, 30 mg catalyst, 24 h on stream) for the reaction feed Ar: HCl: O_2 = 9: 4.5: 1.5.

2.3 In situ Quantification of the Degree of CeO_2 Chlorination

The deactivation of CeO_2-based catalysts in the HCl oxidation reaction is a selective bulk-chlorination process, whereby the active CeO_2 component is transformed into $CeCl_3 \times nH_2O$. In this chapter, we present a dedicated experiment for quantifying the degree of chlorination of the CeO_2-based catalyst in the same reactor (cf. **Chapter 1.4**) used for catalytic tests. This unique experiment allows for the straightforward monitoring of the reactivation kinetics *via* reoxidation. To demonstrate the efficacy of this method, we present a proof-of-principle experiment utilizing two Deacon catalysts: a pure CeO_2 sample and the aforementioned $20CeO_2@ZrO_2$-600 as described in **Chapter 2.1 & 2.2**.

The experimental details have been described in **Chapter 1.4**. To demonstrate the high sensitivity of the present UV-Vis based reactor experiment, an investigation was conducted into the chlorination degree of stable CeO_2-based catalysts that have not undergone bulk-chlorination (cf. **Figure 22a**). The integral chlorine intensities in the dechlorination peaks and the BET surface areas of CeO_2 and $20CeO_2@ZrO_2$ are practically identical (cf. **Figure 22a**). This may be attributed to the presence of a comparable active phase in both samples. The chlorine content at the surface of the CeO_2 particle can be quantified from these experiments. It was found that the chlorination degree of pure CeO_2 is approximately 10%, while that of $20CeO_2@ZrO_2$ is 30%. The former value for pure CeO_2 is in close agreement with the PGAA-derived value of approximately 10% reported in the literature.[31]

Furthermore, dechlorination experiments were conducted on fully deactivated catalysts (cf. **Figure 22b**). With regard to the fully deactivated CeO_2 sample, the replaced chlorine amount of 6.3 $mol_{Cl2} \cdot kg_{cat}^{-1}$ corresponds to a chlorination degree of 68%. The pure CeO_2 sample was not fully chlorinated under the harsh conditions, but rather exhibited a chlorination limitation. This could be attributed to the $CeCl_3$ particles obstructing the CeO_2 surfaces, thereby impeding further chlorination. Quite in contrast, the chlorine peak area due to oxygen replacement for $20CeO_2@ZrO_2$ is 2 $mol_{Cl2} \cdot kg_{cat}^{-1}$, resulting in a chlorination degree of 91%. From the initial reoxidation of Cl_2 observed for the deactivated CeO_2 sample (cf. **Chapter 4.3**), we can ascertain that the chlorination degree of the $20CeO_2@ZrO_2$ composite is 100%. This implies that the entire CeO_2 component is transformed into the hydrated form of $CeCl_3$, which suggests that the thin layer structure facilitates complete chlorination. What is more, it is evident that reactivation for pure CeO_2 takes much longer than that for 20 mol% CeO_2 supported on ZrO_2 due to the fine $CeCl_3$ dispersion and high nucleation rate of CeO_2 on the support surface. In addition, we observe different shapes of the Cl_2 signals during reoxidation.

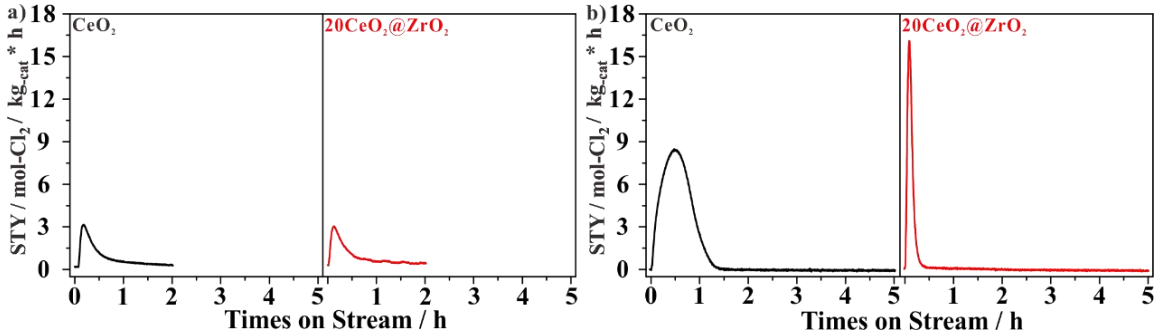

Figure 22: Time needed for reactivation of CeO_2 in comparison to that of $20CeO_2@ZrO_2$ after the activity measurement of **a)** steady state and **b)** fully-deactivated state after 2nd deactivation step.

In light of the aforementioned results, a cutting-edge characterization of fresh, deactivated and reactivated catalysts, in conjunction with a straightforward nucleation and growth model based on the JMAK approach, has been devised (cf. **Chapter 4.3**). The different reoxidation kinetics observed for the two kinds of catalysts can be attributed to the higher nucleation rate of CeO_2 on the ZrO_2 support surface. While the ZrO_2 surface is otherwise inert in the HCl oxidation reaction, it appears to provide sites for the nucleation of CeO_2 particles and to maintain the dispersion of $CeCl_3$ particles in the chlorinated catalyst. The ZrO_2 support thus facilitates the redispersion of the catalyst during chlorination-dechlorination cycles.

3. Conclusion and Perspective

This thesis presents fundamental research on two kinds of ceria-zirconia catalysts for the Deacon process. In order to establish a connection between systematic OSC data and the activity data of pure $Ce_xZr_{1-x}O_2$ solid solutions for HCl and CO oxidation reactions, we initially prepared $Ce_xZr_{1-x}O_2$ catalysts with a constant surface area by varying the calcination temperature. Secondly, we devised a method of depositing CeO_2 on preformed ZrO_2 particles (CeO_2@ZrO_2) using a moderate calcination temperature, with the aim of investigating the influence of the structure of CeO_2@ZrO_2 on the catalytic activity and stability. Finally, the reactivation process of two fully-deactivated CeO_2-based catalysts, namely pure CeO_2 and 20CeO_2@ZrO_2, was studied by oxygen treatment at 430 °C with a dedicated experiment. The main conclusions are as follows:

The $Ce_xZr_{1-x}O_2$ catalysts were prepared by the co-precipitation method and the specific surface area of all samples remains constant at 46 ± 2 m^2/g by selecting the appropriate calcination temperatures. By combining the concentration of ceria in the near-surface region, as determined by XPS experiments, with the linear relationship between ceria concentration *x* and the cell dimensions, as calculated by Rietveld refinement, it can be illustrated that the actual concentration of ceria is consistent with the nominal concentration of ceria. The OSCc of $Ce_xZr_{1-x}O_2$ solid solutions is found to vary as a function of the Ce content exhibiting a volcano curve. Hereinto, $Ce_{0.8}Zr_{0.2}O_2$ is observed to exhibit the highest OSCc value. The activity of $Ce_xZr_{1-x}O_2$ for both the CO and HCl oxidation reactions also exhibits a discernible trend with increasing Ce concentration. Catalytic activity increases with increasing Ce concentration up to 80% and then exhibits a slight decline with further increases in Ce concentration from 90% to 100%. With these specifically prepared $Ce_xZr_{1-x}O_2$ solid solutions we then compared the OSC with the activity of both the CO and the HCl oxidation reaction.The trend in the CO oxidation activity and in OSCc as a function of the composition *x* is virtually identical, thus being compatible with the expected Mars-van Krevelen mechanism. From the close correspondence between the OSCc and the activity of the HCl oxidation, we may infer that this oxidation reaction also proceeds *via* the Mars-van Krevelen mechanism.

CeO_2 on preformed ZrO_2 particles (CeO_2@ZrO_2) catalysts were prepared by incipient wetness impregnation method. The highly dispersed CeO_2 wetting layer, which exhibits an enriched concentration of Ce^{3+}, can be observed in the 5 mol.% CeO_2 on preformed ZrO_2 particles calcined at 600 °C for 5h (5CeO_2@ZrO_2-600). The addition of excess CeO_2 at higher molar ratios (i.e. above 5%) results in the growth of CeO_2 particles attached to the ZrO_2. The distinctive morphology of CeO_2@ZrO_2 is responsible for the high (specific) activity in the Deacon reaction. The 1-2 nm thick CeO_2 wetting layer lead to the exceptionally high specific activity observed in 5CeO_2@ZrO_2-600. Saturation of the wetting layer and formation of adhering CeO_2 particles result in a slight increase in activity above 5 mol% CeO_2. It is noteworthy that stability tests have demonstrated that a 1-2 nm thick layer of CeO_2 exhibits better stability than a mixed $Ce_xZr_{1-x}O_2$ layer (CeO_2@ZrO_2 calcined at 600 °C *versus* 900 °C) under the harsh reaction condition. From this observation, we can infer that the improved stability of the CeO_2 layer calcined at 600 °C is due to the formation of a sharp interface with the ZrO_2 support. Altogether, it is anticipated that this particular core-shell morphology, comprising an active and stable CeO_2 wetting layer on a ZrO_2 particle, could prove beneficial as a support or as active component in other catalytic oxidation reactions as well.

The pure CeO_2 and $20CeO_2@ZrO_2$-600 catalysts were subsequently employed to the dedicated "deactivation-reactivation" experiments to study the process of reactivation and quantify the degree of chlorination for fully-deactivated CeO_2-based catalysts. The catalytic activity of $20CeO_2@ZrO_2$-600 is completely recovered after the second deactivation-reactivation cycle, whereas the activity of pure CeO_2 after reactivation declines steadily. The quantification of the reoxidation peak during the initial reactivation cycle of fully deactivated CeO_2-based catalysts allows us to ascertain that the ceria species from deactivated $20CeO_2@ZrO_2$-600 is fully chlorinated, with a chlorination degree of 77% for pure deactivated CeO_2. In addition, the reactivation process for pure CeO_2 is considerably slower than that for $20CeO_2@ZrO_2$-600, and the shapes of the Cl_2 signals during reoxidation for above two samples are distinct. A modified JMAK model indicates that the accelerated reactivation of the $20CeO_2@ZrO_2$-600 catalyst is attributed to a higher nucleation rate, which is facilitated by the ZrO_2 support surface. While the ZrO_2 surface is otherwise inert in the HCl oxidation reaction, it appears to provide sites for the nucleation of CeO_2 particles and to maintain the dispersion of $CeCl_3$ particles in the chlorinated catalyst. The ZrO_2 support thus facilitates in the redispersion of the catalyst during deactivation-reactivation cycles. We conclude that the choice of catalyst support is crucial to prevent catalyst deactivation in non-steady-state operation.

In light of the above investigations into ceria-zirconia-based catalysts in the Deacon reaction, there are several avenues for further research that are worthy of ongoing investigation.

1. It is essential to investigate the influence of ZrO_2 structures on the physio-chemical properties of $CeO_2@ZrO_2$ catalysts, including Ce morphologies, Ce^{3+}/Ce^{4+} ratios, and OSCc/OSC. This investigation should extend to an examination of the impact of ZrO_2 structures on the catalytic activity of these catalysts in the Deacon reaction and other oxidation reactions. In general, ZrO_2 exhibits three distinct crystalline phases: monoclinic, tetragonal, and cubic. In this thesis, the ZrO_2 with a monoclinic structure was selected as the support directly, in accordance with the findings of the preceding study. It is thus imperative to prepare CeO_2 supported on different ZrO_2 structures and to assess the corresponding catalytic performance.

2. The preparation of kappa-$Ce_{0.5}Zr_{0.5}O_2$ thin layers supported on ZrO_2 with different structures (*m*, *t*, *c*-phase) should be addressed. In one study, the layer morphology of a $Ce_2Zr_2O_8$ kappa phase supported on YSZ can be identified by subjecting $CeO_2@YSZ$ to a high-temperature reduction/mild reoxidation treatment. Furthermore, **Chapter 3.2** demonstrates that the dry impregnation of $CeO_2@ZrO_2$ and subsequent calcination at 600 °C for 5 h results in a highly dispersed layer of the catalytically active CeO_2 phase. It can therefore be concluded that the as-prepared $CeO_2@ZrO_2$ catalysts with various structures (*m, t, c*-phase) can be subjected to a high-temperature reduction/mild reoxidation treatment. The application of advanced techniques such as XRD, Raman, TEM and XPS may provide insight into the structures and surface properties of the compounds under study and could be employed in the investigation of catalytic oxidation reactions.

3. What are the physiochemical properties of inverse catalyst $80CeO_2/ZrO_2$? What is the catalytic performance of the inverse $80CeO_2/ZrO_2$ system in the Deacon reaction? As illustrated in **Figure 14** from **Chapter 4.2**, the catalytic activity of $CeO_2@ZrO_2$ is markedly higher than that of the solid solution with an identical CeO_2 content. To illustrate, the activity of $5CeO_2@ZrO_2$ is 3 times higher than that of $Ce_{0.05}Zr_{0.95}O_2$, the activity of $20CeO_2@ZrO_2$ is still 20% higher than that of $Ce_{0.20}Zr_{0.80}O_2$. However, as the most active sample depicted in **Figure 14** from **Chapter**

4.2 ($Ce_{0.80}Zr_{0.20}O_2$), there is no comparative analysis of the catalytic activity between $80CeO_2/ZrO_2$ and $Ce_{0.80}Zr_{0.20}O_2$. Further research is required to prepare inverse $80CeO_2/ZrO_2$ catalysts and to investigate their applications in catalytic oxidation reactions..

4. The process of "deactivation-reactivation" process could be refined. In **Chapter 3.3**, the reactivation of two bulk-chlorinated CeO_2-based catalysts was investigated, namely pure CeO_2 and $20CeO_2@ZrO_2$. However, it is challenging to discern the morphological alterations occurring in the pure CeO_2 catalyst throughout the deactivation-reactivation cycle. It may be beneficial to conduct "deactivation-reactivation" experiments with CeO_2 nanocubes or octahedrons in order to elucidate the underlying nucleation and growth processes. Furthermore, additional "deactivation-reactivation" experiments are necessary for $5CeO_2@ZrO_2$, given that only a CeO_2 thin layer is present on ZrO_2 in this catalyst. The simplified structure of $5CeO_2@ZrO_2$ is conducive to more accurate fitting of the JMAK model.

4. Scientific Publications

4.1 Publication I: Oxygen Storage Capacity versus Catalytic Activity of Ceria-Zirconia Solid Solutions in CO and HCl Oxidation

H. Over conceived the original idea. The experimental schedule was devised by H. Over and myself. I and H. Over wrote the draft version of the manuscript, and H. Over took the lead in writing and analysis. I prepared the samples and led the most of experiments and analysis. C. Li and I evaluated the HCl oxidation performance. I. Djerdj conducted the Rietveld refinement. O. Khalid evaluated the CO oxidation performance. P. Cop measured the OSC performance. J. Sann and T. Weber contributed the XPS experiments and analysis. S. Werner and K. Turke contributed the N_2-soprtion experiments. Y. Guo and B. M. Smarsly contributed through scientific discussion of the data.

Catalysis Science & Technology

PAPER

View Article Online
View Journal | View Issue

Cite this: *Catal. Sci. Technol.*, 2019, 9, 2163

Oxygen storage capacity *versus* catalytic activity of ceria–zirconia solid solutions in CO and HCl oxidation†

Yu Sun,[ab] Chenwei Li,[ab] Igor Djerdj,[c] Omeir Khalid,[b] Pascal Cop,[b] Joachim Sann,[b] Tim Weber,[b] Sebastian Werner,[b] Kevin Turke,[b] Yanglong Guo,*[a] Bernd M. Smarsly*[b] and Herbert Over*[b]

Received 29th January 2019,
Accepted 27th March 2019

DOI: 10.1039/c9cy00222g

rsc.li/catalysis

$Ce_xZr_{1-x}O_2$ solid solutions were prepared as a function of the composition x with constant specific surface area in order to explore the relationship between oxygen storage capacity (OSC) and activity of the oxidation reactions of CO and HCl. The as-prepared $Ce_xZr_{1-x}O_2$ solid solutions were characterized by X-ray diffraction (XRD), Raman spectroscopy (Raman), and X-ray photoelectron spectroscopy (XPS). The complete (or total) oxygen storage capacity ("complete" OSC: OSCc) at 430 °C is shown to be linearly correlated to the CO oxidation activity at 430 °C as a function of the Ce concentration x, thus being compatible with the expected Mars–van-Krevelen mechanism. For the catalytic HCl oxidation reaction at 430 °C the activity is also shown to be linearly correlated to the OSCc with a maximum activity realized with $Ce_{0.8}Zr_{0.2}O_2$. From the linear relationship of oxidation activity of HCl and OSCc (that in turn is linear to the activity of CO oxidation) we conclude that the HCl oxidation reaction over $Ce_xZr_{1-x}O_2$ solid solutions proceeds *via* the Mars–Van-Krevelen mechanism with the reduction of $Ce_xZr_{1-x}O_2$ being rate-determining.

1. Introduction

Heterogeneous catalysis can be considered as a surface phenomenon to a first approximation where the gas phase comes into contact with the solid catalyst surface to transform educts into desired products. However, besides electron exchange between the reactants and the catalyst, constituents of the catalyst from the bulk and the surface, such as oxygen ions of reducible oxides, may participate in oxidation catalysis that is commonly referred to as the Mars–van-Krevelen mechanism.[1] The amount of oxygen that can be exchanged by a reducible oxide with the gas phase or with an active metal component is called the oxygen storage/release capacity (OSC).[2] This quantity can either be quantified under dynamic conditions (fast or dynamic or plain: OSC) or under steady state conditions (total or complete OSC: OSCc).[3,4] In the OSC experiments the oxide is reduced mostly by molecular hydrogen or CO, while the reduced oxide is re-oxidized with molecular O_2 gas; the required amount of O_2 for the re-oxidation step defines the value of the OSC.

The prototype of a reducible oxide is CeO_2 with its superb Ce^{3+} *versus* Ce^{4+} redox chemistry.[5] The ability to remove/uptake oxygen from the ceria lattice while maintaining structural integrity endows the material with unique properties in catalysis science and technology. In three-way catalysts for instance, CeO_2-based materials serve mainly as oxygen storage components to buffer fluctuations in the exhaust composition where also the concept of OSC originates from.[3,6,7]

Commonly the activity of CeO_2-based catalysts in an oxidation reaction is considered to be correlated to the OSC.[7] However, the use of the OSC as descriptor for oxidation catalysts needs to be questioned, since neither the measurement principle nor the concept is directly transferrable from automotive catalysis.[2,8] OSC experiments do vary among the working groups, employing TGA, TPR/TPO or dedicated OSC apparatuses.[9] Moreover, the OSC data depend critically on the synthesis procedure of the respective reducible oxide as well as on the active surface area.[10–15] Since the reducing agent used in OSC may differ from that of the studied catalytic reaction, such as encountered with the catalytic HCl oxidation, a clear correlation between OSC and the activity may be obscured.

[a] *Key Laboratory for Advanced Materials, Research Institute of Industrial Catalysis, School of Chemistry and Molecular Engineering, East China University of Science and Technology, Shanghai 200237, P. R. China. E-mail: ylguo@ecust.edu.cn*

[b] *Physikalisch-Chemisches Institut, Justus Liebig University, Heinrich-Buff-Ring 17, 35392 Giessen, Germany. E-mail: Bernd.Smarsly@phys.Chemie.uni-giessen.de, herbert.over@phys.chemie.uni-giessen.de*

[c] *Department of Chemistry, Josip Juraj Strossmayer University of Osijek, Cara Hadrijana 8/a, HR-31000 Osijek, Croatia*

† Electronic supplementary information (ESI) available. See DOI: 10.1039/c9cy00222g

Recently, we had studied the activity of Ce-based materials in the HCl oxidation reaction in relation to their stability and the OSC/OSCc.[2,13,16–20] In particular, $Ce_{1-x}Zr_xO_2$ solid solutions were prepared in the form of nanofibers, which allowed for a straightforward assessment of the stability as a function of the composition when exposed to corrosive reaction conditions. It was found that alloying of Zr into CeO_2 substantially enhances the stability, and *ca.* 20% of Zr is sufficient to prevent chloride formation and hence structural degradation.[20] Also, between 0 and *ca.* 30% of Ce a steep increase in STY was observed, while above *ca.* 50% of Ce the STY was found to be highest and within the error bars constant. Amrute *et al.* proposed that the activity of pure CeO_2 powder catalyst is related to the OSCc rather than to the active BET surface area.[21] However, for $Ce_{0.5}Zr_{0.5}O_2$, which can crystallize into the so-called kappa phase κ-$Ce_2Zr_2O_8$,[22] the correlation between OSC and activity is less clear. The ordering of the solid solution $Ce_{0.5}Zr_{0.5}O_2$ into the so-called κ-$Ce_2Zr_2O_8$ phase leads to a profound increase of the OSC/OSCc.[23,24] While the high OSCc of the kappa phase is beneficial for the oxidation of CO, the oxidation of HCl turns out to be not affected by the high OSCc value.[25]

While $Ce_{1-x}Zr_xO_2$ materials thus appear promising catalysts in regard to activity and stability in oxidation reactions, these previous studies, including our own ones, suffer from the fact that the samples differ in several important parameters at the same time: samples exhibiting different Zr contents also possess different BET surfaces areas, because it is difficult to obtain defined BET surface areas by sol–gel syntheses in general. This shortcoming impedes a clear-cut correlation between activity and the OSC as well as between the composition and activity.

It is the main objective of the present study to connect systematic OSC data with activity data of pure $Ce_{1-x}Zr_xO_2$ solid solutions for two important catalytic oxidation reactions, as a function of the composition x, but keeping the specific surface area constant. For improved comparison of OSC and catalytic activity the temperature applied in the OSC measurement and that of the studied catalytic oxidation experiments are chosen to be identical. One reaction is the CO oxidation reaction which is very similar to the OSC procedure using also CO as reducing agent. We expect, therefore, a very close relationship between the activity and the OSC for this reaction as found in several studies in the literature and ascribed to a Mars–van-Krevelen mechanism (the reader is referred to a recent review and references therein).[26] In our study, this comparison is used to set the achievable level of agreement between catalytic activity and OSC. The second reaction, the HCl oxidation reaction (Deacon reaction) using the same $Ce_{1-x}Zr_xO_2$ samples,[21,27] is an important alternative to the presently employed Deacon reaction over RuO_2/rutile-TiO_2 catalysts[28–31] and constitutes the main topic of this study. In terms of the reducing agent the Deacon reaction differs from the OSC procedure (HCl: Deacon *versus* CO: OSC) so that a direct correlation to the OSC is less obvious, although its correlation can be critically compared with that found for the CO oxidation reaction. Special emphasis is furthermore put on preparing and characterizing a substantial number of samples with small Ce contents (below *ca.* 15%). These samples are intended to address the correlation between composition, OSC and activity in more detail, while it needs to be considered that the crystal lattice of $Ce_{1-x}Zr_xO_2$ solid solutions is a function of the composition as well (monoclinic to tetragonal and ultimately to the cubic structure). Hence, by preparing samples with identical specific surface areas the present study proposes a distinct approach to address the complex relationship between the OSC, composition and activity in oxidation reactions. State-of-the-art analysis (Rietveld-refinement, Raman spectroscopy, X-ray photoelectron spectroscopy) are applied to determine the composition, providing an accurate structural characterization of the materials.

2. Experimental details

2.1. Preparation of $Ce_{1-x}Zr_xO_2$ catalysts

Ceria–zirconia solid solutions with different ratios of Ce/Zr were synthesized by the co-precipitation method.[32] Hydrogen peroxide was first dropped into the $Ce(NO_3)_3{\cdot}6H_2O$ solution to obtain a molar ratio of H_2O_2/Ce of 1.5. The corresponding amount of $ZrO(NO_3)_2{\cdot}nH_2O$ solution was then mixed with the solution to attain a molar ratio of Ce/Zr = $(1 - x)/x$. The precipitation of ceria–zirconia precursor was achieved by dropping an ammonia solution into the solution keeping the pH at around 9.5. The precipitate was stirred for 18 h and then washed with deionized water several times until a pH value of around 7 was reached. The precipitate was then dried overnight at 393 K and calcined at various temperatures (between 700 and 800 °C) for 5 h in order to ensure a constant specific surface area among the various $Ce_{1-x}Zr_xO_2$, x = 0,…1 samples. The samples are referred to as CZXXX with XXX being the atomic percentage (% unit) of cerium.

2.2. Characterization of catalysts

The samples were degassed in vacuum for 12 h at 393 K before performing N_2 physisorption experiments with Autosorb 6 of Quantachrome at 77 K. The BET (Brunauer–Emmett–Teller) method was used to determine the specific surface area.

X-ray diffraction (XRD) measurements were conducted in Θ–2Θ geometry on a Panalytical X'Pert PRO diffractometer with a Cu Kα source (40 kV, 40 mA). Rietveld analysis was carried out by using the FullProf program (Version 2.05).

Raman spectra were taken by using a Senterra Raman microscope (Bruker) with a 532 nm laser as the excitation source. All samples were measured at 50× magnification with a spectral resolution of 3–5 cm^{-1}, 250 co-addition, and 3 seconds integration time. The Raman spectra were recorded in backscattering geometry at room temperature and processed with OPUS 7.5 software.

The concentration of Zr and Ce in the near-surface region of the $Ce_xZr_{1-x}O_2$ solid solutions were quantified by X-ray photoemission spectroscopy (XPS) (PHI VersaProbe II) and

counterchecked with Rietveld refinement and the Vegard plot. The photon energy was 1486.6 eV (monochromatized Al-K_α line), the X-ray spot size was ~200 μm with an excitation power of ~50 W. Charging of the sample was compensated by a flow of slow electrons with energies of about 1 eV and Ar^+ ions of about 10 eV. For overview spectra the pass energy was set to 93.9 eV and a step size was set to 0.8 eV, while the detail spectra were acquired with a pass energy of 23.5 eV and a step size of 0.2 eV. The system pressure during the experiment was ~10^{-6} Pa and all spectra were taken at room temperature. The XPS data were analyzed with CasaXPS Version 2.3.17. In order to maintain similar kinetic energies of photoelectrons of Ce and Zr, we chose the Ce4d and Zr3d signals to quantify the relative Ce surface concentration with respect to Zr + Ce.

2.3. Catalytic and OSC measurements

The Deacon reaction measurements were conducted in a home-made fixed-bed flow reactor.[18] The reactor comprises the gas supply, the quartz tube reactor, heated by furnace, and UV/vis analytics for chlorine quantification. The following gases were used in the reaction measurements: HCl 4.5, O_2, 5.0 and Ar 5.0 from AirLiquide, and the flow rate of gases was controlled by digital mass flow controllers (MKS Instruments 1179B). Prior to feeding the gas mixture into the reactor, Ar was dried using a water absorption cartridge (ALPHAGAZ™ purifier H_2O-free, AirLiquide). The Deacon reaction experiments were carried out under so-called "mild" condition where the argon-balanced reaction feeds contained 20 vol% O_2 and 10 vol% HCl that was balanced by 70% Ar. The total mass flow rate was set to 15 cm^3 STP min^{-1} (sccm). Typically, 30 mg of ceria–zirconia mixed oxide was supported between two quartz wool wads in the reactor tube. Under the flowing reactant feed, the reactor was heated to a reaction temperature of 430 °C with a linear rate (computer controlled) of 10 K min^{-1}, held for 4 h (reaction time), then cooled down to room temperature in pure argon atmosphere. The product analysis was accomplished by a fiber-optic UV-vis spectrometer (Ocean Optics USB4000 with a DH-2000-BAL light source) with a Z-shaped flow cell (Teflon®, 50 mm optical path length, FIAlab). The absorbance at a wavelength of λ_{max} = 329 nm (absorption maximum of chlorine) is proportional to the chlorine space time yield (STY) that was calibrated by standard iodometry. The STY is defined as the molar amount of product per time and mass catalyst.

The oxidation experiments of CO were carried out in another home-built fixed-bed flow reactor. The design comprises the gas supply, the quartz tube reactor, heated by a furnace, and analytics for the CO_2 quantification. The flow rates of gases (CO Praxair, quality 4.7, O_2 Praxair, quality 5.0 and N_2, Linde) were controlled by digital mass flow controllers (SevenStar D07-19B). The nitrogen-balanced reaction feeds contained 1 vol% CO, 10 vol% O_2 and 89 vol% N_2 that passed the reactor tube with flow rate of 90 cm^3 STP min^{-1} (sccm). For the catalytic tests, 10 mg of catalyst was supported between two quartz wool wads. The furnace was firstly heated to 150 °C with a rate of 20 K min^{-1}, held for 10 min, and then heated to of 250 °C with a rate of 20 K min^{-1}, held for 10 minutes, and to 350 °C with a rate of 20 K min^{-1}, held for 10 minutes, and finally to 430 °C (reaction temperature) with a rate of 20 K min^{-1}, held for 30 minutes. The gas composition was monitored online using the X-Stream-CO_2 analyzer (Rosement). The STY of CO_2 was calculated on the basis of the CO_2 concentration in the outlet gas stream.

The experiments of oxygen storage capacity (OSC) were carried out by using a stainless-steel tube (i.d. 4 mm, length 60 mm) connected to the gas inlet system by stainless steel leads (i.d. 1.6 mm) *via* Swagelok tube fittings.[16,17] The catalyst (30 mg) was dried at 120 °C for 5 h and loaded into the reactor, supported between two quartz wool wads. The OSC reactor containing the sample was heated to 430 °C with a rate of 10 K min^{-1} using the same furnace and temperature control as for the HCl oxidation experiments. Carbon monoxide (Praxair, quality 4.7) was employed as the reducing agent while oxygen (Praxair, quality 5.0) served as the oxidizing agent. The stream selector (VICI multi-position valve with an outlet for unused streams) allows to switch software-controlled at specified time intervals between three gases (CO, O_2 and Ar: with a flow rate of 2 sccm each) and mix them with the Ar carrier stream (18 sccm). After leaving the OSC reactor, the gases pass through a Swagelok sintered stainless steel filter (pore size 2 μm) and reach the micro-volume thermal conductivity detector (VICI TCD2) operated with pure argon as the base line (detector temperature 373 K, filament temperature 423 K).

To determine the plain or dynamic oxygen storage capacity (OSC), the stream selector was switched to CO for 2 s and to O_2 for 2 s alternatingly with a 80 s Ar purge step in between. Using additional O_2 pulse as a reference, the amount of adsorbed oxygen was calculated that corresponds to the (dynamic) OSC. The complete oxygen storage capacity (OSCc) was determined by reducing the catalyst with a sufficiently long sequence of CO pulses each 10 s long accompanied by 80 s Ar pulse pauses. Subsequently, the selector was switched to O_2 for ten pulses of 2 s duration separated by 80 s pure Ar pulses were applied. The total amount of consumed oxygen is taken to be the value of OSCc.

3. Experimental results

3.1. Characterization of the $Ce_xZr_{1-x}O_2$ samples, keeping the BET surface area constant

The textural and structural characterization of all $Ce_xZr_{1-x}O_2$ samples investigated in this study is summarized in Table 1. The specific surface area of all samples remains invariant at 46 ± 2 m^2 g^{-1} by choosing carefully the calcination temperature. The specific surface area of each sample was measured twice to estimate the scattering among the BET surface data. Compared to pure zirconia and ceria, the ceria–zirconia solid solutions require slightly higher calcination temperatures between 700 °C and 800 °C to maintain the BET surface area.

Table 1 Physicochemical properties of $Ce_xZr_{1-x}O_2$ (CZXXX: XXX atomic percentage of Ce): BET surface area and textural and structural characterization as determined by XRD: M = monoclinic, T = tetragonal, C = cubic phase

Samples	BET surface area ($m^2\ g^{-1}$)[a]		Calcination temperature (°C)	Crystalline size (nm)[b]				
	1st time	2nd time		D(M)	D(T)	D(C)	*M*%[c]	*T*%[c]
CZ000	46	45	615	11.8	7.7		91	9
CZ002	48	48	650	11.3	9.2		76	24
CZ005	45	46	700	11.8	10.3		30	70
CZ007	45	47	700	8.0	10.3		18	82
CZ010	46	46	730	8.8	10.0		10	90
CZ013	47	46	730	11.1	8.5		1	99
CZ016	48	45	790		8.0		0	100
CZ020	47	45	780		7.1			
CZ030	47	44	750		6.0			
CZ040	48	48	760		5.2			
CZ050	46	45	730		5.1			
CZ060	46	46	740		5.3			
CZ070	46	47	750		6.4			
CZ080	47	45	720			6.8		
CZ090	48	47	710			8.4		
CZ100	46	47	540			10.0		

[a] Determined by BET method. [b] Determined by Rietveld refinement. [c] The percentage of monoclinic phase (*M*%) and tetragonal phase (*T*%) were determined by Rietveld refinement.

When increasing the Ce concentration from 0% to 16%, the calcination temperature reaches a maximum value (790 °C).

The ceria–zirconia solid solutions, $Ce_xZr_{1-x}O_2$, adopt three possible structures: monoclinic (*m*), tetragonal (*t*, *t*′, *t*″), and cubic (*c*).[33] There is a continuous transition from the mixed monoclinic + tetragonal phase of pure ZrO_2 towards the cubic phase of pure CeO_2 with increasing concentration of CeO_2. Fig. 1 depicts XRD patterns of fresh ceria–zirconia solid solutions with different ceria concentrations. All samples form a solid solution. There is no evidence for peak splitting due to phase separation in ceria-rich and zirconia-rich solutions.

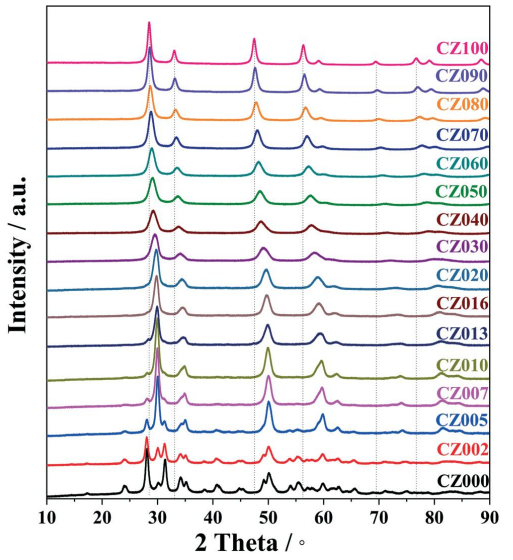

Fig. 1 XRD patterns of the as-prepared CZXXX samples (XXX% = 000–100%).

For pure ZrO_2, Rietveld refinement reveals a mixture of 91% monoclinic and 9% tetragonal phase. The main reflections at 2θ = 24.1°, 28.2°, 31.5°, 34.2°, 40.7°, 49.3° are assigned to the monoclinic phase (ICDD NO. 00-036-0420) and the reflections at 2θ = 30.2°, 35.3°, 50.3° are assigned to the tetragonal phase (ICDD NO. 01-079-1770). With increasing percentage of Ce, the contribution of the monoclinic phase decreases and the percentage of tetragonal phase increases gradually. When the Ce concentration reaches 13–16 at%, the reflections of the monoclinic phase have vanished. For higher Ce concentrations than 16 at% the XRD scans do not change so that no further structural information can be obtained.

The conclusions drawn from the XRD patterns are consistent with Raman spectroscopy of the freshly prepared ceria–zirconia catalysts (Fig. 2). With the increase in the Ce content up to 16 at%, the peaks at 178, 190, 379 cm^{-1} assigned to the monoclinic phase[10] have vanished completely, which is in accordance with previous studies.[20,34]

For the CZXXX (XXX% = 016–100%) samples, it is difficult to distinguish the crystal structure by the XRD patterns due to overlapping reflections of the tetragonal and cubic phase. Therefore, Raman spectroscopy is more suitable for identifying the crystal structure. There are five Raman bands at around 139, 253, 311, 462, 626 cm^{-1} indicating the existence of the *t* phase in the CZ016, CZ020 and CZ030 samples, even though the exact peak positions vary with the ceria content.[35] The Raman resonances at 129, 300, 470 and 620 cm^{-1} are indicative of the formation of *t*″ form.[20,36,37]

For CZ030 sample, the peak at 253 cm^{-1} becomes broad and disappears finally for a Ce concentration of 40 at%.

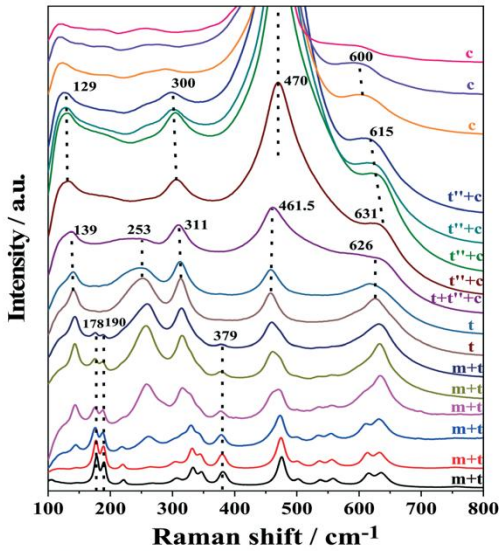

Fig. 2 Raman spectra of as-prepared CZXXX samples (XXX = 000–100 atomic percent of Ce). Color code is identical to that of Fig. 1.

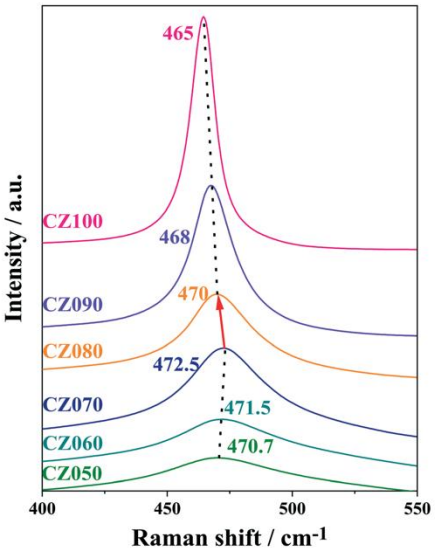

Fig. 3 Raman spectra of as-prepared CZXXX samples (XXX% = 050–100%) with the Raman shift between 400 and 550 cm^{-1}.

Moreover, the Raman mode at 461.5 cm^{-1} (Fig. 3) of CZ030 shifts to 470 cm^{-1} when the ceria concentration increases to 40 at%. From this observation we conclude that the phase transition from t or t' phase to t'' phase start at CZ030 and the transformation of the t or t' lattice is completed for CZ040. In addition, a strong 464 cm^{-1} peak together with a weak signal at 307 cm^{-1} evidences the presence of the cubic phase in CZXXX (XXX% = 030–070%)[34,38] so that the transformation to t'' is rather a transformation towards a mixture of the t'' and the cubic phase. As shown in Fig. 3, for the CZXXX (XXX% = 050–070%), the peak position shifts from 470.7 to 472.5 cm^{-1} due to variation of the ratio between t'' phase and cubic phase.

When the Ce concentration increases to 80 at%, the peak at 300 cm^{-1} being characteristic for the tetragonal t'' phase vanishes completely.[39] Upon increasing further the Ce content the Raman mode at 472.5 cm^{-1} (CZ070) shifts back to lower wavenumbers (*cf.* Fig. 3) that is ascribed to the formation of a pure cubic fluorite structure.[40] The peak at around 600 cm^{-1} is assigned to a defect structure due to the substitution of Zr cation for Ce.[36]

As shown in Fig. 4, the cell dimensions calculated by Rietveld refinement based on a distorted cubic structure reveals a linear dependence on x, the nominal concentration of ceria as defined by the preparation. A similar expansion of the cell parameter was reported for $Ce_{1-x}Zr_xO_2$ powder samples and is summarized in the Vegard plot.[34,41,42] This behavior is expected for $Ce_{1-x}Zr_xO_2$ solid solutions since the Ce^{4+} ion ($r(Ce^{4+}, 8)$ = 0.97 Å) substitutes the position of the smaller Zr^{4+} ion (ionic radius for coordination 8: $r(Zr^{4+}, 8)$ = 0.84 Å).

In order to quantify the concentration of Ce in the near-surface region, we conducted additional XPS experiments of the freshly prepared ceria–zirconia solid solutions. As summarized in Fig. 4, the Ce concentration in the surface region derived from the Zr 3d and Ce 4d spectra exhibits a roughly linear dependence on x, thus being reconciled with the nominal bulk stoichiometry as given by the concentration of Ce and Zr precursors;[2] actually, the surface Ce concentration is a little, but systematically lower than the bulk concentration.

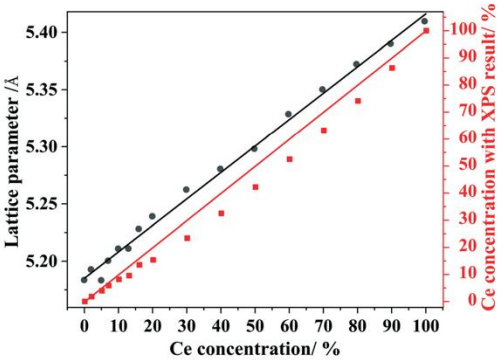

Fig. 4 The cell parameter calculated by Rietveld refinement in comparison with the Ce concentration calculated by XPS spectra.

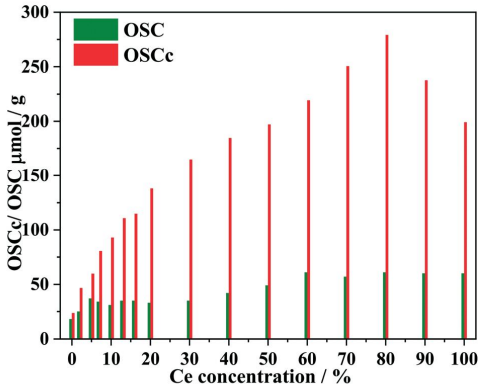

Fig. 5 Plain oxygen-storage capacity, complete oxygen-storage capacity (OSC and OSCc, respectively) of as-prepared CZXXX samples (XXX% = 000–100%).

OSC and OSCc values represent the ability of oxygen storage/release and are considered to play a key role in the catalytic activity of oxidation reactions.[7,9,32] As the Ce content increases from 0% to 80 mol%, the complete oxygen storage capacity (OSCc) increases from 23 µmol (O)/g to 280 µmol (O)/g as summarized in Fig. 5. Upon further increase in the Ce concentration to 90% and 100%, the OSCc value decreases slightly to 238 µmol (O)/g (CZ090) and 200 µmol (O)/g (CeO_2). The OSCc of ceria–zirconia solid solutions varies as a function of the Ce content in the form of a volcano curve.

Quite in contrast, the dynamic oxygen-storage capacity (OSC) keeps almost constant at 35 ± 5 µmol (O)/g in the concentration range of Ce from 5% to 30% and increases then gradually to 59 ± 2 µmol (O)/g when increasing the Ce concentration to 50%. As the Ce concentration increases from 50% to 100 mol%, the OSC remains constant at 59 ± 2 µmol (O)/g.

3.2. Activity experiment: HCl and CO oxidation reaction

The activity experiments for the Deacon reaction are summarized in Fig. 6a. The reactor was first heated to the reaction temperature of 430 °C in pure Ar flow of 15 sccm and then the Ar flow was switched to the reaction mixture (Ar : HCl : O_2 = 7 : 1 : 2) for 4 h while the space time yield (STY) was measured by UV-vis spectroscopy. The activity in Fig. 6a shows a clear trend, *i.e.*, with increasing concentration of Ce up to 80% the activity increases steadily. The highest activity of STY = 17 mol_{Cl_2} kg_{cat}^{-1} h^{-1} is accomplished with CZ070 and CZ080. Compared to pure ZrO_2, CZ080 reveals a 10 times higher activity. For even higher Ce concentrations (90%, 100%) the catalytic activity declines slightly. This result agrees with our previous study on nanofibers[20] but conflicts with a previous publication,[43] where the maximum activity for the HCl oxidation reaction was found for 50% at Ce. However, the presented XRD data indicate that $Ce_{0.5}Zr_{0.5}$ is not phase-pure. Even more surprising, in this report the activity of pure ZrO_2 was quite high,[43] thus being not compatible with other reports on $Ce_{1-x}Zr_xO_2$ nanofibers.[16,20]

The activity experiments on the CO oxidation reaction are summarized in Fig. 6b. The reactor was heated to the reaction temperature of 430 °C in the reaction mixture (N_2 : CO : O_2 = 89 : 1 : 10), and the space time yield (STY) was measured by X-Stream-CO_2 analyzer. The activity also shows a clear trend with increasing concentration of Ce. Starting from ZrO_2, the activity increases again with increasing Ce concentration up to 80%. CZ070 and CZ080 exhibit highest catalytic activity STY = 95 mol_{CO_2} kg_{cat}^{-1} h^{-1}. Similar results were

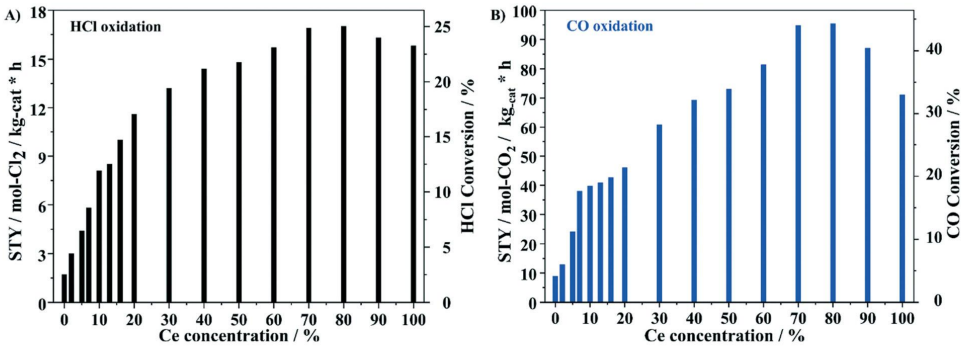

Fig. 6 A) space–time yield (STY) per kilogram of catalyst in the HCl oxidation for as-prepared CZXXX samples (XXX = 0–100). The reaction temperature during the reaction was 430 °C and the reaction condition: Ar : HCl : O_2 = 7 : 1 : 2. A total flow rate of 15 sccm was applied. B) Space–time yield (STY) per kilogram of catalyst in the CO oxidation for as-prepared CZXXX samples (XXX% = 000–100%). The reaction temperature during the reaction was 430 °C and the reaction condition: N_2 : CO : O_2 = 89 : 1 : 10. A total flow rate of 90 sccm was applied. The reaction temperature was identical to that used in the OSC experiments.

reported by Boaro *et al.*[44] Compared to pure ZrO_2, the activity of CZ080 increases by a factor of 10.7. The catalytic activity decreases slightly with further increasing the Ce concentration from 90% and 100%.

3.3. Characterization of CZXXX samples after Deacon reaction

From previous studies we know that CeO_2-based catalyst can undergo structural changes upon the Deacon reaction.[2,16,19] Therefore, we measured the BET surface area of five used catalysts with different Ce concentrations and compared them with the BET surface area of freshly prepared ones. As shown in Table 2, the specific surface area of used samples systematically decreases slightly to 39 ± 2 $m^2\ g^{-1}$. For gaining a deeper insight into the reason for the decrease in specific surface area, we measured the specific surface area of CZ080 as a function of time on stream for the Deacon reaction. As summarized in Table S1,† the specific surface area decreases to 37 $m^2\ g^{-1}$ already after a reaction time of 0.5 h and keeps then constant. The porosity varies also with time, but does not follow the BET surface area. Therefore, agglomeration of the particles to larger particles (likely induced by HCl) cannot cause the reduction in BET surface area. However, the BET surface area enters two quantities, namely the surface area and the mass of the catalyst: BET = surface_area/mass_of_catalyst. The reduced BET surface area may therefore be explained by an increase in mass due to chlorination in the surface near region as observed for shape-controlled CeO_2 particles.[19] A rough estimate indicates that substitution of 12.5% of the oxygen positions by chlorine leads already to mass increase of roughly 10%, $Ce_xZr_{1-x}O_{1.75}Cl_{0.5}$, which may be a reasonable value for the degree of chlorination in the near surface region.

4. Discussion

4.1. The relationship between catalytic activity and OSCc/OSC value

Already from bare visual inspection of Fig. 5 and 6 we can conclude that the activity of the CO and the HCl oxidation reaction follows the OSCc but not the OSC. First, we will discuss the correlation between OSCc and the activity in the CO oxidation reaction. The correlation should be particularly close, since the OSC experiments and the catalytic tests are conducted at the same reaction temperature of 430 °C and with the same reductant, namely CO. In addition, the reduction step of the catalyst and the product CO_2 are identical in the OSCc and the CO oxidation reaction experiment. As indicated in Fig. 7, the correlation between OSCc and STY data are indeed very close. There are three linear regions in the activity data as a function of the Ce-concentration x that are reflected one by one in the OSC data.

From identical trends of the OSCc and the activity of CO oxidation reaction over $Ce_xZr_{1-x}O_2$ catalysts as a function of the composition x, we conclude that CO oxidation proceeds *via* a Mars–Van-Krevelen mechanism, where the reduction of the oxide by CO (1) needs to be rate-limiting:

$$Ce_xZr_{1-x}O_2 + \delta CO(g) \xrightarrow{\text{slow}} Ce_xZr_{1-x}O_{2-\delta} + \delta CO_2 \quad (1)$$

$$Ce_xZr_{1-x}O_{2-\delta} + \delta/2O_2(g) \xrightarrow{\text{fast}} Ce_xZr_{1-x}O_2 \quad (2)$$

Segregation of defects between bulk and surface is fast (3)

This means also that the CO oxidation reaction on $Ce_xZr_{1-x}O_2$ is quite slow when no active component such as Pd or Pt is added.

We need to note that a quantitative comparison of OSC data with literature values is practically impossible since either the employed techniques for OSC measurements varies, *i.e.*, TGA, TPR/TPO or pulse injection of the reducing/oxidizing gas, or the reductant gas varies frequently from CO to H_2 and in addition the temperature changes. Moreover, the synthesis of the reducible oxides under consideration varies among the publications. Altogether, this impedes a serious comparison of OSC values from one working group to those of another working group.[9] However, from the close correspondence of OSCc with the activity in the CO oxidation reaction we may expect that the OSCc determined in our study is at least proportional to the true OSCc, providing confidence to our OSCc data and, as expected from the literature,[45] clear evidence that the CO oxidation proceeds *via* a Mars–van-Krevelen mechanism.

Next we compare the OSC data with the activity data of the HCl oxidation reaction (Fig. 8). Here the reducing agent is HCl that is different from CO (used in OSC experiments), and none of the products are identical (Cl_2 and H_2O *versus* CO_2). Since also the activity of the HCl oxidation reaction follows the trend in the OSCc, the trends in activity of CO and HCl oxidation are very much alike. From this finding we infer that the HCl oxidation reaction proceeds also *via* a Mars–van Krevelen mechanism with the reduction of the oxide by HCl exposure being rate-limiting, *i.e.*,

$$Ce_xZr_{1-x}O_{2-y}Cl_y + 2\delta HCl(g) \xrightarrow{\text{slow}} Ce_xZr_{1-x}O_{2-y-\delta}Cl_y + \delta Cl_2 + \delta H_2O \quad (4)$$

This result is in qualitative agreement with the conclusion on CeO_2 powder catalysts drawn by Amrute *et al.*[21] and those of our previous study on shaped-control CeO_2 and $Ce_xZr_{1-x}O_2$.[2,19] We note that recent *ab-initio* Monte Carlo

Table 2 The BET surface area of freshly prepared sample and samples after 4 h on Deacon stream. The reaction temperature during the reaction was 430 °C and the reaction condition: Ar : HCl : O_2 = 7 : 1 : 2. A total flow rate of 15 sccm was applied. The mass of catalyst is 120 mg

Samples	BET surface area – fresh/$m^2\ g^{-1}$	BET surface area – used/$m^2\ g^{-1}$
CZ000	41	36
CZ010	43	41
CZ040	43	37
CZ080	45	36
CZ100	47	38

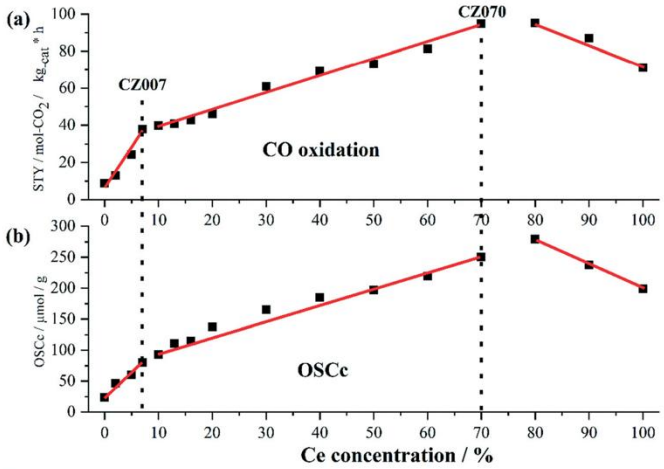

Fig. 7 Direct comparison of the space–time yield (STY) per kilogram of catalyst in the CO oxidation reaction for as-prepared CZXXX samples (XXX = 0–100) (a) with the complete OSC (OSCc) (b). A total flow rate of 90 sccm was applied. The reaction temperature during the reaction was 430 °C and the reaction condition: $N_2 : CO : O_2 = 89 : 1 : 10$. The reaction temperature was identical to that used in the OSC experiments.

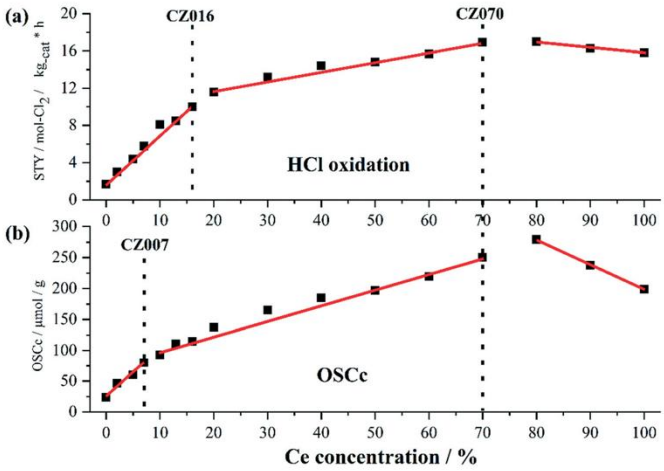

Fig. 8 Direct comparison of the space–time yield (STY) per kilogram of catalyst in the HCl oxidation reaction for as-prepared CZXXX samples (XXX = 0–100) (a) with the complete OSC (OSCc) (b). A total flow rate of 15 sccm was applied. The reaction temperature during the reaction was 430 °C and the reaction condition: $N_2 : HCl : O_2 = 7 : 1 : 2$. The reaction temperature was identical to that used in the OSC experiments.

simulations show the water formation to be the bottleneck in the HCl oxidation reaction over $RuO_2(110)$.[46]

5. Conclusion

Systematic studies of $Ce_xZr_{1-x}O_2$ solid solutions are hampered by the simultaneous variation of several parameters as a function of the composition x. In order to reduce this number, we prepared $Ce_xZr_{1-x}O_2$ solid solutions with identical BET surface area by adopting the calcination temperature. This allows for direct comparison of OSC and activity without performing a normalization step to the BET surface area.

With these specifically prepared $Ce_xZr_{1-x}O_2$ solid solutions we compared the OSC with the activity of two catalytic oxidation reactions, namely the CO and the HCl oxidation reaction at the reaction temperature of 430 °C; the same temperature

is employed in the OSC experiments. Here the CO oxidation reaction is closest to OSCc experiments, both from the reductant and the product point of view. It turns out that trends in the CO oxidation activity and in OSCc as a function of the composition x are virtually identical, thus being compatible with the expected Mars–van-Krevelen mechanism. With this experiment we are able to assess the OSC experiments and to use the CO oxidation reaction as a reference for the interpretation of the HCl oxidation reaction. From the close correspondence of OSCc with the activity of the HCl oxidation we infer that also this oxidation reaction proceeds *via* the Mars–van Krevelen mechanism with the reduction step of $Ce_xZr_{1-x}O_2$ solid solutions being rate-determining.

Conflicts of interest

There are no conflicts to declare.

Acknowledgements

This work was supported by the National Key Research and Development Program of China (2016YFC0204300), National Natural Science Foundation of China (21577035), Commission of Science and Technology of Shanghai Municipality (13521103402, 15DZ1205305) and 111 Project (B08021). Yu Sun gratefully acknowledges the China Scholarship Council for the Joint-Ph.D program between the China Scholarship Council and the Physikalisch-Chemisches Institut of the Justus-Liebig-University Giessen. Igor Djerdj and Bernd Smarsly acknowledge MZO-DAAD bilateral funding scheme for funding the project entitled: "Optimized synthesis and characterization of the CeO_2-based materials, promising catalysts for the oxidation of HCl". We would like to thank the Center of Materials Research (LaMa) at Justus Liebig University Giessen for the support of this project.

References

1 P. Mars and D. W. Van Krevelen, *Chem. Eng. Sci.*, 1954, **3**, 41.
2 C. W. Li, Y. Sun, F. Hess, I. Djerdj, J. Sann, P. Vöpel, P. Cop, Y. L. Guo, B. M. Smarsly and H. Over, *Appl. Catal., B*, 2018, **239**, 628.
3 H. C. Yao and Y. F. Yu Yao, *J. Catal.*, 1984, **86**, 254.
4 D. Duprez, C. Descorme, T. Birchem and E. Rohart, *Top. Catal.*, 2001, **16–17**, 49.
5 A. Trovarelli and P. Fornasiero, *Catalysis by Ceria and Related Materials*, Imperial College Press, London, 2013, and references therein.
6 J. Kašpar, P. Fornasiero and M. Graziani, *Catal. Today*, 1999, **50**, 285.
7 T. Montini, M. Melchionna, M. Monai and P. Fornasiero, *Chem. Rev.*, 2016, **116**, 5987 and references therein.
8 R. J. Gorte, *AIChE J.*, 2010, **56**, 1126.
9 P. Li, X. Y. Chen, Y. D. Li and J. W. Schwank, *Catal. Today*, 2019, **327**, 90.
10 A. Trovarelli, F. Zamar, J. Llorca, C. de Leitenburg, G. Dolcetti and J. T. Kiss, *J. Catal.*, 1997, **169**, 490.
11 S. Abdollahzadeh-Ghom, C. Zamani, T. Andreub, M. Epifani and J. R. Morante, *Appl. Catal., B*, 2011, **108–109**, 32.
12 Z. H. Ren, P. Wang, J. Kong, M. J. Wang and L. P. Chang, *J. Energy Chem.*, 2017, **26**, 647.
13 M. Möller, N. Tarabanko, C. Wessel, R. Ellinghaus, H. Over and B. M. Smarsly, *RSC Adv.*, 2018, **8**, 1864.
14 D. Devaiah, L. H. Reddy, S.-E. Park and B. M. Reddy, Ceria-zirconia mixed oxides: Synthetic methods and applications, *Catal. Rev.: Sci. Eng.*, 2018, **60**, 177.
15 X. Weng, B. Perston, X. Wang, I. Arahams, T. Lin, S. Yang, J. Evans, D. Morgan, A. Carley, M. Bowker, J. Knowles, I. Rehman and J. Darr, *Appl. Catal., B*, 2009, **90**, 405.
16 M. Möller, H. Over, B. Smarsly, N. Tarabanko and S. Urban, *Catal. Today*, 2015, **253**, 2017.
17 M. Möller, S. Urban, P. Cop, T. Weller, R. Ellinghaus, M. Kleine-Boymann, C. Fiedler, J. Sann, J. Janek, L. Chen, P. J. Klar, D. M. Hofmann, J. Philipps, P. Dolcet, S. Gross, H. Over and B. M. Smarsly, *ChemCatChem*, 2015, **7**, 3738.
18 C. H. Kanzler, S. Urban, K. Zalewska-Wierzbicka, F. Hess, S. F. Rohrlack, C. Wessel, R. Ostermann, J. P. Hofmann, B. M. Smarsly and H. Over, *ChemCatChem*, 2013, **5**, 2621.
19 C. W. Li, Y. Sun, I. Djerdj, P. Voepel, C. Sack, T. Weller, R. Ellinghaus, J. Sann, Y. L. Guo, B. M. Smarsly and H. Over, *ACS Catal.*, 2017, **7**, 6453.
20 S. Urban, N. Tarabanko, C. H. Kanzler, K. Zalewska-Wierzbicka, R. Ellinghaus, S. F. Rohrlack, L. Chen, P. J. Klar, B. M. Smarsly and H. Over, *Catal. Lett.*, 2013, **143**, 1362.
21 A. P. Amrute, C. Mondelli, M. Moser, G. Novell-Leruth, N. López, D. Rosenthal, R. Farra, M. E. Schuster, D. Teschner, T. Schmidt and J. Pérez-Ramírez, *J. Catal.*, 2012, **286**, 287.
22 S. Otsuka-Yao, H. Morikawa, N. Izu and K. Okuda, *Nippon Kinzoku Gakkaishi*, 1995, **59**, 1237.
23 S. Otsuka-Yao-Matsuo, T. Omata, N. Izu and H. Kishimoto, *J. Solid State Chem.*, 1998, **138**, 47.
24 T. Yamamoto, A. Suzuki, Y. Nagai, T. Tanabe, F. Dong, Y. Inada, M. Nomura, M. Tada and Y. Iwasawa, *Angew. Chem., Int. Ed.*, 2007, **46**, 9253.
25 S. Urban, I. Djerdj, P. Dolcet, L. Chen, M. Möller, O. Khalid, H. Camuka, R. Ellinghaus, C. Li, S. Gross, P. J. Klar, B. M. Smarsly and H. Over, *Chem. Mater.*, 2017, **29**, 9218.
26 E. Aneggi, M. Borao, C. De Leitenbrug, G. Dolcetti and A. Trovarelli, *J. Alloys Compd.*, 2006, **408-412**, 1096.
27 R. Farra, M. Eichelbaum, R. Schlögl, L. Szentmiklósi, T. Schmidt, A. P. Amrute, C. Mondelli, J. Pérez-Ramírez and D. Teschner, *J. Catal.*, 2013, **297**, 119.
28 K. Seki, *Catal. Surv. Asia*, 2010, **14**, 168.
29 J. Perez-Ramirez, C. Mondelli, T. Schmidt, O. F. K. Schlüter, A. Wolf, L. Mleczko and T. Dreier, *Energy Environ. Sci.*, 2011, **4**, 4786.
30 H. Over and R. Schomäcker, *ACS Catal.*, 2013, **3**, 1034.
31 M. Hammes, M. Valtchev, M. B. Roth, K. Stowe and W. F. Maier, *Appl. Catal., B*, 2013, **132**, 389.
32 E. Aneggi, C. de Leitenburg and A. Trovarelli, *Catal. Today*, 2012, **181**, 108.

33 M. Yashima, T. Hirose, S. Katano, Y. Suzuki, M. Kakihana and M. Yoshimura, *Phys. Rev. B: Condens. Matter Mater. Phys.*, 1995, **51**, 8018.
34 M. Epifani, T. Andreu, S. Abdollahzadeh-Ghom, J. Arbiol and J. R. Morante, *Adv. Funct. Mater.*, 2012, **22**, 2867.
35 E. F. López, V. S. Escribano, M. Panizza, M. M. Carnasciali and G. Busca, *J. Mater. Chem.*, 2001, **11**, 1891.
36 M. Yashima, H. Arashi, M. Kakihana and M. Yoshimura, *J. Am. Ceram. Soc.*, 1994, **77**, 1067.
37 R. Si, Y. W. Zhang, S. J. Li, B. X. Lin and C. H. Yan, *J. Phys. Chem. B*, 2004, **108**, 12481.
38 F. Zhang, C.-H. Chen, J. C. Hanson, R. D. Robinson, I. P. Herman and S.-W. Chan, *J. Am. Ceram. Soc.*, 2006, **89**, 1028.
39 M. Yashima, K. Ohtake, M. Kakihana and M. Yoshimura, *J. Am. Ceram. Soc.*, 1994, **77**, 2773.
40 V. G. Keramidas and W. B. White, *J. Chem. Phys.*, 1973, **59**, 1561.
41 W. T. Gibbons, L. J. Venstrom, R. M. De Smith, J. H. Davidson and G. S. Jackson, *Phys. Chem. Chem. Phys.*, 2014, **16**, 14271.
42 X. Weng, J. K. Cockcroft, G. Hyett, M. Vickers, P. Boldrin, C. C. Tang, S. P. Thompson, J. E. Parker, J. C. Knowles, I. Rehman, I. Parkin, J. R. G. Evans and J. A. Darr, *J. Comb. Chem.*, 2009, **11**, 829.
43 Z. Fei, X. Xie, Y. Dai, H. Liu, X. Chen, J. Tang, M. Cui and X. Qiao, *Ind. Eng. Chem. Res.*, 2014, **53**, 19438.
44 M. Boara, F. Giordano, S. Recchia, V. Dal Santo, M. Giona and A. Trovarelli, *Appl. Catal., B*, 2004, **52**, 225–237.
45 A. Trovarelli, *Catal. Rev.: Sci. Eng.*, 1996, **38**, 439.
46 F. Hess and H. Over, *ACS Catal.*, 2017, **7**, 128.

4.2 Publication II: Highly Active and Stable in the Catalytic HCl Oxidation Reaction: CeO_2 Wetting Layer on ZrO_2 Particle with Sharp Interface

The experimental schedule was devised by H. Over and myself. The draft version of the manuscript was wrote by H. Over and myself. H. Over conceived the original idea and took the lead in writing and analysis. I prepared the samples and evaluated the HCl oxidation performance and analysis. P. Cop measured the OSC performance. I. Djerdj performed the Rietveld refinement. X. Guo performed the ICP-AES and HRTEM experiments and analysis under the supervision of Y. Guo. T. Weber conducted the XPS experiments and analysis. P. Cop, O. Khalid, B. M. Smarsly and Y. Guo contributed through scientific discussion of the data.

ACS Catalysis

Research Article

Cite This: ACS Catal. 2019, 9, 10680−10693

pubs.acs.org/acscatalysis

CeO_2 Wetting Layer on ZrO_2 Particle with Sharp Solid Interface as Highly Active and Stable Catalyst for HCl Oxidation Reaction

Yu Sun,[†,‡] Pascal Cop,[‡,§] Igor Djerdj,[∥] Xiaohan Guo,[†] Tim Weber,[‡,§] Omeir Khalid,[‡,§] Yanglong Guo,*[,†] Bernd M. Smarsly,*[,‡,§] and Herbert Over*[,‡,§]

[†]Key Laboratory for Advanced Materials, Research Institute of Industrial Catalysis, School of Chemistry and Molecular Engineering, East China University of Science and Technology, Shanghai 200237, PR China

[‡]Physikalisch-Chemisches Institut, Justus Liebig University, Heinrich-Buff-Ring 17, 35392 Giessen, Germany

[§]Zentrum für Materialforschung, Justus Liebig University, Heinrich-Buff-Ring 16, 35392 Giessen, Germany

[∥]Department of Chemistry, J. J. Strossmayer University of Osijek, Ulica cara Hadrijana 8/a, HR-31000 Osijek, Croatia

Supporting Information

ABSTRACT: Dry impregnation of CeO_2 on ZrO_2 particles (CeO_2@ZrO_2) and calcination at 600 °C for 5 h result in a highly dispersed layer of the catalytically active CeO_2 phase with an enriched concentration of Ce^{3+}. The distinct morphology of CeO_2@ZrO_2 is responsible for the high (specific) activity in the gas-phase oxidation of HCl (Deacon reaction). Surprisingly, the CeO_2@ZrO_2 catalyst calcined at 600 °C is chemically even more stable toward chlorination under harsh Deacon condition than that calcined at 900 °C, where a solid solution of ZrO_2 and CeO_2 is formed at the solid interface. The improved stability of the CeO_2 layer calcined at 600 °C is traced to its sharp interface formed with the ZrO_2 support. We expect that this kind of active and stable layer morphology of CeO_2 supported on ZrO_2 is beneficial for other catalytic oxidation reactions as well, either as an active component or as a supporting material for another active metal component.

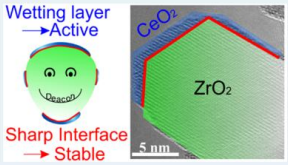

KEYWORDS: *CeO_2 supported on ZrO_2, Deacon reaction, stability, activity, ultrathin layer*

1. INTRODUCTION

The Deacon process is a sustainable way to recycle Cl_2 from the inevitable byproduct HCl generated in many industrial chemical processes, such as polyurethane or polycarbonate production:[1−5]

$$4HCl + O_2 \rightarrow 2H_2O + 2Cl_2;\ \Delta H = -112 kJ/mol$$

A major problem with this reaction is the stability of the catalyst that is readily lost by bulk-chlorination. Currently, RuO_2 supported on rutile-TiO_2 is commercially employed as a catalyst with remarkable low-temperature activity and stability.[4] However, ruthenium is rare on earth so that cost-effective alternatives are desirable. Besides U_3O_8[6] and $CuCrO_2$,[7] pure CeO_2 turned out to be a promising alternative as a Deacon catalyst and was reported to be active at elevated temperatures and remarkably stable.[8,9] In a subsequent study, the same group evaluated various oxide carriers for supporting the active component CeO_2, including Al_2O_3, TiO_2, and ZrO_2.[10] Superior Deacon performance was achieved with CeO_2 supported on preformed ZrO_2 particles (to be referred to as CeO_2@ZrO_2).[10]

Moser et al.[10] identified the optimum catalyst composition to be 9 wt % CeO_2 supported on ZrO_2 (CeO_2@ZrO_2), this composite being subsequently calcined in static air at 900 °C for 5 h. The calcination temperature of 900 °C was not optimized but adopted from the optimum performance of bulk-CeO_2 in HCl oxidation.[8] From Raman spectroscopy, transmission electron microscopy (TEM), and X-ray diffraction (XRD) experiments, the proposed "co-presence of nanostructures of CeO_2 and a mixed Ce−Zr oxide phase" remains somehow elusive to explain the observed high and robust activity in the Deacon process.[10] Recently, Yu and co-workers[11] studied the Deacon performance of powder samples of $Ce_xZr_{1-x}O_2$ solid solutions, using a significant number of samples of variable composition. It turned out that $Ce_xZr_{1-x}O_2$—keeping the BET surface area constant among the various Ce concentrations of solid solutions—reveals a maximum in activity for x = 70−80 mol % of Ce, slightly higher than pure CeO_2 but at least 10 times higher than pure ZrO_2. While pure CeO_2 is not stable toward bulk-chlorination under harsh HCl oxidation conditions (i.e., with excess HCl in the reaction feed), samples with $x \leq 80\%$ were chemically stable.[12] Similar results had been reported earlier for mixed $Ce_xZr_{1-x}O_2$ nanofibers, but the samples featured different surface areas, and thus, the comparability was limited.[13]

The most obvious questions for the Deacon process over CeO_2@ZrO_2 that have not been settled so far are the following: What is the chemical nature of the active phase of CeO_2@ZrO_2? How does the heat treatment, which is a mandatory part of the preparation, affect the performance of

Received: August 16, 2019
Revised: October 10, 2019
Published: October 15, 2019

DOI: 10.1021/acscatal.9b03482
ACS Catal. 2019, 9, 10680−10693

CeO_2@ZrO_2? Are there synergistic effects operative between CeO_2 and ZrO_2? How does the Deacon activity and stability of CeO_2@ZrO_2 compare with those of CeO_2 and $Ce_xZr_{1-x}O_2$ solid solutions? With these questions in mind, we devised dedicated experiments of CeO_2 supported on preformed ZrO_2 particles, employing moderate calcination temperatures to improve activity and to avoid intermixing of CeO_2 and ZrO_2 at the interface. We report here experimental evidence that the activity of supported CeO_2@ZrO_2 is caused by a thin and stable CeO_2 wetting layer coating the ZrO_2 particle surface.

2. EXPERIMENTAL DETAILS

2.1. Preparation of Catalysts. The supported x mol % CeO_2 on ZrO_2 catalysts with varying ceria concentrations (x = 2.5, 5, 8, 11, 15, 20) were prepared by the incipient wetness impregnation method. For example, for the synthesis of the 5 mol % CeO_2@ZrO_2 sample, 0.27 g of the $Ce(NO_3)_3{\cdot}6H_2O$ precursor was first mixed with 1.5 mL H_2O. The ZrO_2 support (1.46 g) was subsequently mixed with the above $Ce(NO_3)_3{\cdot}6H_2O$ solution, followed by stirring for 18 h at room temperature. The mixture was then dried in air at 80 °C for 12 h and calcined in air at various temperatures (between 500 and 900 °C) for 1 or 5 h. The monoclinic ZrO_2 sample was purchased from Saint-Gobain NorPro in pelletized form (diameter = 3 mm, length = 4 mm). The ZrO_2 particles were crushed and subsequently dried in air at 160 °C for 2 h prior to impregnation. Nomenclature of the CeO_2@ZrO_2 samples: $x$$CeO_2$@$ZrO_2$-$y$, with x corresponding to the molar percentage of CeO_2, y referring to the calcination temperature in °C for 5 h.

For comparison reasons, pure ZrO_2 was calcined at 600 and 900 °C for 5 h in each case and employed in catalytic tests. Ceria-zirconia solid solutions with different ratios of Ce/Zr were synthesized by the coprecipitation method.[11,14] The hydrogen peroxide was first dropped into the $Ce(NO_3)_3{\cdot}6H_2O$ solution to obtain a molar ratio of H_2O_2/Ce of 1.5. The corresponding amount of $ZrO(NO_3)_2{\cdot}nH_2O$ solution was then mixed with the solution to attain a molar ratio of Ce/Zr = x/(1 − x), x = 0.05, 0.2, 0.8, 1. The precipitation of ceria-zirconia precursor was achieved by dropping an ammonia solution into the solution keeping the pH at around 9.5. The precipitate was stirred for 18 h and then washed with deionized water several times until the pH value of around 7 was reached. The precipitate was then dried overnight at 120 °C and calcined at various temperatures (between 700 and 800 °C) for 5 h in order to ensure a constant specific surface area among the various $Ce_{1-x}Zr_xO_2$ samples.

2.2. Characterization of Catalysts. Structural information on the catalyst is gained by X-ray diffraction (XRD) which is conducted in Θ-2Θ geometry on a Panalytical X'Pert PRO diffractometer with a Cu Kα source (40 kV, 40 mA). Rietveld analysis was carried out by using the FullProf program (Version 2.05).

For Raman spectroscopy, a Senterra spectrometer by Bruker Optics was employed. The laser wavelength was 532 nm and the laser power was 2 mW. All samples were measured at 50× magnification with a spectral resolution of 3−5 cm^{-1}, 250 coaddition, and 3 s integration time. The Raman spectra were recorded in backscattering geometry at room temperature and processed with OPUS 7.5 software.

The samples were degassed in vacuum for 12 h at 393 K before performing N_2 physisorption experiments with Autosorb 6 of Quantachrome at 77 K. The BET (Brunauer−Emmett−Teller) method was used to determine the specific surface area.

The molar concentration of Ce of the 20CeO_2@ZrO_2-y catalyst was quantified by inductively coupled plasma atomic emission spectroscopy (ICP-AES) using a TJA IRIS ADVANTAG 1000 instrument.

Transmission and scanning transmission electron microscopy (TEM/STEM) characterization were conducted with two different microscopes. A FEI Tecnai G2 F30 microscope (not aberration corrected) equipped with EDAX analyzer (DPP-II) was used to conduct high resolution TEM (HRTEM), high-angle annular dark field scanning transmission electron microscopy (HAADF-STEM), and X-ray energy-dispersive spectroscopy (XEDS). Aberration-corrected high-resolution STEM images were acquired using a Titan Themis G2 microscope operated at 300 kV. XEDS measurements with a resolution at the nanometer scale were performed using an Oxford X-Max^N 100TLE instrument.

The concentration of Zr and Ce in the near-surface region of the catalyst was quantified by X-ray photoemission spectroscopy (XPS) (PHI VersaProbe II). The photon energy was 1486.6 eV (monochromatized Al Kα line), and the X-ray spot size was ∼100 μm × 1.3 mm with an excitation power of ∼80−95 W. Charging of the sample was compensated by a flow of slow electrons with energies of about 1 eV and Ar^+ ions of about 10 eV. For overview spectra the pass energy was set to 187.85 eV, while detail spectra were taken with a pass energy of 23.5 eV. The energy step size was 0.1 eV in the case of the O 1s and C 1s spectra, and for all other spectra, the energy step size was 0.2 eV. The system pressure during the experiment was $\sim 10^{-6}$ Pa, and all spectra were taken at room temperature and energy-corrected by the C 1s hydrocarbon signal at 284.8 eV.

The XPS spectra were analyzed with CasaXPS Version 2.3.17. In order to maintain similar kinetic energies of photoelectrons of Ce and Zr, we chose the Ce 4d and Zr 3d spectra to quantify the relative Ce surface concentration with respect to the total concentration of Zr+Ce. For the deconvolution of the spectra, we followed the same procedure first suggested by Burroughs et al.[15] and later refined by Romeo et al.[16] and Li et al.,[17] with five peaks labeled v, v_0, v′, v″, and v‴ for the $3d_{5/2}$ and another five peaks labeled u, u_0, u′, u″, and u‴ for the spin−orbit split $3d_{3/2}$. We used Gaussian/Lorentzian peak shapes (GL(30)) to fit the peaks and employed a linear background by splitting the Ce 3d region into three sections (v_0 to v″, v‴ to u″, and u‴). We constrained the area ratios of the 5/2 and 3/2 species to 3:2. The spin−orbit-splitting of the lines was constrained to a minimum of 18 eV and a maximum of 18.5 eV.

2.3. Catalytic Tests. The Deacon reaction measurements were conducted in a homemade fixed-bed flow reactor.[18] The reactor comprises the gas supply, the quartz tube reactor, the furnace for heating, and UV−vis analytics for chlorine quantification. The following gases were used: HCl 4.5, O_2 5.0, and Ar 5.0 purchased from AirLiquide, and the flow rates of gases were controlled by digital mass flow controllers (MKS Instruments 1179B). Prior to feeding the gas mixture into the reactor, Ar was dried using a water absorption cartridge (ALPHAGAZ purifier H_2O-free, AirLiquide). The reaction temperature was computer-controlled. The product analysis was accomplished by a fiber-optic UV−vis spectrometer (Ocean Optics USB4000 with a DH-2000-BAL light source) with a Z-shaped flow cell (Teflon, 50 mm optical path length,

DOI: 10.1021/acscatal.9b03482
ACS Catal. 2019, 9, 10680−10693

FIAlab). The absorbance at a wavelength of λ_{max} = 329 nm (absorption maximum of chlorine) is proportional to the chlorine space time yield (STY) that was routinely calibrated by standard iodometry. The STY is defined as the molar amount of product per time and mass catalyst.

For the activity measurement, the argon-balanced reaction feeds contain 20 vol % O_2 and 10 vol % HCl (Ar:HCl:O_2 = 10.5:1.5:3). The furnace was heated to 430 °C with a rate of 10 K/min and held for 1 h under reactant stream. For the stability measurement, three specific reaction conditions, Ar:HCl:O_2 = 10.5:3:1.5, Ar:HCl:O_2 = 11:3:1, and Ar:HCl:O_2 = 9:4.5:1.5 were applied for 24 h. The furnace was heated to 430 °C with a rate of 10 K/min. The total volumetric flow rate for the reaction was set to 15 cm^3 STP min^{-1} (sccm). Only when the catalyst had reached the reaction temperature in pure Ar was the reaction feed switched to the desired O_2 + HCl reaction mixture.

The experiments of oxygen storage capacity (OSC) were carried out by using a stainless-steel tube (i.d. 4 mm, length 60 mm) connected to the gas inlet system by stainless steel leads (i.d. 1.6 mm) via Swagelok tube fittings.[19,20] The catalyst (30 mg) was dried at 120 °C for 5 h and loaded into the reactor, supported between two quartz wool wads. The OSC reactor containing the sample was heated to 430 °C with a rate of 10 K·min^{-1} using the same furnace and temperature control as for the HCl oxidation experiments. Carbon monoxide (Praxair, quality 4.7) was employed as the reducing agent while oxygen (Praxair, quality 5.0) served as the oxidizing agent. The stream selector (VICI multiposition valve with an outlet for unused streams) allows to switch software-controlled the flow at specified time intervals between three gases (CO with a flow rate of 10 sccm, O_2 with a flow rate of 2 sccm, and Ar with a flow rate of 2 sccm each) and mix them with the Ar carrier stream (18 sccm). After leaving the OSC reactor, the gases pass through a Swagelok sintered stainless steel filter (pore size 2 μm) and reach the microvolume thermal conductivity detector (VICI TCD2) operated with pure argon as the baseline (detector temperature 373 K, filament temperature 423 K).

To determine the plain or dynamic oxygen storage capacity (OSC), the stream selector was switched to CO for 10 s and to O_2 for 2 s alternatingly with an 80 s Ar purge step in between. Using additional O_2 pulse as a reference, the amount of adsorbed oxygen was calculated that corresponds to the (dynamic) OSC. The complete oxygen storage capacity (OSCc) was determined by reducing the catalyst with a sufficiently long sequence of CO pulses each 10 s long accompanied by 80 s Ar pulse pauses. Subsequently, the selector was switched to O_2 for 10 pulses of 2 s duration separated by 80 s pure Ar pulses were applied. The total amount of consumed oxygen was taken to be the OSCc.

3. EXPERIMENTAL RESULTS

3.1. Activity Experiment: HCl Oxidation Reaction under Mild Conditions. In Figure 1 we show a set of activity data of the 20CeO_2@ZrO_2 for mild reaction condition Ar:HCl:O_2 = 10.5:1.5:3, where the catalyst is stable, in comparison with the BET surface area for a variety of calcination temperatures. Since the Deacon reaction was performed at 430 °C, we restrict the calcination step to temperatures above 500 °C to avoid thermal alterations of the catalyst during Deacon reaction. In the range from 500 to 700 °C, the activity does hardly vary with calcination temperature,

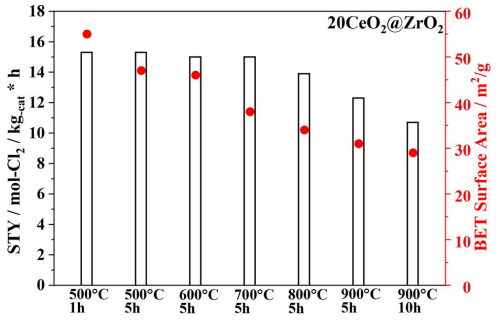

Figure 1. Activity data of the HCl oxidation reaction and BET surface area data for 20CeO_2@ZrO_2 that was calcined to various temperatures and time periods. The activity data are given as STY (black, left scale) for a reaction mixture Ar:HCl:O_2 = 10.5:1.5:3 and a flow rate of 15 sccm, 30 mg of catalyst and a reaction temperature of 430 °C. The BET surface area are given in red (right scale).

while the BET surface area decreases continuously. Above 800 °C, the Deacon activity starts to decline roughly following the decrease in BET surface area.

From these experiments, the optimum calcination temperature was chosen to be 600 °C, which avoids Ce−Zr intermixing and which is still notably higher than the actual reaction temperature of 430 °C. A calcination temperature of 900 °C is considered to be high enough to induce Ce−Zr intermixing (as later shown by TEM and Raman experiments), but the activity is significantly smaller than that achieved for a calcination at 600 °C.

The activity data of CeO_2@ZrO_2 catalysts (calcined at 600 °C) in the Deacon reaction with varying cerium concentrations under mild reaction feed Ar:HCl:O_2 = 10.5:1.5:3 and a reaction temperature of 430 °C are summarized in Figure 2a. The activity of pure ZrO_2 is very low and practically negligible in comparison with CeO_2. There are two distinct regions in the activity data as a function of the ceria concentration. First, the activity increases steeply with a ceria concentration up to 5 mol %, and then the activity increases much more slowly with the ceria concentration up to 20 mol %.

For the present study we select 5CeO_2@ZrO_2-600 and 20CeO_2@ZrO_2-600, which are representative for the two distinct activity regimes in Figure 2a (i.e., represent steep versus shallow increase in the activity with increasing CeO_2 concentration). By in-depth comparison of these two samples, we intend to infer the chemical nature of the active phase (see also Section 3.2). In Figure 2b, we show activity data of 5CeO_2@ZrO_2 and 20CeO_2@ZrO_2 for two specific calcination temperatures of 600 and 900 °C and compare them with corresponding initial BET surface areas; the reaction feed is Ar:HCl:O_2 = 10.5:1.5:3 and the reaction temperature was 430 °C. With an increase of the calcination temperature from 600 to 900 °C, the BET surface area S_{BET} decreases from 49 m^2/g to 38 m^2/g for the 5CeO_2@ZrO_2-900 catalyst, while the activity declines from 11.6 mol-Cl_2/kg_{-cat}·h to 8.2 mol-Cl_2/kg_{-cat}·h. This decrease in activity (29%) is essentially traced to the reduction of the BET surface area (22%).

A similar trend is observed for the 20CeO_2@ZrO_2 catalyst when increasing the calcination temperature. The activity of 20CeO_2@ZrO_2-600 (15 mol-Cl_2/kg_{-cat}·h) declines to 10.7 mol-Cl_2/kg_{-cat}·h, while the BET surface area decreases from 46

DOI: 10.1021/acscatal.9b03482
ACS Catal. 2019, 9, 10680−10693

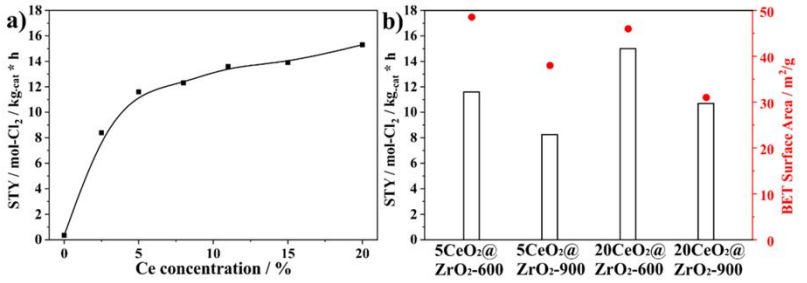

Figure 2. (a) Activity data of the HCl oxidation reaction for xCeO$_2$@ZrO$_2$-600 with different molar ceria concentrations. (b) Activity data of the HCl oxidation reaction and BET surface area data for 5CeO$_2$@ZrO$_2$ and 20CeO$_2$@ZrO$_2$ which was calcined to 600 and 900 °C for 5 h. The activity data are given as STY (black, right scale) for a reaction mixture Ar:HCl:O$_2$ = 10.5:1.5:3 and a flow rate of 15 sccm, 30 mg of catalyst, and a reaction temperature of 430 °C. The BET surface areas of the pristine materials (i.e., prior to the HCl oxidation reaction) are given in red (right scale).

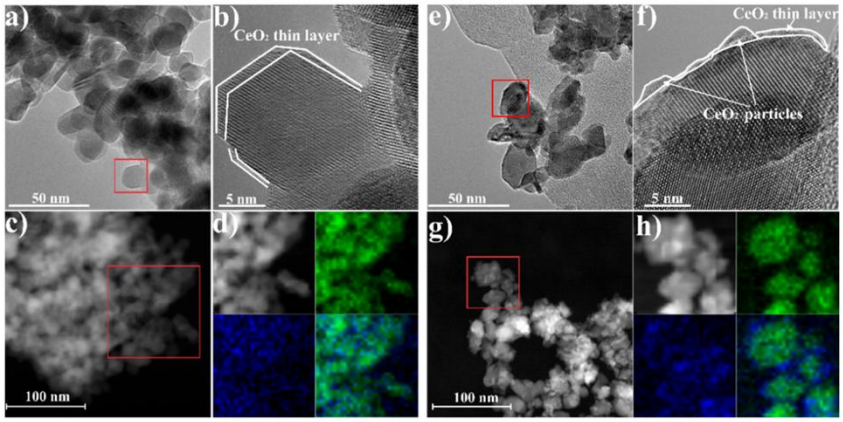

Figure 3. High-resolution TEM images (a,b) and HAADF-STEM image (c) of 5CeO$_2$@ZrO$_2$-600. (d) XEDS map of the red square: green = Zr; blue = Ce, and in the last image, both element mappings are overlaid. High-resolution TEM images (e,f) and HAADF-STEM image (g) of 20CeO$_2$@ZrO$_2$-600. (h) XEDS map of the red square: green = Zr; blue = Ce, and in the last image, both element mappings are overlaid.

m^2/g to 31 m^2/g. Again this decline in the activity (29%) roughly reflects the decline in BET surface area (33%).

3.2. Characterization of the As-Prepared CeO$_2$@ZrO$_2$ Particle System. The TEM analyses of as-prepared 5CeO$_2$@ZrO$_2$-600 and 20CeO$_2$@ZrO$_2$-600 are summarized in Figure 3. The morphology of 5CeO$_2$@ZrO$_2$-600 (cf. Figure 3a,b) is similar to that of pure ZrO$_2$ (Figure S1a-d), where CeO$_2$ particles adhering to ZrO$_2$ particles are not observed. However, in the XEDS map (cf. Figure 3d), CeO$_2$ is shown to be localized at the surface of ZrO$_2$ particle in the form of a thin (but not fully covering) film of 1−2 nm thickness. Quite in contrast, the 20CeO$_2$@ZrO$_2$-600 in Figure 3e,f clearly exhibits additional particles with a mean size of ∼6 nm adhering to the supporting ZrO$_2$ particle. From element mapping in Figure 3h, the particles are ascribed to CeO$_2$ particles. In addition, we can recognize that the ZrO$_2$ particle in Figure 3f is partly covered by a thin CeO$_2$ layer.

High-resolution XEDS element mappings and TEM images visualize the distribution of Ce, Zr of the 20CeO$_2$@ZrO$_2$-600 catalyst in Figure 4. CeO$_2$ is concentrated at the surface of ZrO$_2$ as thin layer, and several CeO$_2$ nanoparticles attached to the ZrO$_2$ surface are clearly discernible.

In Figure S2, we compare the element mapping of 20CeO$_2$@ZrO$_2$-600 with that of 20CeO$_2$@ZrO$_2$-900. Here the lower contrast of Zr and Ce for 20CeO$_2$@ZrO$_2$-900 (cf. Figure S2b) in comparison with 20CeO$_2$@ZrO$_2$-600 (cf. Figure S2a) can be attributed to intermixing of Ce and Zr, a conclusion that is reinforced by the element mapping of a Ce$_{0.2}$Zr$_{0.8}$O$_2$ solid solution (cf. Figure S2c).

For comparison reasons, similar TEM experiments are shown for the 20CeO$_2$@ZrO$_2$-900 sample (cf. Figure 5). For higher calcination temperatures (900 °C), the CeO$_2$-related particles disappear. Instead, a crystalline CeO$_2$ layer is observed that forms an interface with a mixed Ce$_x$Zr$_{1-x}$O$_2$ underlayer.

The XRD pattern of 5CeO$_2$@ZrO$_2$-600 (Figure 6) is practically identical to that of pure ZrO$_2$. Since 1−2 nm thick CeO$_2$ layers are practically invisible in XRD in such mixtures (being almost X-ray amorphous), this finding supports the view that CeO$_2$ first forms a thin layer or small particles (1−2 nm) on the ZrO$_2$ carrier particle. With increasing CeO$_2$

DOI: 10.1021/acscatal.9b03482
ACS Catal. 2019, 9, 10680−10693

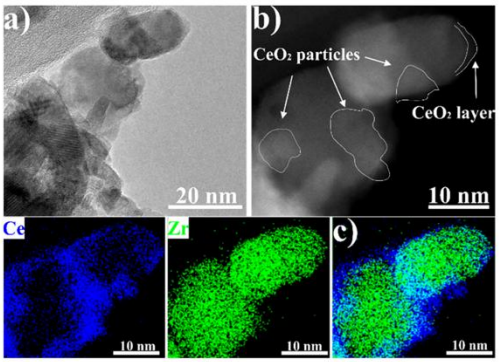

Figure 4. Aberration-corrected high resolution TEM images (a) and HAADF-STEM image (b) of $20CeO_2$@ZrO_2-600. (c) XEDS maps of overlap of Ce (blue) and Zr (green).

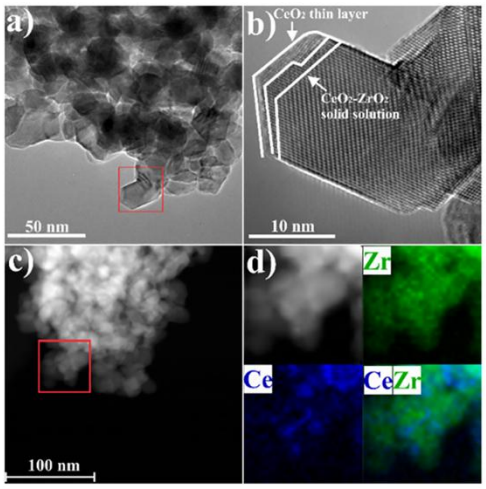

Figure 5. High-resolution TEM images (a,b) and HAADF-STEM image (c) of $20CeO_2$@ZrO_2-900. (d) XEDS map of the red square: green = Zr; blue = Ce, and last image both element mappings are overlaid.

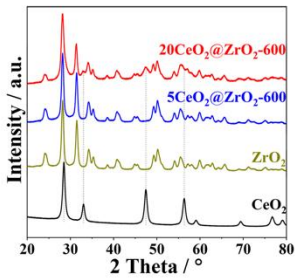

Figure 6. XRD patterns of pure CeO_2, ZrO_2, $5CeO_2$@ZrO_2-600, and $20CeO_2$@ZrO_2-600 catalysts. The dotted lines indicate the position of CeO_2-related peaks in the ZrO_2 X-ray pattern.

loadings above 8 mol % CeO_2 particles attached to the ZrO_2 particles become gradually detectable in XRD (cf. Figure S3a). The XRD pattern of $20CeO_2$@ZrO_2-600 catalyst (cf. Figure 6) consists of the superposition of the cubic phase of CeO_2 (ICDD no. 00-034-0394) and the monoclinic phase of ZrO_2 (ICDD no. 00-036-0420). There is no evidence for the formation of a solid solution.[11,21] The CeO_2- and ZrO_2-related diffraction peak positions of $20CeO_2$@ZrO_2-600 are identical to those of pure CeO_2 and ZrO_2. Therefore, the XRD experiments are consistent with the observed morphology of CeO_2 particle on ZrO_2 particle in the TEM experiments (cf. Figure 3, 4). However, as summarized in the Supporting Information (cf. Figure S4a), the XRD patterns of $20CeO_2$@ZrO_2 hardly varies with calcination temperatures up to 900 °C and different calcination times so that XRD is not sensitive enough to identify intermixing of CeO_2 with ZrO_2, calling for an alternative technique such as Raman spectroscopy (see below).

Rietveld refinement of the XRD data of Figure 6 provide structural and compositional details as summarized in Table 1. The average crystallite sizes of pure CeO_2 particles and ZrO_2 particles are 10 and 12 nm, respectively. For the $5CeO_2$@ZrO_2-600 sample, no ceria-related diffraction signals are discernible. The crystallite size of ZrO_2 turns out to be ~12 nm, similar to that of pure ZrO_2. The quality of the Rietveld refinement can be judged from fitting as exemplified with $20CeO_2$@ZrO_2-600 in Figure S5. For the $20CeO_2$@ZrO_2-600 sample, the average particle size of CeO_2 is around 7 nm which is consistent with the TEM results (cf. Figure 3). We have to note that the average particle size of ZrO_2 in pure ZrO_2, $5CeO_2$@ZrO_2-600, and $20CeO_2$@ZrO_2-600 as determined by TEM (cf. Figure 3 and Figure S1a) is around 24 nm, which differs substantially from those derived from Rietveld refinement. The reason could be the microstructure of ZrO_2 that is composed of crystallites of 12 nm size. From Rietveld refinement, the percentage of CeO_2 turns out to be 16.4 mol %, which is significantly lower than the nominal percentage of 20 mol %. However, taking into account the superposition of the XRD contributions from the different substances and also considering the low intensity of the signals emerging from CeO_2, the accuracy of these values is limited. CeO_2 appears in $20CeO_2$@ZrO_2-600 in two states, one is the thin CeO_2 layer with low molar fraction that cannot be detected by XRD, the other consists of larger CeO_2 particles attached to ZrO_2 particles being visible in XRD. Altogether, the results from Rietveld refinement are consistent with TEM results. ICP-AES quantifies the concentrations of CeO_2 for the $20CeO_2$@ZrO_2-600 and $20CeO_2$@ZrO_2-900 samples to be 20 and 18 mol %, respectively. These values are close to the nominal percentage of 20 mol %.

In order to provide further evidence for the CeO_2 wetting layer on the ZrO_2 particle, we took XPS data from the as-prepared $5CeO_2$@ZrO_2-600 and $20CeO_2$@ZrO_2-600 samples. Recall that the concentration derived from XPS assumes a solid solution of the participating elements. With a morphology of a CeO_2 layer covering partly the ZrO_2 particle, the apparent Ce-related XPS signal should be enhanced and that of the Zr-related signal be damped. Altogether such structure will lead to an apparent increase in the Ce concentration. As indicated in Table 1, the Ce 4d and Zr 3d XPS signals correspond to a Ce concentration of 14% and 53% for $5CeO_2$@ZrO_2-600 and $20CeO_2$@ZrO_2-600 that is 2−3 times higher than the nominal concentration of 5 mol % and 20 mol %, respectively. This

DOI: 10.1021/acscatal.9b03482
ACS Catal. 2019, 9, 10680−10693

Table 1. Physicochemical Properties of CeO_2, ZrO_2, $5CeO_2$@ZrO_2-600, and $20CeO_2$@ZrO_2-600 Catalysts

		crystalline size/nm[b]		CeO_2 concentration/mol %			
samples	S_{BET}/ m^2/g[a]	CeO_2	ZrO_2	*b*	measured by ICP-AES	calculated by XPS	$Ce^{3+}/Ce^{3+}+Ce^{4+}$[c]
CeO_2	46	10	n.a.	n.a.	n.a.	n.a.	24%
ZrO_2-600	44	n.a.	12	n.a.	n.a.	n.a.	n.a.
$5CeO_2$@ ZrO_2-600	49	n.a.	12	n.a.	5	14	48%
$20CeO_2$@ZrO_2-600	46	7	12	16.4	20	53	25%

[a]Determined by BET method. [b]Determined by Rietveld refinement. [c]Calculated by XPS.

finding corroborates nicely a CeO_2 wetting layer covering large portions of the ZrO_2 particle surface. In order to quantify the concentration of Ce^{3+} in the surface selvedge region, we applied photoelectron emission of the Ce 3d state.[22−24] The Ce 3d-spectra (cf. Figure S6) indicate clearly that the Ce^{3+} concentration of $5CeO_2$@ZrO_2-600 relative to that of Ce is significantly increased in comparison to pure CeO_2 and $20CeO_2$@ZrO_2-600 (cf. Table 1). The $Ce^{3+}/(Ce^{3+}+Ce^{4+})$ ratio doubles from 24% for CeO_2 and $20CeO_2$@ZrO_2-600 and to 48% in $5CeO_2$@ZrO_2-600.

In general, Raman spectroscopy is more sensitive than XRD to the presence of a $Ce_xZr_{1-x}O_2$ solid solution. Therefore, we acquired Raman survey spectra of CeO_2@ZrO_2 for different ceria concentration and various calcination temperatures (cf. Figures S3b and S4b in the Supporting Information). From visual inspection of these Raman spectra, it is evident that mainly the dominating phonon mode around 470 cm^{-1} is affected by the calcination temperature and the CeO_2 content.[25] This region of the Raman spectra is magnified and compiled in Figure 7. The contribution of the ZrO_2

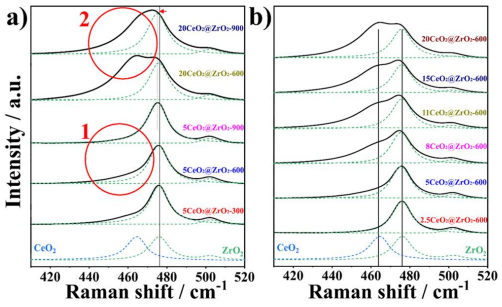

Figure 7. High-resolution Raman spectra of (a) $5CeO_2$@ZrO_2 and $20CeO_2$@ZrO_2 that were calcined to 300, 600, and 900 °C for 5 h. (b) $x CeO_2$@ZrO_2-600 (x = 0, 2.5, 5, 8, 11, 15, 20). The pure spectra of CeO_2 and ZrO_2 are shown as blue and green dashed line, respectively. The ZrO_2 spectrum is overlaid in each spectrum to emphasize the changes in the CeO_2-related phonon band. The red circles 1 and 2 in panel (a) indicate the changes in CeO_2-related phonon band due to increasing the calcination temperature from 600 to 900 °C.

supporting particles (green) that is assumed to remain unchanged is overlaid in each spectrum of Figure 7 to emphasize the changes in CeO_2-related modes. In the Supporting Information (Figure S7), the spectra are modeled by a linear superposition of pure CeO_2 (blue) and ZrO_2 (green) Raman spectra.

As shown in Figure 7a, for the $5CeO_2$@ZrO_2 sample, the band at 460−480 cm^{-1} consists of a superposition of pure CeO_2 and pure ZrO_2 Raman spectra for calcination temperatures of 300 and 600 °C and are therefore compatible with the coexistence of pure CeO_2 and ZrO_2. Upon increasing the calcination temperature to 900 °C ($5CeO_2$@ZrO_2-900), the CeO_2-related peak disappears (red circle 1 in Figure 7a), and only the ZrO_2-related band at 476 cm^{-1} remains. There is no clear indication of the formation of ceria-zirconia solid solution[11] presumably because of the low ceria concentration. However, the ZrO_2-related peak at 476 cm^{-1} slightly shifts to lower wavenumber, which can be attributed to the presence of Ce−Zr mixed oxides.[10,26,27] Because both Raman spectra ($5CeO_2$@ZrO_2-300 and $5CeO_2$@ZrO_2-600) are practically identical, Ce−Zr intermixing in $5CeO_2$@ZrO_2-600 can safely be ruled out for a calcination temperature of 600 °C.

The band at 460−480 cm^{-1} of the $20CeO_2$@ZrO_2-600 sample is also explained by a superposition of pure CeO_2 and pure ZrO_2 Raman spectra and therefore pointing toward a coexistence of CeO_2 and ZrO_2. For the $20CeO_2$@ZrO_2-900 sample (red circle 2 in Figure 7a), in comparison with $20CeO_2$@ZrO_2-600, the CeO_2-related feature changes drastically with calcination temperature. This observation is consistent with the formation of a $Ce_xZr_{1-x}O_2$ solid solution, and in comparison with Raman spectra of $Ce_xZr_{1-x}O_2$ solid solutions (cf. Figure 3 in ref 9), x can be estimated to be ca. 0.8−0.9.

Raman spectra for various ceria concentrations ranging from 0 to 20 mol % but fixed calcination temperature of 600 °C are compiled in Figure 7b. The shoulder at 464 cm^{-1} is assigned to pure CeO_2 that appears already at a ceria concentration of 5 mol % so that Raman spectroscopy demonstrates to be significantly more sensitive than XRD to CeO_2 in CeO_2@ZrO_2 samples. This means that Raman spectroscopy is able to detect even the (X-ray amorphous) ultrathin CeO_2 films (1−2 nm thick) on the supporting ZrO_2 particles.

As shown in Figure 8, the OSCc value of $5CeO_2$@ZrO_2-600 is 23 μmol (O)/g, which is practically identical to the OSC

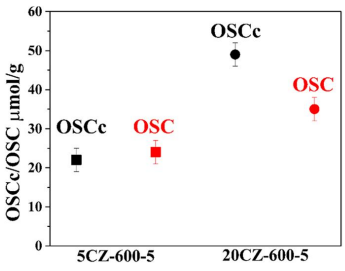

Figure 8. Plain oxygen-storage capacity, complete oxygen-storage capacity (OSC and OSCc, respectively) of CeO_2@ZrO_2-600. $5CeO_2$@ZrO_2-600: square, $20CeO_2$@ZrO_2-600: disk.

DOI: 10.1021/acscatal.9b03482
ACS Catal. 2019, 9, 10680−10693

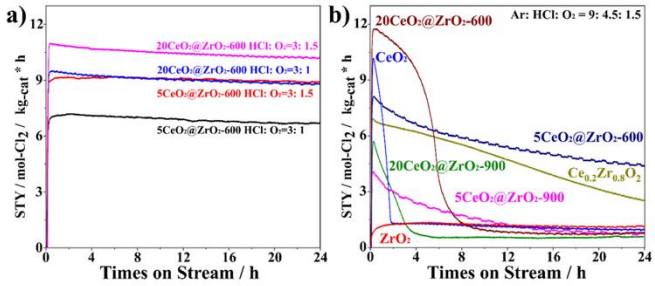

Figure 9. (a) Deacon activity experiments of $5CeO_2$@ZrO_2-600 and $20CeO_2$@ZrO_2-600 at T = 430 °C (flow rate 15 sccm, 30 mg catalyst, 24 h on stream for various mixtures of the reaction feed Ar:HCl:O_2. (b) Deacon activity experiments of CeO_2, ZrO_2, $Ce_{0.2}Zr_{0.8}O_2$, $5CeO_2$@ZrO_2-600, $5CeO_2$@ZrO_2-900, $20CeO_2$@ZrO_2-600, and $20CeO_2$@ZrO_2-900 at T = 430 °C (flow rate 15 sccm, 30 mg catalyst, 24 h on stream) for the reaction feed Ar:HCl:O_2 = 9:4.5:1.5.

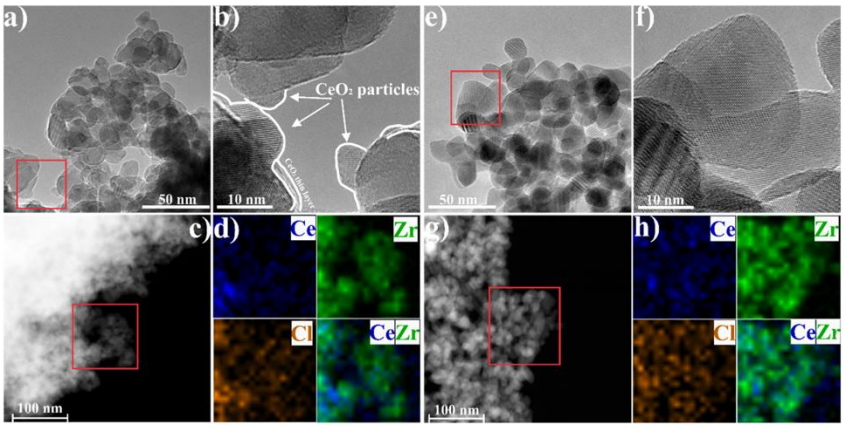

Figure 10. High-resolution TEM images (a,b) and HAADF-STEM image (c) of $20CeO_2$@ZrO_2-600 after the Deacon reaction performed in a gas mixture of Ar:HCl:O_2 = 10.5:3:1.5 for 24 h. (d) XEDS map of the red square: green = Zr; blue = Ce; tan = Cl, and in the last image both element mappings are overlaid. High-resolution TEM images (e,f) and HAADF-STEM image (g) $20CeO_2$@ZrO_2-600 after the Deacon reaction of Ar:HCl:O_2 = 9:4.5:1.5 for 24 h. (h) XEDS map of the red square: green = Zr; blue = Ce; tan = Cl, and last image both element mappings are overlaid.

value of $5CeO_2$@ZrO_2-600 (25 μmol (O)/g). Keeping in mind that OSC represents the capacity of oxygen in the near-surface region of CeO_2, while OSCc is the capacity of surface and bulk CeO_2 oxygen storage,[28,29] we conclude from identical values of OSC and OSCc for $5CeO_2$@ZrO_2-600 a rapid exchange of oxygen that is reconciled with a thin-layer morphology of CeO_2 on ZrO_2. Quite in contrast, the OSCc value of $20CeO_2$@ZrO_2-600 is significantly higher than the corresponding OSC value, thus indicating substantial contributions of oxygen exchange from bulk-like CeO_2 particles.

3.3. Comparative Stability Tests of $5CeO_2$@ZrO_2-600 and $20CeO_2$@ZrO_2-600 in the HCl Oxidation Reaction under Harsh Conditions Including Postreaction Characterization. The stability of the Ce-based catalysts was tested in the HCl oxidation reaction for various reaction mixtures at a fixed reaction temperature of 430 °C (cf. Figure 9). As shown in Figure 9a, steady-state condition is reached after 15 h on stream for $20CeO_2$@ZrO_2-600. It turned out that the $20CeO_2$@ZrO_2-600 and $5CeO_2$@ZrO_2-600 catalysts are both stable up to a reducing reaction mixture of Ar:HCl:O_2 = 11:3:1. Further increase of the HCl partial pressure will lead to chemical instabilities of catalysts caused by bulk chlorination.

The stability results of different Ce-based catalysts under the harshest condition (Ar:HCl:O_2 = 9:4.5:1.5) are summarized in Figure 9b. The $20CeO_2$@ZrO_2-600 catalyst deactivates quickly with time on stream. Quite in contrast, the deactivation rate of $5CeO_2$@ZrO_2-600 is much slower than that of $20CeO_2$@ZrO_2-600. The $5CeO_2$@ZrO_2-600 catalyst deactivated continually, but full deactivation is not achieved after 24 h on stream (and even after 59 h on stream, cf. Supporting Information, Figure S8). Surprisingly, the catalyst $5CeO_2$@ZrO_2-900 deactivates fully after 16 h on stream, thus exhibiting a significantly lower stability than the $5CeO_2$@ZrO_2-600. Also, the $20CeO_2$@ZrO_2-900 deactivates steeply during the initial 5 h on stream, much faster than $20CeO_2$@ZrO_2-600. Counterintuitively, higher calcination temperature results in lower chemical stability of the catalysts.

For Ar:HCl:O_2 = 9.5:4.5:1.5, the pure CeO_2 catalyst is unstable as well because the activity decreases steeply during the initial 2 h on stream, much faster than the $20CeO_2$@ZrO_2-

DOI: 10.1021/acscatal.9b03482
ACS Catal. 2019, 9, 10680−10693

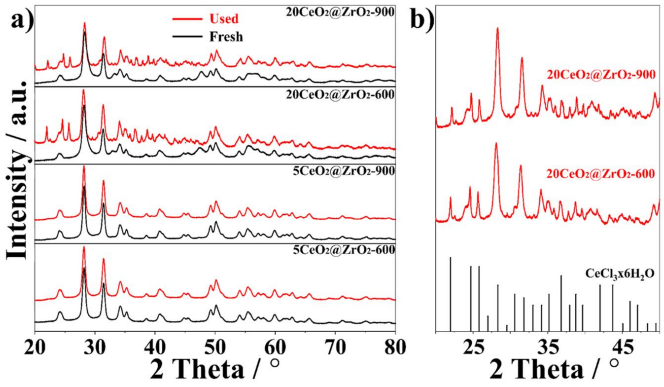

Figure 11. (a) XRD patterns of fresh and used $5CeO_2@ZrO_2$-600, $5CeO_2@ZrO_2$-900, $20CeO_2@ZrO_2$-600, and $20CeO_2@ZrO_2$-900 at T = 430 °C (flow rate = 15 sccm, 30 mg catalyst, 24 h on stream) for the reaction feed Ar:HCl:O_2 = 9:4.5:1.5. (b) Detailed XRD patterns between 20° and 50° of $20CeO_2@ZrO_2$-600 and $20CeO_2@ZrO_2$-900 in comparison with expected positions and intensities of $CeCl_3 \times 6H_2O$ (ICDD no. 00-001-0149).

Table 2. Characterization of the Pure CeO_2, Pure ZrO_2, $5CeO_2@ZrO_2$-600, $5CeO_2@ZrO_2$-900, $20CeO_2@ZrO_2$-600, and $20CeO_2@ZrO_2$-900 after Deacon Reaction under the Reaction Feed Ar:HCl:O_2 = 9:4.5:1.5 (in Total 15 sccm) for 24 h on Stream and a Reaction Temperature of 430 °C, except for the Fourth Row (59 h)

	crystalline size/nm[a]				surface atomic concentration[b]		
samples/Ar:HCl:O_2 mixture	CeO_2	$CeCl_3$	ZrO_2	X/$CeCl_3 \times nH_2O$[a]	Cl/(Ce+Zr)	Ce/(Ce+Zr)	Cl/O
CeO_2	19	11($6H_2O$)/ 62($7H_2O$)	n.a.	76%	190%	100%	93%
ZrO_2	n.a.	n.a.	13	n.a.	48%	0%.	21%
$5CeO_2@ZrO_2$-600	n.a.	n.a.	n.a.	n.a.	54%	9%	24%
$5CeO_2@ZrO_2$-600-59h	n.a.	n.a.	n.a.	n.a.	54%	7%	25%
$5CeO_2@ZrO_2$-900	n.a.	n.a.	n.a.	n.a.	56%	8%	26%
$20CeO_2@ZrO_2$-600	n.a.	32($6H_2O$)	12	16%	100%	31%	45%
$20CeO_2@ZrO_2$-900	n.a.	38($6H_2O$)	12	15%	108%	33%	54%

[a]Determined by Rietveld refinement. [b]Determined by XPS.

600 but also much faster than $5CeO_2@ZrO_2$-600. The $Ce_{0.2}Zr_{0.8}O_2$ solid solution is also not stable under this harsh condition. Pure ZrO_2 is stable even under the harsh reaction conditions of Ar:HCl:O_2 = 9:4.5:1.5, although the overall activity is a factor of 10 smaller than the initial activity of CeO_2.

In Figure 10a,b, TEM images are presented of $20CeO_2@ZrO_2$-600 after the Deacon reaction performed in Ar:HCl:O_2 = 10.5:3:1.5 for 24 h. Clearly, particles adhere to the supporting ZrO_2 particles. The XEDS mapping images (Figure 10c,d) reveal that these particles consist of CeO_2 (bright blue) being attached to the ZrO_2 particles (green). In comparison to TEM images of freshly prepared $20CeO_2@ZrO_2$-600 (cf. Figures 3 and 4), the $20CeO_2@ZrO_2$-600 sample is morphologically stable under the reaction condition of Ar:HCl:O_2 = 10.5:3:1.5 in accordance with the corresponding activity experiments (Figure 9).

Figures 10e,f show the morphology of the $20CeO_2@ZrO_2$-600 catalyst after the Deacon reaction in Ar:HCl:O_2 = 9:4.5:1.5 for 24 h. The adhering CeO_2 particles on ZrO_2 disappear completely, while the morphology of the used $20CeO_2@ZrO_2$-600 catalyst looks similar to that of the pure ZrO_2 catalyst (Figure S1e-h) after exposure to Ar:HCl:O_2 = 9:4.5:1.5 for 24 h. In the XEDS mapping (cf. Figure 10h), there is no indication of large particles of CeO_2 or $CeCl_3 \times nH_2O$. Chlorine and Ce are evenly distributed over the ZrO_2 particles, thus indicating that the $CeCl_3 \times nH_2O$ may be localized at the surface as quite thin nanostructure. However, because of the lower resolution of TEM in this operation mode, it is difficult to distinguish an ultrathin $CeCl_3 \times nH_2O$ layer structure from a thin CeO_2 layer.

The fresh and used catalysts under Ar:HCl:O_2 = 9:4.5:1.5 for 24 h on stream were characterized by XRD (Figure 11). For each deactivated sample, the structure of the ZrO_2 carrier is not affected by the Deacon reaction: it keeps the monoclinic structure, and there is no apparent chlorination discernible. The XRD pattern of the $5CeO_2@ZrO_2$-600 catalyst after Deacon reaction with Ar:HCl:O_2 = 9:4.5:1.5 is similar to that of the fresh $5CeO_2@ZrO_2$-600, although $5CeO_2@ZrO_2$-600 deactivates under such harsh reaction conditions. Therefore, the formed $CeCl_3 \times nH_2O$ needs to be X-ray amorphous that can be realized for instance by ultrathin layer on the supporting ZrO_2 particle. Leaving the catalyst for 59 h on stream, the deactivation of $5CeO_2@ZrO_2$-600 continues, and faint but clearly assigned signatures of $CeCl_3 \times nH_2O$ become evident in XRD (cf. Figure S9). The XRD patterns of the used and the fresh $5CeO_2@ZrO_2$-900 sample are virtually identical. When exposing $20CeO_2@ZrO_2$-600 and $20CeO_2@ZrO_2$-900 to a harsh reaction mixture of Ar:HCl:O_2 = 9:4.5:1.5, where deactivation is encountered, bulk chlorination of CeO_2 is clearly detectable in XRD (Figure 11b). The very same

DOI: 10.1021/acscatal.9b03482
ACS Catal. 2019, 9, 10680−10693

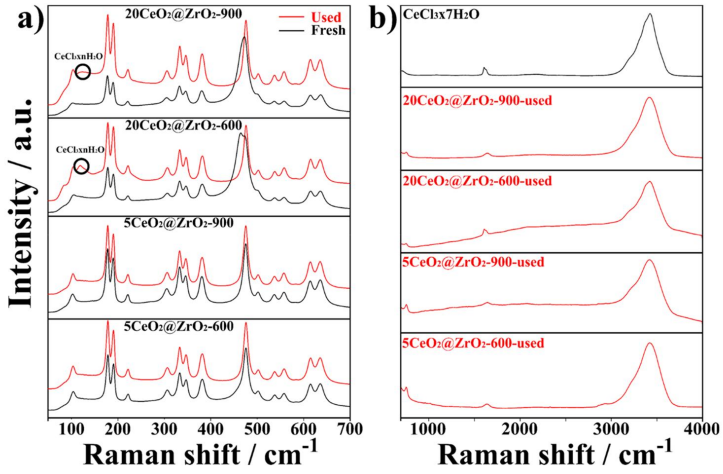

Figure 12. Raman spectra of $5CeO_2@ZrO_2$-600, $5CeO_2@ZrO_2$-900, $20CeO_2@ZrO_2$-600, and $20CeO_2@ZrO_2$-900 before (fresh) and after the Deacon reaction at T = 430 °C (flow rate 15 sccm, 30 mg catalyst, 24 h on stream) for reaction feed Ar:HCl:O_2 = 9:4.5:1.5. (a) Detailed spectra between 100 and 700 cm^{-1}. (b) Detailed spectra between 700 and 4000 cm^{-1} of the used samples.

formation of $CeCl_3 \times 6H_2O$ is observed, when pure CeO_2 is tested under similar reaction condition (cf. Figure S10).

Rietveld refinements of XRD data of different catalysts after used in Deacon reaction are compiled in Table 2. The average size of the supporting ZrO_2 particle is 12 nm and hence identical to that of the fresh ones. For deactivated pure CeO_2, 76% of pure CeO_2 has shown to be transformed to $CeCl_3 \times nH_2O$. The average crystallite size of the formed $CeCl_3 \times nH_2O$ is 62 nm. For the deactivated $20CeO_2@ZrO_2$-600 and $20CeO_2@ZrO_2$-900 samples, the $CeCl_3 \times nH_2O$ concentration is determined to be 16% and 15%, respectively and therefore be slightly lower than the nominal percentage of 20 mol % CeO_2. This difference in Ce concentration may point to a covering $CeCl_3 \times nH_2O$ layer on the CeO_2 wetting layer caused by the selective chlorination of the attached is CeO_2 particle.

The degree of chlorination is also determined by XPS. For the $20CeO_2@ZrO_2$-600 and $20CeO_2@ZrO_2$-900 samples after Deacon reaction with the harsh reaction mixture of Ar:HCl:O_2 = 9:4.5:1.5 the Cl/(Ce+Zr) value is ~100%. Considering that only 20 mol % CeO_2 is in $20CeO_2@ZrO_2$-600, the high values of Cl/(Ce+Zr) and Cl/O evidence substantial chlorination of the CeO_2. The Ce concentration given by the Ce/(Ce+Zr) value decreases by around 20% compared to the fresh $20CeO_2@ZrO_2$-600, being compatible with the consumption of adhering CeO_2 particles due to chlorination and covering the CeO_2 wetting layer with a $CeCl_3 \times nH_2O$ film.

For the $5CeO_2@ZrO_2$-600 samples, the Cl/(Ce+Zr) and Cl/O values are quite high (54%) after exposure to a harsh reaction mixture Ar:HCl:O_2 = 9:4.5:1.5 for 24h. Considering that the Ce content is only 5 mol % instead of 20 mol % as in $20CeO_2@ZrO_2$-600, this finding indicates a substantial chlorination of CeO_2 in $5CeO_2@ZrO_2$-600 consistent with a partial deactivation. The Cl/(Ce+Zr) and Cl/O values of $5CeO_2@ZrO_2$-900 are almost similar to that of $5CeO_2@ZrO_2$-600.

The chlorination of catalyst can readily be followed by Raman spectroscopy (Figure 12). The Raman spectrum of used $20CeO_2@ZrO_2$-600 and $20CeO_2@ZrO_2$-900 sample in Figure 12a exhibit an additional feature at 119 cm^{-1}, while the CeO_2-related contribution at 464 cm^{-1} disappears. The vibrational feature at 119 cm^{-1} is also observed for pure $CeCl_3 \times nH_2O$ so that it can be taken as evidence for bulk-chlorination. In addition, in the spectral region 1000−4000 cm^{-1} (cf. Figure 12b), there appear additional features at 3500 and 1300 cm^{-1}.[30] For comparison reasons, the Raman spectra of $CeCl_3 \times 7H_2O$ are shown in Figure 12b. The $CeCl_3 \times 7H_2O$ spectrum indicates sharper phonon modes at 3500 and 1300 cm^{-1}, which are also observed in the spectrum of all used samples after Deacon reaction at Ar:HCl:O_2 = 9:4.5:1.5. The features at 3500 and 1300 cm^{-1} are attributed to the H_2O. Therefore, the additional spectral features of all used samples after Deacon reaction at Ar:HCl:O_2 = 9:4.5:1.5 in Figure 12b are ascribed to the formation of $CeCl_3 \times nH_2O$.

The $20CeO_2@ZrO_2$-600 catalyst chlorinates under harsh Deacon reaction conditions by selective chlorination of the CeO_2. To further strengthen our conclusion about bulk-chlorination of the active CeO_2 component, we provide Raman spectra of pure CeO_2 after Deacon reaction for various reaction mixtures in Figure S11a,b. Only for Ar:HCl:O_2 = 9:4.5:1.5, the Raman spectrum shows additional features at 3500 and 1300 cm^{-1}.

Surprisingly, even the chlorination of $5CeO_2@ZrO_2$-600 and $5CeO_2@ZrO_2$-900 can be identified with Raman spectroscopy. In Figure 12a, it can be seen that the shoulder of the CeO_2-related peak at 464 cm^{-1} disappears for the $5CeO_2@ZrO_2$-600 after Deacon reaction with Ar:HCl:O_2 = 9:4.5:1.5 for 24 h. In Figure 12b, for $5CeO_2@ZrO_2$-600 and $5CeO_2@ZrO_2$-900 the phonon modes at 3500 cm^{-1} indicate the existence of $CeCl_3 \times nH_2O$.[30] Because there is no sign of $CeCl_3 \times nH_2O$ in XRD and no $CeCl_3 \times nH_2O$ particles are observed in TEM, it can be concluded that $CeCl_3 \times nH_2O$ remains as a nanostructure on the ZrO_2 particle during the process of deactivation, instead of forming separate particles. In Figure S12, we compare the Raman spectrum of fresh ZrO_2 with that of used $5CeO_2@ZrO_2$-600 under the condition of Ar:HCl:O_2 = 9:4.5:1.5.

DOI: 10.1021/acscatal.9b03482
ACS Catal. 2019, 9, 10680−10693

Clearly, there is no difference between two Raman spectra, indicating that the concentration of CeO_2 must be below 2.5 mol %; recall that the 2.5 mol % CeO_2@ZrO_2 sample shows no CeO_2 features in Raman spectroscopy (cf. Figure 7). From the activity data of 5CeO_2@ZrO_2-600 in Figure 9, it is evident that still some CeO_2 needs to be on the ZrO_2 surface. Leaving the catalyst for 59 h on stream, the deactivation of 5CeO_2@ZrO_2-600 continues, and faint but clearly assigned signatures of $CeCl_3 \times nH_2O$ become evident in Raman (cf. Figure S13).

In order to gain further information on the chlorination of the used samples from the XPS, the Ce 3d XP spectra are fitted with a superposition of the reference spectra of CeO_2, Ce_2O_3, and $CeCl_3$ (cf. Figure 13). The Ce^{3+} peaks from CeO_2 are

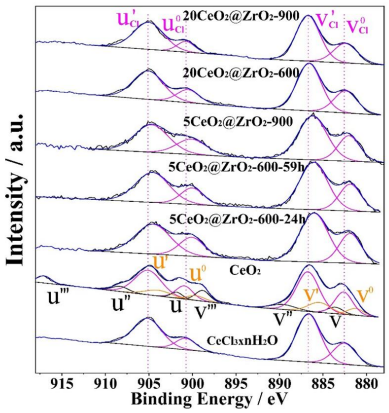

Figure 13. Ce 3d XP spectra of used samples after the Deacon reaction at T = 430 °C (flow rate 15 sccm, 30 mg catalyst, 24 h on stream) for the reaction feed Ar:HCl:O_2 = 9:4.5:1.5. The Ce^{4+} peaks from CeO_2 are labeled by v, v′′, v′′′, u, u′′, u′′′ in black, while the Ce^{3+} peaks from CeO_2 are labeled by v′, v_0, u′, u_0 in yellow. The spectral features of Ce^{3+} in $CeCl_3$ are labeled by v^0_{Cl}, v'_{Cl}, u^0_{Cl}, and u'_{Cl} in magenta.

labeled by v′, v_0, u′, u_0 in yellow. The spectral features of Ce^{3+} in $CeCl_3$ are shifted to higher binding energies than Ce^{3+} of Ce_2O_3, being consistent with a previous study.[17,31] For comparison, we show the Ce 3d XP spectrum of pure $CeCl_3 \times nH_2O$.

For the Ce 3d XP spectrum of 5CeO_2@ZrO_2-600 after Deacon reaction with a reaction mixture of Ar:HCl:O_2 = 9:4.5:1.5 ("harsh" condition) for 24 h, a small Ce^{4+}-related signal is still visible in the energy ranges of 915−920 eV. The Ce^{4+}-related feature disappears after running the reaction for 59 h, together with slightly lower dispersion of Ce on the ZrO_2 particles as indicated in Table 2 (Ce/(Ce+Zr) : 9% → 7%). The Ce 3d XPS of 5CeO_2@ZrO_2-900 is similar to that of pure $CeCl_3 \times nH_2O$, which indicates that the CeO_2 species are fully chlorinated under the harsh reaction condition. Altogether, the Ce 3d XP spectra of the deactivated 20CeO_2@ZrO_2-600 and 20CeO_2@ZrO_2-900 catalysts comprise only features of pure $CeCl_3$, consistent with results from Rietveld refinement. The decomposition of the Ce 3d spectrum of pure CeO_2 after Deacon reaction with Ar:HCl:O_2 = 9:4.5:1.5 at 430 °C indicates significant concentrations of Ce^{4+} and Ce^{3+} in Ce_2O_3.

The Ce 4d XP spectra of various samples after Deacon reaction with a reaction mixture of Ar:HCl:O_2 = 9:4.5:1.5 are compiled in Figure S14. The spectral features at around 122 and 125 eV are assigned to Ce^{4+}.[32] Ce^{4+} is absent in the deactivated 20CeO_2@ZrO_2-600 sample, meaning that only Ce^{3+} is present, consistent with the full transformation of CeO_2 to $CeCl_3 \times nH_2O$ in 20CeO_2@ZrO_2-600. Quite in contrast, the XPS spectra of deactivated pure CeO_2 and $Ce_{0.2}Zr_{0.8}O_2$ solid solution show the coexistence of Ce^{3+} and Ce^{4+}. This difference in chlorination behavior of 20CeO_2@ZrO_2-600 and the $Ce_{0.2}Zr_{0.8}O_2$ solid solution provides further evidence that no solid solution is formed in the 20CeO_2@ZrO_2-600 sample upon calcination at 600 °C for 5 h.

In conclusion, these XPS experiments evidence that the selective chlorination of CeO_2 is responsible for the deactivation of 20CeO_2@ZrO_2-600 and 5CeO_2@ZrO_2-600 under harsh Deacon reaction conditions as encountered with a reaction mixture of Ar:HCl:O_2 = 9:4.5:1.5.

4. DISCUSSION

4.1. Catalytically Active Phase of 5CeO_2@ZrO_2-600 and 20CeO_2@ZrO_2-600. The Deacon activity of pure ZrO_2 is at least 10-times lower than that of CeO_2 or 5CeO_2@ZrO_2-600 and 20CeO_2@ZrO_2-600 (cf. Figure 2a). Therefore, CeO_2 constitutes the active component of the CeO_2@ZrO_2 catalyst in the HCl oxidation reaction.

CeO_2@ZrO_2 calcined at 600 °C for 5 h (cf. Figure 2a) reveals a steep rise in Deacon activity with the CeO_2 concentration up to 5 mol % CeO_2 that is followed by a shallow increase up to 20 mol % CeO_2. Similar results were reported by Moser et al.[10] for CeO_2@ZrO_2 calcined at 900 °C, although in this study, the activity levels off already above 10 mol % of CeO_2.

From high-resolution TEM experiments (cf. Figure 3b) and XEDS maps (cf. Figure 3d), we provide compelling evidence that CeO_2 forms a 1−2 nm thick layer on the supporting ZrO_2 particle in 5CeO_2@ZrO_2-600, practically without growing CeO_2 particles that are attached to ZrO_2. Quite in contrast, the 20CeO_2@ZrO_2-600 sample reveals in TEM (cf. Figure 3f) a thin CeO_2 wetting layer on which small CeO_2 particles (about 6 nm) adhere. These CeO_2 particles with an average size of 6 nm are detectable in XRD (cf. Figure 6) and in Raman spectra (cf. Figure 7).

Therefore, the catalytically active phase is reconciled with the CeO_2 wetting layer on ZrO_2 particle and this dispersion process of CeO_2 saturates already with 5 mol % of CeO_2. The excess CeO_2 at higher mol % (i.e., above 5%) leads then to the growth of CeO_2 particle attached to the CeO_2@ZrO_2 particle, thereby hardly changing the active CeO_2 surface area concomitant with only a slight increase in activity.

Of course, TEM is a local method whose results may not be representative for the whole sample. Therefore, we applied additional averaging methods such as XRD, Raman spectroscopy, and XPS to strengthen our conclusion. The absence of CeO_2-related XRD signals in Figure 6 (X-ray amorphous) and the presence of CeO_2-related vibrations in Raman spectra in Figure 7 are consistent with a 1−2 nm thick CeO_2 layer. However, the strongest evidence for the CeO_2 wetting layer in 5CeO_2@ZrO_2-600 comes from XPS (cf. Table 1) that indicates a substantially (about a factor 3) higher near-surface Ce-concentration than expected from CeO_2 particles supported on ZrO_2.

With the nominal CeO_2 concentration derived by XPS and quantified by Ce/(Ce+Zr) ratio (cf. Table 1), a CeO_2 film thickness of 1.6 ± 0.2 nm can be deduced, assuming that CeO_2

DOI: 10.1021/acscatal.9b03482
ACS Catal. 2019, 9, 10680−10693

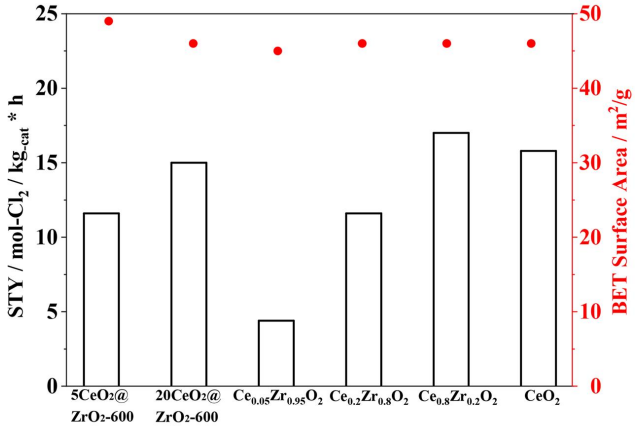

Figure 14. Activity data of the HCl oxidation reaction and BET surface area data for $5CeO_2@ZrO_2$ and $20CeO_2@ZrO_2$ which was calcined to 600 °C for 5 h in comparison with pure CeO_2, $Ce_{0.05}Zr_{0.95}O_2$, $Ce_{0.2}Zr_{0.8}O_2$, and $Ce_{0.8}Zr_{0.2}O_2$. The activity data are given as STY (black, right scale) for a reaction mixture Ar:HCl:O_2 = 10.5:1.5:3 and a flow rate of 15 sccm, 30 mg of catalyst, and a reaction temperature of 430 °C. The BET surface area are given in red (right scale).

covers homogeneously the ZrO_2 particles. A similar estimation of the CeO_2 layer thickness can be conducted on the basis of the saturation behavior of the activity at 5 mol % CeO_2. Assuming that 5 mol % CeO_2 fully covers the ZrO_2 particles with a BET surface are of 45m^2/g, then the thickness of the CeO_2 layer is inferred to be about 1.5 ± 0.3 nm. Both estimations compare remarkably well with that determined by high-resolution TEM (cf. Figure 3b), suggesting that most of the ZrO_2 surface is indeed covered by an ultrathin CeO_2 layer in the $5CeO_2@ZrO_2$-600. Additional support of the CeO_2 wetting layer for $5CeO_2@ZrO_2$-600 comes from comparing OSC and OSCc experiments. Both OSC and OSCc are practically identical for $5CeO_2@ZrO_2$-600, while those of the $20CeO_2@ZrO_2$-600 are substantially different (cf. Figure 8) because of the presence of larger CeO_2 particles. From an electronic point of view, $5CeO_2@ZrO_2$-600 exhibits a much higher ratio $Ce^{3+}/(Ce^{4+}+Ce^{3+})$ of concentrations than $20CeO_2@ZrO_2$-600. This may be correlated with the observed improved performance in the Deacon process. An enhanced Ce^{3+} concentration was recently reported for ultrathin CeO_2 layers on TiO_2 support with its beneficial impact on the low-temperature dehydrogenation of ethanol to acetaldehyde.[33]

Epitaxial CeO_2 layers on ZrO_2-based carriers have been reported only occasionally in the literature. Chueh and co-workers reported the successful growth of single crystalline coherently strained CeO_2 (100) layer on a single crystalline yttrium-stabilized ZrO_2 substrate (YSZ(100)) with a thickness of up to 2.7 nm, employing the pulsed laser deposition method.[34−36] This experiment suggests that CeO_2 is able to wet ZrO_2. In another study, $CeO_2@ZrO_2$ particles were prepared by dry impregnation and subjected to a high-temperature reduction/mild reoxidation treatment that resulted in superior oxygen storage properties in terms of low-temperature capacity and thermal stability.[37,38] With high-resolution scanning, TEM-XEDS the authors identified the layer morphology of a $Ce_2Zr_2O_8$ kappa phase supported on ZrO_2.

In general, a calcination temperature of 600 °C applied for 5 h is not able to induce Ce−Zr intermixing of the two oxides in $5CeO_2@ZrO_2$-600 and $20CeO_2@ZrO_2$-600, thus forming a sharp interface between the thin CeO_2 wetting layer and the supporting ZrO_2 particle. This is evidenced by high-resolution TEM (cf. Figure 3, 4) but most notably by Raman spectroscopy (cf. Figure 7), a technique that is remarkably sensitive to Ce−Zr intermixing. Quite in contrast, calcination at 900 °C for 5 h leads to substantial intermixing of Ce and Zr in $20CeO_2@ZrO_2$-900 as evidenced by TEM (cf. Figure 5) as well as by Raman spectroscopy experiments (cf. Figures 7) and fully consistent with previous studies from the Perez-Ramirez group.[10]

4.2. HCl Oxidation: The Activity Comparison of Different Ceria-Based Catalysts. According to Figure 2a, the specific activity (i.e., the activity per gram CeO_2) is highest for $2.5CeO_2@ZrO_2$-600. For higher CeO_2 concentrations, the specific CeO_2 activity declines. For instance, the activities of $5CeO_2@ZrO_2$-600 and $20CeO_2@ZrO_2$-600 differ by only 15%, although the amount of CeO_2 is quadrupled. The catalytic activity of $CeO_2@ZrO_2$ is much higher than that of the solid solution with the same CeO_2 content (cf. Figure 14). For instance, the activity of $5CeO_2@ZrO_2$-600 is 3 times higher than that of $Ce_{0.05}Zr_{0.95}O_2$, while the activity of $20CeO_2@ZrO_2$-600 is still 20% higher than that of $Ce_{0.20}Zr_{0.80}O_2$.

$20CeO_2@ZrO_2$-600 has a similar activity as pure CeO_2 with similar BET surface area (cf. Figure 14). This precludes a substantially higher intrinsic activity of supported active component CeO_2 (normalized to the BET surface area of the mass of the active CeO_2 component) in comparison with bulk CeO_2. The high specific activity of CeO_2 brings, however, the great benefit of fewer CeO_2 needed for $CeO_2@ZrO_2$ than for a solid solution $Ce_xZr_{1-x}O_2$ of comparable activity. Reducing the total loading of lanthanides (e.g., CeO_2) in heterogeneous catalysis is a major concern from a geo-strategic point of view.

The catalytic activity of both $5CeO_2@ZrO_2$ and $20CeO_2@ZrO_2$ catalysts declines substantially by about 30% when the calcination temperature is increased from 600 to 900 °C (cf. Figure 2b). This effect is only partly explained by a reduction

DOI: 10.1021/acscatal.9b03482
ACS Catal. 2019, 9, 10680−10693

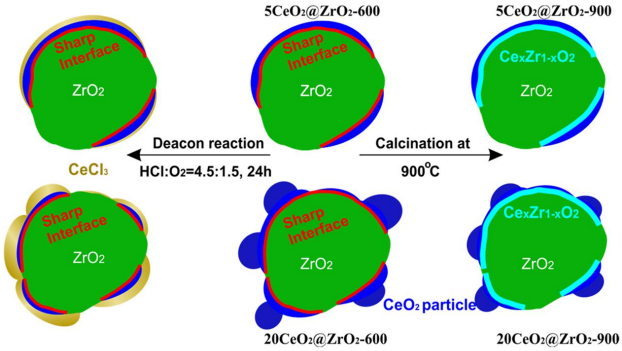

Figure 15. Schematic model (middle) of the fresh catalysts $5CeO_2@ZrO_2$-600 and $20CeO_2@ZrO_2$-600, revealing a CeO_2 wetting layer with a sharp interface to the supporting ZrO_2 particle. On $20CeO_2@ZrO_2$-600 additionally CeO_2 particles adhere to the structure. Under harsh reaction conditions ($HCl:O_2$ = 4.5:1.5), $CeCl_3 \times nH_2O$ covers the catalyst concomitant with a deactivation (left). When the freshly prepared catalyst are calcined at 900 °C, a thin interfacial layer of $Ce_xZr_{1-x}O_2$ is formed (right) that reduces the chemical stability of the CeO_2 layer and CeO_2 particles under harsh Deacon conditions.

in the BET surface area. For the case of $5CeO_2@ZrO_2$ the intrinsic activity per BET surface area decreases significantly by 7% when the calcination temperature is raised from 600 to 900 °C. For the case of $20CeO_2@ZrO_2$, the intrinsic activity increases slightly. In the high-resolution TEM image (Figure 5b), Zr−Ce intermixing is shown to be restricted to the CeO_2−ZrO_2 interface, while the surface still exposes CeO_2 but with a reduced thickness. Tentatively, we ascribe the slight increase in intrinsic activity to a thinning of the exposed CeO_2 layer on $20CeO_2@ZrO_2$-900.

Altogether, there are three different kinds of active ceria species. One species consists of pure CeO_2 particles with crystallite size of ∼10 nm, the other is a 1−2 nm thick CeO_2 layer on ZrO_2 ($5CeO_2@ZrO_2$-600), and the last one is CeO_2 particles attached to CeO_2 film on ZrO_2 particle ($20CeO_2@ZrO_2$-600) with crystallite size of ∼6 nm. There is growing evidence that the 1−2 nm thick CeO_2 layer on ZrO_2 ($5CeO_2@ZrO_2$-600) is the most active ceria species.

4.3. HCl Oxidation: The Stability Comparison of Different Ceria-Based Catalysts. Catalytic tests reveal that $CeO_2@ZrO_2$ with 5 mol % and 20 mol % CeO_2 are stable under Deacon reaction conditions at 430 °C with reaction mixtures up to $Ar:HCl:O_2$ = 11:3:1 (cf. Figure 9a). The morphology of the $20CeO_2@ZrO_2$-600 catalyst is preserved as concluded from high-resolution TEM (cf. Figure 10b). However, increasing the HCl concentration in the reaction feed to $Ar:HCl:O_2$ = 9:4.5:1.5, $20CeO_2@ZrO_2$-600 deactivates fully within 8 h on stream. Quite in contrast, the deactivation of $5CeO_2@ZrO_2$-600 is not completed after 24 h on stream (cf. Figure 9). The stabilization of $5CeO_2@ZrO_2$-600 in comparison to pure CeO_2 is attributed to a promoting effect of ZrO_2 support on the stability of the ultrathin CeO_2 layer. The fastest deactivation occurs for a pure CeO_2 powder sample (average particle size of 10 nm) with a similar BET surface as $5CeO_2@ZrO_2$-600.

As expected from previous studies,[8,12,17,20] the deactivation of $CeO_2@ZrO_2$ is attributed to the selective transformation of CeO_2 to bulk $CeCl_3 \times nH_2O$. From high-resolution TEM, it is evident that the deactivation leads to the disappearance of the adhering CeO_2 particles of $20CeO_2@ZrO_2$-600 (cf. Figures 10e,f and Figure 15 left), a conclusion that is further corroborated by XRD (cf. Figure 11) and Raman spectroscopy (cf. Figure 12).

For the $5CeO_2@ZrO_2$-600 catalyst, the deactivation goes hand in hand with the disappearance of the CeO_2-related shoulder at 460 cm^{-1} and the appearance of strong vibrational modes at 1300 and 3500 cm^{-1}, which are assigned to $CeCl_3 \times nH_2O$. This finding provides evidence that at least part of the CeO_2 layer of $5CeO_2@ZrO_2$-600 is slowly transformed to $CeCl_3 \times nH_2O$; recall that 2.5 mol % CeO_2 is not seen in Raman spectroscopy (cf. Figure 7). Only faint additional diffraction peaks due to $CeCl_3 \times nH_2O$ are observed in XRD of $5CeO_2@ZrO_2$-600 after 59 h (instead of 24 h) on stream. XPS indicates that still some Ce^{4+} is present in $5CeO_2@ZrO_2$-600 after 24 h on stream that practically disappears after 59 h.

Assuming that the highly dispersed CeO_2 layer on the ZrO_2 is mostly responsible for the observed Deacon activity, both catalysts $20CeO_2@ZrO_2$-600 and $5CeO_2@ZrO_2$-600 should behave similarly in the deactivation. Obviously, this is not the case. The faster deactivation of $20CeO_2@ZrO_2$-600 tells us that chlorination starts from the adhering CeO_2 particles, forming $CeCl_3 \times nH_2O$ that is subsequently deposited on the remaining CeO_2 wetting layer on the ZrO_2 particle and thereby deactivating the $20CeO_2@ZrO_2$-600 catalysts quickly after 9 h on stream. In XPS (cf. Figure 13), the Ce 3d and Ce 4d spectra after deactivation of $20CeO_2@ZrO_2$-600 indicate the complete transformation of Ce^{4+} into Ce^{3+} that is compatible with a complete transformation into $CeCl_3$. In comparison to the fast deactivation process of $20CeO_2@ZrO_2$-600, no deposition of $CeCl_3 \times nH_2O$ because of chlorination of adhering CeO_2 particles is expected for $5CeO_2@ZrO_2$-600. This explains the slow deactivation of $5CeO_2@ZrO_2$-600 by a slow chlorination process of the ultrathin CeO_2 layer. Obviously, the ZrO_2 carrier exerts a stabilizing (synergy) effect on the ultrathin CeO_2 layer.

Altogether, these experiments indicate that a 1−2 nm thick CeO_2 wetting layer on ZrO_2 is more stable against chlorination than bulk CeO_2 and adhering CeO_2 particle to ZrO_2.

When increasing the calcination temperature from 600 to 900 °C, one would expect that the deactivation due to chlorination will be slowed down by formation of a $Ce_xZr_{1-x}O_2$ solid solution. Surprisingly, both catalysts

DOI: 10.1021/acscatal.9b03482
ACS Catal. 2019, 9, 10680−10693

$5CeO_2$@ZrO_2-900 and $20CeO_2$@ZrO_2-900 are less stable than the corresponding $5CeO_2$@ZrO_2-600 and $20CeO_2$@ZrO_2-600 catalysts, respectively (cf. Figure 9). From this observation, we infer that a 1−2 nm thick layer of CeO_2 is more stable than a mixed $Ce_xZr_{1-x}O_2$ layer ($5CeO_2$@ZrO_2-600 versus $5CeO_2$@ZrO_2-900). TEM images (cf. Figure 5) of fresh $20CeO_2$@ZrO_2-900 indicate that the adhering CeO_2 particles disappear, while a CeO_2 wetting layer is still exposed forming an interface with mixed $Ce_xZr_{1-x}O_2$ underlayer instead of with ZrO_2 (cf. Figure 15 right). Since the CeO_2 wetting layer of $20CeO_2$@ZrO_2-900 is less stable than that of $20CeO_2$@ZrO_2-600, a sharp interface of the CeO_2 layer with the supporting ZrO_2 particle is considered to promote the stabilization against chlorination.

5. CONCLUSIONS

Incipient wetness impregnation of CeO_2 on preformed ZrO_2 particles (CeO_2@ZrO_2) results in a high dispersion of the active CeO_2 phase concomitant with high specific activity of CeO_2 in the Deacon reaction. From activity, OSC, TEM, XRD, XPS, and Raman experiments, firm conclusions can be drawn about the morphology and the active phase of CeO_2@ZrO_2. The high degree of morphology control in the CeO_2@ZrO_2 system for certain compositions is reminiscent of the control which can be achieved by atomic layer deposition (ALD). The observed 1−2 nm thick CeO_2 wetting layer is responsible for the extraordinarily high specific activity of $5CeO_2$@ZrO_2-600, while saturation of wetting layer and formation of adhering CeO_2 particles result in a shallow increase in activity above 5 mol % CeO_2 (cf. Figure 15, middle part). According to the stability measurement, we infer that a 1−2 nm thick layer of CeO_2 attached to ZrO_2 is chemically more stable against bulk-chlorination than a mixed $Ce_xZr_{1-x}O_2$ layer ($5CeO_2$@ZrO_2-900) or a CeO_2 layer attached to a $Ce_xZr_{1-x}O_2$ interface ($20CeO_2$@ZrO_2-900).

Altogether, a structure of a 1−2 nm thick CeO_2 wetting layer with a sharp interface to the supporting pure ZrO_2 particle and an enriched concentration of Ce^{3+} reveal the highest stability and activity in the Deacon reaction. We expect that this kind of core−shell morphology with the CeO_2 shell adhering to the ZrO_2 core (CeO_2@ZrO_2) may be equally beneficial as support or as active component for other catalytic oxidation reaction.

■ ASSOCIATED CONTENT

Supporting Information

The Supporting Information is available free of charge on the ACS Publications website at DOI: 10.1021/acscatal.9b03482.

High-resolution TEM images of fresh and used ZrO_2 (Figure S1); Comparing XEDS element mappings of $20CeO_2$@ZrO_2-600, $20CeO_2$@ZrO_2-900 and $Ce_{0.2}Zr_{0.8}O_2$ (Figure S2); XRD patterns and Raman spectra of CeO_2@ZrO_2 with different ceria concentration and calcination temperature (Figure S3, S4, S7); Quality of the Rietveld refinement of $20CeO_2$@ZrO_2-600 (Figure S5); Ce 3d XPS of CeO_2, $5CeO_2$@ZrO_2-600 and $20CeO_2$@ZrO_2-600 (Figure S6); Deacon activity experiment of $5CeO_2$@ZrO_2-600 with 59h on stream (Figure S8); XRD patterns of Fresh and used $5CeO_2$@ZrO_2-600 (Figure S9); XRD patterns and Raman spectra of fresh and used CeO_2 and ZrO_2 (Figure S10, S11); Raman spectra of fresh ZrO_2 and used $5CeO_2$@ZrO_2-600 (Figure S12); Raman spectra of fresh and used $5CeO_2$@ZrO_2-600 (Figure S13); Ce 3d and 4d XPS of CeO_2, $Ce_{0.2}Zr_{0.8}O_2$ and $20CeO_2$@ZrO_2-600 (Figure S14) (PDF)

■ AUTHOR INFORMATION

Corresponding Authors

*E-mail: herbert.over@phys.chemie.uni-giessen.de.
*E-mail: Bernd.Smarsly@phys.Chemie.uni-giessen.de.
*E-mail: ylguo@ecust.edu.cn.

ORCID

Bernd M. Smarsly: 0000-0001-8452-2663
Herbert Over: 0000-0001-7689-7385

Notes

The authors declare no competing financial interest.

■ ACKNOWLEDGMENTS

This work was supported by the National Key Research and Development Program of China (2016YFC0204300), National Natural Science Foundation of China (21577035), Commission of Science and Technology of Shanghai Municipality (13521103402, 15DZ1205305) and 111 Project (B08021). Yu Sun gratefully acknowledge the China Scholarship Council for the Joint-Ph.D program between the China Scholarship Council and the Physical Chemistry Institute of Justus-Liebig-University Giessen. We acknowledge support from the Laboratory of Materials Research at the JLU.

■ REFERENCES

(1) Hisham, M. W. M.; Benson, S. W. Thermochemistry of the Deacon Process. *J. Phys. Chem.* **1995**, *99*, 6194−6198.
(2) Pérez-Ramírez, J.; Mondelli, C.; Schmidt, T.; Schlüter, O. F. K.; Wolf, A.; Mleczko, L.; Dreier, T. Sustainable chlorine recycling via catalysed HCl oxidation: from fundamentals to implementation. *Energy Environ. Sci.* **2011**, *4*, 4786−4799.
(3) Over, H.; Schomäcker, R. What Makes a Good Catalyst for the Deacon Process? *ACS Catal.* **2013**, *3*, 1034−1046.
(4) Seki, K. Development of RuO_2/Rutile-TiO_2 Catalyst for Industrial HCl Oxidation Process. *Catal. Surv. Asia* **2010**, *14*, 168−175.
(5) Lin, R.; Amrute, A. P.; Pérez-Ramírez, J. Halogen-Mediated Conversion of Hydrocarbons to Commodities. *Chem. Rev.* **2017**, *117*, 4182−4247.
(6) Amrute, A. P.; Krumeich, F.; Mondelli, C.; Pérez-Ramírez, J. Depleted Uranium Catalysts for Chlorine Production. *Chem. Sci.* **2013**, *4*, 2209−2217.
(7) Amrute, A. P.; Larrazábal, G. O.; Mondelli, C.; Pérez-Ramírez, J. $CuCrO_2$ Delafossite: A Stable Copper Catalyst for Chlorine Production. *Angew. Chem., Int. Ed.* **2013**, *52*, 9772−9775.
(8) Amrute, A. P.; Mondelli, C.; Moser, M.; Novell-Leruth, G.; López, N.; Rosenthal, D.; Farra, R.; Schuster, M. E.; Teschner, D.; Schmidt, T.; Pérez-Ramírez, J. Performance, structure, and mechanism of CeO_2 in HCl oxidation to Cl_2. *J. Catal.* **2012**, *286*, 287−297.
(9) Farra, R.; Eichelbaum, M.; Schlögl, R.; Szentmiklósi, L.; Schmidt, T.; Amrute, A. P.; Mondelli, C.; Pérez-Ramírez, J.; Teschner, D. Do observations on surface coverage-reactivity correlations always describe the true catalytic process? A case study on ceria. *J. Catal.* **2013**, *297*, 119−127.
(10) Moser, M.; Mondelli, C.; Schmidt, T.; Girgsdies, F.; Schuster, M. E.; Farra, R.; Szentmiklósi, L.; Teschner, D.; Pérez-Ramírez, J. Supported CeO_2 catalysts in technical form for sustainable chlorine production. *Appl. Catal., B* **2013**, *132*−*133*, 123−131.
(11) Sun, Y.; Li, C.; Djerdj, I.; Khalid, O.; Cop, P.; Sann, J.; Weber, T.; Werner, S.; Turke, K.; Guo, Y.; Smarsly, B. M.; Over, H. Oxygen storage capacity versus catalytic activity of ceria-zirconia solid

DOI: 10.1021/acscatal.9b03482
ACS Catal. 2019, 9, 10680−10693

solutions in CO and HCl oxidation. *Catal. Sci. Technol.* **2019**, *9*, 2163−2172.
(12) Li, C.; Sun, Y.; Hess, F.; Djerdj, I.; Sann, J.; Voepel, P.; Cop, P.; Guo, Y.; Smarsly, B. M.; Over, H. Catalytic HCl oxidation reaction: Stabilizing effect of Zr-doping on CeO_2 nano-rods. *Appl. Catal., B* **2018**, *239*, 628−635.
(13) Urban, S.; Tarabanko, N.; Kanzler, C. H.; Zalewska-Wierzbicka, K.; Ellinghaus, R.; Rohrlack, S. F.; Chen, L.; Klar, P. J.; Smarsly, B. M.; Over, H. Stable and Active Mixed Zr-Ce Oxides for Catalyzing the Gas Phase Oxidation of HCl. *Catal. Lett.* **2013**, *143*, 1362−1367.
(14) Aneggi, E.; de Leitenburg, C.; Trovarelli, A. On the role of lattice/surface oxygen in ceria-zirconia catalysts for diesel soot combustion. *Catal. Today* **2012**, *181*, 108−115.
(15) Burroughs, P.; Hamnett, A.; Orchard, A. F.; Thornton, G. Satellite Structure in the X-ray Photoelectron Spectra of some Binary and Mixed Oxides of Lanthanum and Cerium. *J. Chem. Soc., Dalton Trans.* **1976**, *17*, 1686−1698.
(16) Romeo, M.; Bak, K.; El Fallah, J.; Le Normand, F.; Hilaire, L. XPS Study of the Reduction of Cerium Dioxide. *Surf. Interface Anal.* **1993**, *20*, 508−512.
(17) Li, C.; Sun, Y.; Djerdj, I.; Voepel, P.; Sack, C.-C.; Weller, T.; Ellinghaus, R.; Sann, J.; Guo, Y.; Smarsly, B. M.; Over, H. Shape-Controlled CeO_2 Nanoparticles: Stability and Activity in the Catalyzed HCl Oxidation Reaction. *ACS Catal.* **2017**, *7*, 6453−6463.
(18) Kanzler, C. H.; Urban, S.; Zalewska-Wierzbicka, K.; Hess, F.; Rohrlack, S. F.; Wessel, C.; Ostermann, R.; Hofmann, J. P.; Smarsly, B. M.; Over, H. Electrospun Metal Oxide Nanofibres for the Assessment of Catalyst Morphological Stability under Harsh Reaction Conditions. *ChemCatChem* **2013**, *5*, 2621−2626.
(19) Möller, M.; Urban, S.; Cop, P.; Weller, T.; Ellinghaus, R.; Kleine-Boymann, M.; Fiedler, C.; Sann, J.; Janek, J.; Chen, L. M.; Klar, P. J.; Hofmann, D. M.; Philipps, J.; Dolcet, P.; Gross, S.; Over, H.; Smarsly, B. M. Synthesis and Physicochemical Characterization of $Ce_{1-x}Gd_xO_{2-\delta}$: A Case Study on the Impact of the Oxygen Storage Capacity on the HCl Oxidation Reaction. *ChemCatChem* **2015**, *7*, 3738−3747.
(20) Möller, M.; Over, H.; Smarsly, B.; Tarabanko, N.; Urban, S. Electrospun ceria-based nanofibers for the facile assessment of catalyst morphological stability under harsh HCl oxidation reaction conditions. *Catal. Today* **2015**, *253*, 207−218.
(21) Epifani, M.; Andreu, T.; Abdollahzadeh-Ghom, S.; Arbiol, J.; Morante, J. R. Synthesis of Ceria-Zirconia Nanocrystals with Improved Microstructural Homogeneity and Oxygen Storage Capacity by Hydrolytic Sol-Gel Process in Coordinating Environment. *Adv. Funct. Mater.* **2012**, *22*, 2867−2875.
(22) Pfau, A.; Schierbaum, K. D. The electronic structure of stoichiometric and reduced CeO_2 surfaces: an XPS, UPS and HREELS study. *Surf. Sci.* **1994**, *321*, 71−80.
(23) Mullins, D. R.; Overbury, S. H.; Huntley, D. R. Electron spectroscopy of single crystal and polycrystalline cerium oxide surfaces. *Surf. Sci.* **1998**, *409*, 307−319.
(24) Henderson, M. A.; Perkins, C. L.; Engelhard, M. H.; Thevuthasan, S.; Peden, C. H. F. Redox properties of water on the oxidized and reduced surfaces of CeO_2(111). *Surf. Sci.* **2003**, *526*, 1−18.
(25) Kosacki, I.; Petrovsky, V.; Anderson, H. U.; Colomban, P. Raman Spectroscopy of Nanocrystalline Ceria and Zirconia Thin Films. *J. Am. Ceram. Soc.* **2002**, *85*, 2646−2650.
(26) Postole, G.; Chowdhury, B.; Karmakar, B.; Pinki, K.; Banerji, J.; Auroux, A. Knoevenagel condensation reaction over acid-base bifunctional nanocrystalline $Ce_xZr_{1-x}O_2$ solid solutions. *J. Catal.* **2010**, *269*, 110−121.
(27) Trovarelli, A.; Zamar, F.; Llorca, J.; Leitenburg, C. d.; Dolcetti, G.; Kiss, J. T. Nanophase Fluorite-Structured CeO_2-ZrO_2 Catalysts Prepared by High-Energy Mechanical Milling. *J. Catal.* **1997**, *169*, 490−502.
(28) Yao, H. C.; Yao, Y. F. Y. Ceria in automotive exhaust catalysts: I. Oxygen storage. *J. Catal.* **1984**, *86*, 254−265.
(29) Trovarelli, A.; Fornasiero, P. *Catalysis by Ceria and Related Materials*; Imperial College Press: London, 2013; Vol.2, 47−81.
(30) Damen, T. C.; Kiel, A.; Porto, S. P. S.; Singh, S. The Raman effects of $CeCl_3$ and $PrCl_3$. *Solid State Commun.* **1968**, *6*, 671−673.
(31) Suzuki Takehiko Ishii, S.; Sagawa, T. X-Ray Photoemission Spectra of 4d and 3d Electrons in Lanthanum- and Cerium-Halides. *J. Phys. Soc. Jpn.* **1974**, *37*, 1334−1340.
(32) Paparazzo, E.; Ingo, G. M.; Zacchetti, N. X ray induced reduction effects at CeO_2 surfaces: An X ray photoelectron spectroscopy study. *J. Vac. Sci. Technol., A* **1991**, *9*, 1416−1420.
(33) Ochoa, J. V.; Farci, E.; Cavani, F.; Sinisi, F.; Artiglia, L.; Agnoli, S.; Granozzi, G.; Paganini, M. C.; Malfatti, L. CeO_x/TiO_2 (Rutile) Nanocomposites for the Low Temperature Dehydrogenation of Ethanol to Acetaldehyde: A Diffuse Reflectance Infrared Fourier Transform Spectroscopy-Mass Spectrometry Study. *ACS Appl. Nano Mater.* **2019**, *2*, 3434−3443.
(34) Siegel, D. A.; Chueh, W. C.; El Gabaly, F.; McCarty, K. F.; de la Figuera, J.; Blanco-Rey, M. Determination of the surface structure of CeO_2(111) by low-energy electron diffraction. *J. Chem. Phys.* **2013**, *139*, 114703.
(35) Shi, Y.; Lee, S. C.; Monti, M.; Wang, C.; Feng, Z. A.; Nix, W. D.; Toney, M. F.; Sinclair, R.; Chueh, W. C. Growth of Highly Strained CeO_2 Ultrathin Films. *ACS Nano* **2016**, *10*, 9938−9947.
(36) Balaji Gopal, C.; García-Melchor, M.; Lee, S. C.; Shi, Y.; Shavorskiy, A.; Monti, M.; Guan, Z.; Sinclair, R.; Bluhm, H.; Vojvodic, A.; Chueh, W. C. Equilibrium oxygen storage capacity of ultrathin CeO_2-delta depends non-monotonically on large biaxial strain. *Nat. Commun.* **2017**, *8*, 15360.
(37) Yeste, M. P.; Hernández-Garrido, J. C.; Arias, D. C.; Blanco, G.; Rodríguez-Izquierdo, J. M.; Pintado, J. M.; Bernal, S.; Pérez-Omil, J. A.; Calvino, J. J. Rational design of nanostructured, noble metal free, ceria-zirconia catalysts with outstanding low temperature oxygen storage capacity. *J. Mater. Chem. A* **2013**, *1*, 4836−4844.
(38) Arias-Duque, C.; Bladt, E.; Muñoz, M. A.; Hernández-Garrido, J. C.; Cauqui, M. A.; Rodríguez-Izquierdo, J. M.; Blanco, G.; Bals, S.; Calvino, J. J.; Pérez-Omil, J. A.; Yeste, M. P. Improving the Redox Response Stability of Ceria-Zirconia Nanocatalysts under Harsh Temperature Conditions. *Chem. Mater.* **2017**, *29*, 9340−9350.

DOI: 10.1021/acscatal.9b03482
ACS Catal. 2019, 9, 10680−10693

4.3 Publication III: Reactivation of CeO_2-based Catalysts in the HCl Oxidation Reaction: In situ Quantification of the Degree of Chlorination and Kinetic Modeling

The experimental schedule was devised by H. Over and myself. I prepared the materials and conducted the experiments and wrote a first draft. F. Hess developed the reoxidation model and performed the theoretical analysis. I. Djerdj performed the Rietveld refinement. Z.Wang performed some of the activity experiments. T. Weber performed the XPS experiments and analysis. H. Over conceived the original idea and took the lead in writing the manuscript with contributions from myself, F. Hess, B. Smarsly and Y. Guo.

Reprinted with permission from Sun Y.; Hess F.; Djerdj I.; Wang Z.; Weber T.; Guo Y.; Smarsly B.M.; Over H. Reactivation of CeO_2-based Catalysts in the HCl Oxidation Reaction: In situ Quantification of the Degree of Chlorination and Kinetic Modeling. *ChemCatChem*. **2020**, 12, 5511-5522. DOI: doi.org/10.1002/cctc.202000907.

Chemistry Europe
European Chemical Societies Publishing

Reactivation of CeO_2-based Catalysts in the HCl Oxidation Reaction: *In situ* Quantification of the Degree of Chlorination and Kinetic Modeling

Yu Sun,[a, b] Franziska Hess,[c, d] Igor Djerdj,[e] Zheng Wang,[a, b] Tim Weber,[b, f] Yanglong Guo,*[a] Bernd M. Smarsly,*[b, f] and Herbert Over*[b, f]

Deactivation of CeO_2-based catalysts in the HCl oxidation reaction proceeds via selective bulk chlorination of the active CeO_2 component to form $CeCl_3 \times nH_2O$. We study the reactivation of two bulk-chlorinated CeO_2-based Deacon catalysts by oxygen treatment at 430 °C, namely pure CeO_2 and 20 mol% of CeO_2 supported on preformed ZrO_2 particles ($20CeO_2@ZrO_2$), with a dedicated experiment. In the flow reactor setup we determine *in-situ* the degree of chlorination of the catalyst by quantifying down-stream with in-situ UV-Vis spectroscopy the total amount of chlorine in the catalyst that is exchanged by reoxidation at 430 °C. The activity of deactivated $20CeO_2@ZrO_2$ can be fully restored by oxygen exposure at 430 °C, while that of pure CeO_2 declines steadily. Since the UV-Vis analytics is fast and sensitive, we can follow the kinetics of reoxidation. To rationalize the observed kinetics, we develop a modified Johnson-Mehl-Avrami-Kolmogorov (JMAK) model based on a nucleation-and-growth approach for the reoxidation of the catalyst starting from the chlorinated phase. The fast reoxidation kinetics of chlorinated $20CeO_2@ZrO_2$ is traced to a fast nucleation rate.

1. Introduction

Catalyst stability is a severe concern in heterogeneous catalysis[1] and many ways of catalyst deactivation have been reported in literature,[2] among which most studies have focused on sintering of the active component with the consequence of a reduction of the active surface area. However, there is a class of catalysts that undergoes chemical transformation under reaction conditions accompanied by a deterioration of catalytic performance. This kind of reaction-induced catalyst transformation is for instance encountered with the HCl oxidation reaction, the so-called Deacon process [Eq. (1)],[3,4] which is employed to recover chlorine from the omnipresent byproduct HCl in many industrial processes:

$$4HCl + O_2 \rightarrow 2H_2O + 2Cl_2; \quad \Delta_r H = -114\,kJ/mol \tag{1}$$

For the Deacon process, low stability of the catalyst has been an ongoing problem that had deferred its industrial commercialization by 130 years. For instance, the original catalyst CuO, invented by Deacon 1868, readily undergoes bulk chlorination towards $CuCl_2$. Since $CuCl_2$ is volatile at a reaction temperature above 400 °C, the catalyst is gradually lost during operation. Only in the year 2000 Sumitomo Chemical commercialized an active and stable Deacon catalyst based on RuO_2 that is supported on rutile TiO_2.[5]

Already very early, the catalyzed HCl oxidation over oxide surface was envisioned to be composed of a reduction step by HCl followed by a reoxidation step of the chlorinated oxide by

[a] Y. Sun, Z. Wang, Prof. Y. Guo
Key Laboratory for Advanced Materials
Research Institute of Industrial Catalysis
East China University of Science and Technology
Shanghai 200237 (P.R. China)
E-mail: ylguo@ecust.edu.cn
[b] Y. Sun, Z. Wang, T. Weber, Prof. B. M. Smarsly, Prof. H. Over
Physikalisch-Chemisches Institut
Justus Liebig Universität
Heinrich-Buff-Ring 17
35392 GießenGiessen (Germany)
E-mail: Bernd.Smarsly@phys.chemie.uni-giessen.de
Herbert.Over@phys.chemie.uni-giessen.de
[c] Prof. F. Hess
Institute of Physical Chemistry
RWTH Aachen
Landoltweg 2
52074 Aachen (Germany)
[d] Prof. F. Hess
Institut für Chemie
Technische Universitaet Berlin
Strasse des 17. Juni 124
10623 Berlin (Germany)
[e] Prof. I. Djerdj
Department of Chemistry
J. J. Strossmayer University of Osijek
Ulica cara Hadrijana 8/a
HR-31000 Osijek (Croatia)
[f] T. Weber, Prof. B. M. Smarsly, Prof. H. Over
Zentrum für Materialforschung
Justus Liebig Universität
Heinrich-Buff-Ring 16
35392 Giessen (Germany)

Supporting information for this article is available on the WWW under https://doi.org/10.1002/cctc.202000907

Chemistry Europe
European Chemical Societies Publishing

molecular oxygen.[6] For the commercialized RuO_2/rutile-TiO_2 catalyst these reduction and oxidation steps are not bulk transformations of the catalysts, but rather take place at the surface only.[7] However, for the case of CeO_2-based catalysts, a promising and viable alternative to RuO_2, it was recognized that they deactivate in the Deacon reaction through bulk chlorination,[8–12] although being partly reactivated with excess oxygen in the reaction feed at reaction temperatures of typically 430 °C.[8,13,14] Improved chemical stability against bulk chlorination is achieved by mixing CeO_2 with ZrO_2, either in the form of solid solutions[15,16] or as CeO_2 deposited on preformed ZrO_2 particles.[17,18] The degree of chlorination that is directly correlated to the deactivation of the catalyst can be quantified in-situ by prompt gamma activation analysis (PGAA),[13,19] but also ex-situ either by thermogravimetric analysis (TGA-MS)[8] or by quantitative X-ray diffraction (XRD: Rietveld refinement).[9,18]

Here, we report a dedicated experiment for quantifying the degree of chlorination of the CeO_2-based catalyst in the very same reactor with which also the catalytic Deacon tests are performed. With this unique experiment, we can readily follow *in-situ* the kinetics of its reactivation via reoxidation. We exemplify this method as a proof-of-principle experiment with two Deacon powder catalysts, one is pure CeO_2 and the other is 20 mol% CeO_2 supported on preformed ZrO_2 particles ($20CeO_2@ZrO_2$). It turns out that the activity of pure CeO_2 is not fully recovered after reoxidation of the previously bulk-chlorinated sample. However, the activity of $20CeO_2@ZrO_2$ is quantitatively recovered after the second reactivation cycle. In addition, the reoxidation of $20CeO_2@ZrO_2$ is much faster compared to that of pure CeO_2. In a phenomenological kinetic model based on a nucleation-and-growth approach, we can describe the faster reoxidation of the supported catalyst by a higher nucleation rate due to the support (ZrO_2) surface.

Experimental Section

Experimental Details

The Deacon reaction was conducted in a custom fixed-bed flow reactor.[20] The reactor comprises the gas supply, the quartz tube reactor, heated by a computer-controlled furnace, and UV/vis analytics (Ocean Optics USB4000 with a DH-2000-BAL light source) for chlorine quantification. The following gases were used in the reaction measurements: HCl (99.995%), O_2 (99.999%) and Ar (99.999%) from AirLiquide, and the flow rate of gases was controlled by digital mass flow controllers (MKS Instruments 1179B). Prior to feeding the gas mixture into the reactor, Ar was dried using a water absorption cartridge (ALPHAGAZTM purifier H_2O-free, AirLiquide). The absorbance at a wavelength of $\lambda_{max}=$ 329 nm (absorption maximum of chlorine) is proportional to the chlorine space time yield (STY) that is defined as the molar amount of product per time and mass catalyst.

Besides catalytic activity tests, the flow reactor with the UV-Vis analytics can be employed to quantify the degree of chlorination of the catalyst after Deacon reaction. In doing so we reoxidized the chlorinated catalysts by oxygen exposure and the replaced chlorine from the catalyst is quantified by UV-Vis spectroscopy. Since the sensitivity of the UV-Vis spectroscopy is high and the data acquisition is fast enough, this dechlorination process of the once (partly) chlorinated catalyst can be followed in-situ as a function of time. Iodometry is employed to calibrate the extinction in the UV-Vis signal to absolute Cl_2 concentrations. The detailed calibration steps are shown in **Section 1.3** of the Supporting Material.

The proposed method for quantifying the degree of catalyst chlorination is *in situ*. In particular, we developed a reliable measurement protocol that is summarized in Figure 1 with the total flow set to 15 cm^3 STPmin^{-1} (sccm) and the catalyst kept at 430 °C. Each reaction step is followed by a purging step with pure Ar to remove the weakly held species from the reactor walls until the baseline of the chlorine UV-Vis signal is stable. The Deacon reaction experiments is first carried out under so-called "mild" condition with the reaction feed $Ar:HCl:O_2 = 10.5:1.5:3$. After the catalytic activity has reached steady state, the activity in terms of space time yield (STY) can be determined. Subsequently pure Ar is purged and the deactivation experiment is performed under so-called "harsh" condition with a feed ratio of $Ar:HCl:O_2 = 9:4.5:1.5$. When the catalyst is fully deactivated due to in-depth chlorination, pure Ar is purged. To quantify the degree of chlorination, the deactivated CeO_2-based catalyst is exposed to 50 vol.% O_2 (balanced by argon) for 5 h at the reaction temperature until the deactivated catalyst is fully reoxidized. During reactivation, oxygen replaces chlorine in the catalyst, and the replaced chlorine can be quantified by UV-Vis spectroscopy. After completion of the reactivation step, the reactor is purged with Ar. This terminates the first deactivation/reactivation cycle. The deactivation/reactivation cycle is repeated twice in order to estimate the activity loss due to restoration.

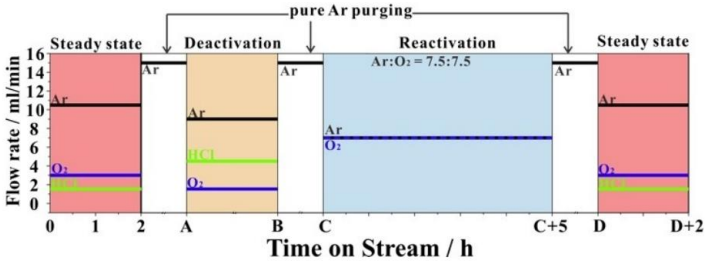

Figure 1. The measurement protocol (reaction feed composition) for determining the degree of chlorination of a CeO_2-based catalyst after full deactivation. The total flow rate is always 15 sccm and the catalyst is kept at 430 °C. Steady state activity experiments are performed before and after restoration (reactivation).

Chemistry Europe
European Chemical Societies Publishing

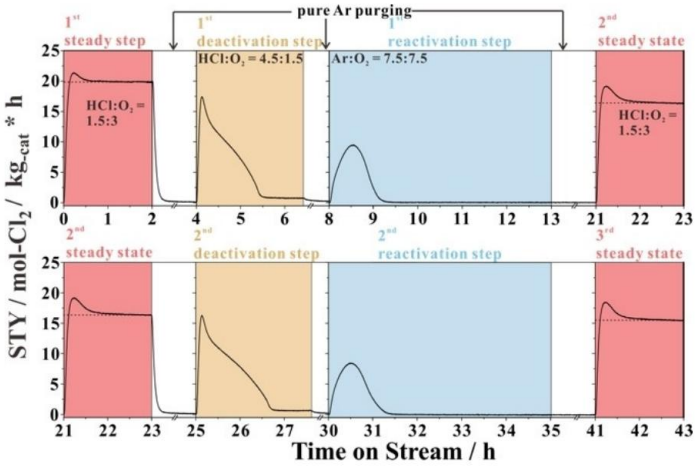

Figure 2. Chlorine evolution of pure CeO_2 under the HCl oxidation reaction at $T = 430\,°C$, total flow rate15 sccm, 26 mg catalyst as a function of time on stream under varying reaction conditions provided by the measurement protocol (cycle) of Figure 1. The cycle was carried out twice to compare the steady state activity (dashed red line) dependent on the restoration cycle.

Further details about catalyst preparation and the employed characterization methods can be found in the **Section 1** of the Supporting Material.

Computational Details

During the reactivation step described in **Experimental Details**, we monitor the reoxidation kinetics through the evolution of Cl_2 as a function of time. We employ a phenomenological approach to model the differences between the reoxidation kinetics of the samples. We first note that the measured Cl_2 signal during reoxidation released by the reaction [Eq. (2)].

$$CeCl_3 + O_2 \rightarrow CeO_2 + \frac{3}{2}Cl_2 \tag{2}$$

represents the derivative of the fraction of the transformed phase (CeO_2), denoted as ε, over time, t: $x_{Cl_2}(t) = \frac{d\varepsilon}{dt}$, i.e., the rate of the phase transformation. The fraction of transformed phase as a function time ε(t) can therefore be obtained by the numerical integral of the Cl_2 signal over time. All our reoxidation signals (e.g., the blue area in Figure 2) have a characteristic shape where the initial rate of transformation is zero, goes through a maximum and then gradually returns to zero. The integral of the Cl_2 signal over time is a sigmoidal function. This behavior suggests a self-accelerating process, which is typical for a nucleation and growth mechanism. Since the phase transformation requires the formation of nuclei of the new phase, the initial growth rate is zero if no nuclei have been formed previously.

The kinetics of such a phase transition can be described using the Johnson-Mehl-Avrami-Kolmogorov (JMAK) approach. The JMAK theory assumes that nucleation occurs randomly at a constant rate per sample volume. Nucleation in the JMAK theory can proceed either spontaneously from an oversaturated (or undercooled) vapor or aided by solid surfaces. As the existence of a supersaturated vapor is highly unlikely in a flow reactor, we assume that available surfaces of catalyst support (SiO_2 and ZrO_2) and untransformed materials (CeO_2, $CeCl_3$) serve as heterogeneous nucleation sites for CeO_2 during reoxidation. However, we note that the JMAK theory cannot distinguish between nucleation mechanisms, and different nucleation mechanisms will only be reflected in different nucleation rates. The nuclei then grow at a constant rate until the whole sample volume is transformed. The transformed dimensionless volume fraction $\varepsilon_B = \frac{V_B}{V_{tot}}$ of phase B (CeO_2) as a function of time can be expressed by the well-known Avrami equation [Eq. (3)].

$$\varepsilon_B(t) = 1 - e^{-k_{eff}\, t^{m+1}}, \tag{3}$$

where k_{eff} is an effective rate constant and m is the order of the growth process, with the integer values 1, 2, 3 corresponding to 1D, 2D and 3D growth.

As will be shown in Sections 3.1 and 3.2 our system does not fulfill some of the assumptions made in the derivation of the standard Avrami equation: (1) Our catalyst does not undergo a pure phase transition. Rather it is a phase transformation due to a chemical reaction of $CeCl_3$ with O_2. (2) The catalyst bed contains some untransformed oxide at the start of the reoxidation reaction, which means that the number of nuclei and the volume fraction of oxidized phase are not zero initially. (3) Our supported sample grows as a layer on top of ZrO_2, which contains approximately 25 % of the supported CeO_2 in $20CeO_2@ZrO_2$. The remaining 75 % form CeO_2 particles. The sample therefore must expose two different growth modes, possibly with different rates. (4) The detected Cl_2 signal represents the derivative of the transformed volume fraction with respect to time, $\frac{d\varepsilon_B}{dt}$. Therefore, we derive a modified JMAK model in the supporting material that accounts for these additional features, whose derivation is shown in detail in Section 2 of the supporting information. Denoting n_{nuc} as the number of nuclei, r as the radius and ε_{CeO_2} as the volume fraction of CeO_2, we finally arrive at three coupled differential equations [Eqs. (4)–(6)].

Chemistry Europe
European Chemical Societies Publishing

$$\frac{dn_{nuc}}{dt} = k_{nuc} \cdot p(O_2)(t), \tag{4}$$

$$\frac{dr}{dt} = k_{grow} \cdot p(O_2)(t), \tag{5}$$

$$\frac{d\varepsilon_{CeO_2}}{dt} = n_{nuc}(t) \cdot \left(1 - \varepsilon_{CeO_2}(t)\right) \cdot \left(\frac{1}{m\Gamma\left(\frac{m}{2}\right)} \cdot 2\,\pi^{\frac{m}{2}} \cdot r(t)^{m-1}\right). \tag{6}$$

Here t, k_{nuc} and k_{grow} represent time and the rate constants. The $\left(\frac{1}{m\Gamma\left(\frac{m}{2}\right)} \cdot 2\,\pi^{\frac{m}{2}} \cdot r(t)^{m-1}\right)$ term in Equation (6) describes the surface area of an m-dimensional sphere, where $\Gamma(z)$ is the gamma function (please see Section 2 in the Supporting Material for full details). Since the switching of gas in our reactor is not instantaneous, we approximate the time-dependence of the O_2 partial pressure with a sigmoid function to account for the transition between Ar and O_2 atmosphere [Eq. (7)]:

$$p(O_2)(t) = p_\infty(O_2) \cdot \frac{t_s \cdot t}{1 + |t_s \cdot t|}. \tag{7}$$

From the known relaxation behavior of our flow reactor we estimate that $t_s = 50\ h^{-1}$, which means that switching is complete after about 15 minutes. In our experimental protocol $p_\infty(O_2) = 0.5$ bar during the reoxidation step. The coupled differential equations are solved numerically and the parameters k_{nuc}, k_{grow} and m are fitted to the experimental reoxidation data as a single data set using a least-squares approach. We employ a squared residual $\bar{S}$ that is averaged over the four experiments [Eq. (8)]:

$$\bar{S} = \frac{\sum_{i=1}^{4} w_i S_i}{\sum_{i=1}^{4} w_i}, \tag{8}$$

where S_i and w_i are the squared residual and weight of experiment i.

The squared residual S_i is defined as the squared difference between the fitted signal $\hat{y}_{i,j}$ and measured signal $y_{i,j}$, summed over all data points j [Eq. (9)]:

$$S_i = \sum_j \left(\hat{y}_{i,j} - y_{i,j}\right)^2 \tag{9}$$

We thereby fit all experiments simultaneously, employing the same k_{grow} and m for both samples. We employ different k_{nuc} for the two samples. Altogether, four parameters are fitted to the experimental data.

2. Results and Discussion

2.1. Reactivation of the bulk-chlorinated CeO_2-based catalyst in the HCl oxidation reaction

We conduct two cycles of deactivation/reactivation for pure CeO_2 catalyst under the HCl oxidation reaction at T = 430 °C as summarized in Figure 2. Firstly, we measure the steady state activity of the CeO_2 catalyst under mild condition (Ar:HCl:O_2 = 10.5:1.5:3) with the STY being 20 $mol_{Cl2}\,kg_{cat}^{-1}\,h^{-1}$. After Ar purging, the catalyst is exposed to a harsh reaction mixture (Ar:HCl:O_2 = 9:4.5:1.5). During 1.5 h on stream, the STY of CeO_2 declines continuously and saturates finally at a residual activity that is likely due to hydrated $CeCl_3$.[11,18] In the next step, the deactivated CeO_2 catalyst is reactivated by the mixed atmosphere of O_2 and Ar (Ar:O_2 = 7.5:7.5). The broad chlorine peak is attributed to the chlorine signal that is formed by the oxidation of $CeCl_3 \times nH_2O$. This reactivation step takes about 1.4 h. With the assumed reaction of Equation (2), we can determine the chlorination degree, defined as $n(CeCl_3)/(n(CeCl_3) + n(CeO_2))$, of the deactivated CeO_2 sample: The integrated chlorine peak area is 6.7 $mol_{Cl2}\,kg_{cat}^{-1}$, combined with the catalyst amount of 26 mg and molar mass of 172.1 g/mol of CeO_2, that results in a chlorination degree of 75 ± 3% for the fully-deactivated CeO_2 catalyst.

Consistent with literature[13] CeO_2 is found to be not fully transformed to hydrated $CeCl_3$. Last, we measure again the steady state activity under mild reaction condition that turns out to be 16.4 $mol_{Cl2}\,kg_{cat}^{-1}\,h^{-1}$ and is hence 17% lower than that of the fresh one.

Subsequently, we repeat the deactivation/reactivation cycle. The pure CeO_2 catalyst under harsh reaction condition fully deactivates after 1.7 h on stream. The replaced chlorine amount of 6.3 $mol_{Cl2}\,kg_{cat}^{-1}$ translates to a chlorination degree of 68 ± 4%, which is slightly lower than after the first deactivation. The activity of the CeO_2 catalyst after the second reactivation is 15.4 $mol_{Cl2}\,kg_{cat}^{-1}\,h^{-1}$, that is 6% lower than after the first and 23% lower than the initial activity.

In summary, we observe that the deactivated CeO_2 catalyst can be restored by reoxidation with pure oxygen, but the steady state activity declines steadily after each restoration step. The decline in chlorination degree may be traced to the formation of larger CeO_2 particles as will be shown in the following section.

In Figure 3, we summarize the same deactivation/reactivation series and evaluation procedure for the $20CeO_2@ZrO_2$ catalyst. For the $20CeO_2@ZrO_2$ sample 20 mol% CeO_2 is coated on preformed ZrO_2 particles, forming a covering ultrathin CeO_2 layer (5 mol% and 1.6 ± 0.2 nm thick) together with adhering CeO_2 particles (15 mol%).[18] The activity of the fresh $20CeO_2@ZrO_2$ catalyst under mild condition is 20.2 $mol_{Cl2}\,kg_{cat}^{-1}\,h^{-1}$. When switching to harsh reaction conditions, the STY of $20CeO_2@ZrO_2$ drops until it has saturated after 7 h on stream with a residual activity that is likely due to ZrO_2 and $CeCl_3 \times nH_2O$. Next, the deactivated $20CeO_2@ZrO_2$ catalyst is fully recovered by exposure to O_2 at 430 °C. In this reactivation step, the reoxidation of $20CeO_2@ZrO_2$ is completed after 0.4 h and is hence substantially faster than the reoxidation of the pure CeO_2 catalyst. The integrated chlorine peak contains 2.3 $mol_{Cl2}\,kg_{cat}^{-1}$. Combined with the amount (30.3 mg) and molar mass (132.8 g/mol) of $20CeO_2@ZrO_2$, this implies a chlorination degree of 100% for fully deactivated $20CeO_2@ZrO_2$.

The activity of reactivated $20CeO_2@ZrO_2$ under mild condition is 18.5 $mol_{Cl2}\,kg_{cat}^{-1}\,h^{-1}$, 8% lower than that of the fresh

Chemistry Europe
European Chemical Societies Publishing

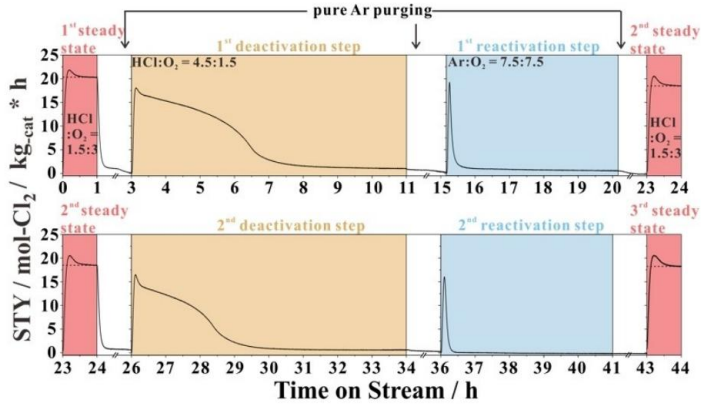

Figure 3. Chlorine evolution of $20CeO_2@ZrO_2$ under the HCl oxidation reaction at T = 430 °C, total flow rate15 sccm, 30 mg catalyst as a function of time on stream under varying reaction conditions provided by the measurement protocol (cycle) of Figure 1. The cycle was repeated twice to compare the steady state activity (dashed red line) dependent on the restoration cycle.

one. In the next deactivation/reactivation cycle, the chlorine peak area due to oxygen replacement contains 2 $mol_{Cl2}kg_{cat}^{-1}$, leading to a chlorination degree of 91 ± 2%. We finally evaluate the activity of $20CeO_2@ZrO_2$ after the second reactivation step to be 18.3 $mol_{Cl2}kg_{cat}^{-1}h^{-1}$ which is practically identical to that of $20CeO_2@ZrO_2$ catalyst after the first reactivation.

2.2. Characterization of the fresh, deactivated and reactivated CeO_2-based catalysts

The structures of the fresh, deactivated and reactivated CeO_2 and $20CeO_2@ZrO_2$ catalysts were thoroughly characterized by XRD (Figure 4a). The observed reflections of the fresh CeO_2 sample belong to the cubic fluorite structure (ICDD NO. 00–034-0394). The $CeCl_3 \times nH_2O$ reflections are detected for the deactivated CeO_2 sample, clearly evidencing bulk chlorination and thus explaining the rapid deactivation of the pure CeO_2 sample. As summarized in Table 2, Rietveld refinement of XRD data of deactivated CeO_2 sample shows that 76% of the pure CeO_2 sample is transformed to $CeCl_3 \times 7H_2O$. This result agrees remarkably well with the fraction of hydrated $CeCl_3$ determined from UV-Vis quantification of the dechlorination peak, providing 77% of $CeCl_3$ for the pure CeO_2 sample. Interestingly, the crystallite size of CeO_2 in the deactivated CeO_2 sample (19 nm) is larger than the initial crystallite size (10 nm). Our interpretation of these results from Rietveld refinement is that small CeO_2 particles are completely transformed to $CeCl_3 \times 7H_2O$ upon

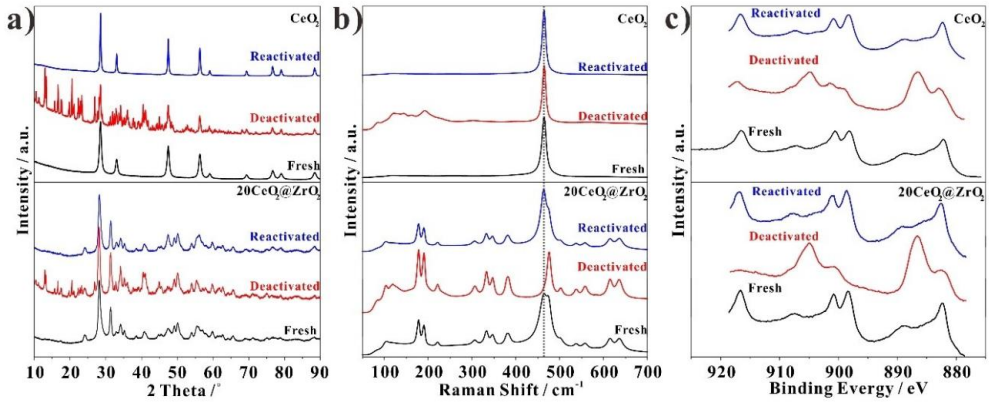

Figure 4. a) XRD patterns, **b)** Raman spectra and **c)** Ce 3d XPS of fresh (black), deactivated (red) and reactivated (blue) CeO_2 (top panel) and $20CeO_2@ZrO_2$ (bottom panel)

Chemistry Europe
European Chemical Societies Publishing

chlorination. Only larger particles remain partly as CeO_2 after chlorination, thus increasing the average size of CeO_2 crystallites. The XRD pattern of reactivated CeO_2 is attributed to a cubic fluorite structure. The width of the reflections of the reactivated sample (Figure 4a: top, blue) has visibly decreased compared to the fresh sample (Figure 4a: top, black). Consistently, we obtain an average crystallite size of around 25 nm for the reactivated CeO_2 sample, substantially larger than the fresh one (10 nm; Table 1). This increase in particle size explains the observed activity loss of the reactivated CeO_2 sample.

The XRD pattern of the fresh $20CeO_2@ZrO_2$ catalyst (Figure 4a: bottom) consists of a superposition of the cubic phase of CeO_2 (ICDD NO. 00–034-0394) and the monoclinic phase of ZrO_2 (ICDD NO. 00–036-0420). For the deactivated $20CeO_2@ZrO_2$ sample, the $CeCl_3 \times nH_2O$ concentration is determined to be 21 mol% in agreement with the nominal percentage of 20 mol% CeO_2 and therefore results in a degree of chlorination of 100%. The reactivated $20CeO_2@ZrO_2$ sample exhibits in XRD a superposition of the cubic phase of CeO_2 and of the monoclinic phase of ZrO_2 with a crystallite size of CeO_2 of around 7.8 nm (Table 1), slightly increased with respect to the fresh sample (6.5 nm, Table 1).

In Figure 4b we summarize the corresponding Raman experiments of fresh, deactivated and reactivated CeO_2 and $20CeO_2@ZrO_2$. The Raman spectrum of fresh CeO_2 is dominated by a strong band at 464 cm^{-1} that corresponds to the F_{2g} mode (Ce–O–Ce vibration) of the CeO_2 fluorite phase.[21,22] The Raman spectrum of deactivated CeO_2 exhibits an additional feature at 119 cm^{-1} that belongs to pure $CeCl_3 \times nH_2O$.[18] Therefore, Raman spectroscopy evidences bulk chlorination in agreement with the XRD results in Figure 4a. The reactivated sample shows only a strong Raman band at 464 cm^{-1}, thus indicating a complete transformation to the CeO_2 fluorite structure.

The double feature at 470 cm^{-1} of $20CeO_2@ZrO_2$ indicates the coexistence of CeO_2 (fluorite structure) and ZrO_2 (with monoclinic structure) (Figure 4b). The Raman spectrum of the deactivated $20CeO_2@ZrO_2$ also exhibits an additional feature at 119 cm^{-1}, while the CeO_2-related contribution at 464 cm^{-1} disappears. This is clear evidence that all the CeO_2 species have been transformed to hydrated $CeCl_3$ after harsh Deacon reaction. The Raman spectrum of the reactivated sample reveals a stronger ceria peak intensity than the fresh one, indicating that ceria particles have grown in size after the reactivation step fully consistent with XRD experiments in Figure 4a.

In Figure 4c, we compile X-ray photoemission (XP) spectra of fresh, deactivated and reactivated CeO_2 and $20CeO_2@ZrO_2$. Compared to the fresh CeO_2, the XP spectrum of the deactivated CeO_2 shows the superposition of $CeCl_3$, Ce_2O_3 and CeO_2 signals,[23,24] suggesting that the CeO_2 has not been fully chlorinated under harsh Deacon condition, which is compatible with the Rietveld refinement of the XRD data. From XPS the chlorination degree turned out to be 64% (Table 2); the detailed fitting of XP spectra can be found in Figure S3. The XPS of reactivated CeO_2 is practically identical to that of the fresh sample that is indicative of a full recovery of the catalyst.

Fresh $20CeO_2@ZrO_2$ exhibits a similar Ce 3d XP spectrum as the pure CeO_2, while that of the deactivated $20CeO_2@ZrO_2$ catalyst comprises only features of $CeCl_3 \times nH_2O$ consistent with the XRD quantification result. The Ce-3d spectrum of the reactivated sample is identical to the fresh one. However, the effective ceria concentration of the reactivated sample decreases from 53% to 41% (Table 2) which means that the ceria particles have partially agglomerated into larger adhering particles. Since XPS is surface-sensitive and the surface-to-volume ratio has decreased upon sintering, the Ce 3d signal intensity declines.

The TEM (Transmission electron microscopy) images and XEDS (X-ray energy dispersive spectroscopy) mappings of deactivated $20CeO_2@ZrO_2$ in Figures 5a, b indicate a uniform distribution of Ce (blue) and Cl (yellow) across the ZrO_2 particles (green). Together with the low catalytic activity of hydrated $CeCl_3$ (cf. Figure 3) we conclude that the hydrated $CeCl_3$ is highly dispersed over the ZrO_2 particles after chlorination. The TEM images of the reactivated sample (Figures 5c, d) reveal that both the adhering thin CeO_2 layer and the CeO_2 particle on ZrO_2 particle structures have been recovered after oxygen treatment at 430 °C. The TEM micrographs and the XEDS mappings look similar to those of the fresh sample (Figure S4), in accordance with the full recovery of the activity.

Table 1. Crystallite size and BET surface area of fresh, deactivated and reactivated CeO_2, $20CeO_2@ZrO_2$ catalysts. Catalytic activity of fresh and reactivated CeO_2, $20CeO_2@ZrO_2$ catalysts.

Samples	Crystalline Size [nm] [a]			Surface area [m^2/g] [b]	STY [mol-Cl_2/kg_{cat} h] [c]
	CeO_2	$CeCl_3 \times nH_2O$	ZrO_2		
CeO_2	10	n.a.	n.a.	46	20.0
Deactivated CeO_2	19	11($6H_2O$)/ 62($7H_2O$)	n.a.	–	
Reactivated CeO_2	25	n.a.	n.a.	26	16.4; 15.4[d]
$20CeO_2@ZrO_2$	6.5	n.a.	12	46	20.2
Deactivated $20CeO_2@ZrO_2$	–	39($7H_2O$)	12	–	
Reactivated $20CeO_2@ZrO_2$	7.8	n.a.	13	33	18.5; 18.3[d]

[a] Determined by Rietveld refinement. [b] Determined by BET method. [c] Determined by fixed-bed flow reactor. [d] STY after first and second reactivation.

Table 2. The concentration of CeO_2, $CeCl_3$ of fresh, deactivated and reactivated CeO_2, $20CeO_2@ZrO_2$ catalysts.

Samples	CeO_2 content [mol%] [a]	Chlorination degree [%]		Surface atomic concentration [b]	
		[a]	[b]	Ce/ (Ce + Zr)	Cl/ (Ce + Zr)
CeO_2	n.a.	n.a.	n.a.	100%	n.a.
Deactivated CeO_2	n.a.	76%	64%	100%	190%
Reactivated CeO_2	n.a.	n.a.	n.a.	100%	n.a.
$20CeO_2@ZrO_2$	16.4	n.a.	n.a.	53%	n.a.
Deactivate $20CeO_2@ZrO_2$	n.a.	100%	100%	31%	100%
Reactivated $20CeO_2@ZrO_2$	23	n.a.	n.a.	41%	n.a.

[a] Determined by Rietveld refinement. [b] determined by XPS.

Chemistry Europe
European Chemical Societies Publishing

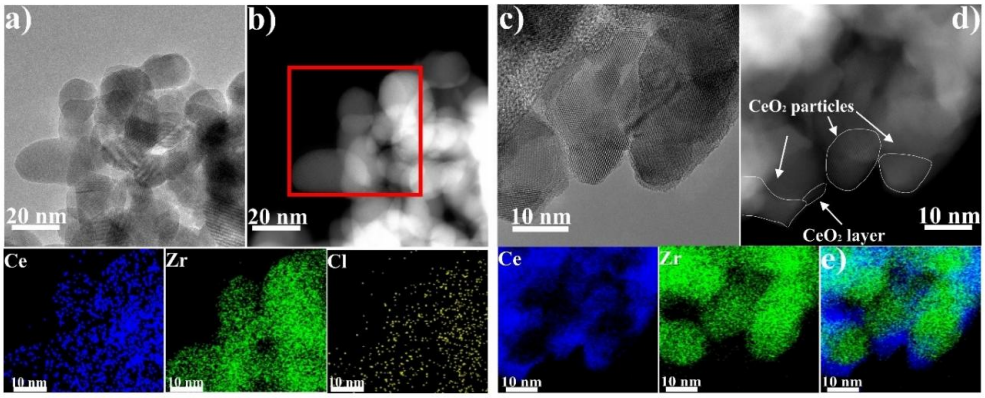

Figure 5. Aberration-Corrected High-Resolution TEM images of **a)** fully deactivated and **c)** reactivated $20CeO_2@ZrO_2$. HAADF-STEM images (High-angle annular dark-field imaging scanning transmission electron microscopy) of **b)** fully deactivated and **d)** reactivated $20CeO_2@ZrO_2$. **e)** XEDS maps of overlap of Ce (blue) and Zr (green) of fully reactivated $20CeO_2@ZrO_2$. XEDS maps show the distribution of Ce, Zr and Cl.

In order to demonstrate the high sensitivity of the present UV-Vis based reactor experiment we investigated the chlorination degree of stable CeO_2-based catalysts that have not suffered from bulk chlorination (cf. Figure 6). The integral chlorine intensities in the dechlorination peaks and the BET surface areas of CeO_2 and $20CeO_2@ZrO_2$ are practically identical (cf. Figure 6). This observation points to a similar chemical nature of the active phases. The amount of chlorine accommodated at the surface of the CeO_2 particle can be determined from these experiments. It turns out that the chlorination degree of pure CeO_2 is about 10%, while that of $20CeO_2@ZrO_2$ is 30%. The former value for pure CeO_2 agrees surprisingly well with the PGAA-derived value of about 10% reported in the literature.[13]

For the case of pure CeO_2 with a BET surface area of maximum 46 ± 2 m^2/g (Table 1: fresh sample, BET surface decreases slightly upon Deacon reaction) and 30 mg catalyst, the total surface area is 1.38 m^2. From surface science experiments we know that the density of surface chlorine on CeO_2(111) is at least 1Cl atom/1.38 nm^2 but not more than 2Cl atoms/1.38 nm^2.[25] The upper limit is therefore $1.46 \cdot 10^{17}$ surface Cl atoms that corresponds to a maximum degree of chlorination of 0.8%. From this estimation we conclude that the found degree of chlorination of 10% corresponds to much more chlorine at CeO_2 than just realized by adsorbed chlorine on the surface.

2.3. Kinetics of the reoxidation process

We show experimentally that the fully and partially chlorinated CeO_2 and $20CeO_2@ZrO_2$ catalysts can be reoxidized and therefore be reactivated by exposure to oxygen. We observe substantial differences between the studied catalysts regarding both the shape of the evolved chlorine signal, and the overall kinetics of the reoxidation process. The overall kinetics can be

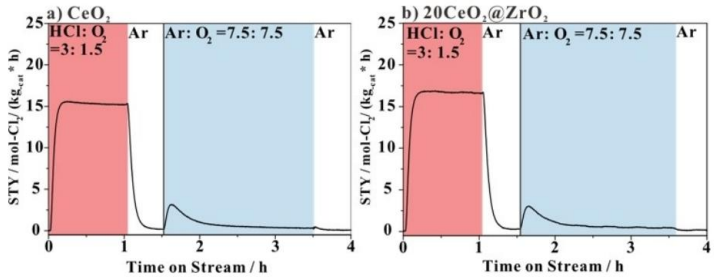

Figure 6. Chlorine evolution of a) pure CeO_2 and b) 20 mol% CeO_2 supported on ZrO_2 ($20CeO_2@ZrO_2$) under the HCl oxidation reaction at $T = 430\,^{\circ}C$, total flow rate15 sccm, 30 mg catalyst as a function of time on stream under varying reaction conditions: first the reaction mixture was $Ar:HCl:O_2 = 10.5:3:1.5$ and then it was switched to $Ar:HCl:O_2 = 7.5:0:7.5$.

Chemistry Europe
European Chemical Societies Publishing

described by the reaction half time $t_{1/2}$, at which half the material has reacted. For the pure CeO_2 sample we obtain a $t_{1/2}$ of 0.52 h and 0.55 h for the first and second reoxidation. For $20CeO_2@ZrO_2$ we obtain 0.12 h for both reoxidation experiments. Moreover, we observe different shapes of the evolved chlorine signal during the reoxidation of the two samples. We employ the phenomenological model described in Experimental Section for the modelling of the experimental data.

For the reoxidation of the supported catalyst $20CeO_2@ZrO_2$ we assume that most CeO_2 is formed in particle shape, and that the CeO_2 film supported on the ZrO_2 particles is negligible in a first approximation, since the reoxidation experiment measures the total Cl_2 evolved in the reoxidation of both the active film and the less active particle, and 75% of the CeO_2 assumes the form of particles in the fresh catalyst. However, we note that the highly dispersed CeO_2 film dominates the catalytic activity of $20CeO_2@ZrO_2$ in the HCl oxidation. We further assume that the growth of the CeO_2 particles in the pure CeO_2 and $20CeO_2@ZrO_2$ catalysts can be described by the same reaction order m and rate constant for growth k_{grow}. However, we expect nucleation to be different in the two samples, using two different parameters k_{nuc,CeO_2} and $k_{nuc,CeO_2@ZrO_2}$ that reflect the absence and presence of the ZrO_2 support. We therefore employ four parameters, m, k_{grow}, k_{nuc,CeO_2} and $k_{nuc,CeO_2@ZrO_2}$, to model all four reoxidation experiments of the completely chlorinated samples (Figures 2, 3).

Since the supported catalyst is expected to exhibit two different growth modes (layer and particle), but our model only describes one growth mode (particle), we expect larger deviations for the supported catalyst. In order to avoid meaningless fit results, we assign the $20CeO_2@ZrO_2$ catalyst a lower weight, which results in better fit of the CeO_2 reoxidation signal. The weights are 1 and 0.5 for the reoxidation of pure CeO_2 and $20CeO_2@ZrO_2$.

While we employ the same reaction order and rate constants to describe the growth both in the pure and supported catalysts, we realize that the samples differ in several ways; for instance, the pure CeO_2 catalyst is not completely oxidized, which possibly influences the reoxidation kinetics.

Our model takes into consideration the state of the deactivated sample through the boundary conditions $r(0)$ (particle radius) and $\varepsilon_{CeO_2}(0)$ (volume fraction of residual CeO_2). The boundary conditions for $r(0)$ and $\varepsilon_{CeO_2}(0)$ for the pure CeO_2 catalyst are chosen based on the experimental result that only 75% of the sample has been chlorinated, that is, $\varepsilon_{CeO_2}(0) = 0.25$. The starting radius of the nuclei is taken from the Rietveld refinement (19 nm). The boundary conditions for the second reoxidation experiment are obtained in similar fashion as listed in Table 3. For the $20CeO_2@ZrO_2$ catalyst, we observe that the first chlorination is complete, so both $\varepsilon_{CeO_2}(0)$ and $r(0)$ are zero. For the second reoxidation experiment, $\varepsilon_{CeO_2}(0) = 0.09$. We have no data on the residual CeO_2 particle radius, so that we chose $r(0) = 5$ nm, slightly smaller than the particle size after reoxidation (7.8 nm). We note that the model results are insensitive to the choice of the initial particle radius for $r(0) < 30$ nm due to the high growth rate obtained in the model fit.

Table 3. Boundary conditions and weights for the kinetic model as obtained from experimental catalyst characterization.

Sample	cycle	$\varepsilon_{CeO_2}(0)$	$r(0)$ [nm]	w
CeO_2	1st	0.24	19	1
CeO_2	2nd	0.32	19	1
$20CeO_2@ZrO_2$	1st	0	0	0.5
$20CeO_2@ZrO_2$	2nd	0.09	5	0.5

Table 4. Fitted parameters for the reoxidation model.

Parameter	Fitted value
m	1.01
k_{grow}	50.9 nm $(h\,bar)^{-1}$
k_{nuc,CeO_2}	5.89 $(h\,nm^3\,bar)^{-1}$
$k_{nuc,CeO_2@ZrO_2}$	192.9 $(h\,nm^3\,bar)^{-1}$

The parameters m, k_{grow}, k_{nuc,CeO_2} and $k_{nuc,CeO_2@ZrO_2}$ are fitted by minimizing $\bar{S}$ through recursive parameter sweeping. The fitting results are given in Table 4. The fitted chlorine signals are displayed as a function of time in Figure 7. The agreement between model and experiment is quite good for both reoxidation cycles of pure CeO_2 (Figure 7a), as well as for the second reoxidation cycle of the supported catalyst (Figure 7b). For the first reoxidation cycle we observe a higher signal intensity, as well as a slow decay of the signal that our model is unable to reproduce. However, our model can describe the overall rate and reaction half time of the reoxidation reaction quite well, resulting in a faster reoxidation of the supported catalyst compared to the pure catalyst. Since our model assumes that the CeO_2 growth rate (50.9 nm $(h\,bar)^{-1}$) is unaffected by the presence of ZrO_2, the difference in the reoxidation kinetics is traced to a nucleation rate in the supported catalyst (192.9 $(h\,nm^3\,bar)^{-1}$) that is a factor of 32 higher than in the pure CeO_2 catalyst (5.89 $(h\,nm^3\,bar)^{-1}$). While ZrO_2 itself is inert in the chlorination and reoxidation reaction, it can provide surface area where CeO_2 particles can nucleate, thereby accelerating the overall reoxidation reaction. Furthermore, we know from TEM imaging (Figure 5c, d) that the $CeCl_3$ particles are well-dispersed over the ZrO_2 surface, contributing to the high observed nucleation rate. While the overall nucleation rates seem similar, we emphasize that the resulting kinetics drastically differ for the two samples, which means that the experiment is highly sensitive to the nucleation rate. The high nucleation rate in the supported sample can be interpreted as the preference to form new CeO_2 particle presumably on the ZrO_2 surface over the growth of existing CeO_2 particles. This can possibly prevent the ripening of CeO_2 particles in successive reduction-oxidation cycles and can be relevant for the long-term stability of the catalyst.

3. Discussion

How does our approach compare with other methods for quantifying the degree of chlorination? So far, mostly Rietveld

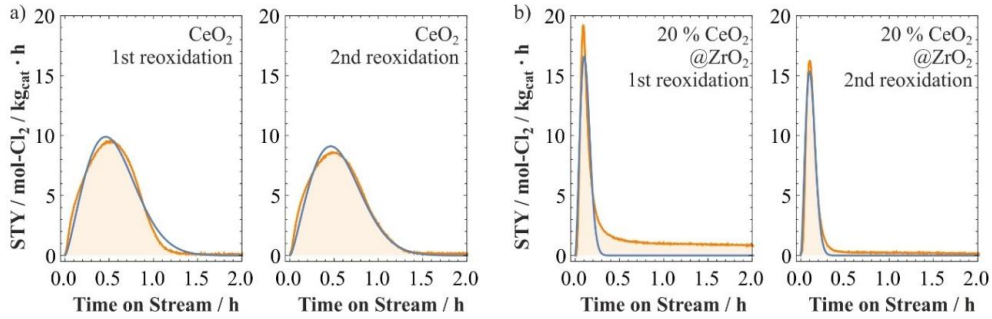

Figure 7. Modeled chlorine evolution curves during reoxidation (blue) employing the model described in Section 2.2 and the boundary conditions and fitted parameters in Tables 3 and 4. Experimentally measured curves are displayed in orange.

analyses of XRD data have been employed to quantify the bulk chlorination of CeO_2-based catalysts.[10,11] This method is only applicable if hydrated $CeCl_3$ is crystalline. Fortunately, this happens to be the case for fully deactivated CeO_2-samples, although the X-ray amorphous part is unknown. However, XRD is not applicable for determining the degree of chlorination of a stable catalyst. Here, X-ray photoemission spectroscopy (XPS) can estimate the degree of chlorination of a stable CeO_2-based catalyst, although this method is not quantitative. From previous XPS studies, there is evidence that the chlorination degree is higher than just a surface coverage of chlorine for pure CeO_2 would presume.[9] TGA together with mass spectrometry can be utilized for quantifying the degree of chlorination without relying on crystallinity of the chloride.[8] However, all three methods suffer from being ex-situ in that the chlorinated catalyst has to be removed from the reactor in order to quantify its degree of chlorination.

Prompt Gamma Activation Analysis (PGAA) is particularly useful for the quantification of the chlorination degree since it can work even under reaction conditions or at least *in situ* in the reactor. PGAA has mostly been employed for biological systems,[27] albeit it is not restricted to such systems. PGAA is quantitative and sensitive, but it requires a neutron source that rules out this method for standard analysis. Both Ce and Cl concentration can be determined separately and therefore the molar ratio Cl/Ce.[28] The uncertainties for quantifying the degree of chlorination are small so that even differences in chlorination degree of the catalysts of a few mol% as a function of the reaction mixture can be determined.[13] The drawback of PGAA is its relatively long data acquisition time (typically 1–2 h time) so that the kinetics of the reoxidation process during reactivation is not accessible.

The present *in situ* approach using UV-Vis detection in the Deacon reactor is fast and sensitive (ca. 1/10 monolayer), so that it is able to resolve the kinetics of the reoxidation step. Our approach is however not operando, since it requires a switch of the reaction mixture. Therefore, firm conclusions about the active phase cannot be drawn, although conclusions about the reactivation process of the catalysts are clear-cut.

It has been recognized that CeO_2-based catalysts deactivate in the Deacon reaction through bulk chlorination.[8,9,11] There is also clear evidence that stoichiometric CeOCl is catalytically not active at all.[14] Figure 8 summarizes the chlorination and oxidation of the pure (top) and supported catalysts (bottom) in a scheme. The deactivation of pure CeO_2 (top) leads to 70% chlorination, but the catalyst can be reactivated under reaction conditions with excess oxygen in the reaction feed at reaction temperatures of typically 430 °C.[8,13] Here we show that the restoration of bulk-chlorinated CeO_2 is almost quantitative. Through quantification of the reoxidation peak during the first reactivation cycle of deactivated CeO_2, we obtained a chlorination degree of 77%. A very similar value was determined by Rietveld refinement of XRD patterns for the deactivated CeO_2, namely 76%. The coexistence of hydrated $CeCl_3$ and CeO_2 in deactivated CeO_2 can equally be verified by the Raman spectroscopy and XPS. This finding can possibly be explained by $CeCl_3$ particles blocking the surfaces of CeO_2 as indicated in Figure 8 (top), thereby preventing further chlorination. Subsequently, we evaluated the catalytic activity of reactivated CeO_2 under the mild Deacon condition. The activity of reactivated CeO_2 is 17% lower than that of the fresh one. From XRD it is evident that the CeO_2 particles have significantly grown in size after reactivation. Particles with smaller initial size may have disappeared more quickly upon chlorination than larger particles as indicated in Figure 8. Upon reoxidation, the growth of residual oxide particles is kinetically favored over nucleation of new particles, consistent with the low nucleation rate obtained in fitting the experimental reoxidation kinetics. The increase of the CeO_2 particle size concomitant with a smaller active surface area could be the reason for the observed decline in the steady state activity of CeO_2. The quantification of the second reoxidation peak yields a chlorination degree of 72%. The decline of the chlorination degree compared to the first time (77%) is rationalized by the growth of larger CeO_2 particles that are less prone to be chlorinated. The catalytic activity of CeO_2 after the second reactivation is 6% lower than after the first reactivation. This finding suggests that the deactivation/

Chemistry Europe
European Chemical Societies Publishing

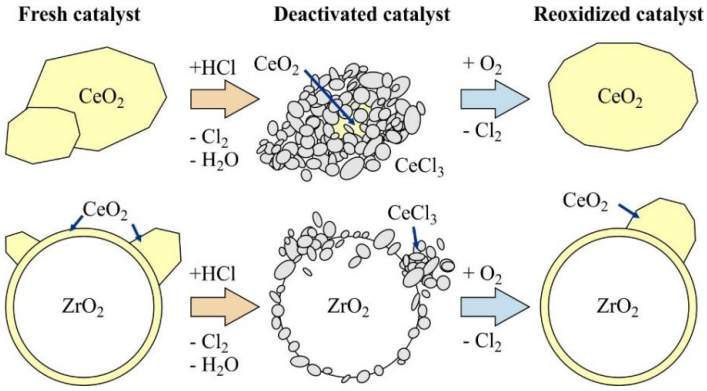

Figure 8. Scheme of chlorination and reoxidation and subsequent particle agglomeration for the pure CeO_2 catalyst (top) and the supported CeO_2@ZrO_2 catalyst (bottom).

reactivation process facilitates progressive sintering of the active component CeO_2.

So far, no reactivation experiments for 20CeO_2@ZrO_2 have been reported. From the first reoxidation Cl_2 peak of deactivated CeO_2 (Figure 3) we determine the chlorination degree of 20CeO_2@ZrO_2 to be 100%, i.e., all CeO_2 is transformed to hydrated $CeCl_3$, consistent with Rietveld refinement of corresponding XRD data. The Raman spectrum and XPS of deactivated 20CeO_2@ZrO_2 agree that the active ceria component in 20CeO_2@ZrO_2 is fully chlorinated. As observed in TEM images of the deactivated catalyst (Figures 5a, b), the $CeCl_3$ phase is dispersed over the ZrO_2 surface as indicated in Figure 8 (bottom). Moreover, the reactivation of 20CeO_2@ZrO_2 proceeds substantially faster than for pure CeO_2 due to the fine $CeCl_3$ dispersion and high nucleation rate of CeO_2 on the support surface. The activity of the 20CeO_2@ZrO_2 sample after the first reactivation is only 8% lower than that of the fresh one. From the XRD experiments we know that during the first cycle the attached CeO_2 particles grow in size (XRD) consistent with a stronger ceria peak intensity in the Raman spectrum. TEM reveals that the CeO_2 wetting layer is fully recovered after reactivation (Figure 5c, d) and takes over most of the catalytically active phase. After the second deactivation step, the chlorination degree is only 91%, which can be attributed to the increase of the CeO_2 particle size as also reconciled with the Rietveld refinement. After the second reactivation step the sample recovers 99% of its catalytic activity. Therefore, we infer that the activity of the 20CeO_2@ZrO_2 catalyst will be stable and not reduced after further "deactivation-reactivation" cycles.

In order to understand the restoration of the 20CeO_2@ZrO_2 morphology and the full recovery of the activity after reactivation, we presume that the formed $CeCl_3 \times nH_2O$ particles need to adhere to the ZrO_2 support with high dispersion. This presumption is confirmed by TEM images (cf. Figures 5c, d). When subsequently the deactivated 20CeO_2@ZrO_2 catalyst is exposed to oxygen, the adhering $CeCl_3 \times nH_2O$ layer transforms back to a thin covering layer of CeO_2 on ZrO_2 without significantly changing the morphology. The constraint of $CeCl_3 \times 6H_2O$ adhering to the ZrO_2 surface restricts the mass transport to surface diffusion on the ZrO_2 surface and keeps the active surface area of exposed CeO_2 constant after reactivation.

It is evident that reactivation for pure CeO_2 takes much longer than that for 20 mol% CeO_2 supported on ZrO_2 (cf. Figure 9). In addition, we observe different shapes of the Cl_2 signals during reoxidation. For a more quantitative description, we employ a phenomenological model based on the JMAK approach where a phase transformation is modeled by a nucleation and growth mechanism. In addition, we need to take into account the different starting conditions in the two samples. Fitting different parameters for the nucleation rates for pure CeO_2 and 20CeO_2@ZrO_2 results in a nucleation rate that is 32 times higher for 20CeO_2@ZrO_2. The result can be explained by the high initial dispersion of $CeCl_3$ and the inert ZrO_2 surface providing nucleation sites for the growth of CeO_2. While only 75% of the catalyst is chlorinated in the pure CeO_2 samples, the fitted nucleation rate is substantially lower, possibly indicating

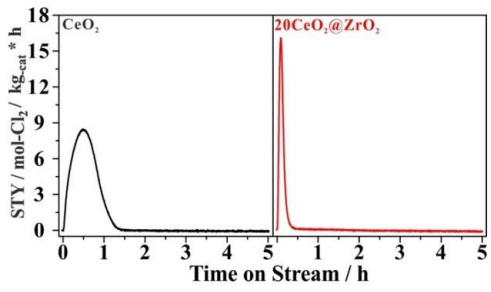

Figure 9. Time needed for reactivation of CeO_2 in comparison to that of 20CeO_2@ZrO_2 after the activity measurement of fully-deactivated state.

Chemistry Europe
European Chemical Societies Publishing

that the CeO_2 surface contributes less to nucleation. This assumption is consistent with the earlier conclusion that the surface of residual CeO_2 is entirely covered by $CeCl_3$ after chlorination (and thereby not available as a site for oxide nucleation), thereby suppressing complete chlorination.[11]

Finally, we raise the question why the CeO_2 layer on ZrO_2 is always restored during reoxidation. While higher stability of the CeO_2 film grown on ZrO_2 compared to CeO_2 particles may be one possible explanation for the reversible film restoration, we currently have no insight into the relative (thermodynamic) stabilities of the CeO_2 film on ZrO_2 versus CeO_2 bulk particles. However, our fitted nucleation rate constants suggest that nucleation appears to be faster when the ZrO_2 surface is exposed. The support surface may thereby aid in the redispersion of the catalyst upon reoxidation.

Our kinetic model for the reoxidation could be further refined by considering additional steps of the reaction and different nucleation sites and growth modes of the formed CeO_2 films and particles, for instance, in the form of a Kinetic Monte Carlo model;[29] however, we cannot meaningfully fit more parameters to the available data. More detailed models to obtain deeper understanding of catalyst degradation and reactivation needs extended experimental data sets under various reaction conditions or a first-principles-based approach.

The deactivation/reactivation cycle of CeO_2 based catalysts in the HCl oxidation reaction can be considered as a redox reaction where the reduction and oxidation step is separated (similar to an electrochemical reaction). Actually in this kind of Born-Haber cycle, chlorine can be produced within a cycle of solid state reactions: metal oxide is chlorinated first to form metal chloride (exothermic) and then in a separate chamber the metal chloride is reoxidized (endothermic) to release the desired product Cl_2 and to recover the metal oxide.[4,6] Therefore, we can ask ourselves how important is the chlorine release in the reoxidation of the CeO_2-based catalyst for the overall conversion of HCl. For the active and stable catalyst, there is only little chlorine at the surface. The replacement of this chlorine species by oxygen amounts only to about 20% of the reached rate under steady state Deacon conditions (cf. Figure 6). Therefore, this contribution is likely to be not relevant for the overall conversion, although it is important for the chemical nature of the catalytically active phase.

4. Conclusion

Pure CeO_2 and 20 mol% CeO_2 supported on preformed ZrO_2 particles ($20CeO_2@ZrO_2$) fully deactivate under harsh HCl oxidation conditions by the formation of Ce bulk chlorides. With an oxidative step in a pure oxygen atmosphere the deactivated catalysts can be reactivated by reoxidation and the replaced chlorine can be quantified in-situ by the UV-Vis analytics in the flow reactor. The catalytic activity of $20CeO_2@ZrO_2$ is completely recovered after the second deactivation/reactivation cycle, while the activity of pure CeO_2 after reactivation declines steadily. UV-Vis data acquisition is fast so that the kinetics of the reactivation step via the reoxidation can readily be followed and be used to model the solid-state reaction mechanism of the dechlorination reaction of hydrated $CeCl_3$ by oxygen. With a simple nucleation and growth model based on the JMAK approach, the different reoxidation kinetics of the two samples can be explained by high nucleation rate of CeO_2 on the ZrO_2 support surface. While the ZrO_2 surface is otherwise inert in the HCl oxidation reaction, it appears to provide sites for the nucleation of CeO_2 particles and keeps $CeCl_3$ particles in the chlorinated catalyst dispersed. The ZrO_2 support thereby aids in the redispersion of the catalyst during chlorination-dechlorination cycles. We conclude that the choice of catalyst support is crucial to prevent catalyst deactivation in non-steady-state operation.

The UV-Vis analytics is very sensitive so that even the chlorination degree of stable catalysts can be quantified with values that are in close agreement with those derived from PGAA experiments. The chlorination degree of stable catalysts is significantly higher than expected from a bare Cl overlayer with severe consequences for the reaction mechanism and hence for its theoretical modeling.

We propose that *in-situ* deactivation and reactivation experiments, coupled with an accurate quantification of the degree of transformation and theoretical modeling can be used to gain a detailed understanding of how the support alters the stability and activity of catalyst required to further improve catalyst-support combinations. In principle, this kind of in-situ experiments can be employed whenever the product or the educt is able to transform the chemical (bulk) composition of catalyst, thus opening the door for further experiments and scientific questions.[30]

Author contribution

Y. Sun prepared the materials and conducted the experiments and wrote a first draft. F. Hess developed the reoxidation model and performed the theoretical analysis. I. Djerdj performed the Rietveld analysis. T. Weber conducted the XPS experiments and analyzed the XPS data; Zhen Wang performed some of the activity experiments. H. Over conceived the original idea and took the lead in writing the manuscript with contributions from Y. Sun, F. Hess, and Bernd Smarsly.

Acknowledgements

This work was supported by the National Key Research and Development Program of China (2016YFC0204300), National Natural Science Foundation of China (21577035), Commission of Science and Technology of Shanghai Municipality (13521103402, 15DZ1205305) and 111 Project (B08021). Yu Sun gratefully acknowledge the China Scholarship Council for the Joint-Ph.D program between the Research Institute of Industrial Catalysis of East China University of Science and Technology and the Physical Chemistry Institute of Justus-Liebig-University Giessen. We acknowledge support from the Laboratory of Materials Research at the JLU. Franziska Hess acknowledges funding by Fond der

Chemischen Industrie in the form of a Liebig fellowship (Li 204/02). Open access funding enabled and organized by Projekt DEAL.

Conflict of Interest

The authors declare no conflict of interest.

Keywords: Deacon reaction · stability · reactivation · *in situ* experiment · Avrami modelling

[1] S. L. Scott, *ACS Catal.* **2018**, 8, 8597–8599.
[2] M. D. Argyle, C. H. Bartholomew, *Catalysts* **2015**, *5*, 145–269.
[3] J. Pérez-Ramírez, C. Mondelli, T. Schmidt, O. F. K. Schlüter, A. Wolf, L. Mleczko, T. Dreier, *Energy Environ. Sci.* **2011**, *4*, 4786–4799.
[4] H. Over, R. Schomäcker, *ACS Catal.* **2013**, *3*, 1034–1046.
[5] K. Seki, *Catal. Surv. Asia* **2010**, *14*, 168–175.
[6] M. W. M. Hisham, S. W. Benson, *J. Phys. Chem.* **1995**, *99*, 6194–6198.
[7] D. Crihan, M. Knapp, S. Zweidingey, E. Lundgren, C. J. Weststrate, J. N. Andersen, A. P. Seitsonen, H. Over, *Angew. Chem. Int. Ed.* **2008**, *47*, 2131–2134; *Angew. Chem.* **2008**, *120*, 2161–2164.
[8] A. P. Amrute, C. Mondelli, M. Moser, G. Novell-Leruth, N. López, D. Rosenthal, R. Farra, M. E. Schuster, D. Teschner, T. Schmidt, J. Pérez-Ramírez, *J. Catal.* **2012**, *286*, 287–297.
[9] C. Li, Y. Sun, I. Djerdj, P. Voepel, C. Sack, T. Weller, R. Ellinghaus, J. Sann, Y. Guo, B. M. Smarsly, H. Over, *ACS Catal.* **2017**, *7*, 6453–6463.
[10] C. Li, F. Hess, I. Djerdj, G. Chai, Y. Sun, Y. Guo, B. M. Smarsly, H. Over, *J. Catal.* **2018**, *357*, 257–262.
[11] C. Li, Y. Sun, F. Hess, I. Djerdj, J. Sann, P. Voepel, P. Cop, Y. Guo, B. M. Smarsly, H. Over, *Appl. Catal. B* **2018**, *239*, 628–635.
[12] R. Lin, A. P. Amrute, J. Pérez-Ramírez, *Chem. Rev.* **2017**, *117*, 4182–4247.
[13] R. Farra, M. Eichelbaum, R. Schlögl, L. Szentmiklósi, T. Schmidt, A. P. Amrute, C. Mondelli, J. Pérez-Ramírez, D. Teschner, *J. Catal.* **2013**, *297*, 119–127.
[14] Farra, F. Girgsdies, W. Frandsen, M. Hashagen, R. Schlögl, R. Teschner, *Catal. Lett.* **2013**, *143*, 1012–1017.
[15] S. Urban, N. Tarabanko, C. H. Kanzler, K. Zalewska-Wierzbicka, R. Ellinghaus, S. F. Rohrlack, L. Chen, P. J. Klar, B. M. Smarsly, H. Over, *Catal. Lett.* **2013**, *143*, 1362–1367.
[16] Y. Sun, C. Li, I. Djerdj, O. Khalid, P. Cop, J. Sann, T. Weber, S. Werner, K. Turke, Y. Guo, B. M. Smarsly, H. Over, *Catal. Sci. Technol.* **2019**, *9*, 2163–2172.
[17] M. Moser, C. Mondelli, T. Schmidt, F. Girgsdies, M. E. Schuster, R. Farra, L. Szentmiklósi, D. Teschner, J. Pérez-Ramírez, *Appl. Catal. B* **2013**, *132–133*, 123–131.
[18] Y. Sun, P. Cop, I. Djerdj, X. Guo, T. Weber, O. Khalid, Y. Guo, B. M. Smarsly, H. Over, *ACS Catal.* **2019**, *9*, 10680–10693.
[19] R. Farra, M. Garcia-Melchor, M. Eichelbaum, M. Hashagen, W. Frandsen, J. Allan, F. Girgsdies, L. Szentmiklosi, N. Lopez, *ACS Catal.* **2013**, *3*, 2256–2268.
[20] C. H. Kanzler, S. Urban, K. Zalewska-Wierzbicka, F. Hess, S. F. Rohrlack, C. Wessel, R. Ostermann, J. P. Hofmann, B. M. Smarsly, H. Over, *ChemCatChem* **2013**, *5*, 2621–2626.
[21] P. Fornasiero, G. Balducci, R. Di Monte, J. Kašpar, V. Sergo, G. Gubitosa, A. Ferrero, M. Graziani, *J. Catal.* **1996**, *164*, 173–183.
[22] Q. Xie, H. Zhang, J. Kang, J. Cheng, Q. Zhang, Y. Wang, *ACS Catal.* **2018**, *8*, 4902–4916.
[23] P. Burroughs, A. Hamnett, A. F. Orchard, G. Thornton, *J. Chem. Soc. Dalton Trans.* **1976**, *17*, 1686–1698.
[24] S. Suzuki Takehiko Ishii, T. Sagawa, *J. Phys. Soc. Jpn.* **1974**, *37*, 1334–1340.
[25] C. Sack, P. Lustemberg, V. Koller, V. Ganduglia-Priovano, H. Over, *J. Phys. Chem. C* **2018**, *122*, 19584–19592.
[26] J. W. Christian, *Formal Theory of Transformation Kinetics*, (Eds.: J. W. Christian), Pergamon, Oxford, **2002**, pp. 529–552.
[27] Zs. Révay, T. Belgya, L. Szentmiklósi, Z. Kis, A. Wootsch, D. Teschner, M. Swoboda, R. Schlögl, J. Borsodi, R. Zepernick, *Anal. Chem.* **2008**, *80*, 6066–6071.
[28] D. Teschner, R. Farra, L. Yao, R. Schlögl, H. Soertjanto, R. Schomäcker, T. Schmidt, L. Szentmiklósi, A. P. Amrute, C. Mondelli, J. Pérez-Ramírez, G. Novell-Leruth, N. López, *J. Catal.* **2012**, *285*, 273–284.
[29] V. P. Zhdanov, *Surf. Rev. Lett.* **2008**, *15*, 605–612.
[30] R. Schlögl, *Angew. Chem. Int. Ed.* **2015**, *54*, 3465–3520; *Angew. Chem.* **2015**, *127*, 3531–3589.

Manuscript received: May 29, 2020
Revised manuscript received: July 2, 2020
Accepted manuscript online: July 10, 2020
Version of record online: September 9, 2020

5. Appendix

5.1 Supporting Information of Publication I

Supporting Information

Oxygen Storage Capacity versus catalytic activity in the CO and HCl oxidation: A Case study of Ceria-Zirconia solid solution

Yu Sun[a,b], Chenwei Li[a,b], Igor Djerdj[c], Omeir Khalid[b], Pascal Cop[b], Joachim Sann, Tim Weber, Sebastian Werner[b], Kevin Turke[b], Yanglong Guo[a,*], Bernd M. Smarsly[b,*], Herbert Over[b,*]

a) Key Laboratory for Advanced Materials, Research Institute of Industrial Catalysis, School of Chemistry and Molecular Engineering, East China University of Science and Technology, Shanghai 200237, PR China
b) Physikalisch-Chemisches Institut, Justus Liebig Upniversity, Heinrich-Buff-Ring 17, 35392 Giessen, Germany
c) Department of Chemistry, J. J. Strossmayer University of Osijek, Ulica cara Hadrijana 8/a, HR-31000 Osijek, Croatia

* *Corresponding authors:* E-mail: herbert.over@phys.chemie.uni-giessen.de; Bernd.Smarsly@phys.Chemie.uni-giessen.de; ylguo@ecust.edu.cn

Table S1. The BET surface area of CZ080 with different reaction time. The reaction temperature during the reaction was 430 ℃ and the reaction condition: Ar: HCl: O_2 = 7:1:2. A total flow rate of 15sccm was applied. The mass of catalyst is 120mg.

Samples	BET Surface Area- Fresh/ m^2/g	Pore Volume / cm^3/g
CZ080	44	0.164
CZ080-0.5h	37	0.145
CZ080-2h	37	0.147
CZ080-4h	36	0.156
CZ080-8h	38	0.156
CZ080-24h	36	0.157

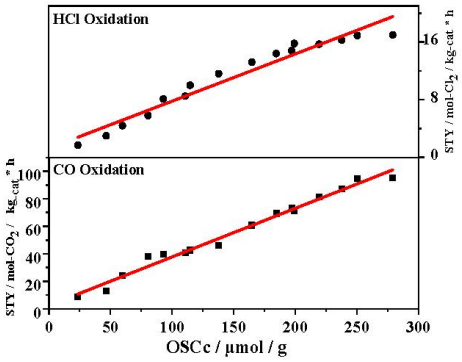

Figure S1: HCl oxidation activity of the as-prepared CZxxx samples (xxx = 0 -100) versus their respective plain and complete oxygen storage capacity (OSCc and OSC, respectively).

5.2 Supporting Information of Publication II

Supporting Information

Highly Active and Stable in the Catalytic HCl Oxidation Reaction: CeO_2 Wetting Layer on ZrO_2 Particle with Sharp Interface

*Yu Sun,[a,b] Pascal Cop,[b,c] Igor Djerdj,[d] Xiaohan Guo[a], Tim Weber,[b,c] Omeir Khalid,[b,c] Yanglong Guo,[*a] Bernd M. Smarsly,[*b,c] Herbert Over[*b,c]*

a) Key Laboratory for Advanced Materials, Research Institute of Industrial Catalysis, School of Chemistry and Molecular Engineering, East China University of Science and Technology, Shanghai 200237, PR China
b) Physikalisch-Chemisches Institut, Justus Liebig University, Heinrich-Buff-Ring 17, 35392 Giessen, Germany
c) Zentrum für Materialforschung, Justus Liebig University, Heinrich-Buff-Ring 16, 35392 Giessen, Germany
d) Department of Chemistry, J. J. Strossmayer University of Osijek, Ulica cara Hadrijana 8/a, HR-31000 Osijek, Croatia

* *Corresponding authors:* E-mail: herbert.over@phys.chemie.uni-giessen.de; Bernd.Smarsly@phys.Chemie.uni-giessen.de; ylguo@ecust.edu.cn

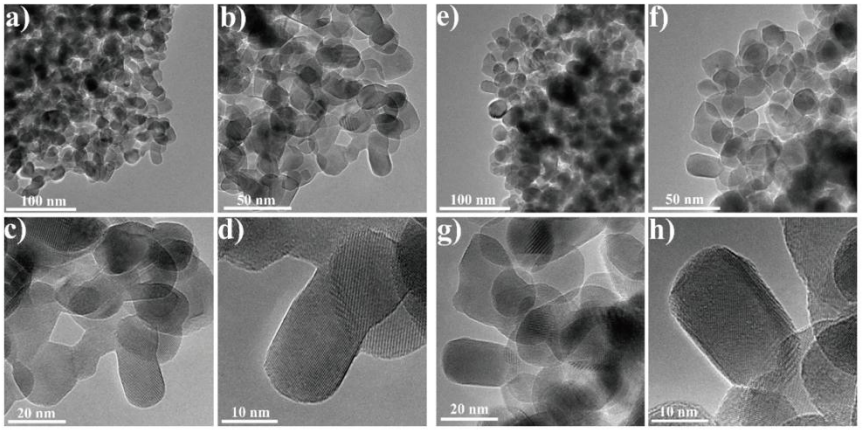

Figure S1: High-Resolution TEM images of ZrO_2 **a-d)** calcined at 600°C for 5 h and **e-h)** after the Deacon reaction at T=430 °C and Ar: HCl: O_2 = 9: 4.5: 1.5 (flow rate 15 sccm, 30 mg catalyst, 24 h on stream).

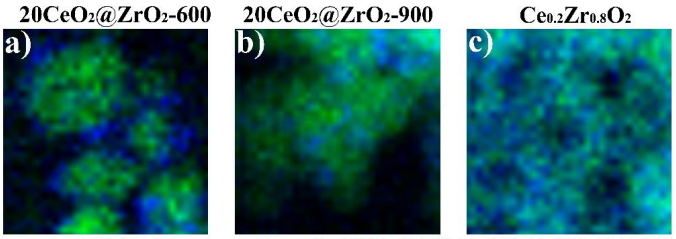

Figure S2: Comparing XEDS element mappings of **a)** $20CeO_2@ZrO_2$-600, **b)** $20CeO_2@ZrO_2$-900, **c)** solid solution $Ce_{0.2}Zr_{0.8}O_2$. Color code: green = Zr; blue = Ce.

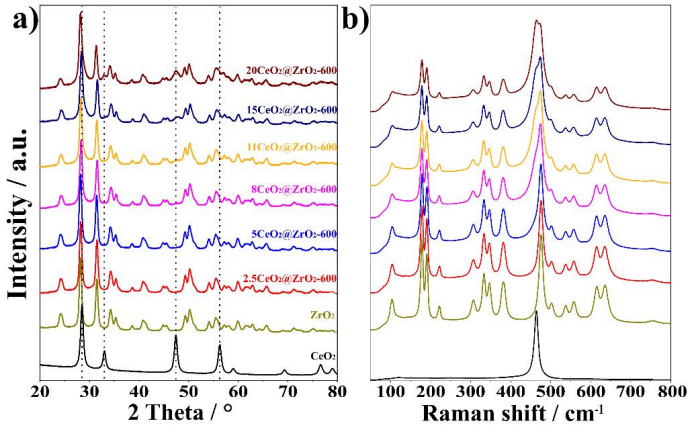

Figure S3: a) XRD patterns and **b)** Raman spectra of x $CeO_2@ZrO_2$-600 (x= 0, 2.5, 5, 8, 11, 15, 20).

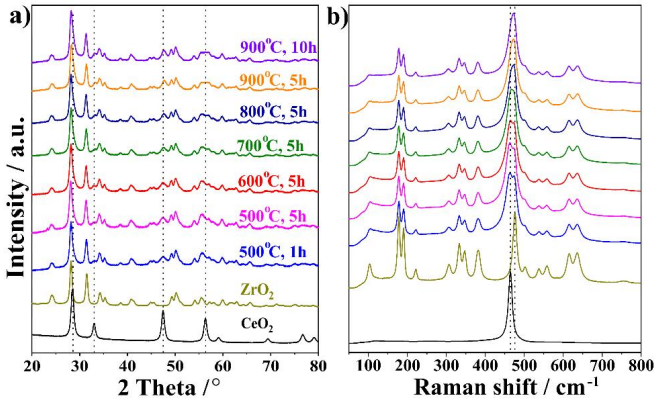

Figure S4: a) XRD patterns and **b)** Raman spectra of $20CeO_2@ZrO_2$ that was calcined to various temperatures and time periods.

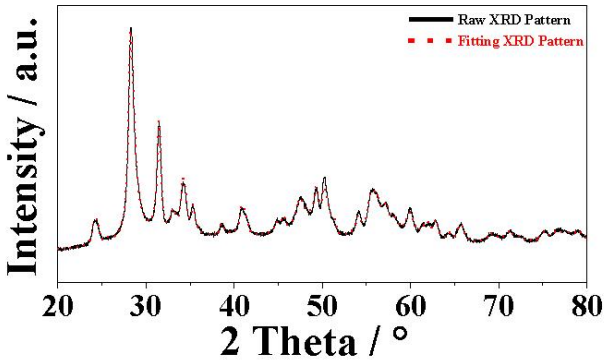

Figure S5: Quality of the Rietveld refinement of $20CeO_2@ZrO_2$-600: comparison of experimental and fitted XRD data.

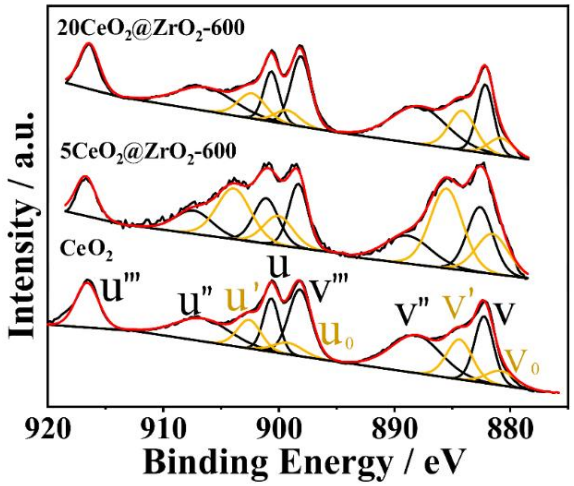

Figure S6: The Ce 3d XP spectra of fresh CeO_2, $5CeO_2@ZrO_2$-600 and $20CeO_2@ZrO_2$-600 samples including a deconvolution into Ce^{4+} and Ce^{3+}. The Ce^{4+} peaks are labelled by v, v'', v''', u, u'', u''' in black, while the Ce^{3+} peaks are labelled by v', v_0, u', u_0 in yellow.

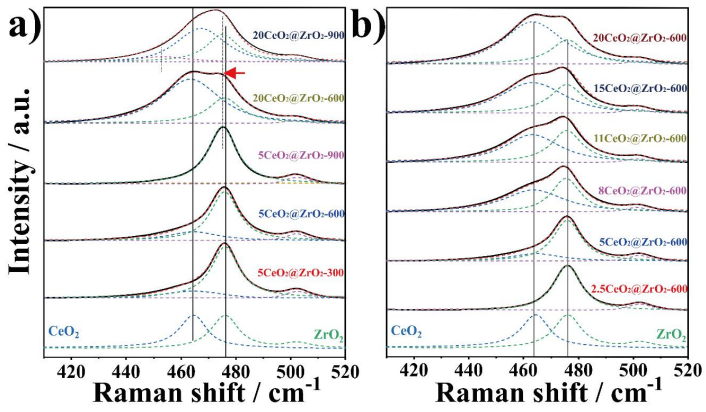

Figure S7: High resolution Raman spectra of **a)** $5CeO_2@ZrO_2$ and $20CeO_2@ZrO_2$ that were calcined to 300 °C, 600 °C and 900 °C for 5h. **b)** $xCeO_2@ZrO_2$-600 (x= 0, 2.5, 5, 8, 11, 15, 20). The pure spectra of CeO_2 and ZrO_2 are shown as blue and green dashed line, respectively. With these spectra the experimental Raman spectra of xCZ-600-5 were fitted by a superposition of the pure CeO_2- and ZrO_2-spectrum, keeping the peak position fixed, but varying the FWHM and the intensity. For the $20CeO_2@ZrO_2$-900, an additional Phonon band needs to be introduced at around 452 cm^{-1}.

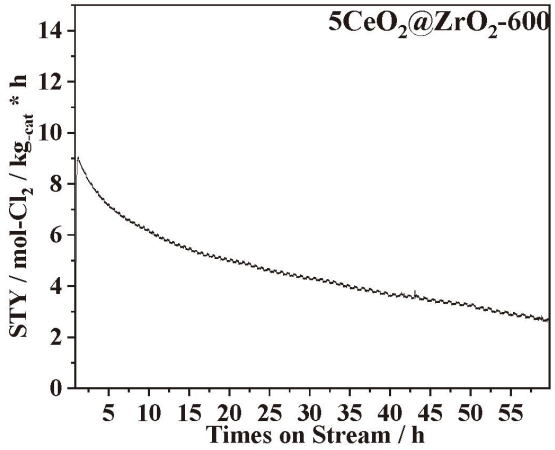

Figure S8: Deacon activity experiments of $5CeO_2@ZrO_2$-600 at T = 430°C (flow rate 15 sccm, 30 mg catalyst, 59 h on stream) for the reaction feed Ar:HCl:O_2 = 9: 4.5: 1.5.

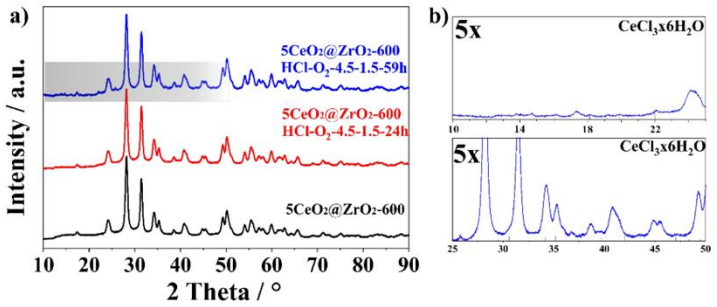

Figure S9: a) XRD patterns of Fresh and used $5CeO_2@ZrO_2$-600. **b)** The detail XRD patterns of $5CeO_2@ZrO_2$-600 after the Deacon reaction in Ar: HCl: O_2=9:4.5:1.5 for 59h.

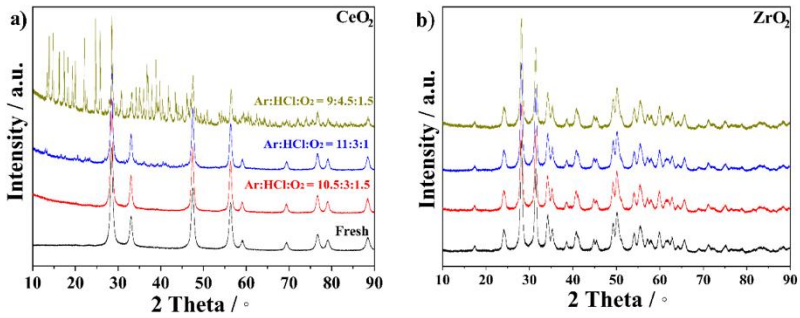

Figure S10: XRD patterns of pure CeO_2 **a)** and pure ZrO_2 **b)** before and after the Deacon reaction at T = 430 °C (flow rate 15 sccm, 30 mg catalyst, 24h on stream) for various mixtures of the reaction feed HCl: O_2 balanced by Ar.

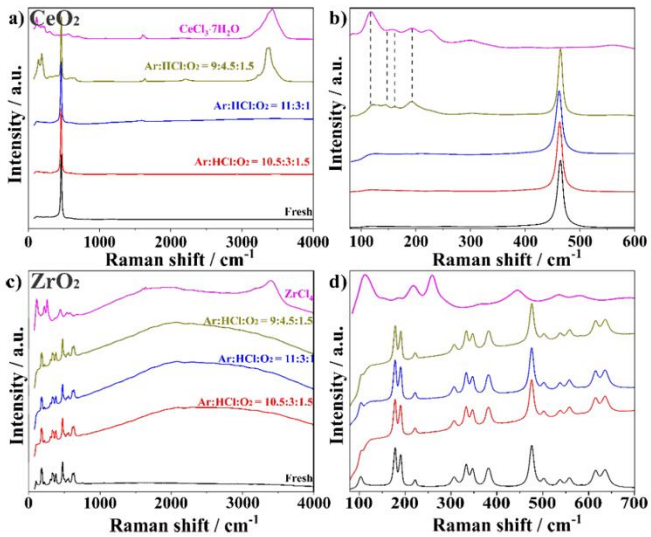

Figure S11: Raman spectra of pure CeO_2 **(a), (b)** and pure ZrO_2 **(c),(d)** before and after the Deacon reaction at T=430°C (flow rate 15 sccm, 30 mg catalyst, 24h on stream) for various mixtures of the reaction feed Ar: HCl: O_2.

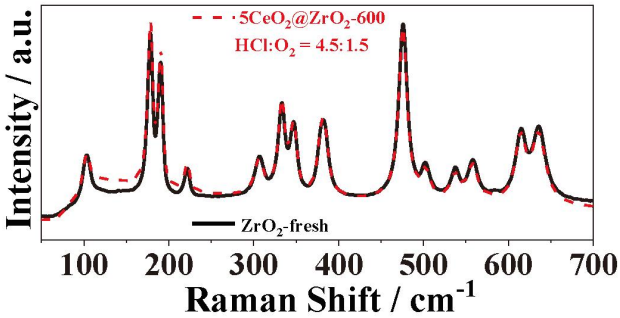

Figure S12: Raman spectra of fresh ZrO_2 and used $5CeO_2@ZrO_2$-600 after the Deacon reaction at T=430 °C (flow rate 15 sccm, 30 mg catalyst, 24 h on stream) under the condition of Ar: HCl: O_2 = 9: 4.5: 1.5.

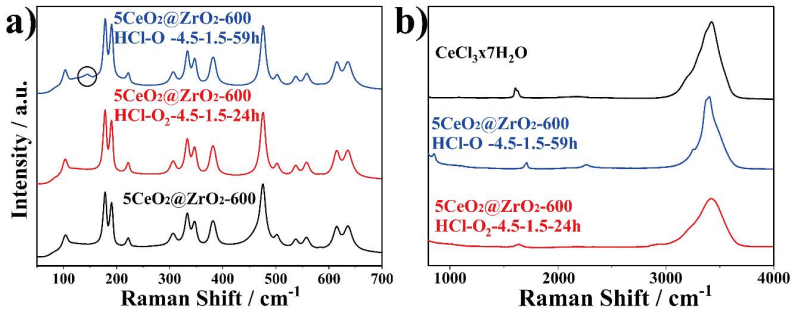

Figure S13: a) Raman spectra of Fresh $5CeO_2@ZrO_2$-600 and $5CeO_2@ZrO_2$-600 after the Deacon reaction in Ar: HCl: O_2=9: 4.5: 1.5 for 24h and 59h.

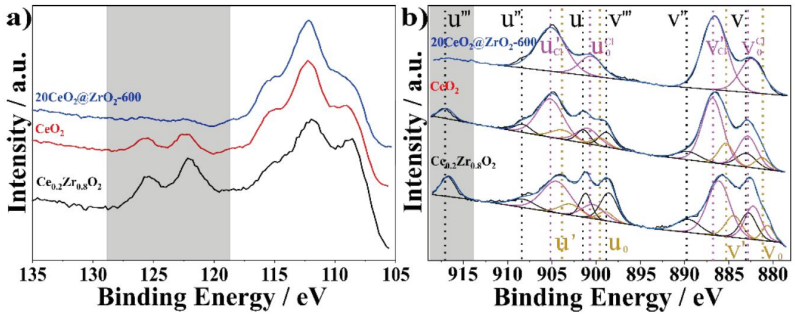

Figure S14: For various samples after the Deacon reaction at T=430°C (flow rate 15 sccm, 30 mg catalyst, 24 h on stream) for the reaction feed Ar: HCl: O_2=9: 4.5: 1.5: **a)** The Ce 4d XP spectra: the grey region is characteristic for Ce^{4+}. **b)** Ce 3d XP spectra. The Ce^{4+} peaks from CeO_2 are labelled by v, v'', v''', u, u'', u''' in black, while the Ce^{3+} peaks from CeO_2 are labelled by v', v_0, u', u_0 in yellow. The spectral features of Ce^{3+} in $CeCl_3$ are labelled by $v^{Cl}{}_0$, v'_{Cl}, $u^{Cl}{}_0$ and u'_{Cl} in magenta.

5.3 Supporting Information of Publication III

ChemCatChem

Supporting Information

Reactivation of CeO_2-based Catalysts in the HCl Oxidation Reaction: *In situ* Quantification of the Degree of Chlorination and Kinetic Modeling

Yu Sun, Franziska Hess, Igor Djerdj, Zheng Wang, Tim Weber, Yanglong Guo,* Bernd M. Smarsly,* and Herbert Over*

1. Experimental Details

1.1 Preparation of catalysts

The pure CeO_2 catalyst was prepared by the well-known ammonia precipitation method [1, 2]. Hydrogen peroxide was first dropped into the $Ce(NO_3)_3 \cdot 6H_2O$ solution to obtain a molar ratio of H_2O_2/Ce of 1.5. The precipitation of the ceria precursor was induced by dropping an ammonia solution into the solution, keeping the pH at around 9.5. The precipitate was stirred for 18h and then washed with deionized water several times until a pH value of around 7 was reached. The precipitate was dried overnight at 120 °C and finally calcined at 540 °C for 5h in order to ensure specific surface area at around 46 m^2/g.

The supported 20 mol% CeO_2 on ZrO_2 catalysts was prepared by the previously published incipient wetness impregnation method [3]. 1.09g of the $Ce(NO_3)_3 \cdot 6H_2O$ precursor was firstly mixed with 1.3ml H_2O. The ZrO_2 support (1.23 g) was subsequently mixed with the above $Ce(NO_3)_3 \cdot 6H_2O$ solution, followed by stirring for 18 h at room temperature. The mixture was then dried in air at 80 °C for 12h and calcined in air at 600 °C for 5h. The monoclinic ZrO_2 sample was purchased from Saint-Gobain NorPro in pelletized form (diameter = 3 mm, length = 4 mm). The ZrO_2 particles were crushed and subsequently dried in air at 160 °C for 2 h prior to impregnation. Nomenclature of the CeO_2@ZrO_2 samples: 20CeO_2@ZrO_2.

1.2 Characterization of catalysts

N_2 adsorption-desorption experiments were performed at 77 K with Autosorb 6 of Quantachrome. The samples were degassed in vacuum for 12h at 393 K before the measurement. The BET (Brunauer-Emmett-Teller) method was used to determine the specific surface area.

X-ray diffraction (XRD) measurements were conducted in Θ-2Θ geometry on a Panalytical X'Pert PRO diffractometer with a Cu Kα source (40 kV, 40 mA).

Rietveld analysis was carried out by using the FullProf program (Version 2.05).

Raman spectra were taken by using a Senterra Raman microscope (Bruker) with a 532 nm laser as the excitation source. All samples were measured at 50x magnification with a spectral resolution of 3-5 cm^{-1}, 250 co-additions, and 3 seconds integration time. The Raman spectra were recorded in backscattering geometry at room temperature and processed with OPUS 7.5 software.

Aberration-Corrected High Resolution STEM images were acquired using a Titan Themis G2 microscope operated at 300 kV. XEDS measurements with a resolution at the nanometre scale were performed using an Oxford X-Max^N 100TLE instrument.

The concentration of Zr and Ce in the near-surface region of the catalyst was quantified by X-ray photoemission spectroscopy (XPS) (PHI VersaProbe II). The photon energy was 1486.6 eV (monochromatized Al-K_α line), the X-ray spot size was ~100 µm × 1.3 mm with an excitation power of ~80-95 W. Charging of the sample was compensated by a flow of slow electrons with energies of about 1 eV and Ar^+ ions of about 10 eV. For overview spectra the pass energy was set to 187.85 eV, while detail spectra were taken with a pass energy of 23.5 eV. The energy step size was 0.1 eV in case of the O 1s and C 1s spectra, for all other spectra the energy step size was 0.2 eV. The chamber pressure during the experiment was ~10^{-6} Pa and all spectra were taken at room temperature and energy-corrected by the C1s hydrocarbon signal at 284.8 eV.

The XPS spectra were analyzed with CasaXPS Version 2.3.17. In order to maintain similar kinetic energies of photoelectrons of Ce and Zr, we chose the Ce4d and Zr3d spectra to quantify the relative Ce surface concentration with respect to the total concentration of Zr+Ce. For the deconvolution of the spectra, we followed the same procedure first suggested by Burroughs et al. [4] and later refined by Romeo et al. [5] and Li et al.[6], with five peaks labeled v, v_0,

v′, v″ and v‴ for the $3d_{5/2}$ and another five peaks labeled u, u_0, u′, u″, and u‴ for the spin-orbit split $3d_{3/2}$. We used Gaussian/Lorentzian peak shapes (GL(30)) to fit the peaks and employed a linear background by splitting the Ce 3d region into 3 sections (v_0 to v″, v‴ to u″, and u‴). We constrained the area ratios of the 5/2 and 3/2 species to 3:2. The spin-orbit-splitting of the lines was constrained to a minimum of 18 eV and a maximum of 18.5 eV.

1.3 The correlation principle between UV-Vis and STY, and the corresponding calibration step of UV-Vis

1.3.1 The correlation principle between UV-Vis and STY

The Lambert-Beer law is employed to correlate the UV-Vis signal with STY, and the UV-Vis signal is also counter-checked by iodometry. The water is removed by a condenser before the gas enters the UV cell so that we can safely ignore the effect of water condensation in the UV cell.

The Absorbance or Extinction; $\mathrm{A/Extinction} = -log_e \frac{\mathrm{I(t)}}{\mathrm{I0}}$ = ε*l*c *Eq.1*

ε = absorptivity of Cl_2 (*constant value* and taken from NIST data bank and counterchecked by iodometry by integrating the absorbance over the time period t_1 to t_2)

l = the path lengths through Cl_2 in the cell (*fixed value*)

c = concentration of Cl_2

$$\int_{t1}^{t2}(Extinction) * dt = \varepsilon * \mathrm{l} \int_{t1}^{t2} c * dt \quad \textit{Eq.2}$$

$\int_{t1}^{t2}(Extinction) * dt$ can be calculated from the UV-Vis spectra (the area is shown in **Figure S1**).

$$(\int_{t1}^{t2} c * dt) = \int_{t1}^{t2} \frac{Cl2\ outcome}{gas\ flow} dt = \frac{1}{gas\ flow} \int_{t1}^{t2} Cl2\ outcom * dt \quad \textit{Eq.3}$$

The amount of Cl_2 produced between t_1 and t_2 can be derived from iodometry. Thus, we can get the value of the constant $\varepsilon * \mathrm{l}$. STY is derived from the molar

concentration c of Cl_2, the volumetric flow rate v, and the mass of the catalyst m_{cat} according to $STY=cv/m_{cat}$.

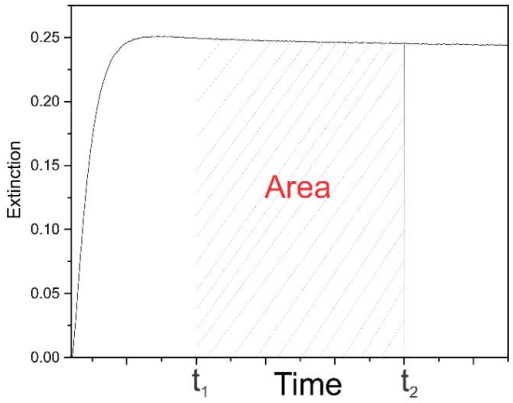

Figure S1. The extinction value as a function of time on stream.

1.3.2 The corresponding calibration step of UV-Vis

As mentioned in the above section, the **ε*l** is a constant value. Therefore, the main purpose of calibration experiment is the quantification of this parameter. The calibration steps are as follows. The $20CeO_2@ZrO_2$ was firstly selected as a model catalyst to perform the calibration experiment. Then the activity of $20CeO_2@ZrO_2$ catalyst was measured under two different mild conditions at 430 °C included Ar: HCl: O_2 = 10.5: 1.5: 3 and Ar: HCl: O_2 = 11: 3: 1 (cf. **Figure S2**) with stable extinction values are 0.21 and 0.13 respectively. Meanwhile, the product Cl_2 has been absorbed by the excess KI solution; the total time of absorbed Cl_2 is 20 minutes. The amount of Cl_2 can be quantified by iodometry using the reaction equations (5) and (6) and quantifying the amount of consumed $Na_2S_2O_3$ (6):

$$I^- + 2KI + Cl_2 = 2KCl + I_3^- \quad Eq.4$$

$$I_3^- + 2Na_2S_2O_3 = 2NaI + Na_2S_4O_6 + I^- \quad Eq.5$$

$$n(Na_2S_2O_3) = ½ * n(Cl_2) \quad Eq.6$$

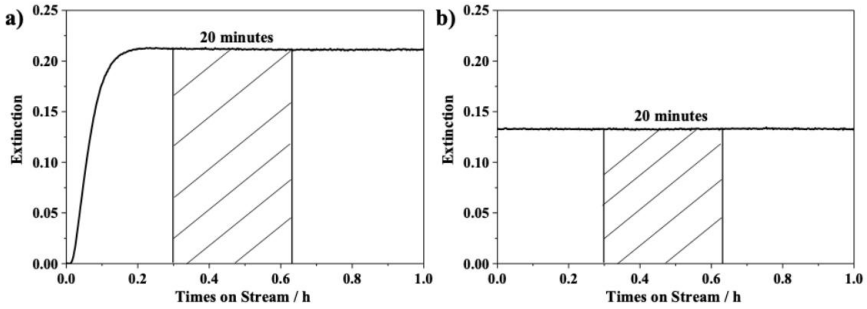

Figure S2. The extinction value as a function of time on stream at 430 °C under different reaction conditions: **a)** Ar: HCl: O_2 = 10.5: 1.5: 3, **b)** Ar: HCl: O_2 = 11: 3: 1.

The correlation between STY and extinction is given by **Eq. 7** with STY being the space time of yield and *m* the amount of the catalyst.

$$STY = 2.7273*Extinction*0.001/m \quad Eq.7$$

2. Derivation of the modified JMAK model

As shown in **Sections 3.1** and **3.2** in the main text our system does not fulfill some of the assumptions made in the derivation of the standard Avrami equation: (1) Our catalyst does not undergo a pure phase transformation. Rather it is a phase transformation following a chemical reaction with O_2. (2) The catalyst bed at the start of the reaction contains some untransformed oxide, which means that the number of nuclei and the volume fraction of oxidized phase are not zero at the start of reaction. (3) Our supported sample grows as a layer on top of ZrO_2, which contains approximately 25% of the supported CeO_2 in $20CeO_2@ZrO_2$. The remaining 75% form CeO_2 particles. The sample therefore must expose two different growth modes, possibly with different rates. (4) The detected Cl_2 signal represents the derivative of the transformed volume fraction with respect to time. We derive a modified JMAK model that accounts for the four features.

The derivation is shown in **Section 2** in the supporting material. We obtain two coupled differential equations.

We derive a modified JMAK model that accounts for the three features. Following the derivation of the Avrami equation, we assume a constant formation rate k_{nuc} of nuclei that is first order in $p(O_2)$, with n_{nuc} indicating the number of nuclei per sample volume (mol/m^3):

$$\frac{dn_{nuc}}{dt} = k_{nuc} \cdot p(O_2)(t) \qquad \textit{Eq. 8}$$

The radius r of a formed particle is assumed to grow at a constant rate k_{grow}. The growth is again first order in $p(O_2)$:

$$\frac{dr}{dt} = k_{grow} \cdot p(O_2)(t) \qquad \textit{Eq. 9}$$

The growth of the volume fraction of the CeO_2 phase depends on the dimensionality m of the growth. For instance, for spherical (3D, *m* = 3) particles, the growth is described as a 3rd order process with respect to the particle radius:

$$\left(\frac{d\varepsilon_{CeO_2}}{dt}\right)_{CeO_2} = n_{nuc}(t) \cdot \left(1 - \varepsilon_{CeO_2}(t)\right) \cdot \frac{4}{3}\pi r(t)^2 \qquad \textit{Eq. 10}$$

If all boundary conditions are assumed as zero and $p(O_2)$ is considered as a constant in time, the solution of this differential equation is the well-known Avrami equation with an additional $p(O_2)$ term. For instance, for m = 3:

$$\varepsilon_B(t) = 1 - e^{-k_{eff}\, t^4} \qquad \textit{Eq. 11}$$

$$k_{eff} = \frac{\pi}{3} k_{nuc} k_{grow}^3\, p(O_2)^3 \qquad \textit{Eq. 12}$$

More generally, employing the dimension of growth, *m*, as a parameter, the volume growth as a function of the radius can be expressed for integer and non-integer values of *m* as

$$\left(\frac{d\varepsilon_{CeO_2}}{dt}\right)_{CeO_2} = n_{nuc}(t) \cdot \left(1 - \varepsilon_{CeO_2}(t)\right) \cdot \left(\frac{1}{m \cdot \Gamma\left(\frac{m}{2}\right)} \cdot 2\, \pi^{\frac{m}{2}} \cdot r(t)^{m-1}\right) \qquad \textit{Eq. 13}$$

The term $\frac{1}{m \cdot \Gamma\left(\frac{m}{2}\right)} \cdot 2\,\pi^{\frac{m}{2}} \cdot r(t)^{m-1}$ generally describes the surface of an m-dimensional sphere, where $\Gamma(z)$ is the Gamma function obtained as the solution of the improper integral:

$$\Gamma(z) \approx \int_0^\infty u^{z-1} e^{-z} dz. \qquad \textit{Eq. 14}$$

Our numerical solver employs accurately computed values of the gamma function.

With $p(O_2)$ a constant in time, one can still obtain an algebraic solution to the equation, even if boundary conditions are not zero. For instance, for three-dimensional growth:

$$\varepsilon_{CeO_2}(t) = 1 - (1 - \varepsilon_0) e^{\frac{k_n \pi}{3\, k_g\, p(O_2)} \left(r_0^4 - (r_0 + k_g\, p(O_2)\, t)^4\right)} \qquad \textit{Eq. 15}$$

We may neglect the influence of $p(O_2)$ in the kinetics as a first approximation because all our experiments were conducted at the same oxidizing gas feed of Ar: O_2 = 7.5: 7.5. However, since the gas feed switching is not instantaneous, deviations close to t = 0 may arise which could be accounted for by describing $p(O_2)(t)$ as a sigmoid function rather than a constant:

$$p(O_2)(t) = p_\infty(O_2) \cdot \frac{t_s \cdot t}{1 + |t_s \cdot t|}, \qquad \textit{Eq. 16}$$

where t_s indicates the steepness of the sigmoid function and $p_\infty(O_2)$ the target $p(O_2)$ set at the instrument. With this time dependency of $p(O_2)$, **Eq. 13** cannot be solved symbolically. Instead, a numerical solver is employed.

The parameters k_{nuc}, k_{grow} and m are fitted using the model described by the coupled differential equations **Eq. 9** and **Eq. 10** and the sigmoid dependency of $p(O_2)(t)$ in **Eq. 16** to the experimental reoxidation data as a single data set using a least-squares approach employing a squared residual S that is averaged over the four experiments:

$$\bar{S} = \frac{\sum_{i=1}^{4} w_i S_i}{\sum_{i=1}^{4} w_i}, \qquad \textit{Eq. 1}$$

Where S_i and w_i are the squared residual and weight of experiment *i*.

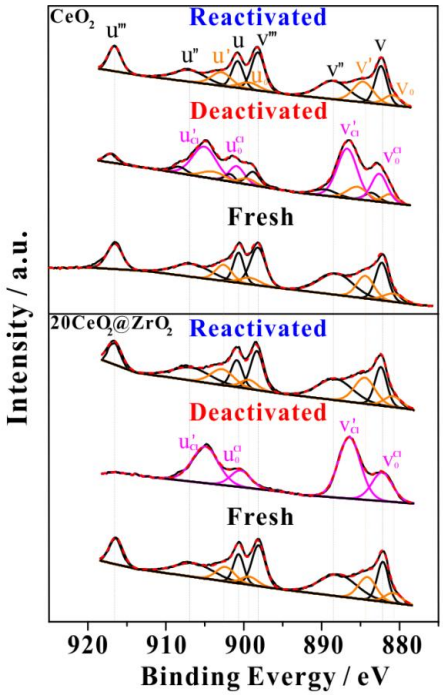

Figure S3. Ce3d XPS of fresh, deactivated and re-activated CeO_2 (top panel) and $20CeO_2@ZrO_2$ (bottom panel). The Ce^{4+} peaks from CeO_2 are labelled by v, v'', v''', u, u'', u''' in black, while the Ce^{3+} peaks from CeO_2 are labelled by v', v_0, u', u_0 in orange. The spectral features of Ce^{3+} in $CeCl_3$ are labelled by v_0^{Cl}, v'_{Cl}, u_0^{Cl} and u'_{Cl} in magenta.

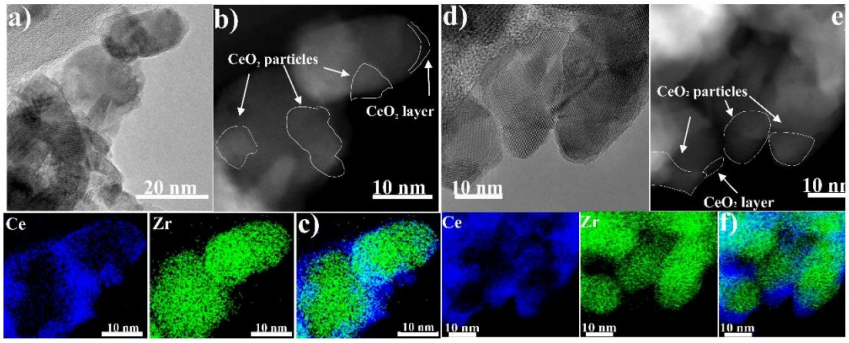

Figure S4. Direct comparison between TEM images of **a)** fresh and **d)** reactivated $20CeO_2@ZrO_2$, HAADF-STEM images of **b)** fresh and **e)** reactivated $20CeO_2@ZrO_2$, XEDS maps of overlap of Ce (blue) and Zr (green) of **c)** fresh and **f)** reactivated $20CeO_2@ZrO_2$. Images of fresh $20CeO_2@ZrO_2$ were taken from **Ref. 3**.

References

1. Y. Sun, C. Li, I. Djerdj, O. Khalid, P. Cop, J. Sann, T. Weber, S. Werner, K. Turke, Y. Guo, B.M. Smarsly, H. Over, Oxygen storage capacity versus catalytic activity of ceria-zirconia solid solutions in CO and HCl oxidation. *Catal. Sci. Tech.* **2019**, *9*, 2163-2172.
2. E. Aneggi, C. de Leitenburg, A. Trovarelli, On the role of lattice/surface oxygen in ceria-zirconia catalysts for diesel soot combustion. *Catal. Today* **2012**, *181,* 108-115.
3. Y. Sun, P. Cop, I. Djerdj, X. Guo, T. Weber, O. Khalid, Y. Guo, B.M. Smarsly, H. Over, CeO_2 Wetting Layer on ZrO_2 Particle with Sharp Solid Interface as Highly Active and Stable Catalyst for HCl Oxidation Reaction. *ACS Catal.* **2019**, *9*, 10680-10693.
4. P. Burroughs, A. Hamnett, A.F. Orchard, G. Thornton, Satellite Structure in the X-ray Photoelectron Spectra of some Binary and Mixed Oxides of Lanthanum and Cerium. *J. Chem. Soc., Dalton Trans.* **1976**, *17*, 1686-1698.
5. M. Romeo, K. Bak, J. El Fallah, F. Le Normand, L. Hilaire, XPS Study of the Reduction of Cerium Dioxide. *Surf. Interface Anal.* **1993**, *20*, 508-512.
6. C. Li, Y. Sun, I. Djerdj, P. Voepel, C.-C. Sack, T. Weller, R. Ellinghaus, J. Sann, Y. Guo, B.M. Smarsly, H. Over, Shape-Controlled CeO_2 Nanoparticles: Stability and Activity in the Catalyzed HCl Oxidation Reaction. *ACS Catal.* **2017**, *7*, 6453-6463.

5.4 List of Peer-Reviewed Publications

1. Yu Sun, Chenwei Li, Igor Djerdj, Omeir Khalid, Pascal Cop, Joachim Sann, Tim Weber, Sebastian Werner, Kevin Turke, Yanglong Guo*, Bernd M. Smarsly*, Herbert Over*. Oxygen Storage Capacity versus catalytic activity in the CO and HCl oxidation: A Case study of Ceria-Zirconia solid solution. Catalysis Science&Technology. 2019, **9**, 2163-2172.

2. Yu Sun, Pascal Cop, Igor Djerdj, Xiaohan Guo, Tim Weber, Omeir Khalid, Yanglong Guo*, Bernd M. Smarsly*, Herbert Over*. CeO_2 Wetting Layer on ZrO_2 Particle with Sharp Solid Interface as Highly Active and Stable Catalyst for HCl Oxidation Reaction. ACS Catalysis. 2019, **9**, 10680-10693.

3. Yu Sun, Franziska Hess, Igor Djerdj, Zheng Wang, Tim Weber, Yanglong Guo*, Bernd M. Smarsly*, Herbert Over*. Reactivation of CeO_2-based Catalysts in the HCl Oxidation Reaction: In situ Quantification of the Degree of Chlorination and Kinetic Modeling. ChemCatChem. 2020, **12**, 5511-5522.

4. **Yu Sun,** Chenwei Li, Yanglong Guo*, Wangcheng Zhan, Yun Guo, Li Wang, Yunsong Wang, Guanzhong Lu*. Catalytic oxidation of hydrogen chloride to chlorine over Cu-K-Sm/γ-Al_2O_3 catalyst with excellent catalytic performance. Catalysis Today. 2018, **307**, 286-292.

5. Chenwei Li, **Yu Sun**, Igor Djerdj, Pascal Vöpel, Carl-Christian Sack, Tobias Weller, Joachim Sann, Rüdiger Ellinghaus, Yanglong Guo*, Bernd M. Smarsly*, Herbert Over*. Shaped-Controlled CeO_2 Nanoparticles: Stability and Activity in the Catalyzed HCl oxidation Reaction. ACS Catalysis. 2017, **7**, 6453-6463.

6. Chenwei Li, **Yu Sun**, Franziska Hess, Igor Djerdj, Joachim Sann, Pascal Vöpel, Pascal Cop, Yanglong Guo*, Bernd M. Smarsly*, Herbert Over*. Catalytic HCl Oxidation Reaction: Stabilizing Effect of Zr-Doping on CeO_2 Nano-rods. Applied Catalysis B: Environment. 2018, **329**, 628-635.

7. Pascal Cop, Ruben Maile, **Yu Sun**, Omeir Khalid, Igor Djerdj, Patrick Esch, Sven Heiles, Herbert Over*, Bernd M. Smarsly*. Impact of Alio-/Isovalent Ions (Gd, Zr, Pr and Tb) on the Catalytic Stability of Mesoporous CeO_2 in the HCl Oxidation Reaction. ACS Applied Nano Materials. 2020, **3**, 7406-7419.

8. Chenwei Li, Franziska Hess, Igor Djerdj, Guangtao Chai, **Yu Sun**, Yanglong Guo*, Bernd M. Smarsly*, Herbert Over*. The stabilizaing effect of water and high reaction temperatures on the CeO_2-catalyst in the harsh HCl oxidation reaction. Journal of Catalysis. 2018, **357**, 257-262.

9. Jelena Bijelic, Anamarija Stankovi, Martina Medvidovi-Kosanovi, Berislav Markovic, Pascal Cop, **Yu Sun**, Sugato Hajra, Manisha Sahu, Jelena Vukmirovic, Dean Markovic, Ákos Kukovecz, Zvonko Jaglicic, Bernd M. Smarsly, Igor Djerdj*. Rational Sol-Gel-Based Synthesis Design and Magnetic, Dielectric, and Optical Properties Study of Nanocrystalline $Sr_3Co_2WO_9$ Triple Perovskite. The Journal of Physical Chemistry C. 2020, **124**, 12794-12807.

6. References

[1] J. Pérez-Ramírez, C. Mondelli, T. Schmidt, O.F.K. Schlüter, A. Wolf, L. Mleczko, T. Dreier. Sustainable Chlorine Recycling *via* Catalyzed HCl Oxidation: from Fundamentals to Implementation. Energy Environmental Science. 2011, 4, 4786-4799.

[2] R. Lin, A.P. Amrute, J. Pérez-Ramírez. Halogen-mediated Conversion of Hydrocarbons to Commodities. Chemical Reviews. 2017, 117, 4182-4247.

[3] C. W. Scheele. On Brown-Stone or Magnesia, and its Properties. Proceedings of the Royal Scientific Academy of Sweden. 1774, 35, 89-116.

[4] Market volume of chlorine worldwide from 2015 to 2022, with a forecast for 2023 to 2030. https://www.statista.com/statistics/1310477/chlorine-market-volume-worldwide/

[5] Sumitomo Chemical Co., Ltd. The Development of Improved Hydrogen Chloride Oxidation Process. Sumitomo Kagaku. 2004, I, 1-11.

[6] H. Deacon. Manufacture of chlorine. US 85370. 1868.

[7] H. Deacon. Improvement in Apparatus for the manufacture of chlorine. US 118209. 1871.

[8] H. Deacon. Improvement in the manufacture of chlorine. US 141333. 1875.

[9] H. Deacon. Improvement in the manufacture of chlorine. US 165802. 1875.

[10] H. Over, R. Schomäcker. What Makes a Good Catalyst for the Deacon Process? ACS Catalysis. 2013, 3, 1034-1046.

[11] F. Hess, B. M. Smarsly, H. Over. Catalytic Stability Employing Dedicated Model Catalysts. Accounts of Chemical Research. 2020, 53, 380-389.

[12] M. W. M. Hisham, S. W. Benson, Thermochemistry of the Deacon Process. The Journal of Physical Chemistry. 1995, 99, 6194.

[13] A.J. Johnson, A.J. Cherniavsky. Chlorine Production. US 2542961. 1951.

[14] W. F. Engel, F. Wattimena. Process for the production of Chlorine. US 3210158. 1965.

[15] F. Wattimena, W. M. H. Sachtler. Catalyst Research for the Shell Chlorine process. Studies in Surface Science and Catalysis. 1981, 7(B), 816-827.

[16] K. Seki. Development of RuO_2/Rutile-TiO_2 Catalyst for Industrial HCl Oxidation Process. Catalysis Survey from Asia. 2010, 14, 168-175.

[17] A.P. Amrute, C. Mondelli, M. Moser, G. Novell-Leruth, N. López, D. Rosenthal, R. Farra, M. E. Schuster, D. Teschner, T. Schmidt, J. Pérez-Ramírez. Performance, structure, and mechanism of CeO_2 in HCl oxidation to Cl_2. Journal of Catalysis. 2012, 286, 287-297.

[18] H.C. Yao, Y.F.Yu Yao. Ceria in automotive exhaust catalysts. Journal of Catalysis. 1984, 86, 254-265.

[19] A. Trovarelli. Catalytic Properties of Ceria and CeO_2-Containing Materials. Catalysis Reviews-Science and Engineering. 1996, 38, 439-520.

[20] M. Scharfe, P.A. Lira-Parada, V. Paunovic, M. Moser, A.P. Amrute, J. Pérez-Ramírez. Oxychlorination-Dehydrochlorination Chemistry on Bifunctional Ceria Catalysts for Intensified Vinyl Chloride Production. Angewandte Chemie International Edition. 2016, 55, 3068-3072.

[21] T. Montini, M. Melchionna, M. Monai, P. Fornasiero. Fundamentals and Catalytic Applications of CeO_2-Based Materials. Chemical Reviews. 2016, 116, 5987-6041.

[22] R. Farra, M. Garcia-Melchor, M. Eichelbaum, M. Hashagen, W. Frandsen, J. Allan, F. Girgsdies, L. Szentmiklosi, N. Lopez, D. Teschner. Promoted Ceria: A Structural, Catalytic, and Computational Study. ACS Catalysis. 2013, 3, 2256-2268.

[23] S. Urban, N. Tarabanko, C. H. Kanzler, K. Zalewska-Wierzbicka, R. Ellinghaus, S. F. Rohrlack, L. Chen, P. J. Klar, B. M. Smarsly, H. Over. Stable and Active Mixed Zr-Ce Oxides for Catalyzing the Gas Phase Oxidation of HCl. Catalysis Letter. 2013, 143, 1362-1367.

[24] M. Möller, N. Tarabanko, C. Wessel, R. Ellinghaus, H. Over, B. M. Smarsly. Electrospinning of CeO_2 nanoparticle dispersions into mesoporous fibers: on the interplay of stability and activity in the HCl oxidation reaction. RSC Advances. 2018, 8, 132-144.

[25] C. Li, Y. Sun, F. Hess, I. Djerdj, J. Sann, P. Vöpel, P. Cop, Y. Guo, B. M. Smarsly, H. Over. Catalytic HCl oxidation reaction: Stabilizing effect of Zr-doping on CeO_2 nano-rods. Applied Catalysis B: Environmental. 2018, 239, 628-635.

[26] M. Moser, T. Schmidt, C. Mondelli, F. Girgsdies, M. E. Schuster, R. Farra, L. Szentmiklósi, D. Teschner, J. Pérez-Ramírez. Supported CeO_2 catalysts in technical form for sustainable chlorine production. Applied Catalysis B: Environmental. 2013, 132-133, 123-131.

[27] P. Li, X. Chen, Y. Li, J. W. Schwank. A review on oxygen storage capacity of CeO_2-based materials: Influence factors, measurement techniques, and applications in reactions related to catalytic automotive emissions control. Catalysis Today. 2019, 327, 90-115.

[28] Z. Fei, X. Xie, Y. Dai, H. Liu, X. Chen, J. Tang, M. Cui, X. Qiao. HCl Oxidation for Sustainable Cl_2 Recycle over the $Ce_xZr_{1-x}O_2$ Catalysts: Effects of Ce/Zr Ratio on Activity and Stability. Industrial & Engineering Chemistry Research. 2014, 53, 19438-19445.

[29] S. Urban, P. Dolcetb, M. Möller, L. Chen, P. J. Klar, I. Djerdj, S. Gross, B. M. Smarsly, H. Over. Synthesis and full characterization of the phase-pure pyrochlore $Ce_2Zr_2O_7$ and the *k*-$Ce_2Zr_2O_8$ phases. Applied Catalysis B: Environmental. 2016, 197: 23-34.

[30] S. Urban, I. Djerdj, P. Dolcet, L. Chen, M. Möller, O. Khalid, H. Camaka, R. Ellinghaus, C. Li, S. Gross, P. J. Klar, B. M. Smrasly, H. Over. In Situ Study of the Oxygen-Induced Transformation of Pyrochlore $Ce_2Zr_2O_{7+x}$ to the *k*-$Ce_2Zr_2O_8$ Phase. Chemistry of Materials. 2017, 29, 9218-9226.

[31] R. Farra, M. Eichelbaum, R. Schlögl, L. Szentmiklósi, T. Schmidt, A.P. Amrute, C. Mondelli, J. Pérez-Ramírez, D. Teschner. Do observations on surface coverage-reactivity correlations always describe the true catalytic process? A Case Study on ceria. Journal of Catalysis. 2013, 297, 119-127.

[32] R. Farra, M. Garcia-Melchor, M. Eichelbaum, M. Hashagen, W. Frandsen, J. Allan, F. Girgsdies, L. Szentmiklosi, N. Lopez, D. Teschner. Promoted Ceria: A Structural, Catalytic, and Computational Study. ACS Catalysis. 2013, 3, 2256-2268.

[33] R. Farra, S. Wrabetz, M.E. Schuster, E. Stotz, N.G. Hamilton, A.P. Amrute, J. Pérez-Ramírez, N. López, D. Teschner. Understanding CeO_2 as a Deacon catalyst by probe molecule adsorption and in situ infrared characterizations. Physical Chemistry Chemical Physics. 2013, 15, 3454-3465.

[34] K. Feng, C. Li, Y. Guo, W. Zhan, B. Ma, B. Chen, M. Yuan, G. Lu. Effect of KCl on the catalytic performance of Cu-K-La/γ-Al_2O_3 catalyst for oxidation of HCl. Chinese Journal of Catalysis. 2014, 35, 1359-1363.

[35] K. Feng, C. Li, Y. Guo, W. Zhan, B. Ma, B. Chen, M. Yuan, G. Lu. An efficient Cu-K-La/γ-Al_2O_3 catalyst for catalytic oxidation of hydrogen chloride to chlorine. Applied Catalysis B: Environmental. 2015, 164, 483-487.

[36] Y. Sun, C. Li, Y. Guo, W. Zhan, Y. Guo, L. Wang, Y. Wang, G. Lu. Catalytic oxidation of hydrogen chloride to chlorine over Cu-K-Sm/γ-Al_2O_3 catalyst with excellent catalytic performance. Catalysis Today. 2018, 307, 286-292.

[36] Z. Fei, H. Liu, Y. Dai, W. Ji, X. Chen, J. Tang, M. Cui, X. Qiao. Efficient Catalytic Oxidation of HCl to Recycle Cl_2 over the CuO-CeO_2 Composite Oxide Supported on Y Type Zeolite. Chemical Engineering Journal. 2014, 257, 273-280.

[37] J. Tang, X. Chen, Z. Fei, J. Zhao, M. Cui, X. Qiao. HCl Oxidation to Recycle Cl_2 over a Cu/Ce Composite Oxide Catalyst. Part 1. Intrinsic Kinetic Study. Industrial & Engineering Chemistry Research. 2013, 52, 11897-11903.

[38] X. Chen, Y. Dai, Z. Fei, J. Tang, M. Cui, X. Qiao. HCl Oxidation to Recycle Cl_2 over a Cu/Ce Composite Oxide Catalyst. Part 2. Single-Tube-Reactor Simulation. Industrial & Engineering Chemistry Research. 2015, 54, 9931-9937.

[39] Z. Ye, R. Pan, K. Chen, Y. Ma, A. Nikiforov, J. Wang. Enhancing stability of copper-based catalysts by regulating of oxygen vacancy for resourcing HCl waste gas. Chemical Engineering Journal. 2024, 497, 154754.

[40] J. Zhao, D. Fu, N. Song, X. Yuan, X. Bi. Reaction Kinetics of HCl Catalytic Oxidation over a Supported Cu-Based Composite Industrial Catalyst. Industrial & Engineering Chemistry Research. 2019, 58, 9246-9256.

[41] J. Zhang, W. Sun, L. Zhao. Understanding the Catalytic Oxidation of Hydrogen Chloride to Chlorine from Thermodynamics and Reaction Kinetics. Industrial & Engineering Chemistry Research. 2022, 61, 13397-13407.

[42] X. Tian, S. Wang, Z. Wang, H. Wang, Y. Zhou, H. Zhong, Y. Mao. Understanding the Promotion Effect of Mn on CuO/Al_2O_3 for Catalyzed HCl Oxidation to Cl_2. ChemCatChem. 2020, 12, 3240-3248.

[43] X. Tian, S. Wang, Z. Wang, H. Wang, H. Zhong, Y. Mao. Sustainable Utilization of Chlorine *via* Converting HCl to Cl_2 over a Robust Copper Catalyst. 2020, 492, 110977-110985.

[44] A.P. Amrute, G.O. Larrazäbal, C. Mondelli, J. Pérez-Ramírez. $CuCrO_2$ Delafossite: A Stable Copper Catalyst for Chlorine Production. Angewandte Chemie International Edition. 2013, 125, 9954-9957.

[45] A.P. Amrute, Z. Lodziana, C. Mondelli, F. Krumeich, J. Pérez-Ramírez. Solid-State Chemistry of Cuprous Delafossites: Synthesis and Stability Aspects. Chemistry of Materials. 2013, 25, 4423-4435.

[46] A.P. Amrute, C. Mondelli, M.A.G. Hevia, J. Pérez-Ramírez. Temporal Analysis of Products Study of HCl Oxidation on Copper- and Ruthenium-Based Catalysts. Journal of Physical Chemistry C. 2011, 115, 1056-1063.

[47] G. Xiang, X. Shi, Y. Wu, J. Zhang, X. Wang. Size effects in Atomic-Level Epitaxial Redistribution Process of RuO_2 over TiO_2. Scientific Reports. 2012, 2, 801.

[48] Y. Liu, S. Li, X. Lu, R. Ma, Y. Fu, S. Wang, L. Zhou, W. Zhu. Insights into the sintering resistance of RuO_2/TiO_2-SiO_2 in the Deacon process: role of SiO_2. Catalysis Science & Technology. 2021, 11, 5460-5466.

[49] J. Liu, F. Dong, Y. Huang, Y. Fu, X. Lu, R. Ma, F. Zhang, S. Wang, W. Zhu. Ce-doped TiO_2 supported RuO_2 as efficient catalysts for the oxidation of HCl to Cl_2. Journal of Environmental Sciences. 2025, 149, 234-241.

[50] J. Shi, J. Li, H. Ma, D. Tu, Q. Zhang, W. Mao, J. Yang, J. Lu. HCl catalytic oxidation over Ru/Ti-Sn oxide catalysts: The influence of supports' crystal and surface structures on catalytic performance. Applied Surface Science. 2021, 570, 151137.

[51] C.H. Kanzler, S. Urban, K. Zalewska-Wierzbicka, F. Hess, S.F. Rohrlack, C. Wessel, R. Ostermann, J.P. Hofmann, B.M. Smarsly, H. Over. Electrospun Metal Oxide Nanofibres for the

Assessment of Catalyst Morphological Stability under Harsh Reaction Conditions. ChemCatChem. 2013, 5, 2621-2626.

[52] W. Wang, P. Timmer, A. Luciano, Y. Wang, T. Weber, L. Glatthaar, Y. Guo, B. M. Smrasly, H. Over. Inserted hydrogen promotes oxidation catalysis of mixed $Ru_{0.3}Ti_{0.7}O_2$ as exemplified with total propane oxidation and the HCl oxidation reaction. Catalysis Science & Technology. 2023, 13, 1395-1408.

[53] C. Mondelli, A. P. Amrute, F. Krumeich, T. Schmidt, J. Pérez-Ramírez. Shaped RuO_2/SnO_2-Al_2O_3 Catalyst for Large-Scale Stable Cl_2 Production by HCl Oxidation. ChemCatChem. 2011, 3, 657-660.

[54] A. P. Amrute, C. Mondelli, T. Schmidt, R. Hauert, J. Pérez-Ramírez. Industrial RuO_2-Based Deacon Catalysts: Carrier Stabilization and Active Phase Content Optimization. ChemCatChem. 2013, 5, 748-756.

[55] D. Teschner, G. Novell-Leruth, R. Farra, A. Knop-Gericke, R. Schlögl, L. Szentmiklosi, M.A.G. Hevia, H. Soerijanto, R. Schomäcker, J. Pérez-Ramírez. In Situ Surface Coverage Analysis of RuO_2 Catalysed HCl Oxidation Reveals the Entropic Origin of Compensation in Heterogeneous Catalysis. Nature Chemistry. 2012, 4, 739-745.

[56] D. Teschner, R. Farra, L. Yao, R. Schlögl, H. Soerijanto, R. Schomäcker, T. Schmidt, L. Szentmiklósi, A. P. Amrute, C. Mondelli, J. Pérez-Ramírez, G. Novell-Leruth, N. López. An integrated approach to Deacon chemistry on RuO_2-based catalysts. Journal of Catalysis. 2012, 285, 273-284.

[57] Y. Gong, R. Liu, L. Jiang, A. Peng, C. Xu, X. Lu, R. Ma, Y. Fu, W. Zhu, S. Wang, L. Zhou. Catalyst Development for HCl Oxidation to Cl_2 in the Fluorochemical Industry. ACS Catalysis. 2022, 12, 1098-1110.

[58] Y. Gong, S. Nie, H. Ji, L. Fu, R. Ma, X. Lu, Y. Fu, W. Zhu. Highly active and stable RuO_2/MgF_2 catalysts for efficient HCl oxidation in the fluorochemical industry. Catalysis Science & Technology. 2024, 14, 1633-1641.

[59] Y. Li, B. Lin, X. Zhang, X. Tian, Y. Zhou. Promotion of ZrO_2 on RuO_2/Al_2O_3 Catalyst for HCl Catalytic Oxidation: Effect of High Temperature Holding in Nitrogen Atmosphere. Industrial & Engineering Chemistry Research. 2024, 63, 7605-7613.

[60] D. Crihan, M. Knapp, S. Zweidinger, E. Lundgren, C. J. Weststrate, J. N. Andersen, A. P. Seitsonen, H. Over. Stable Deacon Process for HCl Oxidation over RuO_2. Angewandte Chemie International Edition. 2008, 120, 2161-2164.

[61] S. Zweidinger, D. Crihan, M. Knapp, J.P. Hofmann, A.P. Seitsonen, C.J. Weststrate, E. Lundgren, J.N. Andersen, H. Over. Reaction Mechanism of the Oxidation of HCl over RuO_2(110). Journal of Physical Chemistry C. 2008, 112, 9966-9969.

[62] H. Over. Atomic-Scale Understanding of the HCl Oxidation Over RuO_2: A Novel Deacon Process. Journal of Physical Chemistry C. 2012, 116, 6779-6792.

[63] A. P. Seitsonen, H. Over. Oxidation of HCl over TiO_2-Supported RuO_2: A Density Functional Theory Study. Journal of Physical Chemistry C. 2010, 114, 22624-22629.

[64] N. López, J. Gómez-Segura, R.P. Marín, J. Pérez-Ramírez. Mechanism of HCl oxidation (Deacon process) over RuO_2. Journal of Catalysis. 2008, 255, 29-39.

[65] M.A.G. Hevia, A.P. Amrute, T. Schmidt, J. Pérez-Ramírez. Transient mechanistic study of the gas-phase HCl oxidation to Cl_2 on bulk and supported RuO_2 catalysts. Journal of Catalysis. 2010, 276, 141-151.

[66] C.W. Li, Y. Sun, I. Djerdj, P. Voepel, C. Sack, T. Weller, R. Ellinghaus, J. Sann, Y. L. Guo, B. M. Smarsly, H. Over. Shape-Controlled CeO_2 Nanoparticles: Stability and Activity in the Catalyzed HCl Oxidation Reaction. ACS Catalysis. 2017, 7, 6453-6463.

[67] C.W. Li, F. Hess, I. Djerdj, G.T. Chai, Y. Sun, Y. L. Guo, B. Smarsly, H. Over. The stabilizing effect of water and high reaction temperatures on the CeO_2-catalyst in the harsh HCl oxidation reaction. Journal of Catalysis. 2018, 357, 257-262.

[68] P. Cop, R. Maile, Y. Sun, I. Djerdj, O. Khalid, H. Over, B. M. Smarsly. Impact of Alio-/Isovalent Ions (Gd, Zr, Pr and Tb) on the Catalytic Stability of Mesoporous CeO_2 in the HCl Oxidation Reaction. ACS Applied Nano Materials. 2020, 3, 7406-7419.

[69] M. Möller, H. Over, B. M. Smarsly, N. Tarabanko, S. Urban. Electrospun ceria-based nanofibers for the facile assessment of catalyst morphological stability under harsh HCl oxidation reaction conditions. Catalysis Today. 2015, 253, 207-218.

[70] A. Trovarelli, P. Fornasiero. Catalysis by Ceria and Related Materials. Imperial College Press, London, 2013.

[71] R. D. Shannon, C. T. Prewitt. Effective Ionic Radii in Oxides and Fluorides. Acta Crystallographica Section B. 1969, 25, 925-946.

[72] A. Trovarelli. Catalytic Properties of Ceria and CeO_2-Containing Materials. Catalysis Reviews-Science and Engineering. 1996, 38, 439-520.

[73] M. Boara, F. Giordano, S. Recchia, V. Dal Santo, M. Giona, A. Trovarelli. On the mechanism of fast oxygen storage and release in ceria-zirconia model catalysts. Applied Catalysis B: Environmental. 2004, 52, 225-237.

[74] M. Yashima, H. Arashi, M. Kakihana, M. Yoshimura. Raman Scattering Study of Cubic-Tetragonal Phase Transition in $Zr_{1-x}Ce_xO_2$ Solid Solution. Journal of the American Ceramic Society. 1994, 77, 1067-1071.

[75] M. Yashima, H. Arashi, M. Kakihana, M. Yoshimura. Synthesis of Metastable Tetragonal (t') Zirconia-Ceria Solid Solutions by the Polymerized Complex Method. Journal of the American Ceramic Society. 1994, 77, 2773-2776.

[76] M. Yashima, T. Hirose, S. Katano, Y. Suzuki, M. Kakihana, M. Yoshimura. Structural changes of ZrO_2-CeO_2 solid solutions around the monoclinic-tetragonal phase boundary. Physical Review B. 1995, 51, 8018.

[77] M. Yashima, T. Mitsuhashi, H. Takashina, M. Kakihana, T. Ikegami, M. Yoshimura. Tetragonal-Monoclinic Phase Transition Enthalpy and Temperature of ZrO_2-CeO_2 Solid Solutions. Journal of the American Ceramic Society. 1995, 78, 2225-2228.

[78] R. D. Shannon, C. T. Prewitt. Effective Ionic Radii in Oxides and Fluorides. Acta Crystallographica Section B. 1969, 25, 925-946.

[79] D. J. Kim, Lattice Parameters, Ionic Conductivities, and Solubility Limits in Fluorite-Structure MO_2 Oxide [M = Hf^{4+}, Zr^{4+}, Ce^{4+}, Th^{4+}, U^{4+}] Solid Solutions. Journal of the American Ceramic Society. 1989, 72, 1415-1421.

[80] M. P. Yeste, J. C. Hernández-Garrido, D. C. Arias, G. Blanco, J. M. Rodríguez-Izquierdo, J. M. Pintado, S. Bernal, J. A. Pérez-Omil, J. J. Calvino. Rational design of nanostructured, noble metal free, ceria-zirconia catalysts with outstanding low temperature oxygen storage capacity. Journal of Materials Chemistry A. 2013, 1, 4836-4844.

[81] C. Arias-Duque, E. Bladt, M. A. Muñoz, J. C. Hernández-Garrido, M. A. Cauqui, J. M. Rodríguez-Izquierdo, G. Blanco, S. Bals, J. J. Calvino, J. A. Pérez-Omil, M. P. Yeste. Improving the Redox Response Stability of Ceria-Zirconia Nanocatalysts under Harsh Temperature Conditions. Chemistry of Materials. 2017, 29, 9340-9350.

[82] Y. Shi, S. C. Lee, M. Monti, C. Wang, Z. A. Feng, W. D. Nix, M. F. Toney, R. Sinclair, W. C. Chueh. Growth of Highly Strained CeO_2 Ultrathin Films. ACS Nano. 2016, 10, 9938-9947.

[83] P. Cop, E. Celik, K. Hess, Y. Moryson, P. Klement, M. T. Elm, B. M. Smarsly. Atomic Layer Deposition of Defined Thin CeO_2 Layers in Ordered ZrO_2 Films and Their Impact on the Ionic/Electronic Conductivity. ACS Applied Nano Materials. 2020, 3, 10757-10766.

[84] M. Epifani, T. Andreu, S. Abdollahzadeh-Ghom, J. Arbiol, J. R. Morante. Synthesis of Ceria-Zirconia Nanocrystals with Improved Microstructural Homogeneity and Oxygen Storage Capacity by Hydrolytic Sol-Gel Process in Coordinating Environment. Advanced Functional Materials. 2012, 22, 2867-2875.

[85] W. T. Gibbons, L. J. Venstrom, R. M. De Smith, J. H. Davidson, G. S. Jackson. Ceria-based electrospun fibers for renewable fuel production *via* two-step thermal redox cycles for carbon dioxide splitting. Physical Chemistry Chemical Physics. 2014, 16, 14271-14280.

[86] G. Postole, B. Chowdhury, B. Karmakar, K. Pinki, J. Banerji, A. Auroux. Knoevenagel condensation reaction over acid-base bifunctional nanocrystalline $Ce_xZr_{1-x}O_2$ solid solutions. Journal of Catalysis. 2010, 269, 110-121.

[87] A. Trovarelli, F. Zamar, J. Llorca, C. d. Leitenburg, G. Dolcetti, J. T. Kiss. Nanophase Fluorite-Structured CeO_2-ZrO_2 Catalysts Prepared by High-Energy Mechanical Milling. Journal of Catalysis. 1997, 169, 490-502.

[88] A. Pfau, K. D. Schierbaum. The electronic structure of stoichiometric and reduced CeO_2 surfaces: an XPS, UPS and HREELS study. Surface Science. 1994, 321, 71-80.

[89] D. R. Mullins, S. H. Overbury, D. R. Huntley. Electron spectroscopy of single crystal and polycrystalline cerium oxide surfaces. Surface Science. 1998, 409, 307-319.

[90] M. A. Henderson, C. L. Perkins, M. H. Engelhard, S. Thevuthasan, C. H. F. Peden. Redox properties of water on the oxidized and reduced surfaces of CeO_2 (111). Surface Science. 2003, 526, 1-18.

[91] V. Koller, P. G. Lustemberg, A. Spriewald-Luciano, S. M. Gericke, A. Larsson, C. Sack, A. Preobrajenski, E. Lundgren, M. V. Ganduglia-Pirovano, H. Over. Critical Step in the HCl Oxidation Reaction over Single-Crystalline CeO_{2-x}(111): Peroxo-Induced Site Change of Strongly Adsorbed Surface Chlorine. ACS Catalysis. 2023, 13, 12994-13007.

[92] I. Kosacki, V. Petrovsky, H. U. Anderson, P. Colomban. Raman Spectroscopy of Nanocrystalline Ceria and Zirconia Thin Films. Journal of the American Ceramic Society. 2002, 85, 2646-2650.